Daniel Lüftner

Orbital tomography: Understanding photoemission of organic molecular films

Doctoral thesis

written at the Department of Physics
University of Graz

under the supervision of
Assoc.-Prof. Dr. Peter Puschnig

Graz, 2015

Abstract

In this work the electronic and geometric structure of interfaces of organic thin films with metallic substrates is studied using the orbital tomography technique. Orbital tomography combines angle resolved photoemission spectroscopy experiments with calculations within the framework of density functional theory and is based on the approximation of the final state by a simple plane wave in the theoretical description of the photoemission process. With this approximation, the experimental data is interpreted as the Fourier transform of the initial state molecular orbitals under investigation.

With the help of orbital tomography, the azimuthal alignment of copper-II-phthalocyanine on Au(110) as well as the level alignment of PTCDA and copper-II-phthalocyanine co-adsorbed on Ag(111) is unambiguously determined. In order to include effects arising from intermolecular band dispersion or from the interaction of he molecules with the substrate, extended systems are included in the simulation of angle resolved photoemission intensity maps. Thereby the experimental photoemission intensity of pentacene on Cu(110) is found to behave like that of the isolated molecule modulated by the band dispersion due to intermolecular interactions. The orbital level alignment of the bulk phase of quinacridone is obtained in excellent agreement with photoemission experiments using an optimally-tuned screened range-separated hybrid functional.

Furthermore, images of individual molecular orbitals are obtained with the only assumption of the wave function to be confined to a region, defined by the spatial extend of the molecule. Using this assumption, an iterative procedure, commonly applied in x-ray diffraction experiments, allows for the recovery of the phase information, that is lost in the experiment. The so obtained orbitals orbitals are found to be in excellent agreement with calculated one electron orbitals obtained within density functional theory.

Kurzzusammenfassung

In dieser Arbeit wird die elektronische und geometrische Struktur von organisch-metallischen Grenzschichten mithilfe der sogenannten Orbitaltomografie untersucht. Diese Methode beruht auf der Näherung des Endzustandes der Photoelektronenspektroskopie durch eine ebene Welle und erlaubt einen systematischen Vergleich von winkelaufgelösten Photoelektronenspektroskopieintensitäten mit der Fourier Transformation der untersuchten Orbitale, welche im Rahmen der Dichtefunktionaltheorie bestimmt werden.

Mithilfe der Orbitaltomografie ist es gelungen, die azimutale Anordnung von Kupferphthalocyanin auf einer Au(110) Oberfläche sowie die elektronische Struktur einer gemischten PTCDA und Kupferphthalocyanin Monolage auf Ag(111) eindeutig zu bestimmen. Effekte von intermolekularer Banddispersion und Wechselwirkungseffekte der Moleküle mit dem metallischen Substrat können in der Simulation berücksichtigt werden. Mit dieser Erweiterung kann gezeigt werden, dass sich die experimentelle Photoemissionsintensität von Pentacen auf Cu(110) durch eine Überlagerung von isoliertem Molekülsignal mit Modulationen durch intermolekulare Banddispersion erklären lässt. Die elektronische Struktur von Chinacridon in einer seiner Kristallstrukturen kann in ausgezeichneter Übereinstimmung mit experimentellen Photoemissionsdaten mit einem so genannten "optimally-tuned range-separated" Hybrid-Funktional berechnet werden.

Weiters werden Bilder von einzelnen Molekülorbitalen ausgehend von gemessenen Photoemissionsdaten präsentiert. Als einzige Näherung wird dabei vorausgesetzt, dass die Wellenfunktion räumlich auf die Größe des Moleküls beschränkt ist. Dadurch kann ein iteratives Verfahren, ursprünglich für Röntgenbeugungsexperimente entwickelt, verwendet werden, mit dem die im Experiment verlorengegangene Phaseninformation wiederhergestellt werden kann. Die so ermittelten Orbitale stimmen gut mit berechneten Ein-Eletronorbitalen aus der Dichtefunktionaltheorie berein.

Contents

Chapter 1

Introduction

The field of organic electronics is steadily growing and in the meanwhile organic devices started to play a role in our everyday lives [1]. Already back in 1948, crystals of metal-free and copper phthalocyanine have been identified as semiconductors and their thermally activated conductivity has been associated with electron bands arising from overlapping intermolecular π-orbitals [2]. It took, however, almost 30 years until the field started to emerge with the discovery of relative high electrical conductivities in polyacetylene, when it is doped with halogens, in 1977 [3]. The authors could vary the properties of the conducting polymer *"from insulator to semiconductor to metal"*[1]. In the second half of the 1980s, the first organic based devices ranging from organic photovoltaics [4] over organic light emitting diodes [5–7] to organic thin-film transistors [8, 9] have been fabricated. Since then, an enormous number of works dealing with the topic of organic based devices have been published and the field is still growing. This may be evidenced by a literature search at the Scopus database[2] using the keywords "*organic device*". For the years 1990 to 2014 this search delivered about 58000 documents, with more than 18% within the last 2 years.

Devices based on organic materials have, compared to their conventional inorganic semi-conducting counterparts, the advantages of mechanical flexibility and low production costs due to the possibility of being produced through printing processes. They are lightweight, their optoelectronic properties are easy tunable and they have further interesting physical properties which allow for a large variety of applications [10, 11], consisting of organic transistors [12, 13], organic solar cells with relative high efficiencies [14–16], organic light emitting diodes that are flexible and have a high performance [17, 18] or photo diodes [19].

[1] from Ref. [3]. In 2000 Alan J. Heeger, Alan G. MacDiarmid and Hideki Shirakawa were jointly awarded for the Nobel Prize in Chemistry for their work on conducting polymers.

[2] Abstract and citation database of peer-reviewed research literature www.scopus.com, February 2015.

For a systematic improvement of such organic devices, a detailed and fundamental understanding of the electronic, chemical and optical properties of the materials is crucial. For interfaces between organic and inorganic materials, which necessarily occur in actual devices, such a fundamental understanding is often still lacking. The experimental techniques to study the electronic structure of such interfaces are scanning tunneling spectroscopy (STS) and ultraviolet photoemission spectroscopy (UPS) [20]. While STS is limited to energies within a few eV from the Fermi level, with UPS it is possible to measure the valence band electronic structure several eV below the Fermi level. However, the interpretation of the measured UPS spectra from thin molecular layers remains difficult as the results depend on the experimental setup like geometry and used photon energy. Also, a direct comparison of the UPS data with calculated density of states (DOS) obtained with *ab initio* density functional theory (DFT) calculations in order to interpret the experimental results is problematic. On the one hand this is due to the limitations of DFT calculations based on standard approximations for exchange-correlation (xc) effects which may lead to wrong orbital level alignment and possibly ordering. More accurate calculations based on more sophisticated theoretical models such as many body perturbation theory are still computational too expensive to treat the whole organic/inorganic interface. On the other hand, individual UPS spectra, taken at specific emission directions, cannot be interpreted as a DOS at all, because transition probabilities that occur in the photoemission process, for instance, depend on the molecular arrangement and further experimental conditions and, therefore on the emission direction, Thus certain molecular states may be underestimated in the individual energy distribution curves.

Recently, a technique called orbital tomography (OT) has been introduced [21, 22]. This technique combines and compares the results of angle resolved photoemission spectroscopy (ARPES) with cuts through the Fourier Transform (FT) of molecular orbitals obtained with DFT and is based on the approximation of the final state of the photoemission process by a plane wave [23–26]. With OT it is not only possible to clearly associate individual molecular orbitals with intensity peaks in the photoemission spectrum, also a deconvolution of such peaks with contributions from various molecular states is possible and a definite level alignment and ordering of the molecule's frontier orbitals may be obtained [22]. Such results are of particular interest, since the frontier orbitals determine the electronic and optical properties of the molecule. There are, however, more potential applications of the OT technique as for instance the molecular orientation of organic films at the interface may be determined [27–29] or information on the spatial structure of individual molecular orbitals may be obtained [25, 26, 30]. In general, it is difficult to probe to the spatial structure of individual orbitals experimentally and the experimental techniques that provide such an information are complex and often hard to interpret. As examples, scanning tunneling

microscopy (STM) utilizing functionalized tips [31–33] or the interpretation of coherent high harmonic radiation of molecules generated from infrared laser pulses [34–36] are mentioned. Mugarza et al. [25] have shown that ARPES data may be used to obtain the wave functions of laterally confined surface states from a stepped Au(111) surface, when using a technique commonly applied in x-ray diffraction [37, 38].

The aim of this work is to study the electronic structure of organic-metallic interfaces using OT and thereby the method should be further developed and expanded. This development is driven by various questions. One of them is, whether it is possible to adapt the oversampling method [25, 37, 38] to two dimensional ARPES data of extended molecular monolayers and recover the phase information, which is lost in the ARPES experiment, leading to two dimensional images of the measured orbitals. A second major issue of this work is the investigation of the influence of the metallic substrate on the photoemission signal. Therefore, extended systems, where the metallic substrate may be included, have to be taken into account in the simulation of photoemission intensities. In further work, the OT approach is applied to clarify the electronic and geometric structure of new organic/metallic interfaces. In particular, hetero-organic monolayers, that consist of more than one type of molecule are investigated. Finally, we address the point of reliable orbital energies, obtained with DFT, which are known to be only approximations to electron removal energies and which may be in error with experiment, when calculated with standard approximations for the xc potential. For that purpose, we perform DFT calculations utilizing hybrid exchange-correlation functionals where a fraction of Fock exchange is included. Doing so, parts of the self interaction error of standard functionals may be mitigated. In addition, the performance of a rather new class of range-separated hybrid xc functionals with optimally tuned parameters is tested and compared to experimental removal- and quasiparticle energies obtained within the GW approximation. As test systems we have chosen the model organic molecules pentacene (5A), 3,4,9,10-perylene tetracarboxylic dianhydride (PTCDA), copper-II-phthalocyanine (CuPc) and quinacridone (5Q) on different coinage metal substrates. On the one hand, these molecules are technologically interesting and play a role in actual organic devices [39–43], on the other hand, they are well studied in numerous fundamental investigations [44–50].

This work is organized as follows. In Chapter 2 an overview of all theoretical methods, which are used in this work, will be given. First DFT will be introduced, covering its basic theorems and equations and the standard approximations for the xc energy. Then we discuss the limitations of these approximations when we are interested in properties such as electron removal energies and show possible ways to remedy the errors that occur in this context within DFT. The next part of Chapter 2 is dedicated to the GW approximation [51], which is a more elaborated method within many-body perturbation theory. We introduce

the concepts of the one particle Greens function, which may be related to the one particle spectral function probed in photoemission experiments, and the self energy operator, which describes the xc effects between the electrons. That is followed by a description of how to perform actual GW calculations in the G_0W_0 approach [52, 53]. The final part of this chapter is a presentation of the OT technique, with a short description of the experimental setup of ARPES followed by the basic equations and approximations used in this method.

Chapter 3 deals with the imaging of molecular orbitals. We introduce the phase recovery procedure and apply it to ARPES data of altogether five molecular orbitals and compare the resulting two dimensional orbital images to those obtained with DFT.

The following Chapters 4 to 6 all deal with the application of OT to various organic/metallic interfaces. Chapter 4 focuses on the determination of the molecular orientation of CuPc on the Au(110) surface with the help of OT and includes results of the full CuPC/Au110 interfaces utilizing a hybrid functional in order to improve the agreement of the experimental and ab-initio electronic structure. In Chapter 5, the electronic and geometric structure of a hetero-organic PTCDA and CuPc monolayer on Ag(111) is extensively studied experimentally, including low energy electron diffraction (LEED), normal incidence x-ray standing wave (NIXSW), STM, STS and ARPES measurements and theoretically using DFT. For that system we observe and explain a rather unexpected interplay of geometric and electronic properties. In Chapter 6 the organic molecule pentacene on Cu and Ag substrates is investigated. For these systems the OT approach is expanded to describe also extended systems. The expansion is necessary to account for effects which arise from intermolecular dispersion or to include substrate effects in the calculation of ARPES momentum maps.

Finally, in Chapter 7, we turn to the problem of the reliability of orbital energies, which are calculated within DFT. We perform a series of calculations of isolated and bulk quinacridone with various approximations for the xc potential and compare the results with those of photoemission experiments and GW calculations and thereby successfully characterize the electronic structure of quinacridone.

Chapter 2

Methodological Background

All theoretical calculations presented in this work are obtained within the framework of density functional theory or within a many-body perturbation theory framework calculated on top of DFT calculations. Therefore in this chapter an overview of the basic ideas, and the limitations of DFT will be given. The first part of this chapter, dealing with DFT, will be thematically guided by the Nobel Lecture of one of the inventors of DFT, Walter Kohn [54]. This section will be followed by an introduction into the GW formalism and in the last section of this chapter, the theoretical modeling of ARPES data used throughout this work, will be presented.

2.1 Density Functional Theory

2.1.1 The many body problem

In order to compute the properties of any system of interacting electrons, i.e. electrons in molecules or solids one has to deal with the many-body problem. The non-relativistic and time-independent Schrödinger equation for the electronic problem is

$$H\Psi = E\Psi. \tag{2.1}$$

Here $\Psi = \Psi(\mathbf{r}_1, \cdots, \mathbf{r}_N)$ is the many-electron wave function, with $\{\mathbf{r}_i\}$ being the coordinate of space and spin of the i-th of N electrons. The Hamiltonian H of eq. 2.1 takes the following form:

$$H = -\sum_{i=1}^{N} \frac{\hbar^2}{2m_e}\nabla_i^2 + \frac{1}{4\pi\varepsilon_0}\sum_{i\neq j}\frac{e^2}{|\mathbf{r}_i - \mathbf{r}_j|} - \frac{1}{4\pi\varepsilon_0}\sum_{i,a}\frac{e^2 Z_a}{|\mathbf{R}_a - \mathbf{r}_i|}. \tag{2.2}$$

The first term accounts for the kinetic energy of the electrons while the second and third term represent the Coulomb interaction between the electrons among themselves and between electrons and nuclei, respectively. Note that, in the Hamiltonian as given by Eq. 2.2, the Born-Oppenheimer approximation [55] is already taken into account, and will it be kept throughout this work. The Born-Oppenheimer approximation can be reasoned by the fact that the atomic nuclei are much heavier than the electrons and for this reason, the motion of the electrons may be decoupled from that of the nuclei. Therefore, the kinetic energy of the nuclei can be neglected, a term which has its origin in the repulsion between the atomic nuclei becomes a constant and the coordinates of the nuclei $\{\mathbf{R}_a\}$ enter the wave function Ψ in a parametric form. Note that, for the remainder of the following two sections, we will make use atomic units, such that the following relation is valid

$$m_e = \hbar = \frac{e^2}{4\pi\varepsilon_0} = 1. \tag{2.3}$$

Although the Born Oppenheimer approximation somewhat reduces the complexity of the problem, we still have to treat the full many-electron wave function. The complexity of this problem scales exponentially with the number of electrons. In order to give an impression of that complexity, consider the following example: If one wants to store the many-body wave function of a simple O_2 molecule on a regular grid with 10 points in each direction, this produces altogether 10^{48} data points. Assuming 128-bit double precision complex numbers, each of the points needs 8 bytes of storage. This leads to the enormous amount of approximately 10^{40} Gbytes of data. The mass of all Digital Versatile Discs (DVDs), of which each may save 4.7 Gbyte and has a mass of 16 g, that is necessary to store this amount of data is of the order of 10^{38} kg and thereby exceeds $\frac{1}{1000}$ of the mass of our galaxy, the Milky way.

This means it is virtually impossible to treat the full many-body wave function and one has to find further approximations for $\Psi(\{\mathbf{r}_i\})$. One of the first attempts was suggested by Hartree, who used a simple product ansatz and approximated Ψ as a product of one-particle wave function $\phi_i(\mathbf{r}_i)$

$$\Psi_P(\mathbf{r}_1, \cdots, \mathbf{r}_N) = \phi_1(\mathbf{r}_1)\phi_2(\mathbf{r}_2)\cdots\phi_N(\mathbf{r}_N). \tag{2.4}$$

These one-particle wave functions are solutions of one-particle Schrödinger equations, where all possible interaction terms are neglected but a so called Hartree potential is introduced, which accounts for an average field of all other electrons. The product ansatz has a major problem: it violates the antisymmetry requirement of a wave function, that is describing a fermion, as clearly may be seen, Ψ_P fulfills:

$$\Psi_P(\mathbf{r}_1, \cdots, \mathbf{r}_i, \cdots, \mathbf{r}_j, \cdots, \mathbf{r}_N) = \Psi_P(\mathbf{r}_1, \cdots, \mathbf{r}_j, \cdots, \mathbf{r}_i, \cdots, \mathbf{r}_N). \tag{2.5}$$

This deficiency of the simple one-particle product may be cured if a Slater-determinant is used instead. The wave function then takes the form

$$\Psi_{SD}(\mathbf{r}_1, \cdots, \mathbf{r}_N) = \frac{1}{\sqrt{N!}} \begin{vmatrix} \phi_1(\mathbf{r}_1) & \phi_2(\mathbf{r}_1) & \cdots & \phi_N(\mathbf{r}_1) \\ \phi_1(\mathbf{r}_2) & \phi_2(\mathbf{r}_2) & \cdots & \phi_N(\mathbf{r}_2) \\ \vdots & \vdots & \ddots & \vdots \\ \phi_1(\mathbf{r}_N) & \phi_2(\mathbf{r}_N) & \cdots & \phi_N(\mathbf{r}_N) \end{vmatrix}. \tag{2.6}$$

In such a representation, each electron $\{\mathbf{r}_i\}$ may be associated with every orbital $\{\phi_j\}$ and the electrons become indistinguishable. Assuming the wave function may be approximated by a single Slater-determinant and using the variational theorem, i.e. minimizing the energy with respect to changes in the orbital, leads to the Hartree-Fock (HF) method. Also the HF approach leads to single-particle Schrödinger equations, the so-called HF equations, where a non-local exchange term is included.

2.1.2 Density Functional theory

All methods mentioned in the previous chapter are based on the wave functions, which depend on $3N$ coordinates. In DFT the basic variable is the electron density $n = n(\mathbf{r})$, which depends on 3 coordinates only (4 if spin is included). However, it is not a priori clear if it is possible to express the properties of the interacting many-electron problem in terms of the density.

The Hohenberg-Kohn theorem

That this is indeed possible was shown by Hohenberg and Kohn [56] and was formulated in two basic theorems. The first of these two theorems states:

> The external potential $v(\mathbf{r})$ is a unique functional of the density $n(\mathbf{r})$, apart from a trivial additive constant.

Hohenberg and Kohn have given the proof by "*reductio ad absurdum*", under the assumption of a non-degenerate ground state density. Here, we follow their proof and repeat it in the following paragraphs.

Consider a system of interacting electrons, that experience an external potential $v(\mathbf{r})$ and have the ground state Ψ. Now assume there is a second potential $v'(\mathbf{r})$ with the (different) ground states Ψ'. Ψ and Ψ' lead to the same density

$n(\mathbf{r})$ but they are different as long as the potentials differ not just by constant (i.e. $v'(\mathbf{r}) - v(\mathbf{r}) \neq \text{const.}$). That is, because they are solutions to different Schrödinger equations with the Hamiltonians H and H', respectively. Exploiting the variational principle, we get the inequality

$$\begin{aligned} E &= \langle \Psi | H | \Psi \rangle \\ &= \int d^3r v(\mathbf{r}) n(\mathbf{r}) + \langle \Psi | T + U | \Psi \rangle < \langle \Psi' | H | \Psi' \rangle \\ &= \int d^3r v(\mathbf{r}) n(\mathbf{r}) + \langle \Psi' | T + U | \Psi' \rangle, \end{aligned} \tag{2.7}$$

where T and U are the kinetic energy and the electro-static interaction energy operator, respectively. Because $v(\mathbf{r})$ and $v'(\mathbf{r})$ lead to the same density $n(\mathbf{r})$ and with $E' = \langle \Psi' | H' | \Psi' \rangle$ it follows

$$E < E' + \int d^3r [v(\mathbf{r}) - v'(\mathbf{r})] n(\mathbf{r}). \tag{2.8}$$

Switching primed and unprimed variables leads to the same result, such that:

$$E' < E + \int d^3r [v'(\mathbf{r}) - v(\mathbf{r})] n(\mathbf{r}). \tag{2.9}$$

The addition of Eq. 2.8 and Eq. 2.9 leads to the contradiction

$$E' + E < E' + E. \tag{2.10}$$

Therefore, $v(\mathbf{r})$ and $v'(\mathbf{r})$ cannot differ by more than a constant, if they give rise to an identical density $n(\mathbf{r})$ and the Hohenberg-Kohn theorem has been proven. Note that the proof presented above has used the assumption of a non-degenerate ground state. Another problem that arises in this context has been raised by Levy [57] and Lieb [58] and is known as the problem of the $v(\mathbf{r})$ represent ability. They have shown that there exist well-behaved densities, which integrate up to the number of electrons but where no corresponding external potential exist that reproduces the density through solution of the Schrödinger equation. However, in practice such cases seem not to limit the applicability of DFT.

Another important finding that follows from the Hohenberg-Kohn theorem is that beside the external potential, also the full Hamiltonian and therefore the many-body wave function may be determined. This has the consequence that the expectation value of any observable is a functional of the density. In particular this is true for the expectation value of the sum of kinetic energy and Coulomb interaction energy, which is a *universal* functional of the density

$$F[n] = \langle \Psi | T + U | \Psi \rangle. \tag{2.11}$$

Consequently, that also holds for the total energy of a system, which is known as the *Hohenberg Kohn minimum principle* or the second Hohenberg-Kohn theorem:

> The total energy of a system is a functional of the density, that takes its global minimum, the ground state energy, at the ground state density.

The theorem will now be demonstrated using the constrained search method according to Levy [57]. The starting point is the ground state energy E of a system of interacting electrons which according to the Ritz minimum principle is given by

$$E = \min_{\tilde{\Psi}} \langle \tilde{\Psi} | H | \tilde{\Psi} \rangle, \tag{2.12}$$

where $\tilde{\Psi}$ is a trial wave function. Hohenberg and Kohn have written the minimal principle in terms of trial densities $\tilde{n}(\mathbf{r})$. In the constrained search method, the minimization is decoupled into two separated steps. In the first step, one minimizes over all wave functions that correspond to a given density. In a second step, one minimizes over all densities in order to gain the ground state energy. If all wave functions that are related to one given density $\tilde{n}(\mathbf{r})$ are represented by $\{\tilde{\Psi}[\tilde{n}]\}$, then the first minimization step may be written as:

$$\begin{aligned} E[\tilde{n}(\mathbf{r})] &= \min_{\{\tilde{\Psi}[\tilde{n}(\mathbf{r})]\}} \langle \tilde{\Psi} | H | \tilde{\Psi} \rangle \\ &= F[\tilde{n}(\mathbf{r})] + \int d^3 r v(\mathbf{r}) \tilde{n}(\mathbf{r}). \end{aligned} \tag{2.13}$$

In Eq. 2.13 the functional $F[\tilde{n}(\mathbf{r})]$ is independent of the external potential and is given by

$$F[\tilde{n}(\mathbf{r})] = \min_{\tilde{\Psi}} \langle \tilde{\Psi} | T + U | \tilde{\Psi} \rangle. \tag{2.14}$$

Now the second step of the minimization is applied and doing so, the total energy of the ground state is obtained by minimizing the functional $E[\tilde{n}(\mathbf{r})]$ with respect to the density

$$\begin{aligned} E &= \min_{\{\tilde{n}(\mathbf{r})\}} E[\tilde{n}(\mathbf{r})] \\ &= \min_{\{\tilde{n}(\mathbf{r})\}} \left[F[\tilde{n}(\mathbf{r})] + \int d^3r v(\mathbf{r})\tilde{n}(\mathbf{r}) \right]. \end{aligned} \tag{2.15}$$

Finally, Eq. 2.15 represents the Hohenberg-Kohn minimum principle.

The Kohn-Sham equations

The Hohenberg-Kohn formulation is a strict formulation of the energy in terms of the density, but it does not provide an expression for $F[n(\mathbf{r})]$, which is necessary to make practicable use of DFT. It was Kohn and Sham [59] who first suggested the form of $F[n(\mathbf{r})]$. They successfully mapped the fully interacting many electron system to a single particle system with an effective one particle potential $v_{\text{eff}}(\mathbf{r})$ that accounts for the Coulomb interactions. This is done in a way that the ground state density of the fully interacting system is the same as that of the non-interacting system to which it is mapped on. The expression for the functional $F[n(\mathbf{r})]$ in the interacting system is

$$F[\tilde{n}(\mathbf{r})] = T_s[\tilde{n}(\mathbf{r})] + \frac{1}{2}\int d^3r d^3r' \frac{\tilde{n}(\mathbf{r})\tilde{n}(\mathbf{r}')}{|\mathbf{r}-\mathbf{r}'|} + E_{xc}[\tilde{n}(\mathbf{r})], \tag{2.16}$$

where $T_s[\tilde{n}(\mathbf{r})]$ is the kinetic energy of the *non-interacting* system, the second term is the classical Hartree energy and the last term $E_{xc}[\tilde{n}(\mathbf{r})]$ is the so-called exchange-correlation energy functional. It is defined by Eqs. 2.14 and 2.16 and includes all remaining electron-electron interactions, which are not captured by the first two terms. Thereby all possible many-body effects are part of $E_{xc}[\tilde{n}(\mathbf{r})]$. Next we apply the variational problem for the density functional with respect to the density and include the constraint that ensures that the density integrates to the correct particle number, by introducing a Lagrangian multiplier μ

$$\frac{\delta}{\delta\tilde{n}(\mathbf{r})}\left[E[\tilde{n}(\mathbf{r})] - \mu\int \tilde{n}(\mathbf{r})d^3r \right]_{\tilde{n}(\mathbf{r})=n(\mathbf{r})} = 0. \tag{2.17}$$

Let us now define the effective potential $v_{\text{eff}}(\mathbf{r})$ as the sum of external, Hartree, and the exchange-correlation potential

$$v_{\text{eff}}(\mathbf{r}) = v_{ext}(\mathbf{r}) + \int d^3r' \frac{n(\mathbf{r}')}{|\mathbf{r}-\mathbf{r}'|} + v_{xc}(\mathbf{r}), \tag{2.18}$$

where the exchange-correlation potential is given by the functional derivative of the exchange-correlation energy at the ground state density $n(\mathbf{r})$

$$v_{xc}(\mathbf{r}) = \left.\frac{\delta E_{xc}[\tilde{n}(\mathbf{r})]}{\delta \tilde{n}(\mathbf{r})}\right|_{\tilde{n}(\mathbf{r})=n(\mathbf{r})}. \tag{2.19}$$

With these definitions, we may now rewrite Eq. 2.17 using the effective potential $v_{\text{eff}}(\mathbf{r})$

$$\begin{aligned} 0 &= \frac{\delta}{\delta \tilde{n}(\mathbf{r})}\left[E[\tilde{n}(\mathbf{r})] - \mu \int \tilde{n}(\mathbf{r}) d^3r\right] \\ &= \frac{\delta T_s}{\delta n(\mathbf{r})} + v_{ext}(\mathbf{r}) + \int d^3r' \frac{n(\mathbf{r}')}{|\mathbf{r}-\mathbf{r}'|} + \frac{\delta E_{xc}[\tilde{n}(\mathbf{r})]}{\delta \tilde{n}(\mathbf{r})} - \mu \\ &= \frac{\delta T_s}{\delta n(\mathbf{r})} + v_{\text{eff}}(\mathbf{r}) - \mu. \end{aligned} \tag{2.20}$$

The energy functional of a non-interacting system of electrons thatis subject to an arbitrary external potential $v_{\text{eff}}(\mathbf{r})$ is given by

$$E_s[\tilde{n}(\mathbf{r})] = T_s[\tilde{n}(\mathbf{r})] + \int d^3r v_{\text{eff}}(\mathbf{r})\tilde{n}(\mathbf{r}). \tag{2.21}$$

By applying again the Hohenberg-Kohn minimum principle for the non-interacting system we gain

$$\begin{aligned} &\frac{\delta}{\delta \tilde{n}(\mathbf{r})}\left[E_s[\tilde{n}(\mathbf{r})] - \mu \int \tilde{n}(\mathbf{r}) d^3r\right]_{\tilde{n}(\mathbf{r})=n(\mathbf{r})} \\ =&\frac{\delta T_s}{\delta n(\mathbf{r})} + v_{\text{eff}}(\mathbf{r}) - \mu = 0. \end{aligned} \tag{2.22}$$

This is essentially the same result as for the interacting system, if the effective potential defined in Eq. 2.18 is used. Thus, Kohn and Sham have concluded that the ground state density of the interacting system can be obtained by solving single-particle Schrödinger equations of the form

$$\left[-\frac{1}{2}\nabla^2 + v_{\text{eff}}(\mathbf{r})\right]\phi_j(\mathbf{r}) = \epsilon_j \phi_j(\mathbf{r}), \tag{2.23}$$

where the ground state density is given by

$$n(\mathbf{r}) = \sum_{j=1}^{N} |\phi_j(\mathbf{r})|^2. \tag{2.24}$$

Eqs. 2.23 are the so-called *Kohn-Sham (KS) equations* (for different indexes j) with $\phi_j(\mathbf{r})$ and ϵ_j being the KS-eigenstates and KS-eigenvalues, respectively. The KS-equations have to be solved self-consistently and the corresponding procedure is usually done as described in the following. The starting point is an initial guess for the density, with which the effective potential v_{eff} may be obtained. Next, one seeks the solution of the of Eqs. 2.23 and gets the single-particle wave functions $\phi_j(\mathbf{r})$ and the corresponding energies ϵ_j. The so obtained wave functions are plugged into Eq. 2.24 in order to obtain an updated density. Finally, the new density is again used to calculate a new effective potential and the next iterative cycle is started by solving the KS equations. This procedure is repeated until the density is converged. Once the ground state density is found, the ground state energy may be evaluated

$$E = \sum_{j=1}^{N_{occ}} \epsilon_j + E_{xc}[\tilde{n}(\mathbf{r})] - \int d^3r v_{xc}(\mathbf{r}) n(\mathbf{r}) - \frac{1}{2} \int d^3r d^3r' \frac{\tilde{n}(\mathbf{r})\tilde{n}(\mathbf{r}')}{|\mathbf{r} - \mathbf{r}'|}. \tag{2.25}$$

In principle the Kohn-Sham method yields the exact ground state density, given the exact expression of the exchange correlation functional is known. However, it is not, and in practice one has to find appropriate approximations for $E_{xc}[\tilde{n}(\mathbf{r})]$. In fact it is the accuracy and efficiency of this approximation that determines the usefulness of the KS procedure for a given physical system.

2.1.3 The exchange-correlation potential

In this section, first the two most common approximation for the exchange-correlation (xc) potential are presented, then their shortcomings and limitations are discussed and possible improvements are presented.

Local Density Approximation

The most simple approximation for the xc potential is the *local density approximation* (LDA), which has already been proposed by Kohn and Sham [59]. It is calculated from the from xc energy functional following Eq. 2.19. The xc energy $E_{xc}[n(\mathbf{r})]$ for the LDA is defined as

$$E_{xc}^{LDA}[n(\mathbf{r})] = \int d^3r n(\mathbf{r}) \epsilon_{xc}^{hom}\big(n(\mathbf{r})\big), \tag{2.26}$$

where ϵ_{xc}^{hom} is the xc energy density of the homogeneous electron gas. Therefore, the contribution to the xc-energy of the non-uniform system at a given $\mathbf{r}$ with a

certain density $n(\mathbf{r})$, is that of the uniform electron gas with that has the same density. The xc energy per particle can be split up into its exchange and its correlation contribution. The corresponding expression for the exchange part is known analytically and may be written as

$$\epsilon_x(n) = -\frac{3}{4}\left(\frac{3}{\pi}\right)^{\frac{1}{3}} n(\mathbf{r})^{\frac{1}{3}}. \tag{2.27}$$

Thus the LDA exchange energy is then

$$E_x^{LDA}[n(\mathbf{r})] = -\frac{3}{4}\left(\frac{3}{\pi}\right)^{\frac{1}{3}} \int d^3r n(\mathbf{r})^{\frac{4}{3}}. \tag{2.28}$$

An analytic expression for the correlation part is generally not known and therefore the correlation term has to be calculated numerically. This has been first done with high precision by Ceperly [60] and Ceperly and Alder [61] using Quantum Monte Carlo simulations. It is quite obvious that the LDA is exact for the homogeneous electron gas and is expected to give good results for non-homogeneous systems that have a slowly varying density as it is the case for instance in metals. For other systems, where the density is varying spatially faster, as it is the case for atoms or molecules, the LDA can not be expected to give accurate results. However, experience shows that the LDA performs surprisingly well also for these systems. As examples, the accuracy of ionization energies of atoms or the dissociation energies of molecules is about 10-20%, while the accuracy of calculated bond lengths utilizing the LDA reaches up to 1% [54], whereat LDA tends to underestimate the bond length. There are several reasons for the, at first unexpected, success of LDA calculations. The LDA satisfies some properties which are valid for the exact xc hole $h_{xc}(\mathbf{r}, \mathbf{r}')$, which describes the probability of finding an electron at position $\mathbf{r}'$ when another electron sits at $\mathbf{r}$. Therefore, it is the hole in the surrounding density, that the electron at $\mathbf{r}$ digs for itself. One of these properties is that the xc hole is normalized to one

$$\int d^3r' h_{xc}(\mathbf{r}, \mathbf{r}') = -1, \tag{2.29}$$

a condition which is also fulfilled by the LDA. While the the shape of the xc hole is only poorly estimated in the LDA, its spherical average, however, is quite reasonable resembled in the LDA [62]. This is in fact another reason for the success of LDA, because the electron-electron interaction only depends on this spherical average. In addition, in the LDA the exchange part is generally, about 10% too small while the correlation energy, which is usually much smaller compared to the exchange part, in terms of their absolute values, is overestimated by up to a factor of 2. Therefore, these two errors tend to cancel each other, at least partially [54] and therefore coincidentally improve the results of LDA calculations.

General Gradient Approximation

One possible way to improve the local density approximation is seemingly achieved by including higher terms in the expansion in gradients of the electron density and thereby taking into account changes of the density. Including second order terms of the form $|\nabla n|^2$ leads to the so-called *gradient expansion approximation* (GEA). However, energy functionals of the form

$$E_{xc}^{GEA}[n(\mathbf{r})] = E_{xc}^{LDA}[n(\mathbf{r})] + \int d^3r C_{xc}\big(n(\mathbf{r})\big)\frac{|\nabla n|^2}{n^{\frac{4}{3}}}, \tag{2.30}$$

do not systematically improve over the LDA, because in realistic cases, the density does not vary slowly over space [63]. An improvement of the results obtained for atoms, molecules and solids may be achieved, when the gradient expansion is done for the xc hole around the electron and appropriate cut-offs for the long range part are introduced. Such types of functionals are known as *generalized gradient approximations* (GGA) and they are formally given by

$$E_{xc}^{GGA}[n(\mathbf{r})] = \int d^3r f\big(n(\mathbf{r}), |\nabla n(\mathbf{r})|\big)n(\mathbf{r}). \tag{2.31}$$

They depend on a function of the density and its gradient $f\big(n(\mathbf{r}), |\nabla n(\mathbf{r})|\big)$. While the energy functional of the LDA is uniquely defined (via Eq. 2.26), for the GGA, there exists a variety of different ways to include the gradient of the density. As examples the common xc functionals of Becke (Becke88) [64], Perdew and Wang (PW91) [65] and that of Perdew, Burke and Ernzerhof (PBE) [66] are listed, but many others exist as well [67–71]. Although the GGA improves the results regarding bond lengths and atomization energies in some cases, such as small molecules consisting of light atoms [54], it still suffers from deficiencies that lead to errors in applied calculations. For instance, it has the same accuracy as LDA regarding the computation of lattice constants of metals, beside the error of GGA calculations has the opposite sign and tends to overestimate the bond length. Furthermore, both, LDA and GGA greatly underestimate the band gap of organic and inorganic semiconductors or insulators. The problems that standard xc functionals, such as LDA and GGA, have regarding the underestimation of the band gap or generally the interpretation of Kohn-Sham energies in terms of electron removal energies as measured in photoemission are the topic of the following section.

2.1.4 Interpretation of Kohn-Sham eigenvalues

One of the aspects of this work is the interpretation of measured photoemission spectra with the help of theoretical simulations. Therefore, the question

arises if the KS-eigenvalues $\{\epsilon_j\}$ are an adequate choice for that purpose. They have been introduced together with the KS single particle wave functions $\{\phi_j\}$ in Eq. 2.23 as auxiliary objects, necessary to calculate the *ground state* density of a non-interacting system that has the same density as the real physical system. Therefore, the KS eigenvalues in principle are not supposed to have a *"directly observable meaning"* [54], in particular not for *excited* state properties. Nevertheless, despite this given fact, in practice the KS eigenvalues are often interpreted as electron removal energies and this is often done with reasonable success. There are several works, which have dealt with the physical meaning of the KS eigenvalues [72–76] and thereby it has been shown, that there exists one exception, and there is one KS eigenvalue which indeed has a meaning. Although, there is no strictly analogue to Koopman's theorem [77] in the KS scheme, Almbladh and von Barth were able show, that the highest occupied KS eigenvalue may be related to the ionization potential, if the *exact* density is used [73]. Furthermore, Janak could show [78] that each occupied KS eigenvalue is the derivative of the energy with respect to the occupation of the corresponding state. In the literature more evidence regarding possible interpretation of KS eigenvalues may be found. For instance, Görling has shown that "*the difference of KS eigenvalues is a well-defined approximation to excitation energies*" [74] and Chong and co workers were able to "*interpret the energies of the occupied KS orbitals as approximate but rather accurate relaxed vertical ionization potentials*" [75].

To summarize, there are situations, where it is indeed reasonable to consider KS eigenvalues for the interpretation of photoemission spectra. However, the band gap problem of standard xc potentials, already mentioned in the previous section, still exists and the ambiguity regarding the interpretation of KS eigenvalues as approximation to electron removal energies remains a problem. In order to shed some light on this issue, two of the main problems of standard DFT calculations using either LDA or GGA in the context of orbital energy interpretations will be discussed. These problems are the presence of so called self interaction errors (SIE) and the absence of a derivative discontinuity (DD) in the xc energy [79].The origin and possible remedies for each of these two issues are the topics of the following section and will be discussed in detail there.

Self Interaction Error and Derivative Discontinuity

To introduce the problems associated with the self interaction error, we write down the expression for the Hartree potential once again:

$$v_H = \int d^3r' \frac{n(\mathbf{r}')}{|\mathbf{r} - \mathbf{r}'|}. \tag{2.32}$$

The calculation of the static Coulomb interaction according to Eq. 2.32 includes the interaction of one electron with *all* electrons of the system. This obviously

includes a spurious interaction of the electron with itself and is the source of the SIE. The exchange correlation term should exactly cancel this error made by evaluating the Coulomb interaction after Eq. 2.32. This is, however, not the case when an approximate functional such as LDA or GGA is used. The SIE would be a minor problem regarding the comparison with photoemission spectra, only if it would be approximately the same for each eigenvalue. Because then the whole spectrum would be shifted rigidly by the SIE and its shape would be preserved. However, this is not the case, because the SIE of one orbital is given by [80]

$$e_j = \langle \phi_j | v_H[|\phi_j|^2] | \phi_j \rangle + \langle \phi_j | v_{xc}[|\phi_j|^2] | \phi_j \rangle, \tag{2.33}$$

and it is therefore orbital dependent. The reason for this dependence may be easily rationalized when considering the fact that the Coulomb potential, which in the end determines the SIE, decays with $\frac{1}{r}$. As a consequence does the SIE of one KS eigenvalue depend on the spatial shape and extent of the corresponding orbital. In particular it has been shown, that the degree of localization of an orbital determines its SIE [80] and consequently the comparison between photoemission spectra and DFT spectra of systems which consist of a mixture of states with different degree of localization is expected to be very poor [81].

The SIE is one possible source of errors but it is not responsible for the band gap problem of LDA or GGA. Obviously, it is possible, that the highest occupied and the lowest unoccupied orbital may have the same amount of localization and therefore suffer from a similar SIE but the band gap remains underestimated. That means, even if SIEs only play a minor role, the GGA/LDA spectra may only agree with experiment up do a rigid shift. Such kind of uncertainties are related to the DD, as will be discussed now. The DD is a property of the exact xc functional and physically reflects the discontinuity, that the chemical potential μ has to obey as a function of occupation at an integer particle number, as shown by Perdew et al. [82]. In DFT, μ is defined as the functional derivative of the total energy with respect to the density, as follows from Eq.2.17, where μ has been introduced to ensure electron number conservation

$$\mu = \frac{\delta E_{tot}}{\delta n(\mathbf{r})}. \tag{2.34}$$

Perdew et al. have generalized Eq. 2.34 to charge variations that do not conserve the particle number by extending the HK functional to densities which integrate to non-integer particle number. This was achieved by introducing densities obtained from a statistical mixture of pure states for the N electron and the $N+1$ electron states [79, 82]. They showed that the energy versus particle number is made up of piecewise linear segments and is therefore continuous while its derivative ($= \mu$) is not. The slopes of the linear segments between the $N-1$ and

N point, and the N and $N+1$ point are ionization potential (IP) and electron affinity (EA), respectively. Thus, the discontinuity becomes comprehensible, and simply reflects the necessity that the IP and the EA are not equal which would mean that the fundamental gap is zero. In the KS formalism, the energy terms of the external and the Hartree potential are continuous with respect to the density and do not carry any discontinuities, so that the discontinuity may arise from the non-interacting kinetic energy or from the xc energy only [76]. Although it is possible that the kinetic energy carries part of the discontinuities, in the KS scheme the xc energy usually exhibits discontinuities, and as a consequence, there are particle number discontinuities in the xc potential v_{xc}, which is known as the already introduced DD, Δ_{xc}. According to Janak's theorem [78], each KS eigenvalue that is occupied is given by the derivative of the energy with respect to the occupation of that state

$$\epsilon_j = \frac{\delta E}{\delta n_j}, \tag{2.35}$$

which is the slope of the piecewise linear curve mentioned earlier. For the exact KS HOMO eigenvalue Eq.2.35 means that the negative IP is the slope at the integer particle number, if it is approached from below, such that

$$\epsilon_H(N-\delta) = -IP. \tag{2.36}$$

Here δ represents a positive infinitesimal which ensures that the N particle number point is indeed approached from below. The physical reason for the equality of Eq. 2.36 lies in the asymptotic behavior of the potential as summarized in Ref. [76]. For the unoccupied KS LUMO such a relation does not exist, but one can approximate the EA of the N-particle system with the IP of the $N+1$-particle system, so that we find

$$\epsilon_H(N+1-\delta) = -EA = \epsilon_H(N+\delta). \tag{2.37}$$

The expression at the right hand-side of Eq. 2.37 follows from the straight-line behavior which, at least approximately, equalizes the slope right of the N-particle with that left of the $N+1$-particle point. Furthermore, one has to consider the jump of the xc potential introduced above which has the consequence that we can write

$$\epsilon_H(N+\delta) = \epsilon_L(N-\delta) + \Delta_{xc}. \tag{2.38}$$

If we combine Eqs. 2.37 and 2.38 we obtain for the KS LUMO

$$\epsilon_L(N) = -EA - \Delta_{xc}. \tag{2.39}$$

We see that even if the KS HOMO does reflect the negative IP and the xc functional is exact, the KS LUMO will not be equal to the EA and the KS band gap will underestimate the correct fundamental gap by as much as the DD Δ_{xc}.

$$E_g = IP - EA = \epsilon_L - \epsilon_H + \Delta_{xc}. \tag{2.40}$$

Note that the discussion about the DD so far, was based on considerations of properties of the exact xc functional, which is unknown. For approximate functionals, which explicitly depend on the density and its gradient in the case of GGA, there cannot be any DD and these functionals average over the DD [76, 83]. So that, the LDA/GGA KS HOMO underestimates $-$IP by the half of Δ_{xc} and the corresponding LUMO overestimates $-$EA by approximately the same amount. Note, however, that the KS framework is exact and that the IP of finite systems may be calculated from total energy difference between the N and the $N-1$-electron system.

Possible ways of improvement

Fortunately, strategies have been found to handle the shortcomings discussed so far, and the errors may be, at least partly, extirpated. There exists a multitude of approaches, and some of them, which are utilized in this work, will be presented here. To begin with the SIE, we remember that this error ideally should be canceled appropriately by the xc term. That has lead to the strategy of using so-called hybrid functionals to reduce the SIE. In a hybrid functional one incorporates fractions of non-local HF exchange and combines it with exchange and correlation terms from a standard DFT xc functional

$$E_x^{HF} = -\frac{1}{2}\sum_{i,j} f_i f_j \int\int d^3r d^3r' \frac{\phi_i^*(\mathbf{r})\phi_j^*(\mathbf{r}')\phi_i(\mathbf{r}')\phi_j(\mathbf{r})}{|\mathbf{r}-\mathbf{r}'|}. \tag{2.41}$$

Here the indices i, j represent band index and wave vector of the one-electron Bloch states ϕ_i and ϕ_j with the corresponding occupation numbers f_i and f_j. The combination of HF and KS exchange can be either done globally as for instance in the PBE0 functional [84, 85] and the B3LYP functional [86] or in a range separated manner such as the short range hybrid functional of Heyd, Scuseria and Ernzerhof (HSE) [87, 88]. In PBE0 a fraction of 0.25 exact exchange is included in the xc part and combined with exchange and correlation from the PBE functional

$$E_{xc}^{PBE0} = 0.25\, E_x^{HF} + 0.75\, E_x^{PBE} + E_c^{PBE}. \tag{2.42}$$

The B3LYP functional, which is an abbreviation for Becke, three parameter, Lee Yang Parr, is given by

$$E_{xc}^{B3LYP} = E_x^{LDA} + a_0(E_x^{HF} - E_x^{LDA}) + a_x \Delta E_x^{B88} + \\ + E_c^{VWN} + a_c(E_c^{LYP} - E_c^{VWN}), \tag{2.43}$$

with the three parameters being $a_0 = 0.2$, $a_x = 0.72$ and $a_c = 0.81$. It was developed from a hybrid functional suggested by Becke [89] and combines HF exchange E_x^{HF} with local exchange E_x^{LDA} and the gradient corrections of the Becke88 exchange functional [64]. The correlation part consists of a combination of the Lee-Yang-Parr correlation energy which includes a local and a gradient dependent part [68] and the local Vosko-Wilk-Nusair correlation functional [90].

In a range-separated hybrid functional, the Coulomb interaction is split into a short range (SR) and a long range (LR) using a suitably smooth switching function such as the error function (see also Eq. 7.1). The HSE functional uses pure PBE exchange in the LR part and a combination of PBE exchange and HF exchange in the SR, while the correlation is treated in the PBE flavor over the whole range

$$E_{xc}^{HSE} = 0.25\, E_x^{HF,SR}(\gamma) + 0.75\, E_x^{PBE,SR}(\gamma) + E_x^{PBE,LR}(\gamma) + E_c^{PBE}. \tag{2.44}$$

Note, that all of the exchange contributions depend on the parameter γ, which is the so-called range-separation parameter and has a value of 0.11bohr^{-1} in the HSE functional [88]. The inverse of γ determines a characteristic length at which the SR interactions are negligible and the LR part begins to dominate. There are more possible variations of range separated hybrid functionals, for instance LR hybrid functionals, which are discussed in Chap. 7 in more detail.

Using a hybrid functional may indeed improve the agreement between the KS eigenvalues and results of photoemission experiments [81]. However, in order to improve the problems connected with the band gap and consistently the DD, it will not be sufficient to optimize the xc functional within the KS formalism, since there, the problems also occur for the exact xc functional, as already pointed out above. Thus, clearly any possible improvement connected with the band gap problem has to be searched outside the KS scheme. It is found within the generalized Kohn-Sham (GKS) theory proposed by Seidl et al. [91]. The GKS is an alternative, and exact realization of DFT, with the advantage, that differences between the one-particle eigenvalues incorporate, at least parts, of the DD Δ_{xc}. The idea of Seidl et al. was to replace the full interacting system by a model system which takes into account electron-electron interactions and uses part of the exchange and correlation contribution to the total energy. Furthermore, it should remain possible to represent the system by a single Slater determinant. Therefore, an energy functional $S[\Psi_{SD}] = S[\{\phi_j\}]$ of the N-electron Slater determinant

Ψ_{SD}, which is made up of the orbitals $\{\phi_j\}$, is introduced. From that functional $S[\{\phi_j\}]$ an energy functional of the density $F^S[n(\mathbf{r})]$ is constructed, derived using a constrained minimum principle

$$F^S[n(\mathbf{r})] = \min_{\{\phi_j\}\to n(\mathbf{r})} S[\{\phi_j\}], \tag{2.45}$$

where the density is calculated like in the KS scheme according to Eq. 2.24. The total energy is then given as a sum of $F^S[n(\mathbf{r})]$, a term that accounts for interaction of electrons with the ions (external potential) and a "remainder" term $R^S[n(\mathbf{r})]$ where everything else is included. The constrained search formalism is applied and the energy expression is minimized within the space of all possible Slater determinants and from that the ground state density constructed. With a Lagrange procedure similar to that for the KS scheme, the GKS equations are finally obtained [91]

$$\left[O^S[\{\phi_j\}] + v_{ext}(\mathbf{r}) + v_R(\mathbf{r})\right]\phi_j = \epsilon_j\phi_j. \tag{2.46}$$

The operator $O^S[\{\phi_j\}]$ is in general nonlocal and orbital specific. $v_R(\mathbf{r})$ is the "remainder" potential and calculated as the functional derivative of the remainder energy term, which is generally unknown and has to be approximated. There are numerous ways to map the real physical system in the GKS scheme, which depend on the choice of $S[\{\phi_j\}]$ and the KS formalism actually represents one possible choice. The KS mapping is achieved by setting $S[\{\phi_j\}]$ equal to the kinetic energy and the operator $O^S[\{\phi_j\}]$ then becomes the kinetic energy operator of the non-interacting system. The remainder potential for that case is the sum of Hartree potential and xc potential and this way the KS equations (Eq. 2.23) are recovered. Another possible realization, already presented in the work of Seidl et al. lead to the so called Hartree Fock Kohn Sham equations, and they are obtained by constructing $O^S[\{\phi_j\}]$ as the sum of the single particle kinetic energy operator and the Hartree-Fock operator. The corresponding remainder potential $v_R(\mathbf{r})$ is then a pure correlation potential and generally not known, but in contrast to the HF method, this procedure remains exact. There are many other possibly approximative realizations of the GKS scheme and in fact the hybrid functionals introduced above may be viewed within the GKS scheme [92]. However, such conventional hybrids often do not solve the band gap problem. In order to get fundamental gaps from DFT in good agreement with experiment, an appropriate choice of the the nonlocal operator in the GKS equations is necessary. This choice has to be done in a way, that the discontinuity of the chemical potential is mostly carried by the nonlocal operator. This is in contrast to the KS scheme where the discontinuity is carried by the xc potential, which has lead to the DD. Anyway, for a reasonable choice of $O^S[\{\phi_j\}]$ the DD in the remainder potential may be minimized up to a point where the GKS LUMO may well be compared

to the electron affinity and experimental gaps are well reproduced. That this is indeed possible has been shown for instance by using LR range-separated hybrid functionals [93, 94] and is also covered in Chap. 7.

2.2 The GW approximation

The second basic theory which is applied in this work is the so called GW method. The use of this different theoretical framework is motivated by its capability to be able to predict the outcome of photoemission experiments, within an ab-initio approach. As discussed in the previous section, DFT is sometimes problematic when KS eigenvalues are used as approximation to electron removal energies. It is therefore convenient to directly calculate quasi-particle energies even if they are only used as a benchmark for DFT calculations. The ab-initio method of choice for that purpose is within many body perturbation theory and in particular the GW approximation of the self energy introduced by Hedin [51] in 1965, within many body perturbation theory. Compared to DFT, the computational effort is by far greater, as the method scales with the fourth power of the problem size and still today many people work on improving the computational efficiency of the GW approach [95, 96]. In this section a brief introduction to the basics of the GW method will be given. This is mostly based on the review article of Aryasetiawan and Gunnarsson [97] and Hedin's orginal work [51].

2.2.1 The one particle Green's Function

The central object of the GW method is the one-particle Green's function. That is reasoned by the fact that the one particle spectral function, which is actually probed by the photoemission and the inverse photoemission experiment, respectively, may be directly related to the one particle Green's function $G(\mathbf{r}_1, t_1; \mathbf{r}_2, t_2)$ [98]. The Green's function describes the propagation of an additional electron from the space-time coordinates $(\mathbf{r}_2, t_2)$ to $(\mathbf{r}_1, t_1)$. The definition is given via

$$iG(\mathbf{r}_1, t_1; \mathbf{r}_2, t_2) = \langle N|T\big[\psi(\mathbf{r}_1, t_1)\psi^\dagger(\mathbf{r}_2, t_2)\big]|N\rangle, \tag{2.47}$$

where $|N\rangle$ represents the *interacting* ground state of the N electron system and T is the time ordering operator which ensures that

$$iG(\mathbf{r}_1, t_1; \mathbf{r}_2, t_2) = \begin{cases} \langle N|\psi(\mathbf{r}_1, t_1)\psi^\dagger(\mathbf{r}_2, t_2)|N\rangle & t_1 > t_2 \\ -\langle N|\psi^\dagger(\mathbf{r}_1, t_1)\psi(\mathbf{r}_2, t_2)|N\rangle & t_1 < t_2. \end{cases} \tag{2.48}$$

The field operators $\psi(\mathbf{r}, t)$ and $\psi^\dagger(\mathbf{r}, t)$, introduced in Eq. 2.47, are annihilation and creation operators, respectively and annihilate or create an electron at the

space-time point $(\mathbf{r}, t)$. The one particle Green's function may, therefore, physically be interpreted as the probability amplitude of the addition of an electron at $(\mathbf{r}_2, t_2)$ and its propagation to $(\mathbf{r}_1, t_1)$ for $t_1 > t_2$ and as the probability amplitude for the creation of a hole at $(\mathbf{r}_1, t_1)$ and its propagation to $(\mathbf{r}_2, t_2)$ for $t_2 > t_1$ [97]. Whereat the time evolution of the field operators in the Heisenberg picture is given by

$$\psi(\mathbf{r}, t) = e^{iHt}\psi(\mathbf{r})e^{-iHt}, \tag{2.49}$$

where H is the many-body Hamiltonian (Eq. 2.2), which may be rewritten in terms of the field operators as

$$H = \int d^3r\psi^\dagger(\mathbf{r})h(\mathbf{r})\psi(\mathbf{r}) + \frac{1}{2}\int d^3r d^3r'\psi^\dagger(\mathbf{r})\psi^\dagger(\mathbf{r}')v(\mathbf{r}, \mathbf{r}')\psi(\mathbf{r})\psi(\mathbf{r}'). \tag{2.50}$$

Here we introduced the abbreviation $h(\mathbf{r})$ for the one particle term of H, which consists of the kinetic energy term and a second term, that accounts for the interaction with the nuclei

$$h(\mathbf{r}) = -\frac{1}{2}\nabla^2 + \sum_a \frac{Z_a}{|\mathbf{R}_a - \mathbf{r}|}. \tag{2.51}$$

In the Hamiltonian of Eq. 2.50, $v(\mathbf{r}, \mathbf{r}')$ is the Coulomb potential and denotes the two-particle interactions

$$v(\mathbf{r}, \mathbf{r}') = \frac{1}{|\mathbf{r} - \mathbf{r}'|}. \tag{2.52}$$

Further it is useful to write down the eigenvalue equations for the N-particle ground state and for the $N + 1$ particle excited system, respectively as

$$H|N\rangle = E_N|N\rangle \tag{2.53}$$
$$H|N + 1, s\rangle = E_{N+1,s}|N + 1, s\rangle, \tag{2.54}$$

with E_N and $E_{N+1,s}$ being the corresponding eigenvalues and the index s numbers the excited states of the system.

Next we want to derive the spectral or Lehmann representation of the one particle Green's function $G(\mathbf{r}_1, t_1; \mathbf{r}_2, t_2)$. For the sake of simplicity, we will only treat the case of $t_1 > t_2$ for the moment. We start by plugging the time evolution of the field operator in the Heisenberg picture (Eq. 2.49) into the upper part of Eq. 2.48. The resulting one-particle Green's function may be written as

$$\begin{aligned} G(\mathbf{r}_1, t_1; \mathbf{r}_2, t_2) &= -i\langle N|e^{iHt_1}\psi(\mathbf{r_1})e^{-iHt_1}e^{iHt_2}\psi(\mathbf{r_2})e^{-iHt_2}|N\rangle \\ &= -i\langle N|\psi(\mathbf{r_1})e^{-i(H-E_N)t_1}e^{i(H-E_N)t_2}\psi(\mathbf{r_2})|N\rangle, \end{aligned} \tag{2.55}$$

where the second line simply follows from Eq. 2.53. Now we insert the completeness relation in Fock space, where only the $N+1$ particle numbers have to be taken into account because all other scalar products will vanish, such that

$$1 = \sum_s |N+1, s\rangle\langle N+1, s|, \tag{2.56}$$

is inserted two times into Eq. 2.55 between the field operator and the exponential function in each case. Doing so, the expression for $G(\mathbf{r}_1, t_1; \mathbf{r}_2, t_2)$ becomes

$$G(\mathbf{r}_1, t_1; \mathbf{r}_2, t_2) = -i\sum_s f_s(\mathbf{r_1})f_s^*(\mathbf{r_2})e^{-i(\epsilon_s)(t_1-t_2)}\Theta(\epsilon_s - \mu), \tag{2.57}$$

where Θ denotes the Heaviside step function and μ is the chemical potential. For the case of an additional hole, the $N-1$ system, where $t_2 > t_1$ the derivation may be done the same way and thereby one obtains the full Green's function $G(\mathbf{r}_1, t_1; \mathbf{r}_2, t_2)$, which then is given by

$$\begin{aligned} G(\mathbf{r}_1, t_1; \mathbf{r}_2, t_2) = -i\sum_s f_s(\mathbf{r_1})f_s^*(\mathbf{r_2})e^{-i(\epsilon_s)(t_1-t_2)} \\ \times [\Theta(t_1-t_2)\Theta(\epsilon_s-\mu) - \Theta(t_2-t_1)\Theta(\mu-\epsilon_s)]. \end{aligned} \tag{2.58}$$

The excitation energies ϵ_s and wave functions f_s introduced in Eqs. 2.57 and 2.58 are defined as

$$\epsilon_s = E_{N+1,s} - E_N,\ f_s(\mathbf{r}) = \langle N|\psi(\mathbf{r})|N+1, s\rangle \ \text{ for } \ \epsilon_s > \mu \tag{2.59}$$

$$\epsilon_s = E_N - E_{N-1,s},\ f_s(\mathbf{r}) = \langle N-1, s|\psi(\mathbf{r})|N\rangle \ \text{ for } \ \epsilon_s < \mu. \tag{2.60}$$

Finally we take the Fourier-transform of Eq. 2.58 and end up with the spectral representation of the one particle Green's function

$$G(\mathbf{r}_1, \mathbf{r}_2, \omega) = \sum_s \frac{f_s(\mathbf{r_1})f_s^*(\mathbf{r_2})}{\omega - \epsilon_s + i\eta\,\mathrm{sgn}(\epsilon_s - \mu)}. \tag{2.61}$$

From Eq. 2.61 it becomes clear that the quasi-particle excitation energies are the poles of the Green's function. The spectral function or the density of excited

states $A(\mathbf{r}_1, \mathbf{r}_2, \omega)$ mentioned at the beginning of this section is defined as the imaginary part of $G(\mathbf{r}_1, \mathbf{r}_2, \omega)$

$$A(\mathbf{r}_1, \mathbf{r}_2, \omega) = \frac{1}{\pi}|\mathbf{Im}G(\mathbf{r}_1, \mathbf{r}_2, \omega)| = \sum_s f_s(\mathbf{r_1}) f_s^*(\mathbf{r_2}) \delta(\omega - \epsilon_s). \tag{2.62}$$

2.2.2 The self-energy Σ and Hedin's equations

The previous section has shown that the one particle Green's function is indeed a very useful object. In addition to calculating the excitation spectrum, it may be also used to calculate the ground state energy or the expectation value of any operator in the ground state [97]. It still has to be clarified how to calculate the Green's function itself. For that purpose the concept of the self energy will be introduced and Hedin's equations will be presented without an in depth derivation or a proof. A detailed derivation can be found, for instance, in the appendix of Hedin's original work [51] or in Ref. [97] where the functional derivative method by Schwinger and Martin and Schwinger is used [99, 100].

The equation of motion of the one particle Green's function may be derived from the Heisenberg equation of motion of the field operator, which is given by

$$\begin{aligned} i\frac{\partial \psi(\mathbf{r}, t)}{\partial t} &= [\psi(\mathbf{r}, t), H] \\ &= \left[h(\mathbf{r}) + \int d^3r' v(\mathbf{r}, \mathbf{r}') \psi^\dagger(\mathbf{r}', t) \psi(\mathbf{r}', t) \right] \psi(\mathbf{r}, t), \end{aligned} \tag{2.63}$$

The bottom line of Eq. 2.63 is derived by using the Hamiltonian given in Eq. 2.50 and the anti-commutation relations of the field operator

$$\{\psi(\mathbf{r}), \psi(\mathbf{r}')\} = \{\psi^\dagger(\mathbf{r}), \psi^\dagger(\mathbf{r}')\} = 0 \tag{2.64}$$

$$\{\psi(\mathbf{r}), \psi^\dagger(\mathbf{r}')\} = \delta(\mathbf{r} - \mathbf{r}') \tag{2.65}$$

In order to write down the equation of motion for the Green's function, we introduce the abbreviation $1 = (\mathbf{r}_1, t_1)$ as it is usually done at this point. Furthermore $\delta(1, 2)$ is defined as $\delta(\mathbf{r}_1 - \mathbf{r}_2 \delta(t_1 - t_2)$ and $v(1, 2) = \dfrac{\delta(t_1 - t_2)}{|\mathbf{r}_1 - \mathbf{r}_2|}$. With these conventions the equation of motion reads [97]

$$\left(i\frac{\partial}{\partial t} - h(1) \right) G(1, 2) = \delta(1, 2) - i \int d3 v(1, 3) G(1, 3, 2, 3^+). \tag{2.66}$$

Eq. 2.66 involves a special case of the two-particle Green's function, which in general takes the form

$$G(1,2,3,4) = \langle N|T\big[\psi(1)\psi(2)\psi^\dagger(3)\psi^\dagger(4)\big]|N\rangle. \tag{2.67}$$

The consequence of Eq. 2.66 is that the knowledge of the two-particle Green's function is necessary in order to obtain the one-particle Green's function. In a subsequent step, it may be shown that the 3 particle Green's function must be known for evaluating the 2 particle Green's function and if one keeps track along this route, one finally will end up again with the full many-body Schrödinger equation and it becomes obvious, that a different strategy to obtain the Green's function has to be chosen. The strategy of choice, is to treat the interaction between particles as a perturbation to the non interacting system. This system may be characterized by G_0, the non interacting Green's function, which corresponds to the Hamiltonian $H_0 = h(\mathbf{r}) + v_H(\mathbf{r})$ and which is known. Everything else that is unknown is put into the so-called self energy, which is defined by (in frequency space) Dyson's equation

$$\Sigma(\mathbf{r}_1, \mathbf{r}_2; \omega) = G_0^{-1}(\mathbf{r}_1, \mathbf{r}_2; \omega) - G^{-1}(\mathbf{r}_1, \mathbf{r}_2; \omega) \tag{2.68}$$

The self energy Σ contains all the many-body xc effects, it is not Hermitian, nonlocal and frequency dependent. Physically it may be interpreted as the potential felt by the additional (or removed, in the case of the hole) electron from the interacting system. Σ may be used to rewrite the equation of motion of the one particle Green's function as [1]

$$\left(i\frac{\partial}{\partial t} - h(1) - v_H(1)\right)G(1,2) = \delta(1,2) + \int d3\Sigma(1,3)G(3,2), \tag{2.69}$$

or alternatively in frequency space

$$\left(\omega - h(\mathbf{r}_1) - v_H(\mathbf{r}_1)\right)G(\mathbf{r}_1, \mathbf{r}_2; \omega) = \delta(\mathbf{r}_1 - \mathbf{r}_2) + \int d^3r_3\Sigma(\mathbf{r}_1, \mathbf{r}_3; \omega)G(\mathbf{r}_3, \mathbf{r}_2; \omega). \tag{2.70}$$

To summarize, the self energy determines the one-particle Green's function and consequently the one-particle excitation energies, and the problem is now reformulated in terms of the self energy, which we still have to calculate. This can be achieved by self-consistently solving a set of integro-differential equations formulated by Hedin. Thereby the excitations energies of the many-body system can be obtained. These so called Hedin equations equations are listed here.

[1] A derivation of this relation is based on Schwinger's Functional derivative method [99, 100]

$$\Sigma(1,2) = i \int d(3,4) W(1^+,3) G(1,4) \Gamma(4,2,3) \tag{2.71}$$

$$G(1,2) = G_0(1,2) + \int d(3,4) G_0(1,3) \Sigma(3,4) G(4,2) \tag{2.72}$$

$$\Gamma(1,2,3) = \delta(1,2)\delta(1,3) + \int d(4,5,6,7) \frac{\delta\Sigma(1,2)}{\delta G(4,5)} G(4,6) G(7,5) \Gamma(6,7,3) \tag{2.73}$$

$$P(1,2) = -i \int d(3,4) G(2,3) G(4,2) \Gamma(3,4,1) \tag{2.74}$$

$$W(1,2) = v(1,2) + \int d(3,4) v(4,2) P(3,4) W(1,3). \tag{2.75}$$

In this set of equations $W(1,2)$ is the *screened* Coulomb interaction, $P(1,2)$ is the polarizability and $\Gamma(1,2,3)$ is called the Vertex function. Within this *exact* set of equation the complexity of the many-body problem is transferred to the, still, rather complex vertex function, which includes a functional derivative and has to be approximated. Hedin's suggestion for this approximation was to completely drop the second part of the vertex function in Eq. 2.73. The name of the resulting approximation is derived from the updated expression for the self energy $\Sigma(1,2)$, which is now given by Eq. 2.76 and it is therefore called GW approximation. The new set of equations is then

$$\Sigma(1,2) = iW(1^+,3) G(1,4) \tag{2.76}$$

$$G(1,2) = G_0(1,2) + \int d(3,4) G_0(1,3) \Sigma(3,4) G(4,2) \tag{2.77}$$

$$\Gamma(1,2,3) = \delta(1,2)\delta(1,3) \tag{2.78}$$

$$P(1,2) = -iG(2,3) G(4,2) \tag{2.79}$$

$$W(1,2) = v(1,2) + \int d(3,4) v(4,2) P(3,4) W(1,3). \tag{2.80}$$

The equations for the screened Coulomb interaction and the Green's function, which only implicitly depend on the vertex function, remain unchanged in the GW approximation. Note that the expression for $G(1,2)$ is again Dyson's equation (Eq. 2.68). Eq. 2.80 may be reformulated in terms of the dielectric matrix defined as

$$\epsilon(1,2) = \delta(1,2) - \int d(3) v(1,3) P(3,2). \tag{2.81}$$

The resulting expression for the screened Coulomb interaction involves the inverse of the dielectric matrix and is calculated via

$$W(1,2) = \int d(3)\epsilon^{-1}(1,3)v(3,2). \tag{2.82}$$

With this equation the formal presentation of the GW method is finalized, and the subsequent section will show how the method is actually used in practice and it will deal with some of the limitations, which one has to face when applying this method.

2.2.3 G_0W_0: GW in practical calculations

In practice, GW calculations are commonly done according to the scheme proposed by Hybertsen and Louie [52, 53], which is the topic of this section. As it was shown in the last section, the goal is to find the solutions of the quasi-particle equation, which may be obtained by inserting the Green's function in the Lehmann representation (Eq. 2.61) into the corresponding equation of motion (Eq. 2.70)

$$H_0(\mathbf{r}_1)\phi_i^{QP}(\mathbf{r}_1) + \int d^3r_2\Sigma(\mathbf{r}_1,\mathbf{r}_2;\epsilon_i)\phi_i^{QP}(\mathbf{r}_2) = \epsilon_i\phi_i^{QP}(\mathbf{r}_1). \tag{2.83}$$

Here H_0 includes kinetic-, Hartree- and the interaction energy of electron with nuclei and $\phi_i^{QP}(\mathbf{r})$ are the quasi-particle wave functions. In the G_0W_0 approach we start with the non interacting case G_0, and use the KS orbitals ϕ_i^{KS} in place of the quasi-particle wave functions. Doing so, the comparison of Eq. 2.83 with the KS-equations (Eq. 2.23) yields the possibility of calculating the quasi-particle energies perturbatively from the KS-eigenvalues using the self energy operator as the perturbation

$$\epsilon_i^{GW} = \epsilon_i^{KS} + \langle\phi_i^{KS}|\Sigma(\epsilon_i^{GW}) - V_{xc}|\phi_i^{KS}\rangle. \tag{2.84}$$

Note that in Eq. 2.84, the self energy still depends on the quasi-particle energies ϵ_i^{GW}, which are not yet known. But that issue may be handled by an Taylor expansion of the self energy around the Kohn-Sham eigenvalues up to the linear term, such that

$$\Sigma(\epsilon_i^{GW}) = \Sigma(\epsilon_i^{KS}) + (\epsilon_i^{GW} - \epsilon_i^{KS})\frac{\partial\Sigma}{\partial\omega}. \tag{2.85}$$

When this expression is inserted into Eq. 2.84 we obtain the final expression for the quasi-particle energies with

$$\begin{aligned} \epsilon_i^{GW} &= \epsilon_i^{KS} + Z_i \langle \phi_i^{KS} | \Sigma(\epsilon_i^{GW}) - V_{xc} | \phi_i^{KS} \rangle \\ \text{with } \; Z_i &= \big(1 - \frac{\partial \Sigma}{\partial \omega}\big)^{-1}. \end{aligned} \tag{2.86}$$

For the evaluation of the self energy we make use of Eq. 2.76, which in its spectral representation may be expressed as

$$\Sigma(\mathbf{r}_1, \mathbf{r}_2; \omega) = i \int d\omega' G(\mathbf{r}_1, \mathbf{r}_2, \omega + \omega') W(\mathbf{r}_1, \mathbf{r}_2, \omega'). \tag{2.87}$$

As already mentioned, the Green's function is calculated from the non-interacting case by inserting the KS eigenstates and eigenvalues into the Green's function in its spectral representation

$$G(\mathbf{r}_1, \mathbf{r}_2, \omega) = \sum_i \frac{\phi_i^{KS}(\mathbf{r_1}) \phi_i^{* \, KS}(\mathbf{r_2})}{\omega - \epsilon_i^{KS} \pm i\eta}. \tag{2.88}$$

The second ingredient for the self energy is the screened Coulomb interaction $W(1,2)$. It is formally calculated using Eq. 2.82 and involves the computation of the dielectric matrix $\epsilon(1,2)$. In the GW formalism this is done within the random phase approximation (RPA), which means that the irreducible polarization, needed for the evaluation of the dielectric matrix is calculated from Eq. 2.79. In the scheme of Hybertsen and Louie, the momentum space representation of Eq.2.81 is utilized [53]

$$\epsilon_{\mathbf{GG'}}(\mathbf{q}, \omega) = \delta_{\mathbf{GG'}} - v(\mathbf{q} + \mathbf{G}) P_{\mathbf{GG'}}(\mathbf{q}, \omega), \tag{2.89}$$

where $\mathbf{G}$ and $\mathbf{G'}$ are reciprocal lattice vector and $\mathbf{q}$ is a wave vector inside the first Brillouin zone. In the RPA one uses the independent particle polarizability $P_{\mathbf{GG'}} = P^0_{\mathbf{GG'}}$, which may be for instance calculated after the formulation by Adler and Wiser, where a sum over transition matrix elements between occupied and unoccupied states is involved. In their formulation the polarizability, again in momentum space, reads as

$$\begin{aligned} P^0_{\mathbf{GG'}}(\mathbf{q}, \omega) = \sum_{n,n',\mathbf{k}} & \langle n, \mathbf{k} | e^{i(\mathbf{q}+\mathbf{G})\mathbf{r}} | n', \mathbf{k}+\mathbf{q} \rangle \langle n', \mathbf{k}+\mathbf{q} | e^{i(\mathbf{q}+\mathbf{G'})\mathbf{r}} | n, \mathbf{k} \rangle \\ & \times \frac{f(\epsilon_{n',\mathbf{k}+\mathbf{q}}) - f(\epsilon_{n,\mathbf{k}})}{\epsilon_{n',\mathbf{k}+\mathbf{q}} - \epsilon_{n,\mathbf{k}} + \omega}. \end{aligned} \tag{2.90}$$

Here, $|n, \mathbf{k}\rangle$ and $\epsilon_{n,\mathbf{k}}$ are the states and the corresponding energies of a DFT calculation and the $f(\epsilon)$ are occupation factors. The sum in Eq. 2.90 runs over all

occupied states with label n and an in principle infinite number of unoccupied states, labelled n'. In practice the number of unoccupied states is treated as a convergence parameter but it may still reach up to several thousand states, depending on the system under study. It is, therefore, computational very expensive to evaluate the dielectric matrix and it is, in fact, one of the bottlenecks of the GW method. With its evaluation, however, everything that is needed to set up the self energy is known and the quasi-particle equation may be finally solved.

To summarize, the first step of a typical GW calculation based on the G_0W_0 approach consists of a standard DFT calculation. Then the so obtain eigenvectors and eigenvalues are used to calculate the approximate Green's function (Eq. 2.88) and the independent particle polarizability (Eq. 2.90). Then the dielectric matrix is calculated from P^0 and in a subsequent step the screened Coloumb interaction may be obtained. Knowing these ingredients, the self energy operator can be constructed Eq. 2.87 and finally the perturbative quasi-particle energies may be calculated. On the one hand, the G_0W_0 approach, presented here, has the advantage of having moderate computational demands, but on the other hand, it suffers from the fact that it depends on the results a DFT calculation and all its deficiencies. This is known as the starting point dependency and is of particular importance for systems, where the KS eigenvalues tend to be no good approximations for the electron removal energies, as it is, for instance, the case for molecules that consist of a mixture of localized and delocalized orbitals in the energy range of interest [101]. These problems have already been discussed in Section 2.1.4 and are also one of the topics of Chapter 7 of this work.

2.3 Angle resolved photoemission spectroscopy

In the previous sections the methods with which the spectral function of photoemission spectra may be interpreted have been discussed. However, the angle dependent photoemission intensity is proportional to spectral function multiplied by a factor that depends on the matrix element for the transition from initial to fianl state and therefore on the electron momentum as well as on the polarization and energy of the photon [98] and the focus of this work lies not only in the understanding of the spectral function, but also in the understanding of this angular dependence of the photoemission intensities, which is the topic of this section. Therefore, we give a very brief introduction to the experimental setup of a typically ARPES experiment as it will be used in this work. This introduction is followed by the description of the theoretical model that is applied throughout this work, in order to compute photoemission intensities of organic molecular films.

2.3.1 The experimental setup of ARPES

Angle resolved photoemission spectroscopy is *the* method of choice to directly study the electronic structure of surfaces. It is based on the photoelectric effect, discovered by Hertz in 1887 [102] and explained by Einstein in 1905 [103], who introduced the quantum nature of light and the concept of the photon. He deduced that the maximum kinetic energy of an electron that escapes from the material by absorbing a photon, illuminated on the sample, is given by

$$E_{kin}^{max} = h\nu - \Phi \tag{2.91}$$

where $h\nu$ is the energy of the photon and Φ is a surface specific constant, nowadays known as the work function. In a typical ARPES experiment the sample is illuminated with monochromatic light of a certain energy $h\nu$ and the photo emitted electron is detected as a function of its kinetic energy and its emission angle. The corresponding experimental geometry of the experiments presented in this work is illustrated in Fig. 2.1a

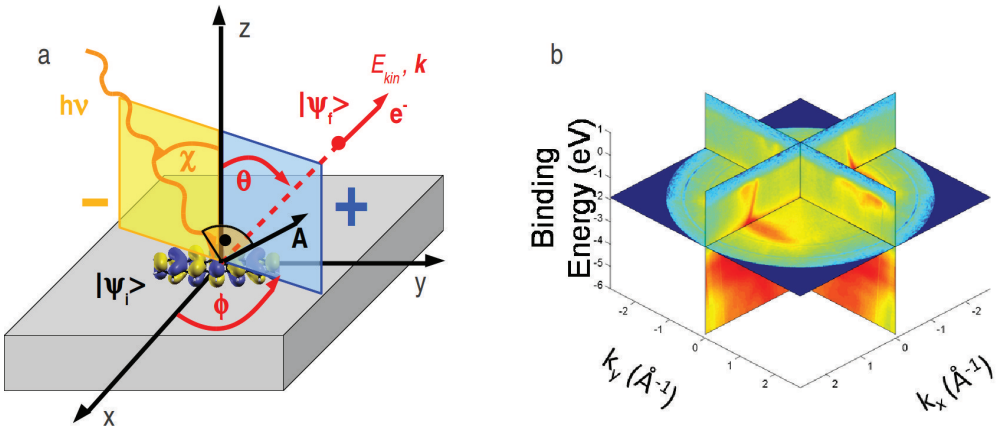

Figure 2.1: (a) Schematic illustration of the geometry of an ARPES experiment. The sample is illuminated with photons of a certain energy $h\nu$ under the angle χ. An electron is excited from its initial state $|\Psi_i\rangle$ to the final state $|\Psi_f\rangle$. The outgoing electron is detected as a function of its kinetic energy and the polar angle θ. The sample is rotated along its azimuthal angle ϕ, and therby the whole subspace above the sample surface is measured (Reproduction of Fig. 6.2). (b) Typical result of an ARPES experiment. The intesnity is recorded as a function of binding energy and momenta parallel to the surface (k_x and k_y). The result is represented as a combination of a CBE momentum map (horizontal cut through the data set at one specific binding energy) and two band maps (vertical cuts though the data at $k_x = 0$ and $k_y = 0$, respectively)

Most of the experiments presented in this work were performed at the synchrotron radiation facility BESSY II, Helmholtz-Zentrum-Berlin. The incident photons,

which in this work, have energies between 30 and 35 eV, illuminate the sample surface with an angle χ with respect to the surface normal. The outgoing electrons are detected with a toroidal electron energy analyzer, for which a detailed description may be found in Ref. [104]. In this setup, the polarization direction is in the specular plane, which also contains the photoelectron trajectory measured. With the toroidal energy analyzer it is possible to simultaneously collect electrons, with polar angles θ lying between $\pm 80°$, as a function of their kinetic energy within a window of 1 or 2 eV. By a stepwise rotation of the sample along the surface normal in steps of 1°, the azimuthal angle ϕ is varied over 180° and thereby, the whole half-space above the sample is covered. During the experimental procedure the electrons' energies and their momenta parallel to surface are conserved, while the momentum normal to the surface is not, due to a potential step at the surface and the broken translational symmetry in that direction. The kinetic energy of the outgoing electron is the photon energy lowered by the sample's work function and the binding energy E_B of the electron (see also Eq. 2.91)

$$E_{kin} = h\nu - \Phi - E_B \tag{2.92}$$

The parallel momenta components k_x and k_y may be obtained from the angular distribution of the photo emitted electrons via the relations

$$k_x = \sqrt{\frac{2m_e E_{kin}}{\hbar^2}}\,\sin\theta\,\cos\phi, \tag{2.93}$$

$$k_y = \sqrt{\frac{2m_e E_{kin}}{\hbar^2}}\,\sin\theta\,\sin\phi. \tag{2.94}$$

The typical outcome of an experiment described above, shown in Fig. 2.1b, is the intensity as a function of binding energy and parallel momenta components. If a horizontal cut, *i.e.* a cut at one specific energy, is made through this extensive data set, one obtains a so-called constant binding energy- (CBE) or momentum map (see e.g. Figs. 3.4 and 6.3). When studying well ordered, organic molecular monolayers on metallic substrates, these momentum maps may be related to specific orbitals of the organic molecule. The utilization of this fact is one of the topics of this work and the method used for calculating such momentum maps is presented in the next section.

2.3.2 Simulation of ARPES experiments

In the previous section a rather simple description of the photoemission process has been given. However, the excitation process is in fact very complicated, as the sample, in reality, represents a full many-body system which in principle

has to be treated as a whole. Because this in not possible in practice, it is convenient, and also done in this work, to use the independent particle picture and the sudden approximation at this point [98, 105]. Doing so, all many-body interactions and any possible relaxation of the system during the emission process are not accounted for. Since, we do not study systems where strong correlation effects are expected to play a major role nor are we interested in details of line shapes or possible satellites that may appear, but rather are interested only in the angular dependence of the intensities at the moment, these approximations are indeed expedient. For a solid, the problem is often further simplified by using the three-step model, where the process is split into three independent parts. These are, an optical excitation from the initial to the final bulk Bloch state, then the travel of the electron to the surface and finally the transmission of the electron through the surface into the vacuum [20]. In this work, however, we make use of the one-step model. Here the photoemission intensity is based on first order perturbation theory and the photoemission intensity is proportional to the transition probability from initial state Ψ_i to final state Ψ_f, which is given by Fermi's golden rule [23, 106].

$$I \propto |\langle \Psi_f | H_{int} | \Psi_i \rangle|^2 \times \delta(E_{kin} + \Phi - E_B - h\nu). \tag{2.95}$$

Here H_{int} describes the interaction of the system with the electromagnetic field of the photon, characterized by its vector potential $\mathbf{A}$ and the δ function expresses the energy conservation. The interacting Hamiltonian is obtained by transforming the momentum operator $\mathbf{p}$ of the unperturbed Hamiltonian H_0 according to $\mathbf{p} \rightarrow \mathbf{p} - \frac{e}{c}\mathbf{A}$. The resulting Hamiltonian is

$$\begin{aligned} H &= \frac{1}{2m_e}\left[\mathbf{p} - \frac{e}{c}\mathbf{A}\right]^2 + eV(\mathbf{r}) = \\ &= \underbrace{\frac{\mathbf{p}^2}{2m_e} + eV(\mathbf{r})}_{H_0} + \underbrace{\frac{e}{2m_e c}\left(\mathbf{Ap} + \mathbf{pA}\right) + \frac{e^2}{2m_e c^2}\mathbf{A}^2}_{H_{int}} = \end{aligned} \tag{2.96}$$

The quadratic term in the vector potential is usually small and may be neglected. The Hamiltonian may be further simplified if the dipole approximation is applied, in which the vector potential is treated as constant and $\nabla \mathbf{A} = 0$ (Coulomb gauge). Although, the dipole approximation is not necessarily valid at the surface and the term $\nabla \mathbf{A}$ might be of importance [98], this is not the case in this work, where the main focus lies on a rather qualitative understanding of angle-resolved emission patterns. In conjunction with the commutation relation of the momentum operator and the vector potential $[\mathbf{p}, \mathbf{A}] = i\hbar\nabla\mathbf{A}$, the dipole approximation may be used to rewrite Eq. 2.95 by exploiting $\mathbf{Ap} + \mathbf{pA} = 2\mathbf{Ap}$

$$I \propto |\langle \Psi_f | \mathbf{Ap} | \Psi_i \rangle|^2 \times \delta(E_{kin} + \Phi - E_B - h\nu). \tag{2.97}$$

The treatment of initial and final state has not been discussed so far. As already mentioned, the sudden approximation will be applied and no interaction of the photoelectron with the system is taken into account. Within this approximation the final state Ψ_f may be factorized into two independent parts using an appropriate antisymmetric operator, which ensures that the system fulfills the antisymmetry requirement. The two parts are the wave function of the outgoing electron ψ_f and the wave function Ψ_f^{N-1} of the $N-1$ particle system left behind. The same may be done for the initial state, when it is approximated by a single Slater determinant. The matrix element of Eq. 2.97 then simplifies to one-electron matrix elements in the independent particle picture and the photoemission intensity becomes [107]

$$I \propto \sum_i |\langle \psi_f | \mathbf{Ap} | \psi_i \rangle|^2 \times \delta(E_{kin} + \Phi - E_i - h\nu). \tag{2.98}$$

The results based on this relation, still depend on the choice of the one electron final state ψ_f. The most simple choice, that can be made is that of a plane wave (PW) [24], which is characterized by its wave number and the direction it leaves the sample. The PW as a final state has the convenient implication that the evaluation of Eq. 2.98 is simplified to a FT of the initial state one electron wave function ψ_i under the condition that it may be measured selectively. Thus, a direct relation of the square root of the measured photo-current and the orbital in reciprocal space $\tilde{\psi}_i$, corrected by a weakly $\mathbf{k}$-dependent polarization factor, is established [26].

$$\sqrt{I} \propto |\mathbf{Ak}| \times |\tilde{\psi}_i|. \tag{2.99}$$

With this simple relation the following steps have to be carried out, in order to obtain simulated CBE momentum maps of adsorbed organic molecules in practice. The procedure is also illustrated in Fig. 2.2

As a starting point, the KS one electron orbital $\psi_j(\mathbf{r})$ (depicted in Fig. 2.2a) is taken as the initial state and then in a first step Fourier transformed to momentum space. The resulting orbital $\tilde{\psi}_j(\mathbf{k})$ in reciprocal space is depicted in Fig. 2.2b. In a subsequent step, the square of the absolute of that orbital is cut through by a hemisphere (transparent red hemisphere of Fig. 2.2b). The radius of that hemisphere reflects the energy conservation and is therefore defined by the kinetic energy of the outgoing electron

$$r_k = \sqrt{\frac{2m_e E_{kin}}{\hbar^2}} \tag{2.100}$$

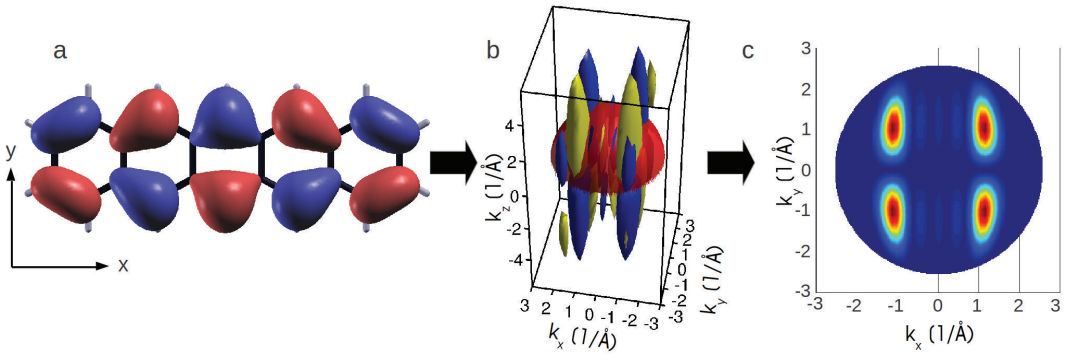

Figure 2.2: Illustration of the steps necessary for obtaining simulated ARPES momentum maps used throughout this work, based on the result of a DFT calculation of an isolated molecule, on the example of the organic molecule pentacene. a) Real space image of the highest occupied molecular orbital of pentacene as it results from DFT. b) A Fourier Transform leads to the orbital representation in reciprocal space. c) A hemisperical cut through the orbital leads to a k_x,k_y distribution pattern of that orbital (momentum map)

The so obtained data may be interpreted as a CBE photoemission pattern of the corresponding molecular orbital. The comparison of calculated momentum maps after the procedure presented here (i.e. according to Eq. 2.99 with slices through the experimentally obtained, valence band photoemission data cube $I(k_x, k_y, E_B)$ is becoming known as *orbital tomography*. This technique is shown to be extremely powerful and may be used to clarify the electronic and/or geometric structure of molecular adsorbate systems. It may seem quite surprising, that orbital tomography, which is based on the calculation of an isolated molecule and the assumption on a PW final state, is able to explain experimental momentum maps measured on extended molecular monolayers adsorbed on a metallic substrate. That, this is indeed possible, at least on a qualitative level, has been shown in numerous works [22, 26, 108–110] and this list may well be extended by parts of this work [111–114].

ARPES data of extended systems

If one is interested in the effects of intermolecular dispersion of the molecular states or effects arising from molecule substrate interactions on to the momentum maps, the extended system, either as a freestanding layer or including the substrate, has to be considered. For such a case, the computation of ARPES data is no longer based on the DFT calculation of an isolated molecule but on the calculation of the extended systems, with the Kohn-Sham eigenvalues $\varepsilon_{n\mathbf{q}}$ and eigenstates $\psi_{n\mathbf{q}}$ as a result. The photoemission intensity is then given by

$$I(k_x, k_y; h\nu, \mathbf{A}) \propto \sum_{n}^{\text{occ}} \sum_{\mathbf{q}}^{\text{BZ}} |\langle \psi_f | \mathbf{A} \cdot \mathbf{p} | \psi_{n\mathbf{q}} \rangle|^2 \times \delta(\varepsilon_{n\mathbf{q}} + \Phi + E_{\text{kin}} - h\nu). \quad (2.101)$$

The summation in Eq. 2.101 runs over all occupied initial states and all $\mathbf{q}$ points sampling the Brillouin zone. Using a plane wave for the final state the weakly angle dependent geometry factor again may be factorized and the intensity becomes

$$I(k_x, k_y; h\nu, \mathbf{A}) \propto \sum_{n}^{\text{occ}} \sum_{\mathbf{q}}^{\text{BZ}} |\mathbf{A} \cdot \mathbf{k}|^2 \left| \langle e^{i\mathbf{kr}} | \psi_{n\mathbf{q}} \rangle \right|^2 \times \delta(\varepsilon_{n\mathbf{q}} + \Phi + E_{\text{kin}} - h\nu). \quad (2.102)$$

In the corresponding DFT calculations, utilizing the VASP code, the Kohn-Sham eigenfunctions are represented using a plane wave basis set and the initial Bloch states $|\psi_{n\mathbf{q}}\rangle$ are, apart from a normalization factor, given by

$$|\psi_{n\mathbf{q}}\rangle = \sum_{\mathbf{G}}^{|\mathbf{G}|<G_{cut}} c_{n\mathbf{q}}(\mathbf{G}) e^{i(\mathbf{q}+\mathbf{G})\mathbf{r}}. \quad (2.103)$$

Here the $\mathbf{G}$ are reciprocal lattice vectors and the sum runs over all reciprocal lattice vectors below a certain energy cut-off. The resulting transition matrix element $\langle e^{i\mathbf{kr}} | \psi_{n\mathbf{q}} \rangle$ of Eq. 2.102 is then for this case

$$\begin{aligned} \langle \psi_{n\mathbf{q}} | e^{i\mathbf{kr}} \rangle &= \int d^3r \sum_{\mathbf{G}} c^*_{n\mathbf{q}}(\mathbf{G}) e^{-i(\mathbf{q}+\mathbf{G})\mathbf{r}} e^{i\mathbf{kr}} \\ &= \sum_{\mathbf{G}} c^*_{n\mathbf{q}}(\mathbf{G}) \int d^3r e^{-i(\mathbf{q}+\mathbf{G}-\mathbf{k})\mathbf{r}} \\ &= \sum_{\mathbf{G}} c^*_{n\mathbf{q}}(\mathbf{G}) \delta_{\mathbf{G},\mathbf{k}-\mathbf{q}}. \end{aligned} \quad (2.104)$$

However, when the substrate is included in the calculations, the plane wave final state approximation is no longer a suitable choice, since it may lead to an overestimated photoemission signal of the substrate states. The reason for that lies in the fact that in the photoemission experiment only the topmost layers of the substrate are probed due to the limited mean free path of the emitted electron.

The most appropriate choice for the final state would be a so called *time reversed LEED state* [23], whose full description is beyond the scope of this work. Here,

we account for the limited mean free path by simply choosing a damped plane wave for the final state. The damped plane wave has an empirical form using two parameters z_0 and γ. For that purpose, the unit cell used in the DFT calculation is divided into two parts in the z-direction, that is the direction of the surface normal, at z_0. The part above the substrate ($z > z_0$) is treated by a pure plane wave, while below z_0 the plane wave is exponentially damped with the parameter γ in the exponent, whose inverse $\frac{1}{\gamma}$ represents the mean free path length. Thus, the final state for the range $0 < z < z_0$ is given by

$$|\psi_f\rangle_d = e^{i\mathbf{kr}} e^{\gamma(z-z_0)}. \tag{2.105}$$

A schematic view of the damped final state in the direction normal to the surface is shown in Fig. 2.3. In order to compute the photoemission intensities with this damped final state, $|\psi_f\rangle_d$ is inserted into Eq. 2.101 and the matrix elements are evaluated for all Bloch bands $\psi_{n\mathbf{q}}$ at each reciprocal lattice point $\mathbf{q}$. For the case of a damped plane wave, the transition matrix element is evaluated for each spatial direction separately and may consequently be written as

$$\begin{aligned}\langle\psi_{n\mathbf{q}}|\mathbf{A}\cdot\mathbf{p}|\psi_f\rangle_d = \mathbf{A}(i\mathbf{k}+\gamma\mathbf{e_z})\sum_{\mathbf{G}} c^*_{n\mathbf{q}}(\mathbf{G})\delta_{G_x,k_x-q_x}\delta_{G_y,k_y-q_y} \\ \times e^{-\gamma z_0}\int_0^{z_0} dz e^{(-ig_z+\gamma)z}\int_{z_0}^{c} dz e^{-ig_z z}\end{aligned} \tag{2.106}$$

Here we have abbreviated $g_z = G_z + q_z - k_z$ and introduced the lattice constant in the z-direction c. The evaluation of the integral is straight forward and the matrix element is given by

$$\begin{aligned}\langle\psi_{n\mathbf{q}}|\mathbf{A}\cdot\mathbf{p}|\psi_f\rangle_d = (i\mathbf{A}\mathbf{k}+A_z\gamma)\sum_{\mathbf{G}} c^*_{n\mathbf{q}}(\mathbf{G})\delta_{G_x,k_x-q_x}\delta_{G_y,k_y-q_y} \\ \times\left(\frac{e^{-ig_z z_0}-e^{\gamma z_0}}{-ig_z+\gamma}-\frac{e^{-ig_z c}-e^{-ig_z z_0}}{-ig_z}\right)\end{aligned} \tag{2.107}$$

One has to keep in mind, even with the damped plane wave, our approach remains a relatively simple model for the photoemission process, in particular when the substrate is included. However, one may gather important insights, for instance, when comparing results for both, plane wave (according to Eq. 2.102) and damped plane wave final state (according to Eq. 2.105). Thereby, the emission contributions from adsorbate and substrate states can be clearly distinguished.

Inspired by the experiments which may be performed utilizing the toroidal analyzer, the analysis of the electronic structure of the adsorbate system with the

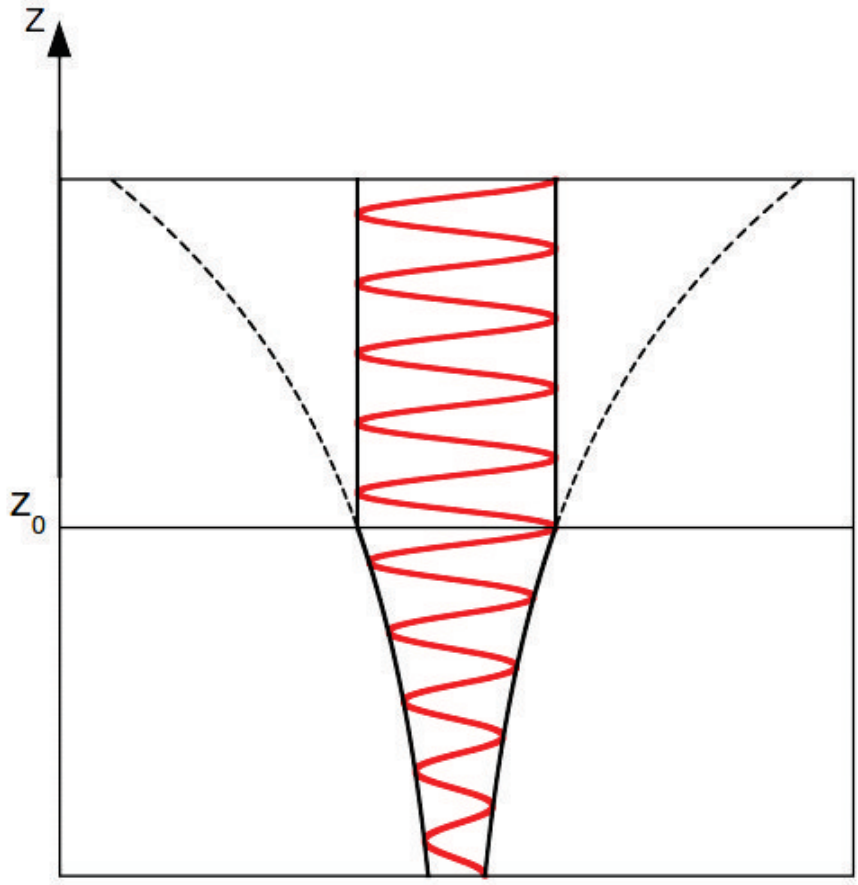

Figure 2.3: The red line shows schematically the damped plane wave final state in the z-direction of the unit cell. Above z_0 the final state is treated as a pure plane wave, below z_0 it is exponentially damped by the factor $e^{\gamma(z-z_0)}$, which is shown as the black envelope of the damped plane wave.

help of the computation of the photoemission intensities according to the scheme explained above can be done in three different modes. These are, CBE momentum maps $I(k_x, k_y)$ at a specific binding energy E_B, the band map which show the intensity as a function of binding energy and one parallel momentum $I(E_B, k_{x,y})$ and so called constant initial state (CIS) scans $I(E_{Ph}, k_{x,y})$, where the photon energy dependence of one specific state is studied as a function of one parallel momentum.

Chapter 3

Imaging the wave functions of adsorbed molecules

This chapter deals with the problem of the lost phase information in the photoemission experiment and the possibility of obtaining images of individual molecular states using ARPES data, taken from molecular monolayers of pentacene and PTCDA on Ag(110). Already in Ref. [26], it has been shown that it is possible to obtain two dimensional orbital images via an inverse Fourier Transform of measured ARPES momentum maps. In that work the lost phase information has been imposed to the measured data according to symmetry arguments. However, such a procedure is not generally applicable and needs additional input from theoretical considerations. In this work we only assume the wave function to be confined to a region, defined by the size of the molecule under study and recover the phase information by an iterative procedure commonly applied in x-ray diffraction, based on the oversampling method. With this approach, which already has been successfully applied to one dimensional, spatially confined surface states [25], we could obtain images of 5 molecular orbitals and compare them with the results of DFT calculations. The work has been published [111] in the Proceedings of the National Academy of Sciences of the United states of America and this chapter is essentially a reproduction of the article including the supplementary information [1].

Author contributions

It was my supervisor, Peter Puschnig, who had the idea for this work and already presented images of orbitals from ARPES measurements in Ref. [26], however

[1] Reproduced with permission from the National Academy of Sciences, the original article may be found online at http://dx.doi.org/110.1073/pnas.1315716110

Imaging the wave functions of adsorbed molecules

Daniel Lüftner[a], Thomas Ules[a], Eva Maria Reinisch[a], Georg Koller[a], Serguei Soubatch[b,c], F. Stefan Tautz[b,c], Michael G. Ramsey[a], and Peter Puschnig[a,1]

[a]Institute of Physics, Karl-Franzens University Graz, 8010 Graz, Austria; [b]Peter Grünberg Institut (PGI-3), Forschungszentrum Jülich, 52425 Jülich, Germany; and [c]Jülich Aachen Research Alliance, Fundamentals of Future Information Technology, 52425 Jülich, Germany

Edited by Peter Feibelman, Sandia National Laboratories, Albuquerque, NM, and accepted by the Editorial Board November 7, 2013 (received for review August 20, 2013)

Figure 3.1: Header of the article [111] as it was published in the Proceedings of the National Academy of Sciences of the United states of America, including the title and all contributing authors. This chapter is beside some small modifications identical to the article and its supporting information.

there the phase information has been imposed by symmetry arguments only. The ARPES experiments of pentacene on Ag(110) have been performed by Thomas Ules and Eva Maria Reinisch, under the supervision of Georg Koller and Michael Ramsey. The PTCDA data was measured by our colleagues from Jüllich, Serguei Soubatch and F. Stefan Tautz. The experimentally obtained data has been processed and prepared by me, in order to be able to use it for the iterative procedure. I have implemented the iterative procedure and had the idea of including the symmetry as a possible constraint in the iterative procedure. Consequently I have performed all the phase recovery calculations as well as the DFT calculations of the isolated molecules. Together with Peter Puschnig and Michael Ramsey, I have written the initial draft of the manuscript, prepared the figures and discussed the data and manuscript with all co authors.

Abstract

The basis for a quantum mechanical description of matter are electron wave functions. For atoms and molecules, their spatial distributions and phases are known as *orbitals*. Although orbitals are very powerful concepts, experimentally only the electron densities and -energy levels are directly observable. Regardless whether orbitals are observed in real space with scanning probe experiments, or in reciprocal space by photoemission, the phase information of the orbital is lost. Here we show that the experimental momentum maps of angle resolved photoemission from molecular orbitals can be transformed to real space orbitals via an iterative procedure which also retrieves the lost phase information. This is demonstrated with images obtained of a number of orbitals of the molecules pentacene ($C_{22}H_{14}$) and PTCDA ($C_{24}H_8O_6$), adsorbed on silver, that are in excellent agreement with ab-initio calculations. The procedure requires no a priori knowledge of the orbitals and is shown to be simple and robust.

Significance Statement

In quantum mechanics, the electrons in a molecule are described by a mathematical object termed the wave function or molecular orbital. This function determines the chemical and physical properties of matter and consequently there has been much interest in measuring orbitals, despite the fact that strictly speaking they are not quantum mechanical observables. We show how the amplitude and phase of orbitals can be measured in good agreement with wave functions from ab-initio calculations. Not only do such measurements allow wave functions of complex molecules and nanostructures to be determined they also open up a window into critical discussions of theoretical orbital concepts.

3.1 Introduction

As the electronic, optical and chemical properties of nanostructures are defined by their electronic orbitals, in the last decades experimentalists have striven to image them. This is despite the fact that orbitals are not, strictly speaking, quantum mechanical observables. Molecules are arguably the best defined nanostructures, and for simple diatomic molecules, such as N_2, both the amplitude and the phase of the highest occupied molecular orbital (HOMO) in 3 dimensional space have been recovered [34]. This tomographic reconstruction requires higher harmonics generated from intense femtosecond laser pulses, focused on a series of molecular alignments, together with theoretical modeling [34]. Although offering the exciting prospect of imaging orbitals on the time scale of chemical reactions, being both complex and only appropriate for simple molecules and orbitals, the technique is not generally applicable for the task of orbital reconstruction. Alternatively, scanning probe techniques offer real space imaging of large molecules with submolecular resolution on surfaces. Although great advances have been made with understanding and controlling scanning probe tips, so-called tip functionalization [33], tips are still a factor of uncertainty. With an appropriate tip, the correct nodal structure of orbitals can be directly observed. Moreover, with tip molecules of p-wave structure the relative phase of the sample wave function may be inferred [115]. Unfortunately, as the wave functions of the substrate generally spill out beyond the adsorbed molecules, decoupling layers such as NaCl are necessary to avoid direct tunnelling into the substrate.

The full angle dependence of valence band ultraviolet photoelectron spectroscopy from molecular films has been shown to contain rich information on the orbital structure [27, 116]. In the past few years a number of studies on molecular films have demonstrated a strong connection between the angular intensity distribution measured in ultraviolet photoemission experiments and the Fourier transform of the initial state orbitals [21, 22, 26, 28, 108, 109, 117, 118]. This relation

can be justified in the so-called one-step-model of the photoemission process, wherein the excitation occurs in a single step from an initial state to a final state [23]. When approximating this final state by a free electron state, one can show that the photoemission intensity follows an angular dependence given by the Fourier transform of initial state wave function [119]. Thus, it is tempting to use angle-dependent photocurrent data as measured in angle-resolved photoemission spectroscopy (ARPES) to recover the real-space distribution of the initial orbital by applying an inverse Fourier transform [26]. However, this is not possible in general due to fact that the phase information of the wave function is lost in the measurement.

In this work, we develop an unbiased and widely applicable procedure, based on a scheme proposed for one dimensional surface states confined by surface step edges of Au(111) [25], that can be used to regain the lost phase information and thereby enable the reconstruction of real space orbitals. It only demands the wave function under study to be spatially confined. Here we will assume that the wave functions are confined to a region defined by the van der Waals (vdW) size of the molecules, a requirement well-justified for many molecular adsorbate systems. Based on ARPES momentum maps of adsorbed monolayers on a Ag(110) surface, we demonstrate our method by reconstructing two-dimensional orbital images of the lowest unoccupied molecular orbital (LUMO) and the HOMO of PTCDA, as well as of the LUMO, HOMO, and HOMO-1 of pentacene (5A) that are in remarkable agreement with one-electron wave functions from density functional theory (DFT). In the photoemission process it is not a priori clear that the one-electron orbitals should result. Indeed, in going from an N to an $N-1$ final state, a Dyson orbital would be the more strictly correct description, a Dyson orbital representing the overlap between the N electron wave function with the $N-1$ electron wave function before and after the ionization, respectively [120]. In principle, a Dyson orbital should be based upon many-body perturbation theory and could include the molecule as well as the substrate. However, Dyson orbitals obtained within the framework work DFT and applied to isolated molecules often closely resemble the theoretical one-electron orbitals which in turn account for measured ARPES momentum maps [117]. Our results here thereby show that relaxation is often only playing a minor role and the frozen orbitals approximation is in fact reasonable.

3.2 The problem of the phase

Fig. 3.2 illustrates the problem which one encounters when attempting to retrieve a real space image of the orbital from an inverse Fourier transform of an experimental ARPES map. Panel (a) shows a model wave function $\psi(x)$ in one dimension, which has a sinusoidal shape of wave number k_0 and is spatially confined

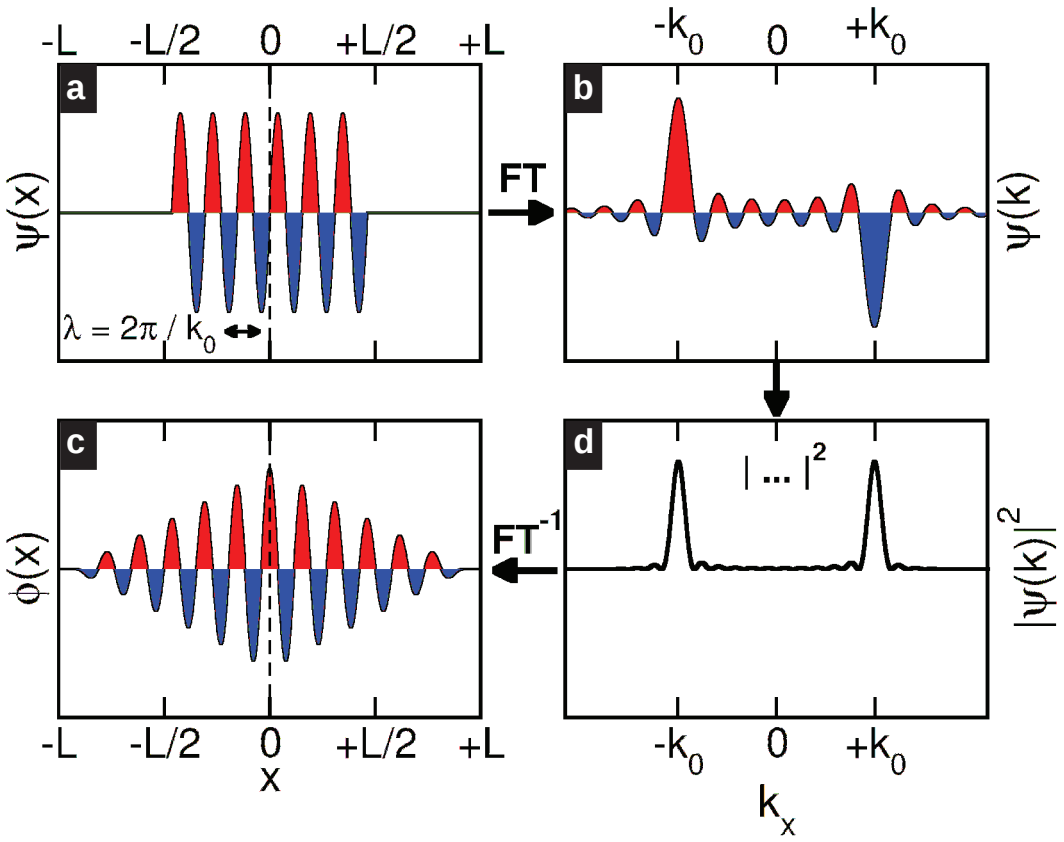

Figure 3.2: The phase problem for a one-dimensional wave function. (a) The model 1D wave function of sinusoidal shape with wave number k_0 and spatial extent L is Fourier transformed yielding (b). When taking the absolute value as in the measurement process (c) and subsequently transforming back to real space, the resulting real-space function (d) generally has the wrong phase and a spatial extent $2L$, twice as large as the original wave function.

to a region of length L. For instance, $\psi(x)$ could be viewed as a one-dimensional schematic representation of the HOMO of para-sexiphenyl [26]. When calculating its Fourier transform (FT) depicted in panel (b), the wave function in momentum space $\tilde{\psi}(k_x)$ is also anti-symmetric and shows main peaks at $\pm k_0$. Experimentally, the intensity distribution observed in angle-resolved photoemission experiments is proportional to the *square of the absolute value* $\left|\tilde{\psi}(k_x)\right|^2$. Thus, as evident from panel (c), information on the sign of the wave function, or more generally on its phase, is lost in the measurement process. When attempting to obtain the spatial distribution of the orbital by performing an inverse Fourier transform (FT^{-1}) of its measured momentum distribution, one does not recover the original wave function $\psi(x)$, as can be seen from panel (d). The resulting real-space function

$\phi(x)$ has both the wrong phase (now being symmetric) and also a spatial extent which is twice as large ($2L$) as that of the original wave function $\psi(x)$. Mathematically, the so obtained function, $\phi(x)$, is the auto-correlation of the wave function $\psi(x)$ with its complex conjugate. This shows that phase information is indeed crucial to obtain the correct real space distribution of a molecular orbital from a momentum distribution measured via ARPES. In an earlier publication [26], we have suggested that in certain cases the missing phase information can be guessed and imposed onto the measured data, thereby enabling the reconstruction of real space wave functions from ARPES data. However, such a procedure is biased and moreover not generally applicable.

3.3 Iterative phase recovery

Fig. 3.3 illustrates how the phase information is recovered by an iterative procedure. The starting point is an experimental ARPES intensity map as shown in panel (a). In this example, we use ARPES data taken from an ordered monolayer of PTCDA/Ag(110) containing only one molecule in the unit cell, recorded at a constant binding energy (CBE) of 1.9 eV below the Fermi level, which has been shown to correspond to the electron emission from the HOMO of PTCDA [21, 22]. Note that the black isolines denote the square root of the ARPES intensity, i.e., the absolute value of the wave function $\left|\tilde{\psi}(k_x, k_y)\right|$, while the unknown complex phase, $\arg\left(\tilde{\psi}(k_x, k_y)\right)$, is shown as a color map and arbitrarily set to a constant value in this case. In the first step of the iteration, an inverse Fourier transform leads to the real space function displayed in panel (b). As we have already noticed for the 1D example of Fig. 3.2, the resulting real space function $\phi(x, y)$ must be expected to have a too large spatial extent. Therefore, the second step consists in modifying $\phi(x, y)$ *outside* a pre-defined spatial region. For simplicity, we choose a rectangular region (green dashed lines) of area 14.8×7.2 Å^2, which roughly corresponds to the vdW size of PTCDA, and reduce $\phi(x, y)$ by a given factor outside this confinement box. This leads to $\phi'(x, y)$ shown in panel (c). In the third step, a Fourier-transform of $\phi'(x, y)$ yields the new momentum distribution $\tilde{\psi}'(k_x, k_y)$ in panel (d), which differs from the original $\tilde{\psi}(k_x, k_y)$ in both absolute value (isolines) and phase (colour map). To close the iteration loop, the new *phase* distribution of $\tilde{\psi}'(k_x, k_y)$ is kept and imposed on the experimental ARPES map of (a).

When continuing the steps of this iterative procedure, the resulting real space function $\phi(x, y)$ gradually changes such that its probability density inside the confinement box is maximized. Interim results of the 15th and 250th iteration steps in momentum and real space are displayed in panels (e–h) of Fig. 3.3. Note that for the 250th iteration, after which no further change in the appearance of

the wave function is seen, we have switched to a more conventional graphical representation of the wave function. Thus, panels (g) and (h) display the real part of the wave function in momentum and real space, respectively, as a density plot, where red indicates positive, blue negative values.

3.4 Reconstructed versus theoretical orbitals

We have successfully applied this iterative procedure to a number of ARPES CBE (k_x, k_y) maps of molecular monolayers adsorbed on metallic surfaces and retrieved the corresponding molecular orbitals. Fig. 3.4 compiles a set of five molecular orbitals which are discussed in this work. Panels (a)–(e) are CBE momentum maps of the PTCDA HOMO and LUMO [26], and of the HOMO-1, HOMO and LUMO of pentacene. All data has been taken on well-ordered monolayers adsorbed on the Ag(110) surface. Upon bonding on the substrate, the molecular states are broadened into resonances where their full width at half maximum is only slightly broader than the 150–200 meV energy resolution of the toroidal electron energy analyzer. The CBE maps are taken at the binding energies indicated in Fig. 3.4 and show data integrated over an energy range of 60 meV. Due to energy resolution of the toroidal electron energy analyzer, however, the maps cover a somewhat larger energy window. Note that for both molecules, there is charge transfer from the metal into the molecule's LUMO, thereby enabling its detection by the photoemission experiment.

When subjecting the experimental data to the iterative phase recovery, one obtains the orbital images depicted in Fig. 3.4 which are shown in comparison to the respective DFT orbitals calculated for the isolated PTCDA and pentacene. In all five cases, the reconstructed orbitals show an excellent agreement with the theoretical predictions, thereby demonstrating the power of the method. Comparing the experimental orbitals to the calculated one-electron orbitals of Fig. 3.4, two questions need to be considered: (i) What is actually displayed in a calculated orbital and (ii) should it be expected to agree with the experimental orbitals? Clearly, in Fig. 3.4 not only are the nodal structures of the orbitals well reproduced, but also the sizes and shapes of the lobes in the patterns appear to be in excellent agreement between experiment and theory. Usually, three-dimensional theoretical orbitals are represented by iso-surfaces, where the sizes and shapes of the lobes in theoretical orbital images are influenced by the choice of the isovalue; isosurfaces displayed in Fig. 3.4 are 10 % isosurfaces, as commonly used in displaying calculated orbitals, i.e. 90 % of the charge density is located within the displayed surface. Clearly this fits our experimental data well, whereas for scanning tunneling microscopy (STM) images DFT orbitals with approximately 1 % isosurfaces (enclosing 99 % of the charge) seem to match the HOMO and LUMO of 5A [31]. This is presumably due to the STM tip probing the prob-

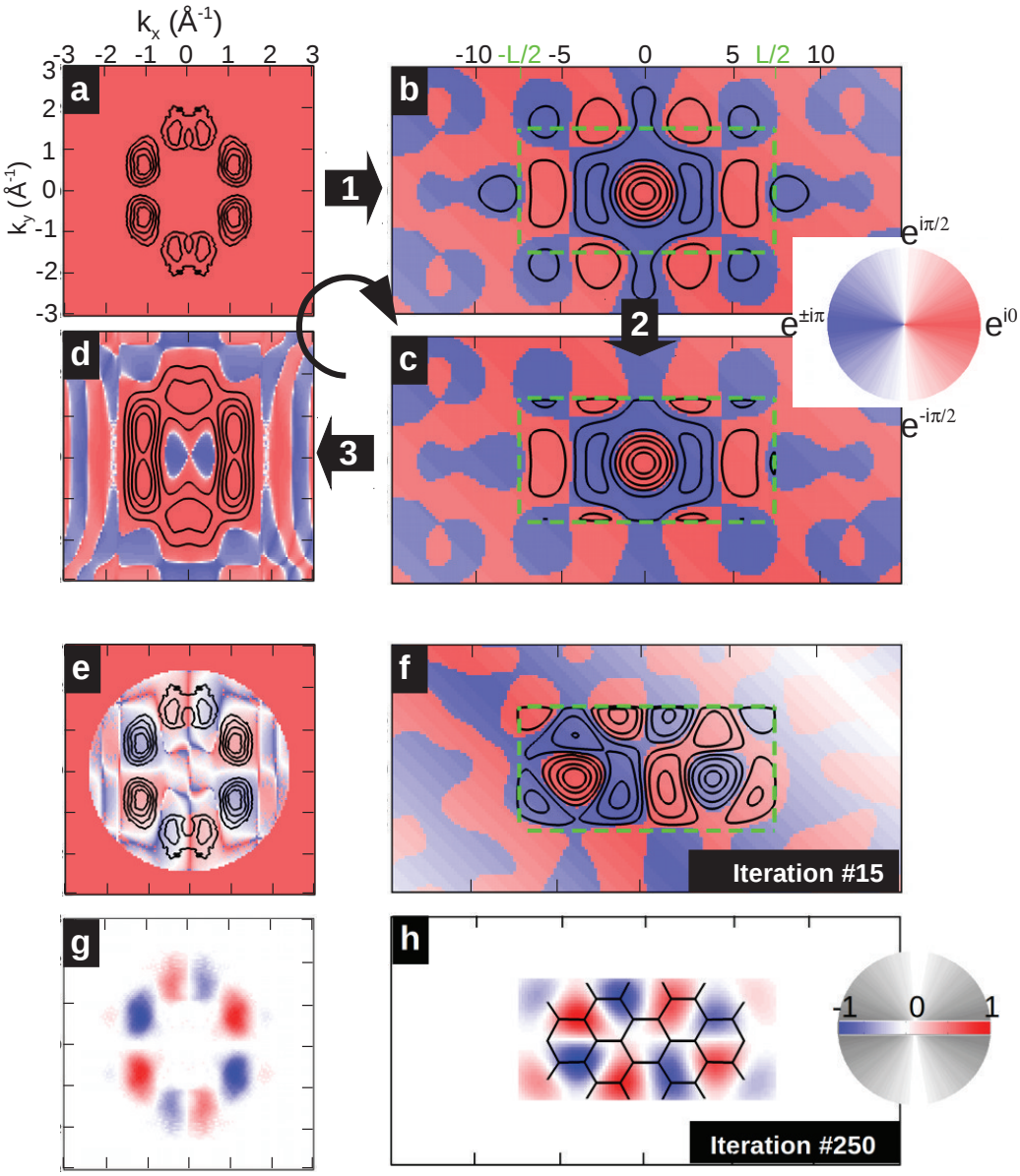

Figure 3.3: The iterative wave function reconstruction algorithm, using the example of the PTCDA HOMO. Panel (a) displays the experimental ARPES momentum map. Black isolines represent the square root of the measured intensities, while the color indicates the phase. An inverse Fourier transform leads to (b). The absolute value of the wave function is reduced to 10 % outside the confinement box (green, dashed rectangle) in panel (c), its Fourier transform leads to (d). Panels (e) and (f), and (g) and (h) show the 15th and 250th step in the iterative procedure, respectively. In panels (g) and (h), we show the real part of the reconstructed wave function, in k-space and real space, respectively.

ability density well above the molecule. A comparison of our data with STM results can be found in the supporting information (SI) Fig. 3.7. An alternative way of comparing the theoretical with the orbitals reconstructed from ARPES is to represent also the theoretical orbitals as two-dimensional plots. For the π orbitals of the planar molecules treated in this work, this can be accomplished by projecting out the z-dependence of carbon p_z orbital. This leads to the images shown in Fig. 3.8 which is a duplicate of Fig. 3.4 except for the theoretical orbital images which are replaced by the 2D-projections mentioned above.

Of particular note in the shape agreement between the reconstructed orbitals and the calculated ones are, for instance, the asymmetric curvatures on each side of the lobes close to the long axis of the PTCDA LUMO, or the increasing bend in the lobes of the 5A LUMO moving from the center to the end of the molecule. The 5A HOMO data shows clearly that the quasi-periodicity of the electron density is larger than the periodicity of the carbon backbone. This leads to the density shifting from the apex carbon sites in the center of the molecule to the bond between the apex and the terminal carbons at the end of the molecule. Such a shift would not be expected for an infinitely long acene. On careful inspection there are some features in the reconstructed orbitals which differ from those of the calculated orbitals of isolated molecules. For instance, the outermost lobes of the 5A LUMO, although showing a maximum on the long molecular axis, have extensions perpendicular to it that are greater than predicted by the calculation. Also, the lobe shape of the PTCDA HOMO is not in perfect in agreement with the 10 % isosurface DFT orbital. On assessing the agreement or disagreement of reconstructed orbitals with calculated ones in Fig. 3.4, it has to be kept in mind that an agreement with orbitals calculated for *isolated* molecules is perhaps remarkable, since reconstructed orbitals are for molecules *adsorbed on a surface*. Although the interaction with Ag is relatively weak, there is charge transfer to the LUMOs in both cases and thus orbital distortions cannot be ruled out.

As in the discussion above, generally, the comparison of experimental and calculated orbitals has been subjective [31, 34]. In contrast, our data, having both the phase information and more than one orbital for one molecule, allows a more critical analysis of how good the experimentally obtained wave functions are. Since orbitals of any particular system are orthogonal to each other, we can use this criterion to show that our reconstructed orbitals are indeed realistic in the quantum mechanical sense. In the case of PTCDA, the calculated overlap between the experimental HOMO and LUMO is 10 % (90 % orthogonality). For 5A the three orbital combinations yield even better orthogonalities in the range of 93 to 99 %. This not only suggests the orbitals to be objectively good, it also provides the possibility of introducing a further objective criterion in the reconstruction procedure, if deemed necessary.

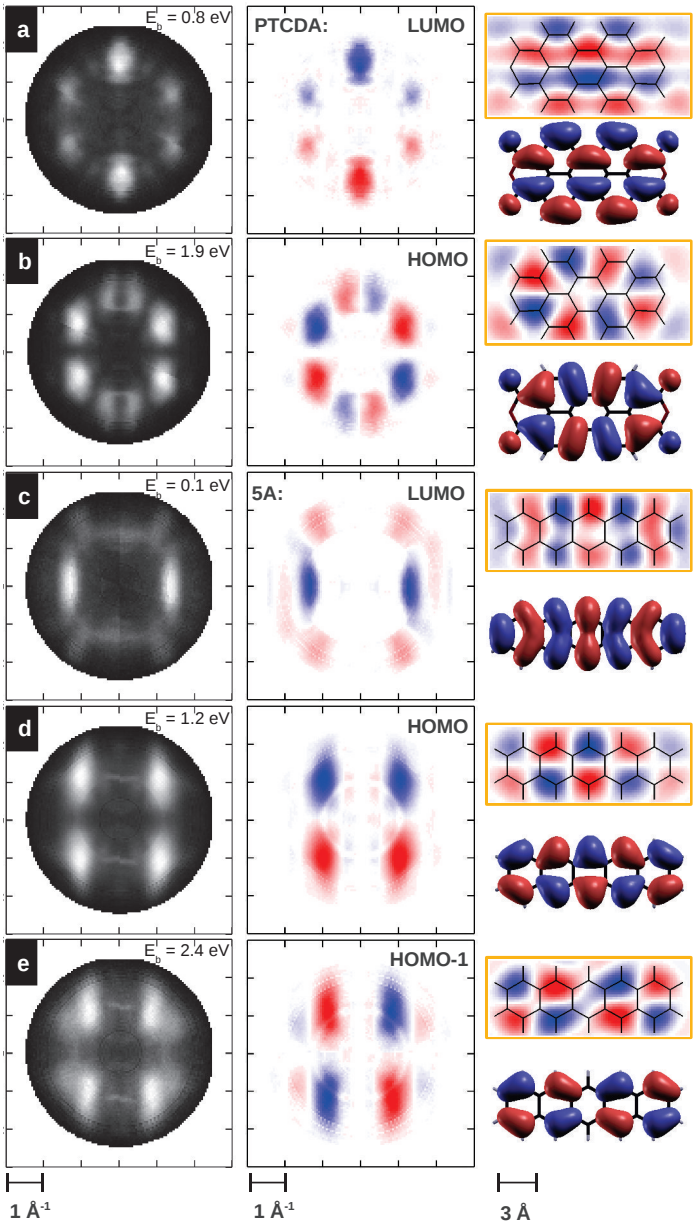

Figure 3.4: Compilation of orbitals reconstructed from ARPES data in this work. The left column shows experimental CBE ARPES maps of the PTCDA LUMO (a) and HOMO (b), and the pentacene LUMO (c), HOMO (d) and HOMO-1 (e). The middle column shows the CBE maps with the recovered phase information. The right column displays the reconstructed real space orbitals (orange box) which are compared to corresponding Kohn-Sham orbital images obtained from density functional theory (without box). The wave function confinement regions are 14.8×7.2 Å^2 and 14.8×5.4 Å^2 for PTCDA and pentacene, respectively.

3.5 How can the lost phase be recovered?

Several questions may be posed concerning the mathematical procedure to recover the unknown phase: (i) How can the phase be restored from intensity information only? (ii) How stable is the procedure, e.g. do results depend on the chosen initial phase or the assumed confinement box size? (iii) How can two-dimensional momentum maps be used to get information on three-dimensional orbitals?

(i): At first glance, it appears that the phase information is created from nowhere, since intensity information in momentum space eventually leads to intensity *and* phase information in real space. However, considering the well-known properties of discrete Fourier transforms and the fact that the wave function goes to zero outside the confining box, this apparent under-determinacy can be resolved. Our data resolution in momentum space of $\Delta k \simeq 0.05$ Å^{-1} converts to a real space domain size of $X^2 = (2\pi/\Delta k)^2 \simeq 126^2$ Å^2. Comparing this with the area of the molecule A, the so-called oversampling ratio X^2/A amounts to $\simeq 150$. By forcing the wave function to be zero in the large area outside the molecular region during the iterative procedure, the missing phase information is compensated. Successful orbital reconstruction requires an oversampling ratio of at least 2 but, as is the case here, the algorithm becomes more stable if the ratio is larger.

(ii): For starting the iterative phase recovery, an initial guess of the phase has to be made. In the example of Fig. 3.3, a constant k-independent phase has been chosen. However, a random k_x- and k_y-dependent starting phase leads essentially to the same result, as evidenced in Fig. 3.5 of the SI. That such an extremely different and even unphysical starting point leads to the same result emphasizes the robustness of the orbitals shown in Fig. 3.4 with respect to the initial choice of phase. The question of how to select a suitable confinement region is slightly more subtle. Firstly, it is evident from the mathematical properties of Fourier transforms that the real space orbitals $\phi(x, y)$ are only determined up to an arbitrary translation vector (R_x, R_y). Since the FT of the translated orbital $\phi(x - R_x, y - R_y)$ differs from that of $\phi(x, y)$ only by a k-dependent phase factor, an incorrect confinement box results in orbitals $\phi(x, y)$ which may be arbitrarily translated inside the confinement box. This can be seen clearly as a 0.3 Å shift in the 5A LUMO of Fig. 3.4(c) when using a box size appropriate for the HOMO wave function in Fig. 3(d). The problem of cyclical translation within the confinement box is even more pronounced for the HOMO-1 of 5A (see Fig. S2 in the SI). For objectivity, and to emphasize the robustness of the procedure, we have chosen a simple rectangular box with constant size for all pentacene orbitals. Only for HOMO-1 is the orbital's overall position fixed by imposing inversion symmetry in the iterative procedure.

(iii): The last question concerns the fact that the reconstructed orbital images shown in Fig. 3 are interpreted as planar two-dimensional sections through three-dimensional orbitals. Such a simplified relation is possible since all wave functions

studied in this work are π-orbitals belonging to nearly planar molecules. In such cases, the three-dimensional structure of orbitals in momentum space is dominated by features with a weak k_z-dependence that is essentially equal to that of an atomic p_z state, as is exemplified for the HOMO of pentacene in Fig. 2B of Ref. [26]. Therefore, the hemispherical cut through 3D momentum space measured in ARPES may be interpreted as a 2D cut through the real space π-orbital. We emphasize, however, that our phase recovery method is not restricted to such cases. By measuring CBE momentum maps for various photon energies, the full 3D structure of the orbital in momentum space may be mapped out, with which it should be possible to reconstruct the complete 3D orbital structure in real space.

3.6 Potentials and limitations

The simple FT relation between real and reciprocal space strictly holds only for a plane wave (PW) final state. It should be noted that the more complex independent atomic center (IAC) description of the photoemission process reduces to the PW final state when the atomic sites have the same atomic orbitals and when the experimental geometry is such that the polarization vector and emitted electrons are close to each other [26]. This is the case for the molecules investigated here. Moreover, as they contain only light atoms, scattering effects are expected to be small, and the results presented here for delocalized π-orbitals indicate that the PW final state approximation is in fact reasonable. Related to the issue of scattering, we have observed no differences for different molecular orientations and/or substrate surfaces. For instance, the reconstructed HOMOs of pentacene on silver and copper are essentially identical, although the molecules align across and along the atomic rows of the substrate, respectively. As yet we have come across no system in which the PW final state fails. But it is possible that for molecules containing high Z atoms scattering may become problematic.

As opposed to local scanning probe techniques, our photoemission momentum maps collect the emitted electrons from large sample areas. Thus, our method works best, without the need of deconvolution, when the molecules all have the same orientation. This is often the case on anisotropic substrates such as the (110) surfaces of face centered cubic metals, as used in this work. The results here have been obtained for well-ordered monolayers. However, long range order is not a prerequisite. Indeed, it can be detrimental, as significant intermolecular orbital overlap could lead to strongly dispersing bands, such that a description in terms of molecular orbitals is no longer appropriate. This is for instance the case for the LUMO of the monolayer of pentacene on Cu(110). Interestingly, however, at lower coverages the molecules remain aligned while diffusing over the surfaces at room temperature, and the orbital reconstruction is possible.

In conclusion, we have demonstrated that both the amplitude and the phase of the wave functions of adsorbed molecules can be simply recovered from angle resolved photoemission data. The orbitals obtained are not only in qualitatively good agreement with calculated orbitals, they also possess the orthogonality required of true wave functions. As such, the results open up a window into discussions of theoretical orbital concepts. On the more applied side, as the phase recovery procedure makes almost no assumptions, we believe ultimately it should be possible to obtain the orbital structure even of unknown molecules such as species formed in surface reactions. We foresee that with the new generation of electron analyzers with large acceptance angles that are now commercially available the technique of orbital reconstruction will find many applications.

3.7 Experimental Details

Experiments were performed in-situ in ultra-high vacuum with the toroidal electron analyzer attached to the U125/2-SGM beamline at the BESSYII synchrotron radiation facility in Berlin. A photon energy of 30 eV and a photon incidence angle of 40° with respect to the surface normal were used. The polarization direction is in the specular plane, containing the measured photoelectron trajectory. The toroidal energy analyzer collects photoelectrons in a kinetic energy window of 1 eV width over a polar emission angular range of $\theta = \pm 80°$ simultaneously. The full hemisphere of emitted electrons was obtained by rotating the azimuthal angle ϕ in 1° steps. The angular emission data were converted to parallel momentum components $k_x = \sqrt{2m_e E_{kin}/\hbar^2}\sin\theta\cos\phi$ and $k_y = \sqrt{2m_e E_{kin}/\hbar^2}\sin\theta\sin\phi$.

The Ag(110) substrate was cleaned in-situ by standard sputter anneal cycles. The molecules were evaporated from effusion cells onto the substrate at room temperature and their monolayers controlled by low energy electron diffraction. For pentacene a $\begin{pmatrix} 3 & -1 \\ 1 & 4 \end{pmatrix}$ monolayer structure was investigated where the majority of the molecules are oriented parallel to the [001] azimuth. For PTCDA the so-called brick wall monolayer structure, c(4×6), was investigated with all the molecules also parallel to [001].

3.8 Computational Details

Theoretical orbitals are obtained within DFT utilizing the ABINIT code [121]. The all-electron potentials are replaced by extended norm-conserving, highly transferable Troullier-Martins pseudopotentials [122], with a plane-wavecutoff of 50 Rydberg. Interaction between molecules is avoided by a super cell approach with a box size of $50 \times 50 \times 25$ $Bohr^3$ and Γ point sampling of the Brillouin zone.

In the iterative procedure we make use of the oversampling method developed from coherent diffraction techniques [37, 38]. Thereby, we take advantage of a dense experimental sampling in momentum space ($\Delta k = 0.05$ Å^{-1}) which leads to a real space domain size $X = 2\pi/\Delta k$ much larger than the typical size of molecules. We implement a modified version of the Fineup algorithm [37, 123], as explained in the *Iterative Phase Recovery* section.

Acknowledgments

We acknowledge financial support from the Austrian Science Fund (FWF) P21330-N20 and P23190-N16. We further acknowledge the Helmholtz-Zentrum Berlin - Electron storage ring BESSY II for provision of synchrotron radiation at beamline U125/2-SGM. The authors thank C. Wagner and R. Temirov (Forschungszentrum Jülich) for STM images in Fig. S3 e and g of the SI.

3.9 Supplementary information

3.9.1 Data preparation

Before the iterative procedure can be applied to the measured momentum maps, background intensity has to be subtracted from the ARPES data. To get rid of contributions arising from the diffuse substrate emission, the average polar angle Θ intensity distribution of different azimuthal angles Φ where no molecular features are present is subtracted from the whole raw intensity data $I(\Theta, \Phi)$. Beside these subtractions for all measured orbitals, in the case of 5A/Ag(110) there is a small amount of a second domain with molecules rotated 90° with respect to the main domain, which may impede the reconstruction procedure. The second domain may be seen for instance in the LUMO map at a k_y-value of 1.4 Å^{-1} (Fig. 3 panel (c), but is also present in the other orbitals momentum maps. To handle this circumstance we rotate the corresponding experimental momentum map by 90° and subtract 10% of the so rotated data from the original momentum map, getting rid of contributions from the minor domain.

The real space resolution of the orbitals is given by the maximum momentum value of the respective ARPES maps, which in turn is governed by the kinetic energy of the photoemitted electrons. Since the kinetic energies for the studied orbitals lie around 25 eV if photons of 30 eV are used, maximum k-values around $k_{\max} = 2.5$ Å^{-1} result. The resolution in real space would be therefore $\Delta x = \pi/k_{\max} = 1.25$ Å. In order to obtain smoother orbital images, we expand the momentum space domain size to approximately 17.5 Å^{-1} and set the data outside the measured $k_{\max} = 2.5$ Å^{-1} zero. Thereby, we can interpolate orbitals in real

space on a denser grid with a spacing of $\pi/17.5 = 0.2$ Å. The data produced with these preparation steps was used as an input for the iterative procedure.

3.9.2 Random initial phase

For a further proof of the robustness of our method, the supplementary Fig. S1 shows once again the iterative procedure, but now with a randomly k_x, k_y distributed phase as a starting point. The data and the color code used in this example are the same as for Fig. 2 of the main part. In panel (a) the first iteration of the procedure can be seen. Note the random distribution of the phase on the top left. After the first inverse Fourier transform, the so obtained real space intensity distribution, depicted on the right of panel (a), shows no similarity to an actual molecular orbital, but resembles a random distribution. The arrow number four shows the last step that closes one iteration cycle, which consists of applying the newly obtained complex phase (bottom left of panel (a)) to square root of the measured intensity $\sqrt{I}$ (left of panel (b)). The real space wave function obtained in the second second cycle, on the right of panel (b) still looks like an irregular distribution. After 50 iterations (panel (c)) the real space orbital is already close to the one obtained with the constant phase, and after the 250th iteration (panel d)) the converged result is indeed the same as for reconstruction starting with a constant phase (Fig. 2 in paper). Performing several reconstructions with different initial random complex phase patterns leads to essentially identical results, apart from minor details, thereby maintaining the good agreement with the calculated DFT orbitals.

3.9.3 Applying the symmetry and comparison to STM

The issue of orbital translation is illustrated in supplementary Fig. 3.6 for the HOMO-1 orbital of 5A. Comparing the reconstructed orbital (a) with the Kohn-Sham orbital (c), the concordance between these two is not as good as for the other four orbitals. On closer inspection, one may infer a better agreement if the reconstructed orbital is cyclically shifted in the direction indicated with the arrow. Such a shift may indeed result from the reconstruction algorithm, since a translation of the orbital in real space only leads to a constant phase factor in momentum space, due to the mathematical properties of Fourier transforms already mentioned in the discussion section of the main text. Therefore, the reconstruction algorithm cannot distinguish between a function $\phi(x, y)$ and the constant shifted function $\phi(x-R_x, y-R_y)$ multiplied with a phase factor $\exp(i\xi)$. In order to solve this ambiguity, we may choose to fix the position of the orbitals center in the middle of the confining box by applying inversion symmetry to the wave function during the iteration cycles. Doing so, we obtain the reconstructed

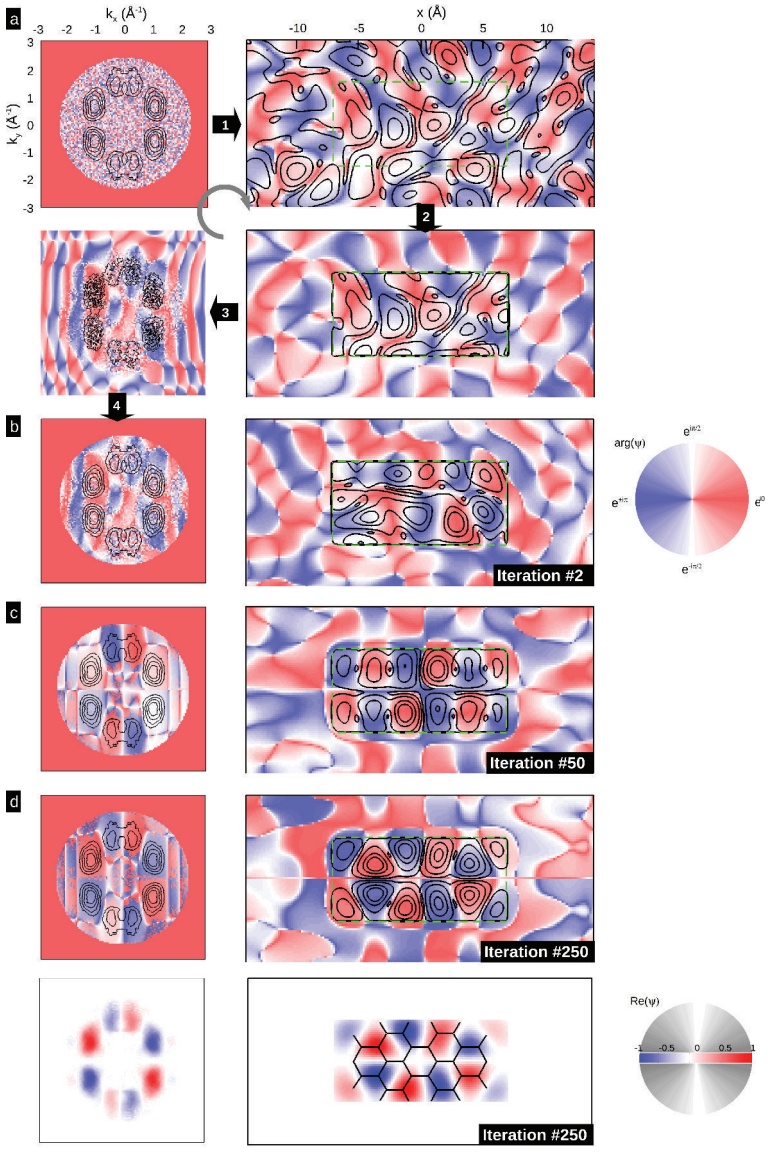

Figure 3.5: Illustration of the iterative wave function reconstruction algorithm with a random complex phase distribution as the starting point, using the example of the PTCDA HOMO. Black isolines represent the square root of the measured intensities, while the colour indicates the phase. Panel (a) displays the first iteration. Panels (b), (c) and (d) show reciprocal- (left) and real space (right) picture of the wave function in the second, 50th and 250th iterations. At the bottom of panel (d) we show the real part of the reconstructed wave function in k-space and real space.

orbital shown in panel (b), whose shape is actually in good agreement with the DFT calculation.

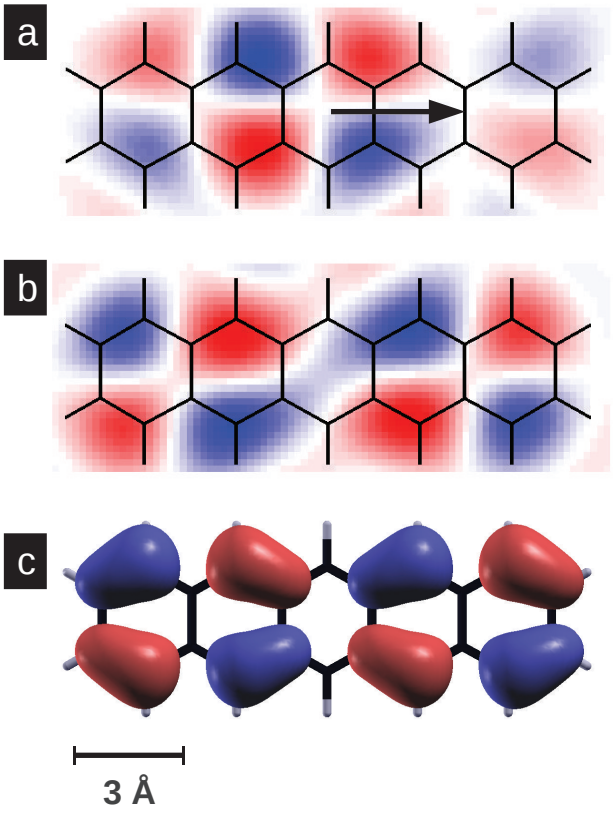

Figure 3.6: Illustration of the cyclic translation that can result from incorrect spatial confinement. (a) Real space reconstruction of the HOMO-1 orbital of 5A without any further constraints beside the spatial confinement of the orbital. (b) Real space reconstruction of the HOMO-1 orbital applying inversion symmetry to the orbital during the iterative procedure. (c) Kohn Sham orbital image of the HOMO-1 of 5A.

We relate the reconstructed orbitals to those measured with STM (see Fig. 3.7). As mentioned in the introduction, STM measurements probe the local density of states of the orbital at the position of the tip. Thus, no information on the phase of the wave function can be obtained in STM. In contrast, our ARPES-based reconstruction algorithm provides information about the phase, which we consider a major advantage over orbital imaging in scanning tunnelling microscopy. As expected, there are clear similarities in the results of the two techniques, e.g. regarding the nodal structure of all orbitals (supplementary Fig. 3.7 a to h). However, there are also clear differences: Firstly, the lateral extensions of the orbitals in the STM measurements are larger than the reconstructed ones, most notably in the case of 5A (supplementary Fig. 3.7 a to d). We think that this

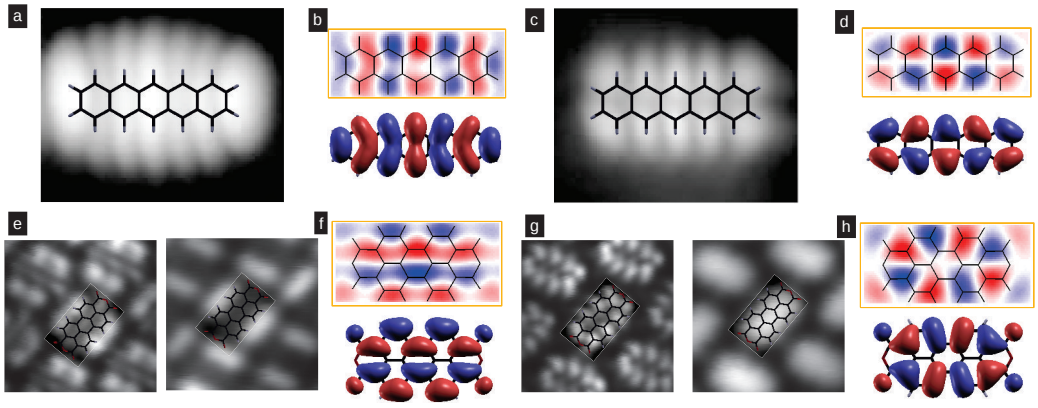

Figure 3.7: Comparison between the orbitals reconstructed iteratively from ARPES data and images of orbitals measured with STM. Panels (a) and (c) show STM images of the 5A LUMO and HOMO on NaCl/Cu(111) using a pentacene tip, taken from Ref.[31]. Panels (b) and (d) show 5A LUMO and HOMO reconstructed from ARPES (top) and the corresponding Kohn-Sham orbital images (bottom). Panels (e) and (g) show STM images of the PTCDA LUMO and HOMO on Au(111) using a CO tip (left) and a bare metal tip (right). Panels (f) and (h) show PTCDA LUMO and HOMO reconstructed from ARPES (top) and the corresponding Kohn-Sham orbital images (bottom).

is related to the fact that the probability density is detected at distances further away from the molecule, while in ARPES the orbital is cut in reciprocal space, which determines the size of the lobes. Secondly, supplementary Fig. 3.7 e to f illustrate the ambiguity of orbital images obtained from STM, arising from the influence of the tip. Thirdly, the ARPES-based reconstruction algorithm is not restricted to the LUMO and HOMO states of a molecule and should work independent of the chosen substrate.

Finally, in Fig. 3.8 which shows the same experimental data as Fig. 3.4 of the main text, the reconstructed orbitals are compared to *two-dimensional* projections of the theoretical orbitals. These 2D projections, $\phi(x, y)$, are obtained from the computed three-dimensional orbitals, $\psi(x, y, z)$, in the following way

$$\phi(x, y) = \int dz\, \psi(x, y, z) \cdot z e^{-c|z|}. \tag{3.1}$$

Here, the function $ze^{-c|z|}$ resembles the z-dependence of a carbon p_z orbital where the parameter c is chosen accordingly.

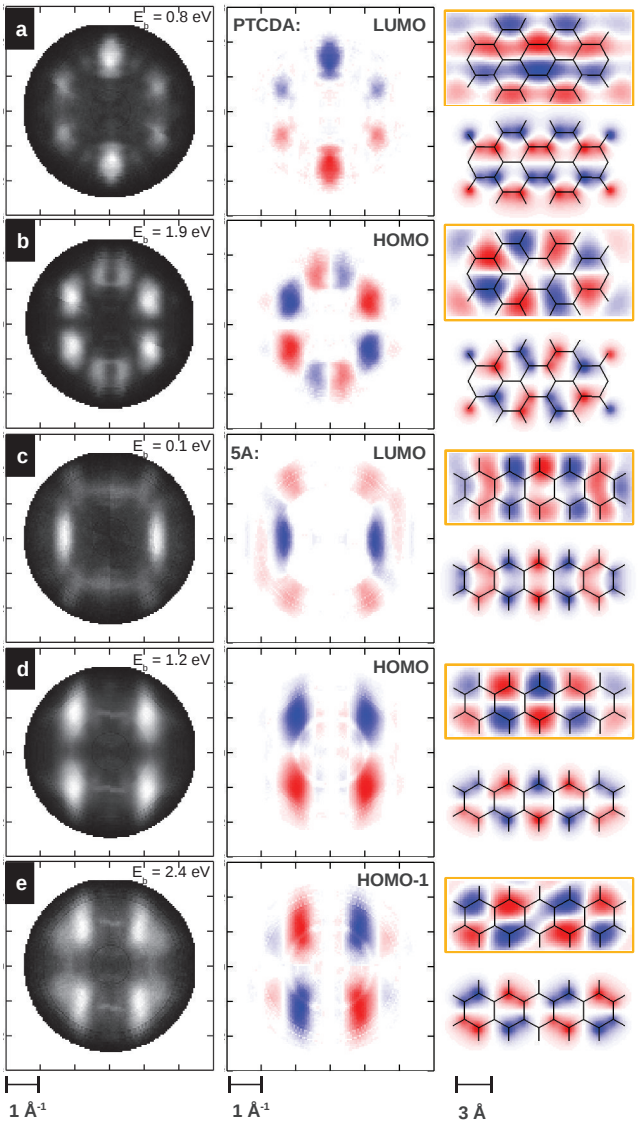

Figure 3.8: Compilation of orbitals reconstructed from ARPES data in this work (same data as in Fig. 3 of the main text except for the theoretical orbital images). The left column shows experimental CBE ARPES maps of the PTCDA LUMO (a) and HOMO (b), and the pentacene LUMO (c), HOMO (d) and HOMO-1 (e). The middle column shows the CBE maps with the recovered phase information. The right column displays the reconstructed real space orbitals which are compared to corresponding two-dimensional projections of Kohn-Sham orbital as explained in the text. The wave function confinement regions are 14.8×7.2 Å^2 and 14.8×5.4 Å^2 for PTCDA and pentacene, respectively.

Chapter 4

CuPc/Au(110): Determination of the azimuthal alignment by combination of a angle-resolved photoemission and density functional theory

In this chapter we make use of the OT technique in order to clarify the orientation of a monolayer of the organic molecule CuPc on a Au(110) surface, which is further confirmed by DFT calculations of the molecule-metal interface. Here, special care has to be taken of the DFT eigenvalue spectrum of this system, because in the energy range of interest there is mixture of delocalized states and states localized on the central metal atom of the molecule. Therefore the electronic structure of the interface is studied carefully, utilizing different approximations for the exchange correlation potential including a hybrid functional for the full interface. The work has been published in the Journal of Electron Spectroscopy and Related Phenomena. This chapter is a reproduction of the article [1].

Author contributions

The initial calculations of this work have been performed by my colleague Matus Milko at his time in Graz. He has done the calculations of the isolated molecule

[1] Reprinted from J. Electron Spectrosc. Relat. Phenom., Vol. 195, D. Lüftner et al., CuPc/Au(110): Determination of the azimuthal alignment by combination of a angle-resolved photoemission and density functional theory, pp. 293-300. Copyright 2014, with permission from Elsevier. The article may be found online at http://dx.doi.org/10.1016/j.elspec.2014.06.002

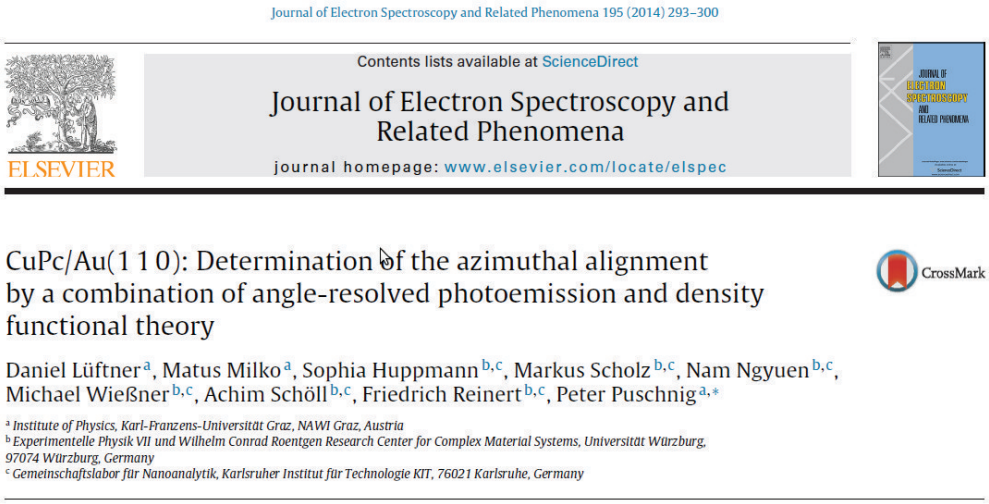
Journal of Electron Spectroscopy and Related Phenomena 195 (2014) 293–300

Contents lists available at ScienceDirect

Journal of Electron Spectroscopy and Related Phenomena

journal homepage: www.elsevier.com/locate/elspec

CuPc/Au(1 1 0): Determination of the azimuthal alignment by a combination of angle-resolved photoemission and density functional theory

Daniel Lüftner[a], Matus Milko[a], Sophia Huppmann[b,c], Markus Scholz[b,c], Nam Ngyuen[b,c], Michael Wießner[b,c], Achim Schöll[b,c], Friedrich Reinert[b,c], Peter Puschnig[a,*]

[a] Institute of Physics, Karl-Franzens-Universität Graz, NAWI Graz, Austria
[b] Experimentelle Physik VII und Wilhelm Conrad Roentgen Research Center for Complex Material Systems, Universität Würzburg, 97074 Würzburg, Germany
[c] Gemeinschaftslabor für Nanoanalytik, Karlsruher Institut für Technologie KIT, 76021 Karlsruhe, Germany

Figure 4.1: Header of the article [113] as it was published in the Journal of Electron Spectroscopy and Related Phenomena, including the reference, the title and all contributing authors with their affiliation. This chapter is beside some small modifications identical to the article.

and determined azimuthal alignment of the molecules with the help of the calculated momentum maps, which he confirmed by calculations of the adsorbed monolayer. When Matus left the institute, I took care of the calculations and performed the geometry optimizations including the semi empirical van der Waals dispersion corrections. Furthermore I repeated all the groundstate calculations with the newly obtained, optimized geometric structures, using the different xc potentials, presented in the article. The experiments were performed by our colleagues from Würzburg, mainly by Sophia Huppmann, who already included parts of the results in her master thesis [124]. The first draft of the manuscript was finalized by Peter Puschnig and me, based on Matus' initial text about the results he obtained in his calculations. Furthermore I was involved in iterating the manuscript to its final version which is presented here together with all contributing authors.

Abstract

Here we report on a combined experimental and theoretical study on the structural and electronic properties of a monolayer of Copper-Phthalocyanine (CuPc) on the Au(110) surface. Low-energy electron diffraction reveals a commensurate overlayer unit cell containing one adsorbate species. The azimuthal alignment of the CuPc molecule is revealed by comparing experimental constant binding energy $(k_x k_y)$-maps using angle-resolved photoelectron spectroscopy with theo-

retical momentum maps of the free molecule's highest occupied molecular orbital (HOMO). This structural information is confirmed by total energy calculations within the framework of van-der-Waals corrected density functional theory. The electronic structure is further analyzed by computing the molecule-projected density of states, using both a semi-local and hybrid exchange-correlation functional. In agreement with experiment, the HOMO is located about 1.2 eV below the Fermi-level, while there is no significant charge transfer into the molecule and the CuPc LUMO remains unoccupied on the Au(110) surface.

4.1 Introduction

The interface of organic thin films with noble metal surfaces has attracted considerable attention in the past years [116, 125–127]. On the one hand, this interest is driven by the application in organic electronic devices such as light emitting diodes, field effect transistors, or solar cells. On the other hand, the desire to understand the basic physical properties at metal-organic interfaces represents a more fundamental motivation. Here, a surface science approach combined with theoretical investigations is particularly useful when studying the adsorption of organic monolayers adsorbed on metallic surfaces. While various surface science techniques are capable of measuring the overlayer periodicities, adsorption sites, heights and orientations and are able to reveal the electronic structure of the interface, often only a combination of experiment and theory allows for creating a coherent picture of the system under study. One example are images from scanning tunneling microscopy (STM) where *ab-initio* electronic structure calculations are often necessary to overcome ambiguities in interpreting STM images. Another example is the interpretation of ultra-violet photoelectron spectroscopy experiments, in particular its angle-resolved variant. This will be theme of this contribution.

Angle-resolved photoelectron spectroscopy (ARPES) is *the* technique to study the occupied electronic band structure of solids by measuring the kinetic energy of the photoemitted electrons versus their angular distribution [20]. Particularly, many questions in nanophysics and interface engineering are often addressed by this experimental technique which, in combination with density-functional-theory calculations, leads to important physical insights. In recent years it has been shown that for highly-ordered layers of organic molecules, ARPES also provides a route to obtain information about the spatial structure of individual molecular orbitals [21, 26, 27, 30, 128]. By comparing measured ARPES data with simulations of the photoemission intensity based on density-functional theory (DFT) and approximating the final state of the photoemission process by a plane wave, molecular orbitals can be identified and molecular orientations can be determined [22, 28, 29, 117]. To date this approach, which has been termed *orbital*

tomography [21], has allowed the orbital density reconstruction of the highest occupied molecular orbital (HOMO) and lowest unoccupied molecular orbital (LUMO) in highly-oriented monolayer films of sexiphenyl on Cu(110) [26] and pentacene and PTCDA on Ag(110) [111], respectively, and has enabled the analysis of the molecule-substrate hybridization in PTCDA and NTCDA layers on Ag(110) [21, 117, 118, 129]. It has also been used to unambiguously assign molecular emissions in coronene and hexa-benzo-coronene films on Ag(111) [28] and to analyse monolayers and bilayers of PTCDA on Ag(110) [22, 108, 109, 130]. In terms of determining molecular orientations, the orbital tomography method has led to the tilt angle of pentacene multilayer film [26] and azimuthal orientation of tetra-phenyl-porphyrine in a monolayer film on Cu(110) [29].

In this work, we focus on a monolayer film of copper-phthalocyanine (CuPc) on Au(110) surface. Phthalocyanines are among the most studied functional molecular materials due to their interesting optical and electronic properties and their potential in nonlinear optics, optical data storage, electronic sensors, xerography, solar energy conversion, nuclear chemistry, molecular magnetism, electrochromic displays and heterogeneous catalysis [131]. Their sub-monolayer to monolayer growth on various noble metal surfaces and the structural and electronic properties of the resulting interface has been studied intensively [47, 132–139]. In terms of DFT calculations, both, various metal-Pc's [140] as well as the metal-free Pc [141] have been investigated on Au(111) and Au(110) surfaces, respectively, and the spin and orbital configuration of MePc chains assembled on the Au(110) have recently been investigated [142].

The goal of the present investigation is to fully characterize the CuPc/Au(110) interface of a fully developed monolayer in terms of its structural and electronic properties by means of a combined experimental and theoretical approach. In particular, the origin of the 1.2 eV binding energy peak in UPS data [135] needs to be clarified and the azimuthal alignment of the molecule to be determined. Moreover, it has been disputed whether the molecule adsorbs completely flat or exhibits a tilt angle with respect to the substrate surface [134, 138]. In terms of electronic structure, the level alignment and orbital ordering of the adsorbed CuPc is of prime interest. While the electronic structure of isolated CuPc molecule has been computed by means of high-level theoretical approaches [101, 143], it remains to be answered how issues arising from the self-interaction error of semi-local exchange-correlation functionals impact the electronic structure of such extended interfaces [80].

4.2 Method

4.2.1 Experimental details

The samples were prepared in an ultra-high vacuum chamber with a base pressure of $1 \cdot 10^{-9}$ mbar attached to an analysis chamber for ARPES. A Au(110) single crystal was utilized applying a standard cleaning procedure of annealing and sputtering cycles. Surface cleanliness and order was checked by X-ray photoelectron spectroscopy (XPS) and low energy electron diffraction (LEED). The CuPc films were prepared by organic molecular beam epitaxy from a home made Knudsen cell with growth rates of about 0.03 monolayer per minute. The completion of the monolayer was identified by LEED by the well-known (5×3)-reconstruction [134, 135] and verified by XPS and ARPES. The quality of the lateral order was improved by an additional annealing step of 10 minutes at 280°C. The ARPES measurement were carried out at room temperature with a monochromatized Helium discharge lamp (SPECS UVS300) using the He I_α-line at 21.22 eV. Photoelectrons were detected with a Scienta SES200 electron analyzer with an acceptance angle of $\pm 7°$. (k_x, k_y) momentum maps were derived by additional tilting the perpendicular polar angle in steps of 2° and azimuthal rotation by 10°. The intensity maps were corrected for the photoelectron emission characteristics by a cosine-function according to Lambert's law. In addition, the data was normalized to the channelplate function which was derived by measuring a polycrystalline Au-foil.

4.2.2 Computational details

All theoretical results presented here are obtained within the framework of density functional theory (DFT). Two types of calculations have been performed. First, orbital energies and corresponding wave functions of an isolated CuPc molecule are calculated by using either a generalized gradient approximation (GGA) in the Perdew-Burke-Ernzerhof flavor [66] for exchange and correlations effects or by employing a hybrid functional according to Heyd et al. (HSE) [88, 144]. These wave functions serve as input for the subsequent simulation of ARPES intensity maps within the one-step model of photoemission [23] and for which we approximate the final state by a plane wave [26]. Second, we have also performed calculations of an adsorbed monolayer on the Au(110) surface which we analyze in terms of molecule-projected density of states curves and charge density difference plots and for which we employ either a van-der-Waals-corrected GGA or HSE for exchange-correlation effects.

Simulation of ARPES maps

For the free CuPc molecule, we utilize the plane wave code ABINIT [121]. The all-electron potentials are replaced by extended norm-conserving, highly transferable Troullier-Martins pseudo potentials [122] using a plane wave cut-off of 50 Ryd. We employ a super cell approach with a box size of $50 \times 50 \times 22$ Bohr^3 and Γ point sampling of the Brillouin zone. The geometry of the free molecule is optimized by using a generalized gradient approximation (GGA)[66] for exchange-correlation effects. Due to the odd number of valence electrons in one CuPc molecule, all calculation are performed in a spin-polarized manner.

The orbitals ψ_i of the optimized molecule are utilized to evaluate the intensities of the ARPES within the so called one-step model [23].

$$\begin{aligned} I(\theta, \phi; E_{kin}, \omega) &\approx \sum_i |\langle \psi_f(\theta, \phi; E_{kin}) | \mathbf{A} \cdot \mathbf{p} | \psi_\mathbf{i} \rangle|^\mathbf{2} \\ &\times \delta(E_i + \Phi + E_{kin} - \hbar\omega), \end{aligned} \tag{4.1}$$

Here, θ and ϕ are the azimuthal and polar angle respectively, E_{kin} is the kinetic energy of the emitted electron and ω denotes the frequency of the incoming photon, Φ is the work function, and $\mathbf{p}$ and $\mathbf{A}$ are the momentum operator and the vector potential connected to the incoming radiation. We further approximate the final state ψ_f by a plane wave [24]. As outlined in more detail in a previous paper [26], and also noted earlier [25, 145], these approximations lead to the simple result that the PE intensity from a given initial state i is proportional to the square modulus of the Fourier transform of the initial state wave function $\tilde{\psi}(\mathbf{k})$

$$I_i(\theta, \phi; E_{kin}) \approx |\tilde{\psi}(\mathbf{k})|^\mathbf{2} |\mathbf{A} \cdot \mathbf{k}|^\mathbf{2}. \tag{4.2}$$

modulated by a weakly angle-dependent factor $|\mathbf{A}\cdot\mathbf{k}|^\mathbf{2}$ which depends on the angle between the polarization vector $\mathbf{A}$ of the incoming photon and the direction of the emitted electron. Note that in the simulated momentum maps shown below, we have chosen to neglect this factor, thus the simulated results only show the first factor of Eq. 4.2, *i.e.*, the Fourier transform of the initial state.

Adsorbed monolayer calculations

Electronic structure calculations for the $p(5 \times 3)$ CuPc/Au(110) interface have been carried out within a repeated slab approach using the VASP code [146, 147]. The Au(110) substrate is modeled by 4 layers of Au with an additional vacuum layer of 10 Å. Either a GGA [66] or the hybrid functional HSE [88, 144] are used for exchange-correlation effects, and the projector augmented waves (PAW) [148] approach was used allowing for a relatively low kinetic energy cut-off of about 400 eV. We use a Monkhorst-Pack $4 \times 3 \times 1$ grid of k-points [149], and a first-order

Methfessel-Paxton smearing of 0.05 eV [150]. To avoid spurious electrical fields, a dipole layer is inserted in the vacuum region [151]. In order to circumvent issues concerning van-der-Waals interactions which are ill-described in standard GGA functionals [45, 152], we employ the empirical correction scheme according to Grimme [153] and take the Au van-der-Waals parameters from Amft et al. [154]. In the geometry optimizations, we allow for relaxations of the topmost Au-layer and all atoms in the molecule. As for the isolated molecule, also here all calculations are performed in the spin-polarized mode.

4.3 Results

4.3.1 Experimental results

Fig. 4.2a shows a PES spectrum of CuPc/Au(110) in a narrow energy window below the Fermi edge for three different coverages. The sub-monolayer regime is displayed as dashed line, while the completed monolayer is shown as black full line. In addition, a PES spectrum corresponding to a multilayer coverage is shown as grey line. In the sub-monolayer and monolayer regime, we observe a peak at a binding energy of 1.2 eV which is shifted to about 1.5 eV in the multilayer film in agreement with earlier observations [135]. In order to clarify the origin of this molecular emission at the monolayer coverage, we have measured the angular dependence of this emission in an energy window of 400 meV around 1.22 eV in order to obtain a full (k_x, k_y) momentum map at constant binding energy. This data is shown after symmetrization according to the two-fold symmetry of the substrate in Fig. 4.2b where red (purple) colors indicate high (low) photoemission intensity. In addition to features arising from molecular emissions, that can be identified as being relatively broad in k-space, there are also sharper features, for instance, around $(k_x, k_y) = (1.3, 0.0)$ or around normal emission, which can be traced back to substrate emissions. In order to emphasize the molecular features, we have applied a fitting routine to the experimental data. The background arising from the Au(110) surface was respected by a linear function and the HOMO signal by a Gaussian peak (see Fig. 4.2a). This automated procedure might have a certain error in the intensity determination of a single spectrum, but this is averaged out in the images of the angular distribution of the Gaussian contribution as displayed in Fig. 4.2c. As will be demonstrated below, this momentum map can be utilized to unambiguously assign it to a given molecular orbital. Moreover, it also reveals the azimuthal alignment of the CuPc molecule on the surface.

Before doing so, we further characterize the structure of the complete monolayer of CuPc/Au(110) by means of LEED which is shown in Fig. 4.3a at a beam energy of 14 eV. It reveals a commensurate structure with a rectangular 5×3 overlayer unit cell [134]. Using the substrate's unit cell vectors of $a_s = 4.08/\sqrt{2} =$

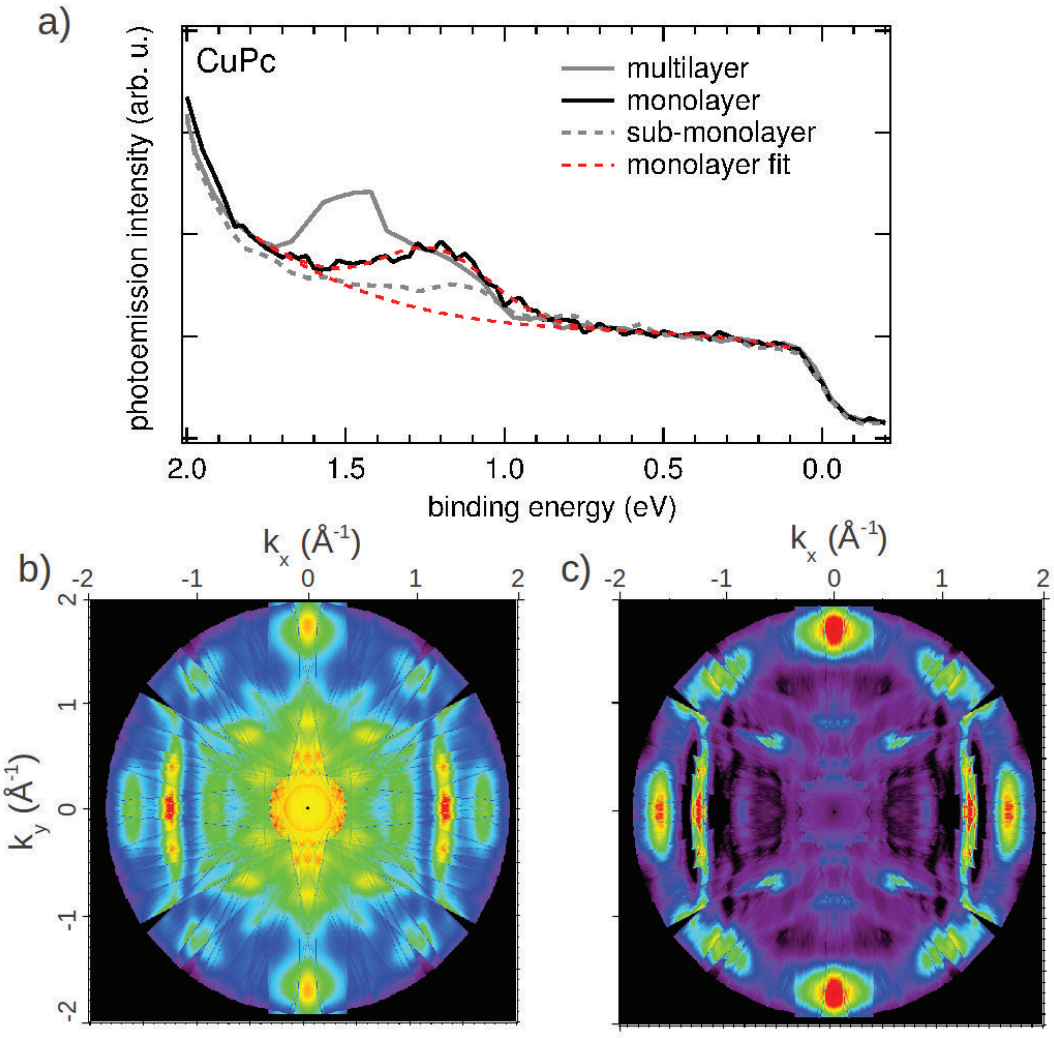

Figure 4.2: (a) Thickness-dependent PES spectra in a binding energy range between 2 eV and the Fermi edge. The dashed, black, and grey lines correspond to a sub-monolayer, monolayer, and multilayer coverage, respectively. The emission angle was 50°. The fitting procedure of the monolayer spectrum utilizing a linear background and a Gaussian peak is illustrated by the red dashed lines. (b) Experimental ARPES map of a monolayer of CuPc's recorded at the HOMO energy (400 meV integration window around 1.22 eV). (c) The experimental data of panel (b) with suppressed background. For the mathematical treatment a Gausian was used for the CuPc HOMO and a linear function for the background from the substrate.

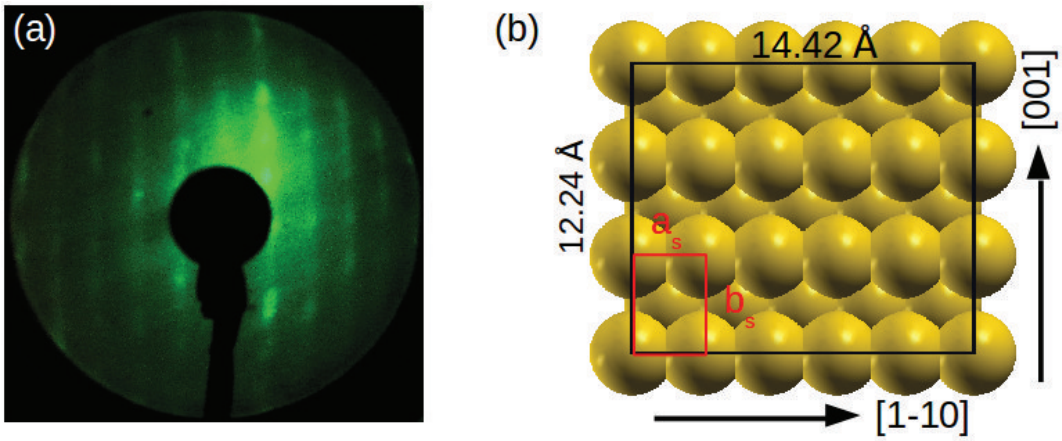

Figure 4.3: (a) Low energy electron diffraction pattern of CuPc/Au(110) as measured. (b) Surface supercell deduced from LEED. The red rectangle symbolizes the unit cell of the unreconstructed Au(110), whereas black rectangle shows the 5×3 unit cell of the overlayer. Here and in the following we choose the x axis along the substrate's $[1-10]$ direction, and the y axis parallel to the [001] direction.

2.88 Å and $b_s = 4.08$ Å, experiment reveals a CuPc/Au(110) surface unit cell of $a = 14.42$ Å and $a = 12.24$ Å, thus having an area of $a = 176.5$ Å^2.

4.3.2 Isolated molecule calculations

In this section, we show how the comparison of simulated ARPES maps of various CuPc states leads to the identification of the molecular emission discussed above and at the same time also reveals the azimuthal alignment of the molecule. Fig. 4.4a and b shows gas phase spectra of CuPc computed within the GGA and HSE approximations for exchange-correlation effects, respectively. Note that the energy scale is with respect to the vacuum level, E_{vac}, and that we have introduced an artificial broadening of 0.1 eV. The gray areas display the total density of states while the blue and red lines, respectively, denote molecular states of π and σ symmetry. In the gas phase, CuPc belongs to the D_{4h} point group and thus its orbitals can be labeled according the irreducible representations of D_{4h}. In this work, we focus on the four frontier orbitals denoted as a_{1u}, e_g the two spin-split states $b_{1g}^{\uparrow}$ and $b_{1g}^{\downarrow}$ whose energetic positions are indicated in Figs. 4.4a and b. The a_{1u} and e_g are anti-symmetric with respect to reflection at the molecular plane, thus are of π symmetry, while the b_{1g} orbitals are symmetric and thus are of σ symmetry. As can be seen from the corresponding orbital images in Fig. 4.4c computed within GGA, the two π orbitals are delocalized about the carbon macrocycle of the molecule, while the b_{1g} state is concentrated around the central Cu atom.

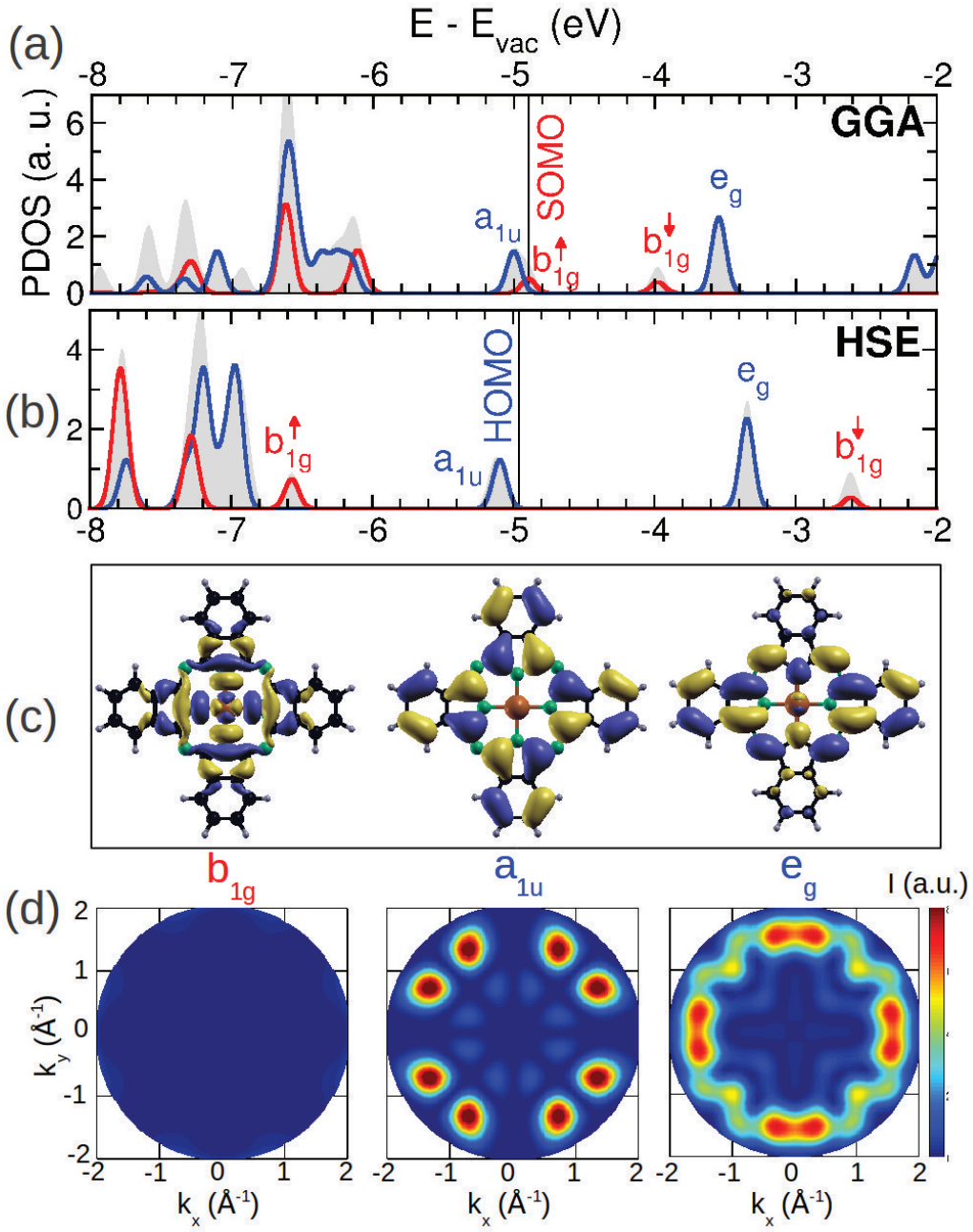

Figure 4.4: (a) and (b) Gas phase spectra of CuPc computed within GGA and HSE *xc*-approximations, respectively. Gray areas show the full DOS, while the red (blue) line displays the DOS projected onto σ and π states. Symmetry labels of selected states are shown, the vertical black lines indicates the Fermi level. (c) shows orbital images of the b_{1g}, a_{1u}, and e_g states, while panel (d) shows the corresponding momentum maps as described in the text.

As has been highlighted in earlier theoretical work [80, 101, 143, 155], this distinct degree of localizations gives rise to pronounced self-interaction errors which are present in approximate functionals such as the GGA. This can be clearly observed when comparing the spectra calculated within GGA and HSE in Figs. 4.4a and b. The most pronounced difference when incorporating a fraction of exact exchange according to the HSE prescription, is the downward (upward) shift of the $b_{1g}^{\uparrow}$ ($b_{1g}^{\downarrow}$) state. As a consequence, the two delocalized π-orbitals a_{1u} and e_g turn out to the HOMO and LUMO of the molecule in full accordance with previous study [101]. As has been demonstrated [156], the improved description of the electronic structure within the hybrid functional HSE is not only due to a partial correction of the self-interaction error but also due to the changed interpretation of eigenvalues within a generalized Kohn-Sham framework [91].

Following Eq. 4.2, we simulate ARPES momentum maps of the three frontier molecular orbitals b_{1g}, a_{1u}, and e_g using a final kinetic energy of 15.8 eV. The results are depicted in panel d) of Fig. 4.4 where the e_g map is in fact a superposition of two maps arising from the two degenerate e_g states. Note that our results closely resemble ARPES maps of the HOMO of NiPc and CoPc as obtained from the more sophisticated independent atomic center approximation including single scattering events [128] which also sheds new light on an early dispute about the validity of the single plane-wave approximation for such large π-conjugated molecules [157, 158]. We also stress that our maps are computed from the GGA orbitals, but the corresponding maps of the HSE orbitals are almost indistinguishable from the former on the scale shown in the figure. While the two π-states give rise to a characteristic structure as a function of k_x and k_y, our plane-wave final state approach predicts a much smaller overall PE intensity which is hardly visible when using the same intensity range in the color map as for the other two maps. When comparing these maps with the experimental map from Fig. 4.2c, no resemblance can be recognized even when considering that the sharp experimental features around $(k_x, k_y) = (1.3, 0.0)$ Å^{-1} and $(-1.3, 0.0)$ Å^{-1} originate from the *sp*-bands of Au. In particular, the strongest experimental features along the principal x and y directions are absent in the a_{1u} HOMO map, and appear split into two peaks in the e_g LUMO map. Most likely, also the $b_{1g}^{\uparrow}$ can not be the origin of the PES signature at 1.2 eV due to weak PE cross section of this σ state and its relatively large binding energy predicted from the gas phase HSE calculations.

In order to reconcile theory and experiment, we have to take into account the possibility that CuPc does not align along the high symmetry directions of the substrate but rather chooses to adsorb with a different azimuthal orientation. Taking into account the two-fold symmetry of the Au(110) substrate, this implies the existence of two mirror domains which are present in the experimental samples and the fact that the measured ARPES map of Fig. 4.2c is in fact a superposition of these two mirror domains [108]. When simulating various az-

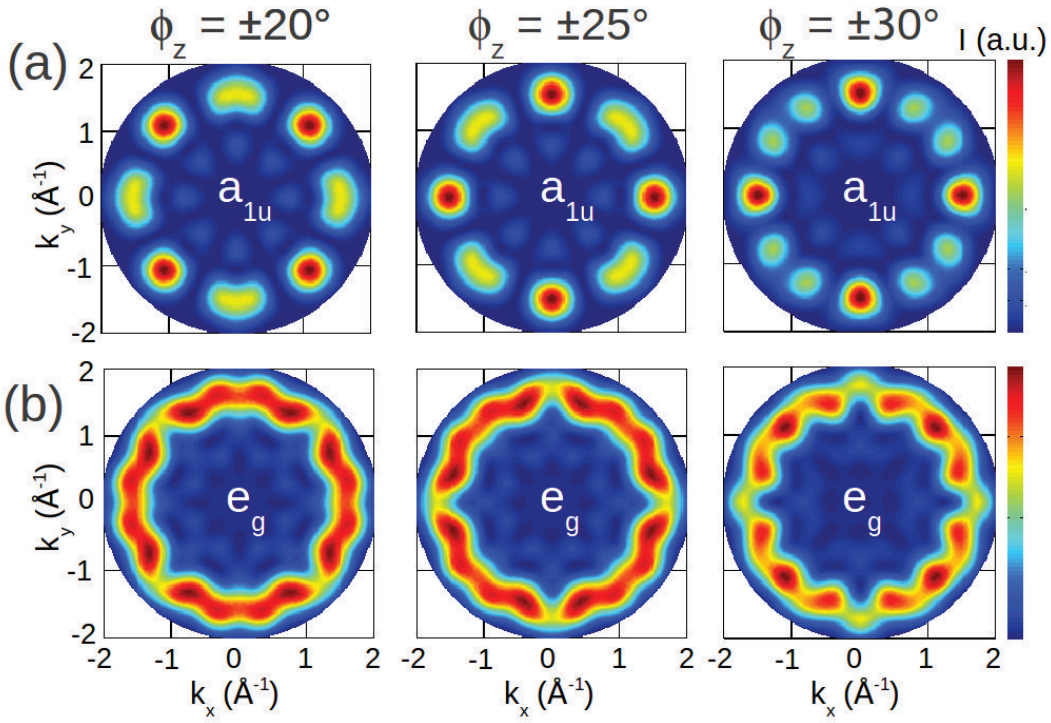

Figure 4.5: Simulated ARPES maps of the CuPc HOMO (a_{1u}) and LUMO (e_g) are shown in panels (a) and (b), respectively. Three azimuthal orientations of the CuPc molecule with respect to the high-symmetry substrate directions are presented, $\phi_z = \pm 20°$ (left), $\phi_z = \pm 25°$ (middle) and $\phi_z = \pm 30°$ (right).

imuthal orientations of CuPc, as characterized by the rotation angle ϕ_z of one CuPc molecule around the z-axis normal to the molecular xy-plane, and assuming equally weighted mirror domains, one obtains the images displayed in Fig. 4.5.

Panel (a) of Fig. 4.5 shows simulated maps of the HOMO orbital (a_{1u}) while panel (b) shows the corresponding results for the LUMO orbital (e_g) computed for three different azimuthal orientations ϕ_z. A comparison with the experimental map in Fig. 4.2c shows that the best agreement is found for the HOMO map with an angle of $\phi_z = 25°$ (Fig. 4.5, top row, middle column). While it is perhaps not unexpected that the emission observed at 1.2 eV binding energy is due to the HOMO of CuPc, and not due to the LUMO which remains unoccupied owing to the comparably weak metal-molecule interactions on Au surfaces, the comparison with the simulated maps provides clear evidence for the origin of the molecular feature seen in the PES data of Fig. 4.2a. Moreover, the mutual agreement also allows us to determine the azimuthal orientation of the molecule. Given the rather strong dependence of the simulated maps on the angle ϕ_z, we estimate the error bars of this approach to be better than 5°.

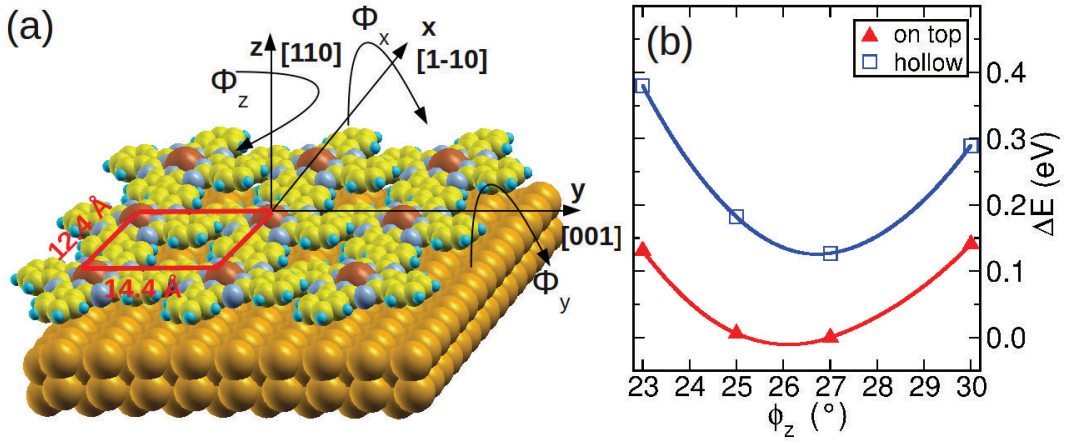

Figure 4.6: (a) Definition of the tilting angles (ϕ_x and ϕ_y) as well as the rotation angle (ϕ_z) describing the molecular orientation on the surface. (b) Total energy of the CuPc/Au(110) interface as a function of the azimuthal orientation ϕ_z for a fixed tilt of $\phi_x = 3°$ and $\phi_y = 9°$. The red (blue) symbols are for the on-top (hollow) adsorption site of the central Cu atom.

4.3.3 Geometry relaxations

In order to confirm these findings, we determine the best adsorption site and orientation of a monolayer of CuPc/Au(110) in the experimental overlayer unit cell by means of total energy and force calculations within van-der-Waals corrected DFT [153, 154]. Taking into account the area of the surface unit cell, we can conclude that there is only one molecule per unit cell. We consider two adsorption sites characterized by the position of the Pc's central copper atom with respect to the substrate's gold atoms: in the first Cu is positioned directly on top of a gold atom of the topmost Au layer, while in the second, the Cu atom is placed in a hollow position between two Au-rows. As shown in Fig. 4.6, the orientation of the molecule is characterized by the three angles ϕ_x, ϕ_y, ϕ_z. Here, ϕ_z is the already familiar azimuthal orientation, and ϕ_x and ϕ_y describe tilts of the molecule away from a perfect planar adsorption geometry.

In a fist attempt, we rigidly rotate the molecule stepwise by one of these angles and successively perform single-point total energy calculations. Here, the geometry of the molecule and the surface is kept constant and the vertical Cu-Au interatomic distance is fixed to 3 Å. As we are interested mainly in the orientations with respect to ϕ_z, Fig. 4.6b displays total energy differences as a function of ϕ_z, while the other two angles are kept as parameters. For geometric reasons, ϕ_x and ϕ_y must be restricted to rather small values of $\approx 3-10°$. Exceeding these numbers would cause parts of the molecule to approach the surface too close which would be energetically unfavorable. On the other hand, when these angles drop bellow $\approx 3°$, *i.e.* perfectly flat lying molecule adjacent molecules would

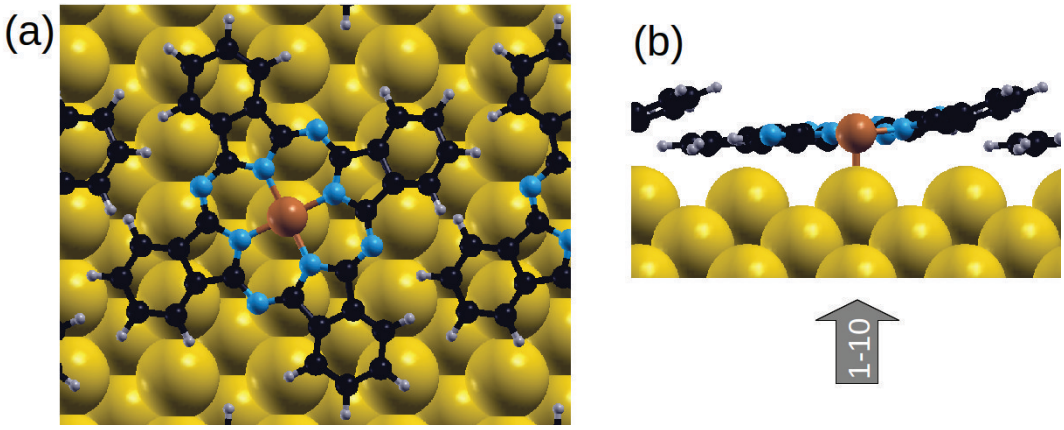

Figure 4.7: Top view (a) and side view along the (1-10) direction (b) of the relaxed CuPc/Au(110) structure.

start to overlap with each other which would be again disadvantageous. Fig. 4.6b shows results for the optimal values of these angles which have been determined to $\phi_x = 3°$ and $\phi_y = 9°$. We see that for both adsorption sites, the best azimuthal angle lies between 25° and 27°, where the on-top geometry is the energetically favored one yielding an azimuthal alignment of about $\phi_z = 26°$ which is in nice agreement with the value deduced from the ARPES momentum maps.

In order to refine this adsorption geometry, we fully relax the CuPc/Au(110) system only freezing in the three bottom-most Au layers. As a starting point for the relaxation, we use the azimuthal molecular alignments obtained from the mapping of the potential energy landscape described above, and we have stopped the geometry optimization when all forces fall below 0.02 eV/Å. The resulting adsorption geometry is depicted in Fig. 4.7. Note that the top site of the central Cu atom remains to be the energetically favorable and that the Cu atom has moved closer to the surface to a distance of 2.80 Å. In addition there appears a slight bending of the CuPc molecule, however, the azimuthal alignment as determined above from the rigid total energy calculations remains unaltered after this full geometry relaxation.

4.3.4 Electronic structure

Knowing the correct adsorption site and geometry, we can analyze the electronic structure of the CuPc/Au(110) interface in more detail. Fig. 4.8 shows the projected density of states (PDOS) plots obtained from a GGA (panel a) and a HSE (panel b) calculation. For each type of exchange-correlation potential, the figure shows the PDOS for a free-standing layer (top) and the adsorbed monolayer (bottom). We use the same color code as in Fig. 4.4, thus the gray areas are the DOS projected onto the entire CuPc molecule, and the red (blue) lines indicate

the PDOS of the molecular σ (π) states. The position of the Fermi level is shown as vertical black line.

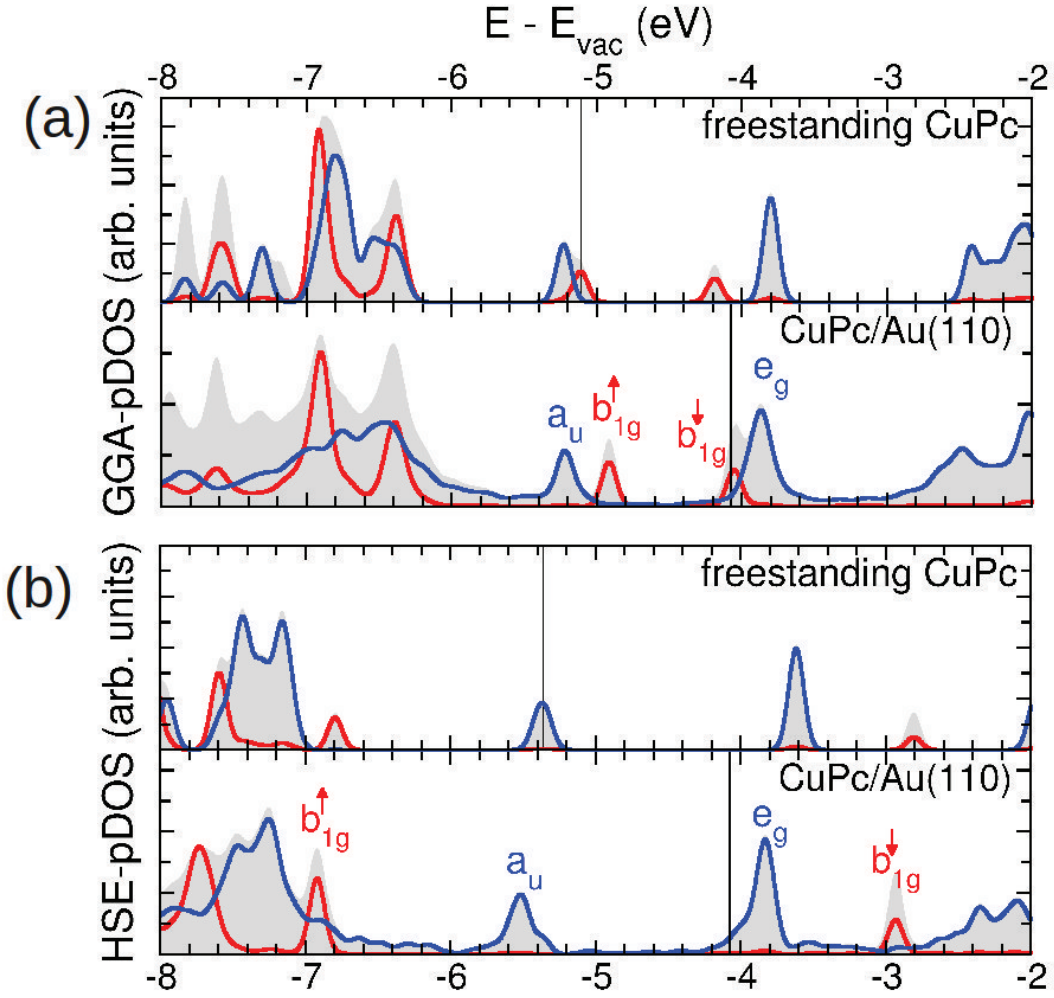

Figure 4.8: (a) and (b) Projected density of states curves for a free-standing layer of CuPc (top) and the adsorbed monolayer CuPc/Au(110) (bottom) computed within GGA (panel a) and HSE (panel c) *xc*-approximations, respectively. Gray areas show the DOS projected onto the CuPc molecule, while the red (blue) line displays the DOS projected onto σ and π states of CuPc. Symmetry labels of selected states are shown, the vertical black lines indicates the Fermi level.

The electronic structure of the *free-standing layer* is quite similar to the one of the isolated molecule owing to the fact that intermolecular interactions are weak. We also observe that the GGA-PDOS results suffer from the same self-interaction problems which have already been discussed in the context of the isolated CuPc. Most importantly, HSE shifts the $b_{1g}^{\uparrow}$ level downward by the considerable amount of 1.7 eV leading to the fact that the HOMO (LUMO) level

in the HSE calculation clearly is the a_{1u} (a_{1u}) state. HSE predicts the ionization potential (electron affinity) of the free-standing layer to be 5.35 eV (3.60 eV), thus a gap of 1.75 eV.

When taking into account the interaction with the Au(110) substrate in the *full CuPc/Au(110)* calculation, the molecular levels shift only moderately and appear weakly broadened with respect to the free-standing layer. While the GGA-PDOS has the already familiar problem that it underestimates (overestimates) the binding energy of the occupied (unoccupied) b_{1g} states, this deficiency is nicely corrected by applying the hybrid functional HSE calculations, which turn out to be quite costly for the full CuPc/Au(110) system. In the HSE result, the HOMO is at 5.5 eV below the vacuum level, thus slightly shifted downward with respect to the free-standing layer. The binding energy of the HOMO is 1.25 eV and 1.40 eV for GGA and HSE results. Thus, in contrast to the situation for b_{1g}, the GGA data agrees slightly better with the experimental value of 1.2 eV. As already inferred from the comparison of the experimental ARPES maps with the simulations, the CuPc LUMO remains unoccupied and is situated at an energy of 3.8 eV below the vacuum energy and thus slightly above the Fermi level.

Using Fig. 4.8, we can also analyse the work function of the system, for which our calculations yield a value of 4.13 eV for Au(111) surface covered by one complete monolayer of CuPc. Compared to the work function of 4.90 eV for 4 layer-thick Au(111) slab this indicates a reduction of 0.77 eV. Note that although the self-interaction errors disarrange the positions of the b_{1g} states in the GGA calculation, it yields the same work function as the hybrid functional calculation. These computed values can be compared to experimental data which show a work function reduction of 0.95 eV [135] with respect to a work function of 5.20 eV for the clean Au(110) surface [159]. We can understand the reduction of the work function from by analyzing the charge rearrangements leading to a bond dipole [160]. To this end, we define the charge density difference $\Delta\rho$ as the charge density of the full system (ρ_f) minus the sum of the charge densities of two the subsystems, *i.e.*, the freestanding molecular layer ρ_m and the Au(110) slab (ρ_s)

$$\Delta\rho(\mathbf{r}) = \rho_f(\mathbf{r}) - (\rho_m(\mathbf{r}) + \rho_s(\mathbf{r})). \tag{4.3}$$

A real space plot of the plane-averaged charge density difference can be seen in Fig. 4.9. Here, red areas highlight regions of charge accumulation, while blue areas mark regions of charge depletion. We see that above the molecule charge is depleted while in the interfacial region between the molecule and the topmost Au-layer charge is accumulated followed by a series of weaker bond dipoles of decaying amplitude, but no overall significant charge transfer to the molecule takes place. When solving the one-dimensional Poisson equation for this charge density difference, *i.e.* integrating it twice along the z coordinate, we obtain the change in the electro-static potential induced by the adsorption of the molecule

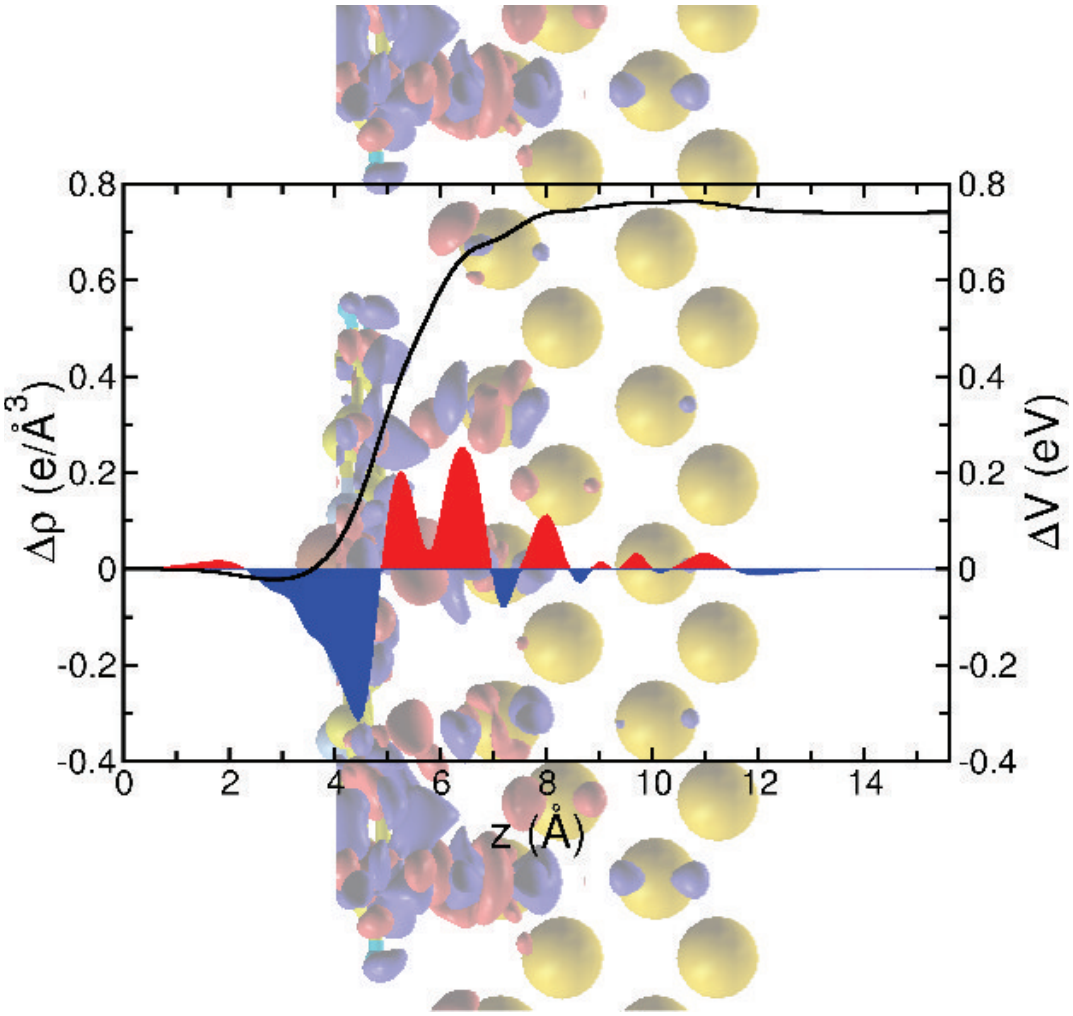

Figure 4.9: Plane-averaged charge density difference (red-blue curve, left axis) and electrostatic potential (black curve, right axis) as a function of the vertical direction z. The background graphics visualizes the adsorbed molecule on the surface projected onto the yz plane, including the 3D charge density difference plotted as iso-surface representation. Note that the scale of the graphs in z-direction are matching.

shown as black line in Fig. 4.9. From this analysis, we can deduce a potential jump of about 0.77 eV across the CuPc/Au(110) interface which is the reason for the reduction of the work function upon the adsorption of the CuPc monolayer. Here, 0.72 eV arise from the charge rearrangements (bond dipole) while a minor contribution (0.05 eV) comes from a molecular dipole induced by slight geometry distortions upon adsorption.

4.4 Conclusions

In this combined experimental and theoretical investigation, the structural and electronic properties of the completed monolayer of Copper-Phthalocyanine on a Au(110) surface have been revealed. While our low-energy electron diffraction data confirms the (5×3) super structure containing one molecule per surface unit cell already reported earlier [134, 135], we apply the orbital tomography method using ARPES momentum maps to determine the azimuthal alignment of the molecule. Thereby, we unambiguously assign the molecular emission at 1.2 eV binding energy to the HOMO orbital of CuPc and the comparison with theoretical momentum maps further yields an azimuthal molecular rotation angle of 25°. This value is confirmed by total energy calculations within van-der-Waals corrected DFT which also leads to the adsorption site in which the central Cu atom is situated on top of a Au atom and to the adsorption height of 2.80 Å. We calculate the electronic structure of the CuPc/Au(110) interface, both using a generalized gradient approximation and utilizing a hybrid functional for exchange-correlation effects. The latter is shown to greatly improve the energetic positions of the Cu-localized b_{1g} states, while the computed work function modifications and the binding energies of the molecular π states turn out to be less sensitive to the choice of xc-functional. In summary, we disclose that the presented approach, combining momentum maps from angle-resolved photoemission spectroscopy with corresponding PE intensity simulations, demonstrated on the model interface CuPc/Au(110) has great potential for characterizing the structural and electronic properties of similar systems.

Acknowledgement

M.M. and P.P. acknowledge support from the Austrian Science Fund (FWF) project P23190-N16. A.S. and F.R. thank the Deutsche Forschungsgemeinschaft (grants GRK 1221 and RE1469/9-1) and the Bundesministerium für Bildung und Forschung (contract 03SF0356B) for finance.

Chapter 5

Unexpected interplay of bonding height and energy level alignment at heteromolecular hybrid interfaces

In this chapter a hetereo-organic monolayer system, that consists of more than one type of molecule is investigated. With the help of the OT technique which has been applied to the system, we were able to distinguish between the emission contributions of the different contributing molecules and using NIXSW measurements the adsorption heights of the constituents could be individually obtained. Supporting DFT calculations, which confirmed the experimental findings, enabled us to give a possible explanation to the complex bonding behavior at this heteromolecular-metal interface. The work has been published in Nature Communications and the header is shown in Fig. 5.1. This chapter is a reproduction of the article and its supplementary information [1].

Author contributions

This work was motivated by the results of the numerous experiments, which have been performed by Benjamin Stadtmüller and his colleagues in Jüllich under the supervision of Christian Kumpf and Stefan Tautz. The ARPES experiments were also assisted by the co authors from the surface science group in Graz (for details see the Author contributions of the original publication [112]). Benjamin has also written the first version of the manuscript and is consequently the first author,

[1] Reproduced with permission from the Nature Publishing Group, the original article is available online at http://dx.doi.org/10.1038/ncomms4685

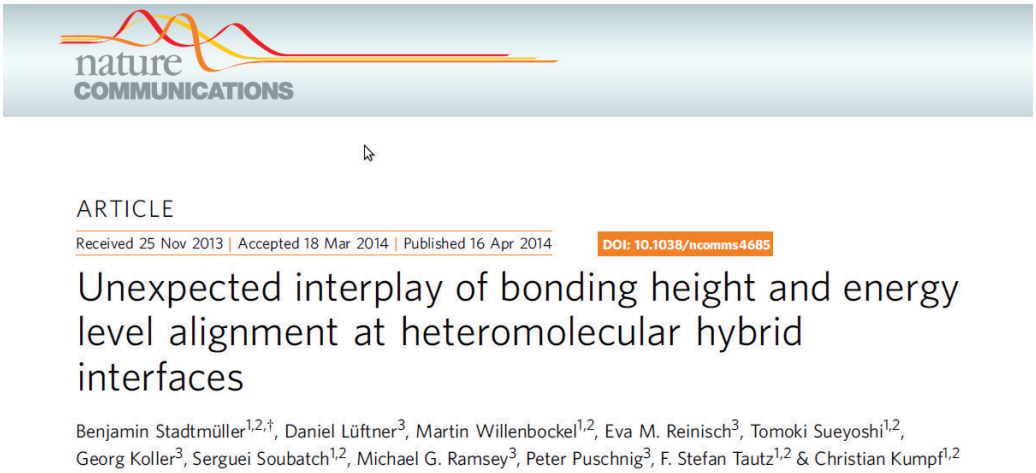

Figure 5.1: Header of the article [112], which was published in Nature Communications, showing title and all contributing authors. Chapter 5 is a slightly modified reproduction of this article and its supplementary information.

as he is the main contributor to this work. I have performed and extensively analyzed all ab-initio DFT calculations presented in this work. Furthermore I was part of numerous discussion about the experimental and calculated data and the manuscript itself with all contributing authors. Finally, I have prepared the figures related to the calculations and written parts of the supplementary Information.

Abstract

Although geometric and electronic properties of any physical or chemical system are always mutually coupled by the rules of quantum mechanics, counterintuitive coincidences between the two are sometimes observed. The coadsorption of the organic molecules 3,4,9,10-perylene tetracarboxylic dianhydride and copper-II-phthalocyanine on Ag(111) represents such a case, since geometric and electronic structures appear to be decoupled: One molecule moves away from the substrate while its electronic structure indicates a stronger chemical interaction, and vice versa for the other. Our comprehensive experimental and ab-initio theoretical study reveals that, mediated by the metal surface, both species mutually amplify their charge-donating and -accepting characters, respectively. This resolves the apparent paradox, and demonstrates with exceptional clarity how geometric and electronic bonding parameters are intertwined at metal-organic interfaces.

5.1 Introduction

In chemistry, there is a general tendency that stronger bonds go along with shorter bond lengths. For covalent bonds, this is well known; for instance, in the sequence from single to triple bonds, the bond length decreases while the bond strength increases. Shorter bonding distances imply more wave function overlap, stronger hybridization and (in case of polar bonds) more charge exchange, all of which promote stronger chemical interaction and can thus be interpreted as electronic signatures thereof. Therefore, it would be very surprising if observations which would normally go along with a stronger chemical interaction coincide with a larger bonding distance. Yet, such a counterintuitive relationship is precisely what we observe in the particular case of a metal-organic hybrid interface presented here.

For adsorbed organic molecules, the relevant geometric parameter (the 'bond length') is the vertical adsorption height above the metal. Hence, one would expect that a smaller adsorption height should correspond to stronger chemical interaction. Indeed, it was recurrently observed that on more reactive surfaces, where chemical interaction is stronger, the adsorption heights tend to be smaller.[44, 45, 47, 136, 161–168] This empirical correlation is often a result of both local and extended (that is, π-) bonds [168] and of the charge spill-out profile above the surface (see below).

In the electronic structure an observation that usually goes along with smaller adsorption height and thus stronger chemical interaction is a downshift of the lowest unoccupied molecular orbital (LUMO), that is, an increase of its binding energy. In the case of 'weak chemisorption', which is the relevant situation for the molecule-substrate combination discussed in this paper, this includes an at least partially filling of the LUMO which hence becomes detectable in photoelectron spectroscopy. Two effects are at the origin of this relationship between adsorption height and LUMO binding energy. Firstly, the work function of the metal controls both adsorption height and LUMO binding energy: if the work function is low, the spatial extent of the charge spill out is small. This favors both small adsorption heights [44, 168–170] and – assuming vacuum level alignment – large LUMO binding energies. Note that the push-back effect, that is, the Pauli repulsion of the electronic charge spill-out of the metal caused by the approaching molecule, even strengthens this correlation: a larger push-back tends to reduce adsorption height and work function further, yielding even larger orbital binding energies. Second, the interaction of the negatively charged LUMO with its image dipole increases the LUMO binding energy, the more so the closer the molecule is to the surface. The normal relationship between geometric and electronic structure for molecules adsorbing on metal surfaces therefore is: *A smaller bonding distance, which is the geometric signature of a stronger chemical interaction, coincides with a increased binding energy of the relevant frontier orbital (here: the LUMO).*

This relationship has been demonstrated for many organic materials. Two examples are the aromatic molecules copper-II-phthalocyanine (CuPc) and 3,4,9,10-perylene tetracarboxylic dianhydride (PTCDA). Their adsorption on noble metal surfaces (Ag, Cu and Au) has been investigated intensively within the last years. [21, 47, 108, 130, 135–137, 139, 166, 170–177] Here we focus on the adsorption of these two molecules on the Ag(111) surface, where both molecules exhibit weak chemisorption.[178, 179]

The adsorption behaviour of both molecules exhibits some characteristic differences: the charge transfer from the surface to the molecule is stronger for PTCDA than for CuPc, which agrees with the adsorption heights found for both adsorbate systems. Furthermore, while PTCDA molecules on Ag(111) attract each other and hence form compact islands in the submonolayer regime (Fig. 5.2a),[180] CuPc (and other phthalocyanine) molecules repel each other on Ag(111) and thus yield a dilute phase (Fig. 5.2b) and a low-density phase with a continuously changing unit cell size as function of coverage.[136, 139, 181] This remarkable disparity emerges from a different interplay between intermolecular and molecule-substrate interactions in the two *homo*molecular systems. While a repulsive intermolecular force is present in both systems due to the molecule-surface bond dipole, this is exceeded by the attractive interaction between the quadrupole moments of neighbouring PTCDA molecules. It is therefore interesting to examine whether a mixed, *hetero*molecular phase between the two can be prepared, and how the differences in the intermolecular and molecule-substrate interactions affect the geometric and electronic properties of the film. Although technologically relevant, such heteromolecular adsorbate systems have rarely been systematically investigated in the literature so far.[182–195]

As it turns out, at least three well-ordered mixed monolayer film structures with different CuPc/PTCDA stoichiometries exist on Ag(111). For the present investigation, we have selected a phase that contains one CuPc and two PTCDA molecules per unit cell and is commensurate with the Ag(111) surface; in the following, we refer to it as the *mixed brick-wall* (MBW) phase (see scanning tunneling microscopy image and low-energy electzron diffraction pattern shown in Fig. 5.2c,d, respectively). At first sight, both molecules retain their weak chemisorptive interaction with the substrate, but a closer look at adsorption heights and orbital binding energies reveal very interesting changes: in the MBW film the adsorption height for PTCDA (CuPc) is larger (smaller) than in the respective homomolecular films (see below and Fig. 5.2e). Hence, the adsorption height suggests a weakening of the PTCDA-Ag and a strengthening of the CuPc-Ag bond. But the LUMO binding energies show a very different behavior that *breaks the normal relationship between adsorption height and orbital binding energies*: we find that the PTCDA (CuPc) LUMO shifts to larger (smaller) binding energies, to the extent that the PTCDA LUMO becomes completely filled, while the CuPc LUMO is emptied; from the point of view of charge transfer, PTCDA

is the winner who takes it all.

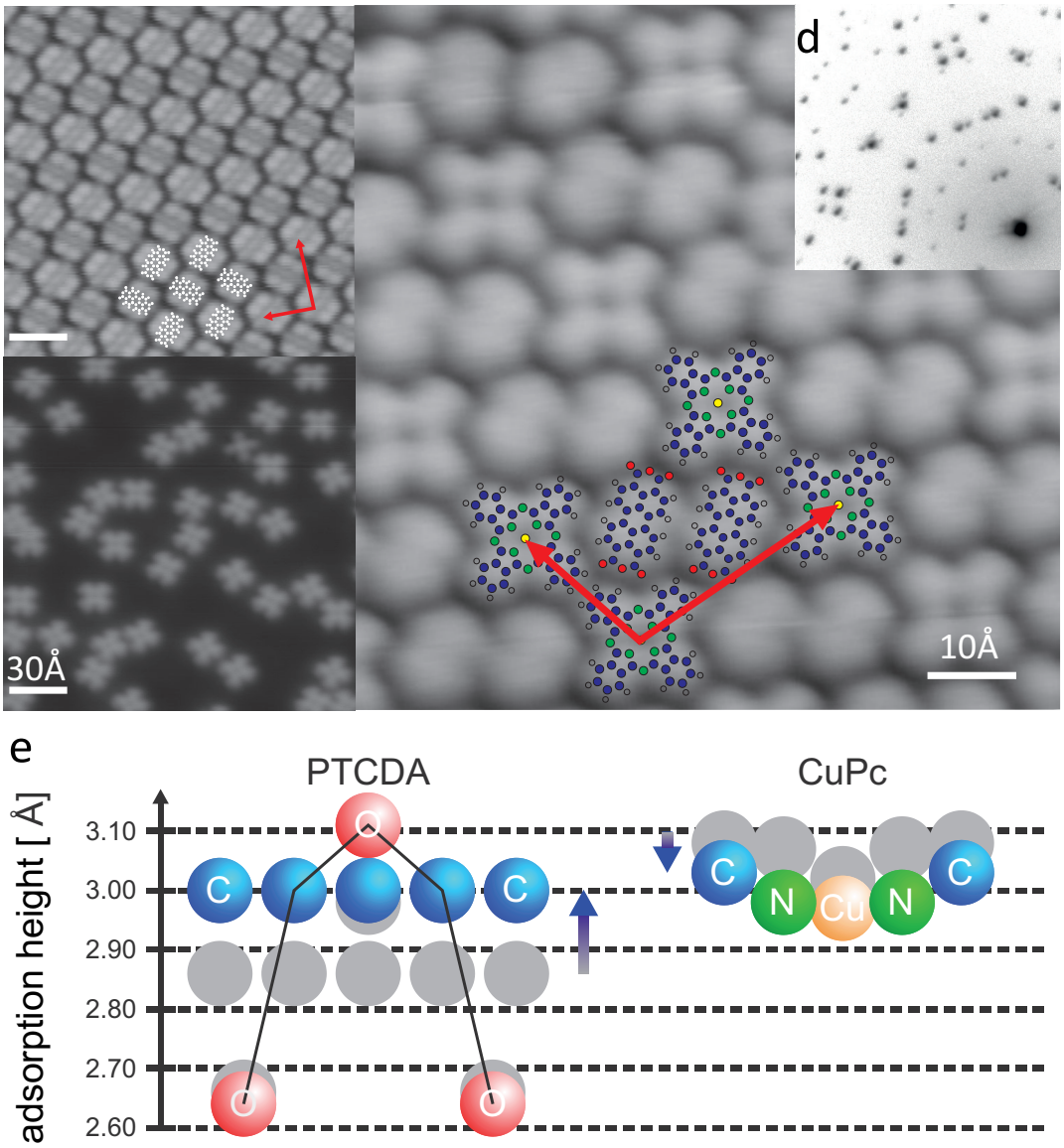

Figure 5.2: (a-c) STM images of the homomolecular phases of (a) PTCDA/Ag(111), (b) CuPc/Ag(111) and (c) the MBW phase recorded at LHe temperature after room temperature deposition and at a sample bias of $U_{\mathrm{Bias}} = -0.34\,\mathrm{V}$, $0.34\,\mathrm{V}$, and $0.20\,\mathrm{V}$, respectively. The typical cross-like and elliptic shapes of CuPc and PTCDA molecules, respectively, are visible and illustrated by the atomic models superimposed in the figures. (d) Corresponding high resolution LEED image indicating a commensurate structure. (e) Vertical adsorption geometry as revealed by NIXSW. The adsorption heights of all involved atomic species are illustrated for the MBW phase (colored spheres) and the homomolecular adsorption systems (gray sphere).

5.2 Results

5.2.1 Molecular adsorption heights

In the following we analyse this remarkable situation in detail, first concentrating on the adsorption height. It can be measured with the highest precision (better than 0.05 Å) and chemical sensitivity by the NIXSW (normal incidence X-ray standing wave) technique. (For details regarding this and other experimental and computational methods see the Supplementary Information.) In Fig. 5.2e the vertical adsorption geometries are shown for all atomic species of the heteromolecular MBW phase (colour), and for the homomolecular monolayer structures (grey).[139, 170] All measured adsorption heights including their errors can be found in Table 5.1. In both homomolecular phases (grey spheres) the molecules are distorted with respect to their planar geometries in the gas phase. The carboxylic oxygen atoms of PTCDA are closer to the surface than the perylene core due to the formation of a local Ag-O bonds.[170] However, with 2.86 ± 0.01 Åthe perylene core is still at a height significantly smaller than the sum of the van der Waals radii of the involved atomic species, which gives rise to a delocalized π-bond across the metal-organic interface and the significant charge transfer into the PTCDA LUMO, clearly seen with various spectroscopic techniques.[108, 196, 197] The distortion of CuPc is smaller and its overall adsorption distance is larger, indicating a weaker molecule-substrate interaction.[139] In the heteromolecular MBW phase (colored spheres in Fig. 5.2e) the perylene core of PTCDA is located significantly *higher* than in the homomolecular phase, at 3.00 ± 0.02 Å. According to the normal coupling between adsorption height and chemical interaction strength, this would indicate a weakening of the PTCDA-metal π-bond. For CuPc the situation is the opposite: its adsorption height becomes *smaller* upon mixing with PTCDA (in changes from 3.08 ± 0.02 to 3.04 ± 0.02 Å), while its distortion is almost unchanged. Note that as a result of their mutual influence, both molecular backbones (and π-systems) adsorb approximately at the *same* height in the MBW phase.

5.2.2 Electronic structure

The changes of interaction strength as inferred from geometry should be reflected in the electronic properties of the adsorbates, that is, in the energetic positions of the relevant frontier molecular orbitals.[44, 45, 116, 182] Figure 5.3a shows the valence band structure of the MBW film and both homomolecular structures, recorded by conventional ultraviolet photoelectron spectroscopy (UPS). For both homomolecular films, two features are visible: the peaks at higher binding energies correspond to the respective highest occupied molecular orbitals (HOMOs) and those in the vicinity of the Fermi level represent the former LUMOs

and are visible in photoelectron spectroscopy only because they become partially filled due to charge transfer from the substrate and shift below the Fermi edge.[108, 139, 197] The partially filled LUMOs are an unambiguous proof for the chemisorptive interaction in both homomolecular films. For the heteromolecular structure one might naively expect a superposition of these two spectra, which is correct regarding the HOMO region. Both HOMO peaks are only slightly shifted compared with the homomolecular phases. However, for the LUMO levels close to the Fermi edge the situation is different: only one peak is visible at a significantly larger binding energy compared with both homomolecular films. Whether this *'Fermi edge peak'* corresponds to the LUMO of PTCDA or CuPc or both cannot be judged from the spectrum shown in Fig. 5.3a. However, in any case, since it is not cut by the Fermi level, it corresponds to molecular orbital(s) that is/are completely occupied.

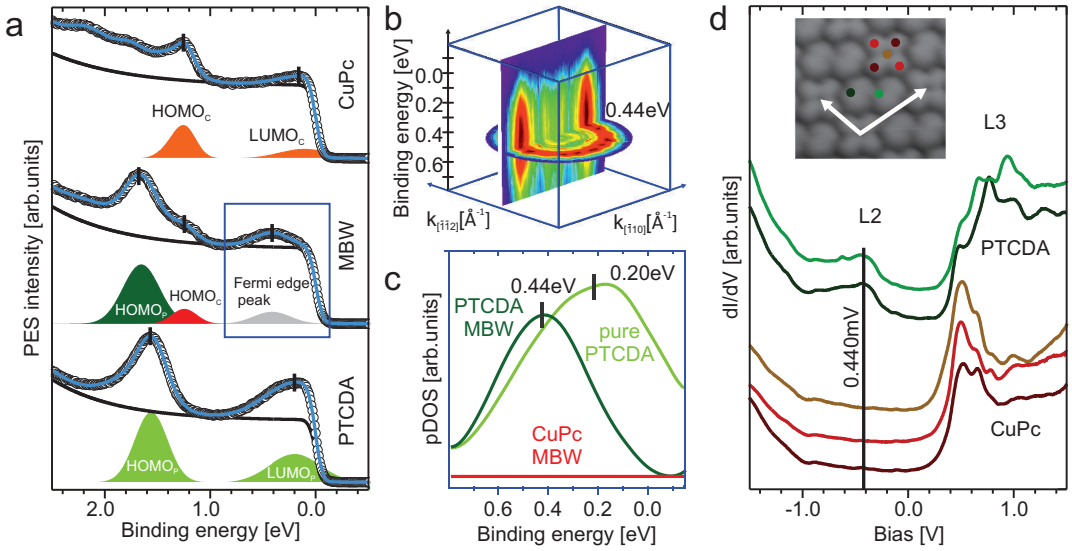

Figure 5.3: (a) Conventional UPS data for homomolecular CuPc/Ag(111), the MBW and the homomolecular (herringbone) PTCDA/Ag(111) phase (from top to bottom). (b) Full tomographic 3D data cube $I(k_x, k_y, E_B)$. An animated illustration can be found in the online version of the paper. (c) pDOS (resulting from the orbital tomography analysis) for the LUMOs of PTCDA and CuPc in the MBW phase as well as for the LUMO of PTCDA in its homomolecular phase. (d) Scanning tunneling spectra recorded at five different positions which are marked and color-coded in the STM image shown as inset.

More insight in the origin of the Fermi edge peak can be gained from molecular orbital tomography, a recently developed analysis method for ARUPS data.[22, 108] In orbital tomography, the angular distribution of photoelectrons is used as a k-space fingerprint of the emitting molecular orbital, allowing its identification by its symmetry and spatial probability distribution. Measuring a k-resolved data

cube of photoelectron intensities in the binding energy range of the Fermi edge peak (Fig. 5.3b) and deconvoluting it in k-space into a superposition of momentum maps from all orbitals that could possibly contribute, we obtain the orbital-specific experimental projected densities of states (pDOS) displayed in Fig. 5.3c. In addition to the LUMOs of CuPc and PTCDA in the heteromolecular MBW phase, we also included the LUMO of PTCDA in the homomolecular phase, which is discernible from the MBW-PTCDA LUMO due to different in-plane orientations of the molecules. This parasitic contribution had to be considered since homomolecular PTCDA and heteromolecular MBW phases coexisted on this sample (in contrast to other samples used for UPS and NIXSW data acquisition). A substrate contribution was also considered in the fit (not shown). For more details of the orbital tomography analysis of the ARPES data see Fig. 5.5.

The results (see Fig. 5.3c) are remarkable: apart from the contribution from the parasitic homomolecular PTCDA islands (light-green curve), only one contribution is non-zero, namely, that for PTCDA in the MBW geometry (dark-green curve). It shows a maximum at $E_B = 0.44\,\mathrm{eV}$, matching the peak position of the conventional UPS experiment (Fig. 5.3a). The pDOS of CuPc (red curve), however, vanishes completely in the entire relevant binding energy region. This clearly demonstrates that the Fermi edge peak stems exclusively from the PTCDA LUMO. Also, the LUMO binding energy of PTCDA has increased in the MBW phase, leading to an enhanced charge transfer from the substrate, which fills up the orbital completely. In contrast, the LUMO binding energy of CuPc has decreased, with the consequence that CuPc releases all of its acquired charge. Hence, the electronic signatures that normally go along with shorter bonding distances and thus stronger chemical interaction appear here in conjunction with larger bonding distances (for PTCDA), and vice versa for CuPc.

The results of our ARPES molecular tomography analysis are confirmed by STS (scanning tunneling spectroscopy). This local technique gives direct access to the valence structure of individual molecules. In Fig. 5.3d, spectra recorded at five different positions that are characteristic for the geometric shapes of the CuPc and PTCDA LUMOs are plotted. For both PTCDA molecules in the unit cell, the LUMO resonance is detected at the binding energy of the Fermi edge peak (0.44 eV), while for all positions on the CuPc molecule the spectrum in the corresponding region is flat.

Our experimental results regarding geometric and electronic structures appear paradoxical. We therefore turn to density functional theory (DFT), which has become very reliable for verifying and predicting adsorption heights and electronic energy levels for both homo- and heteromolecular adsorbate systems (see, for example, refs [45, 161, 192–194] and references therein). Here we employed a generalized gradient approximation for exchange-correlation effects [66] and an empirical van der Waals correction according to Grimme.[153] The calculations yield adsorption heights in good agreement with experiment, both for the ho-

momolecular and the heteromolecular phases (see Table 5.1). Moreover, they confirm the frontier orbital binding energies and charging states of the CuPc and PTCDA LUMOs as determined by experiment. This can be seen in Fig. 5.4a where the pDOS of the MBW phase and of the homomolecular PTCDA/Ag(111) and CuPc/Ag(111) phases are displayed. The question thus arises: how can we understand the counterintuitive behaviour of geometric structure (adsorption heights) and electronic properties (LUMO binding energies) that is found in experiment and theory?

5.3 Discussion

On the way to a cogent model of the heteromolecular phase, we first turn to the remarkable fact that in the MBW phase PTCDA and CuPc equalize their adsorption heights. To first order, the adsorption height of a molecule on a metal is determined by the contact distance between the molecular backbone and the electron density that spills out from the surface. Hybridization with molecular orbitals, charge transfer and the so-called push-back effect will modify the charge profile above the bare surface. This reorganization is material specific, and depends on the chemical character of the molecule and the balance between chemisorption and physisorption for the given interface. But once these changes have been effected, the adsorbate essentially floats in contact on this rearranged electron density profile. This state of affairs precludes strongly dissimilar adsorption heights of neighboring molecules, since it is energetically unfavourable either to have a laterally structured evanescent metallic electron density or to have one of the molecular species sinking too deep into the laterally averaged electron spill out (PTCDA) or hovering too far above it (CuPc). Therefore, we must expect an equalization of the adsorption heights if the two molecules are laterally intermixed on a molecular length scale.

But why are the adsorption heights of CuPc and PTCDA in their homomolecular phases different in the first place? Looking at the work function changes that both molecules effect on the surface, we observe that PTCDA increases the bare work function of Ag(111) to $4.76 \pm 0.02\,\mathrm{eV}$, while CuPc reduces it to $4.15 \pm 0.02\,\mathrm{eV}$. Note that all numbers given here are valid for closed monolayer films. Our DFT calculation, which reproduces these experimental values with great accuracy (see Table 5.2), allows an analysis of these changes: The work function change has two contributions, the *bond dipole* that arises from the charge reorganization and transfer on adsorption, and the *bending dipole* that stems from the adsorption-induced molecular distortion. It turns out that in the case of PTCDA/Ag(111) the charge transfer from the metal into the molecule is dominant, it contributes $+0.50\,\mathrm{eV}$ to the work function change. For CuPc/Ag(111), it is the push-back effect that contributes most strongly with $-0.55\,\mathrm{eV}$. These numbers (note the

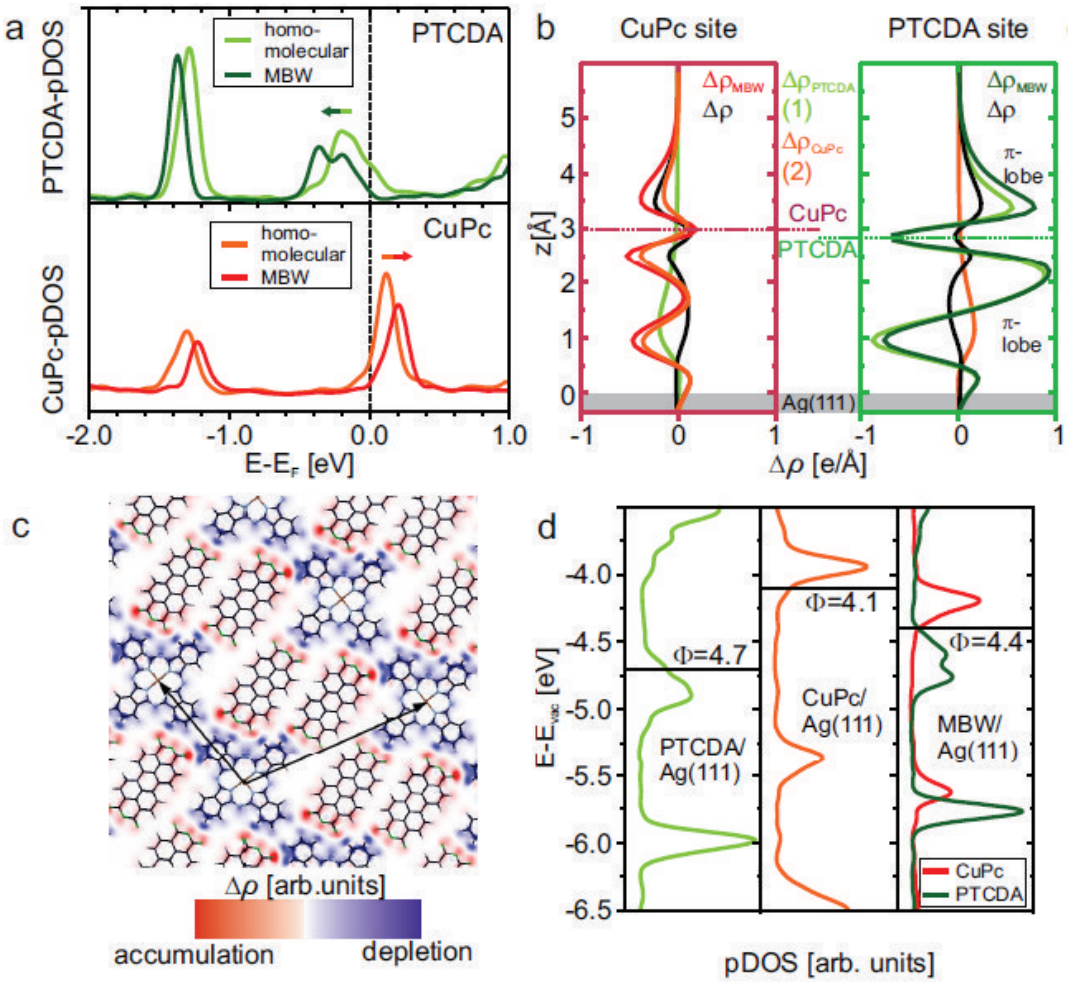

Figure 5.4: Electronic structure revealed by DFT: (a) Spin-up pDOS of the π-orbitals of PTCDA (upper panel) and CuPc (lower panel) in their homo- and heteromolecular phases, respectively. The spin-down pDOS is shown in Fig. 5.6. (b) Charge density reorganization $\Delta\rho$, horizontally integrated in the adsorption site area, for CuPc (left panel) and PTCDA (right panel), plotted versus the distance to the surface (molecular planes at $z \approx 3.0$ Å). (c) Charge density difference plot showing depletion (blue) and accumulation (red) of electronic charge in a plane parallel to the surface 0.5 Å above the molecular plane (in a height of maximum DOS of the LUMO orbitals). (d) pDOS of the π orbitals of PTCDA and CuPc in the homomolecular PTCDA/Ag(111) (left), the homomolecular CuPc/Ag(111) (middle) and the heteromolecular MBW phase (right). Energies are aligned with the vacuum level, the Fermi energies are indicated by black lines revealing the work functions.

opposite signs) reveal the different character of PTCDA and CuPc when they adsorb on Ag(111): The chemical component (charge transfer) of the bonding

with Ag(111) is more prominent for PTCDA than it is for CuPc, while the reverse is true for the physisorptive contribution (push-back). This is the origin of the different adsorption heights: PTCDA pulls charge from the evanescent electron density into its LUMO and can therefore approach the surface more closely, while CuPc mainly pushes the evanescent electron density back into the metal, which precludes a closer approach, even though a (smaller) charge transfer from Ag(111) to CuPc is observed as well (see above).[136, 139]

Figure 5.4b reveals the reorganization of the charge density that goes along with the equalization of adsorption heights on formation of the MBW phase. We have, separately for each type of molecule in the MBW phase, integrated the electron density reorganization $\Delta\rho_{\mathrm{MBW}}$ in the horizontal plane over the area of the respective molecules and plotted their z-dependence (red and dark-green lines). For comparison we have calculated the analogous quantities for two reference structures, namely (1) PTCDA molecules in the MBW unit cell from which CuPc has been removed ($\Delta\rho_{\mathrm{PTCDA}}$, light-green line shown in Fig. 5.4b) and (2) CuPc molecules in the MBW unit cell from which PTCDA has been removed ($\Delta\rho_{\mathrm{CuPc}}$, orange line). The differences of these electron density reorganization profiles, $\Delta\rho = \Delta\rho_{\mathrm{MBW}} - (\Delta\rho_{\mathrm{CuPc}} + \Delta\rho_{\mathrm{PTCDA}})$, are plotted as black curves (for more details see Fig. 5.7). The electron depletion of the CuPc π-lobes (left panel, orange curve, at $\approx 2.5\,\text{Å}$ and $\approx 3.5\,\text{Å}$) is a consequence of the push-back dominated interaction of CuPc with Ag(111) (although a small charge transfer into the molecule is also visible at some z), whereas the electron accumulation in the corresponding region of PTCDA (right panel, light-green line, at $\approx 2.2\,\text{Å}$ and $\approx 3.4\,\text{Å}$) originates from charge transfer into its LUMO. Furthermore, the figure reveals two important facts: first, we observe that in reference structure (2), CuPc pushes electrons into the PTCDA vacancies (right panel, orange curve, shallow maximum at $\approx 1.0\,\text{Å}$), while in reference structure (1) PTCDA sucks up electrons from the CuPc vacancies (left panel, light-green curve, minimum at $\approx 1.0\,\text{Å}$). Second, once the vacancies are filled again by the corresponding molecules, the electron density surplus at the PTCDA site is redistributed and yields an increased electron density in the π-lobes of the PTCDA molecule (right panel, dark green curve, the peaks at $\approx 2.2\,\text{Å}$ and $\approx 3.4\,\text{Å}$ are larger compared with the light green curve), while the electron density deficiency at the CuPc site is redistributed to yield a reduced electron density in the π-lobes of CuPc (left panel, the minima in the red curve at $\approx 2.5\,\text{Å}$ and $\approx 3.5\,\text{Å}$ are deeper than in the orange curve). The charge accumulation and depletion at PTCDA and CuPc sites, respectively, also influences the interaction of the frontier orbitals with the metal states, since it manifests itself in a population/depopulation of the respective LUMOs, also illustrated by the lateral map shown in Fig. 5.4c, taken at $z = 3.5\,\text{Å}$. Note, however, that the electron densities also change directly above the substrate ($z \approx 1\,\text{Å}$). This modifies the Pauli repulsion between the adsorbates and the metal and cancels the net attractive force acting on PTCDA

in reference structure (1) as well as its net repulsive counterpart on CuPc in reference structure (2), and thus explains how the two molecules equalize their heights in the heteromolecular phase: the electronic charge that CuPc sheds from its LUMO and repels from its site is redirected towards PTCDA, with the result that PTCDA both floats on this 'cushion' of charge and accepts more of it into its LUMO, while CuPc sinks into the remaining 'depression' of the electron density. The necessity to equalize the heights of the two adsorbates thus harmonizes very well with the different chemical characters (relative donor versus relative acceptor) of the two molecules.

Finally we want to understand the regulation of the mutual charge transfer between molecules and surface in context with the orbital alignments and work function. For the MBW/Ag(111) structure we have measured a work function of 4.44 ± 0.02 eV. This is half way between the values for PTCDA/Ag(111) and CuPc/Ag(111) and in excellent agreement with the calculated work function of 4.40 eV. We revealed the latter value from calculated pDOS which are plotted in Fig. 5.4d, for both hetero- and homomolecular systems with aligned vacuum levels. More importantly, this figure shows that the LUMOs of PTCDA and CuPc move away from the common Fermi level in opposite directions, owing to the work-function averaging and the very different electron affinities of the molecules. The investigation of similar systems have revealed similar trends for core levels and filled valence levels (for example, the HOMO)[198]. In our case, the LUMO shift explains why in the heteromolecular phase the charge transfer into the PTCDA (CuPc) LUMO is larger (smaller) than in the respective homomolecular phases. Note that the different electron affinities of CuPc and PTCDA, which of course are an expression of their different chemical characters, change slightly on formation of the heteromolecular phase. In comparison with the respective homomolecular phases, the increase (decrease) of electronic charge transfer into PTCDA (CuPc) causes a more (less) negative charging of the molecule, and thereby reduces (increases) its electron affinity.

To verify the role of the metal surface and its work function for the energy level alignment, we have carried out a computational control experiment: we calculated the level alignments for a *free standing* MBW layer, i.e., without surface. Compared with the full MBW/Ag(111) structure we observe substantially smaller LUMO shifts (relative to the vacuum level, for details see Fig. 5.8). This proves that the frontier orbital alignment observed on mixing the two species is caused by their interaction with the metal surface, not by direct intermolecular interactions. Furthermore, we find that the MBW phase is stabilized by 0.21 eV when charge reorganisation between the PTCDA and CuPc sites (that is, surface-mediated charge transfer between the two molecules) is allowed, compared with a situation of direct intermolecular and separated molecule-substrate interaction only (see Table 5.3).

Incidentally, the different chemical characters of the two adsorbates also explain

why in the heteromolecular system island formation prevails (as opposed to the repulsive interaction observed for the homomolecular CuPc/Ag(111)): the opposite bond dipoles of PTCDA and CuPc attract each other, thus promoting the formation of a compact layer, even if the arrangement of molecules in the MBW phase is less amenable to the formation of a network of hydrogen bonds. The DFT calculation shows that the *total* bond dipole in the MBW phase is nearly zero ($-0.02\,\mathrm{eV}$), indicating a cancellation of the individual bond dipoles of CuPc and PTCDA.

In conclusion, the electronic and geometric properties of the MBW phase emerge in the following way: If only CuPc is present on Ag(111), it will push the evanescent electron density back (not withstanding a small metal-molecule charge transfer), owing to its (compared with PTCDA) less electron-affine character; this limits its approach to the surface. If PTCDA is added, this charge repelled by CuPc, instead of being merely pushed back into the surface, is laterally redirected towards the electron-affine PTCDA. This charge reorganization, which leads to a tangible energy gain, has two consequences: first, the adsorption heights of CuPc and PTCDA nearly equalize, with PTCDA floating up and CuPc sinking in. This can be interpreted as a consequence of *local* work function changes: CuPc increases the local work function at the PTCDA site, while PTCDA reduces it at the CuPc site. Secondly, the *global* work function of the mixed interface acquires a value that is intermediate between CuPc/Ag(111) and PTCDA/Ag(111). This in turn controls the energy level alignment such that CuPc reduces its charge take up from the surface, while PTCDA increases it. In other words, the two coadsorbates mutually amplify their natural chemical characters vis à vis Ag(111): in the vicinity of CuPc, PTCDA becomes a stronger acceptor, while in the vicinity of PTCDA, CuPc becomes even less of an acceptor, and – relative to PTCDA – turns into a donor. Since the chemical interaction of both molecules with the metallic states of the substrate is dominated by the LUMO, this means that the chemical component of the molecule-surface interaction is strengthened for PTCDA and weakened for CuPc.

It is noteworthy that PTCDA *both* floats up on an electron density cushion *and* takes up negative charge. Similarly, CuPc sheds negative charge *and* sinks into an electron density depression. This breaks the normal relationship between adsorption height and LUMO binding energy. Ultimately, this breaking of the normal coupling can be traced back to the mutual amplification: in the heteromolecular case, it is the metal *together with the respective partner molecule* that determines the behaviour. The apparently paradoxical behaviour between geometric structure (adsorption height) and electronic properties (frontier orbital binding energy) of the heteromolecular MBW phase is resolved, and has thus revealed very clearly how observables such as vertical adsorption height, frontier orbital binding energies and charge transfer, for homomolecular as well heteromolecular systems, are linked and influence each other. The insight at this level has an

obvious impact on the challenge of engineering the interfaces of heteromolecular materials for applications.

Acknowledgements

We acknowledge financial support from the Deutsche Forschungsgemeinschaft (KU 1531/2-1), and the Austrian Science Fond (FWF, P23190-N16, P21330-N20). T.S. thanks the Alexander von Humboldt foundation for a postdoctorial fellowship. We also thank T. Ules, F.C. Bocquet, C. Schüssler-Langeheine, M. Ostler, T. Seyller and the staff of BESSY II / Helmholtz-Zentrum Berlin for their support during the beamtime.

5.4 Supplementary Information

5.4.1 Experimental details

Sample preparation

The sample preparation, as well as all experiments, were performed under ultra-high vacuum conditions. The (111)-oriented silver surface was prepared by repeated cycles of argon ion bombardment and annealing at $T_{\mathrm{sample}} = 730\,\mathrm{K}$. Afterwards the organic material was deposited using a dedicated evaporator system. The heteromolecular MBW phase can be prepared following two different approaches which both result in the same structure: For the first approach a submonolayer film ($< 0.4\,\mathrm{ML}$) of CuPc is prepared at room temperature, and $\approx 0.6\,\mathrm{ML}$ PTCDA are added afterwards. The MBW structure forms immediately, and its homogeneity can be improved by annealing at 570 K for 10 min. In the second approach $\approx 0.8\,\mathrm{ML}$ CuPc are deposited on a closed layer of PTCDA/Ag(111) and the sample is annealed at 570 K for 10 min. We have used both approaches and in all cases confirmed the success of the preparations by low energy electron diffraction.

It should also be mentioned that during each experiment we carefully checked the samples for radiation damage. On the relevant time scales of the experiments, no significant influence on the data was observed.

Low energy electron diffraction

The low energy electron diffraction data were obtained at $E_{\mathrm{kin}} = 27.2\,\mathrm{eV}$ using a high-resolution spot profile analysis LEED instrument (Omicron). This

device operates with very low electron flux ($I_{\mathrm{Drain}} \approx 5\,\mathrm{nA}$) which allows a non destructive investigation of organic samples. The recorded diffraction patterns were calibrated (regarding k-space units) by using the SPA-LEED pattern of the well known PTCDA monolayer structure (herringbone phase) on Ag(111).

Scanning tunneling microscopy and spectroscopy

All scanning tunneling microscopy (STM) and spectroscopy (STS) experiments were carried out at low temperature ($T_{\mathrm{sample}} < 10\,\mathrm{K}$) using a commercial Createc LT-STM. The topographic STM images shown in Fig. 5.2 were recorded in constant current mode with sample bias $U_{\mathrm{Bias}} = -0.34\,\mathrm{V}$ (Fig. 5.2a), $U_{\mathrm{Bias}} = 0.34\,\mathrm{V}$ (Fig. 5.2b), and $U_{\mathrm{Bias}} = 0.20\,\mathrm{V}$ (Fig. 5.2c). The differential conductance (dI/dV) curves were recorded using the lock-in technique (modulation frequency $\nu = 780\,\mathrm{Hz}$ and amplitude $5\,\mathrm{mV}$). The fact that the lateral periodicity of the ordered structures and the unit cell size was very accurately known from SPA-LEED experiments allowed us to corrected the STM images for distortions.

Normal Incidence X-Ray Standing Waves

The NIXSW data were recorded at end-station ID32 of the European Synchrotron Radiation Facility (ESRF) in Grenoble, France. The (111) reflection of the silver substrate ($E_{\mathrm{Bragg}} \approx 2.36\,\mathrm{keV}$ at normal incidence) was used in order to create a standing wave field which shows an intensity modulation in the direction perpendicular to the Bragg planes. While scanning the photon energy through the Bragg condition, the standing wave field shifts through the crystal by half the Bragg-plane spacing, which results in a characteristic modulation of the x-ray intensity at any specific vertical position above the silver surface, i.e., in particular at the height of any atomic species within the molecules.[199–201] This modulation can be recorded using secondary emission signals from these atoms, such as – in the present case – core level photoelectrons, and from its shape and intensity the vertical position of the emitting atomic species can be determined with very high accuracy ($\Delta h < 0.05\,\mathrm{Å}$). Here we have used C1s, N1s, O1s and Cu2p core level emissions that were detected using a hemispherical electron analyzer (SPECS PHOIBOS 225). The analyzer was mounted in an angle of 90° with respect to the incoming photon beam in order to avoid non-dipolar effects. The photoelectron yield curves were analyzed using the XSW analysis software *Torricelli*.[202] The resulting adsorption heights are summarized in Table 5.1. Details of the data evaluation, which followed the general approach reported in Ref. [49], will be given in a forthcoming publication.

Ultraviolet photoelectron spectroscopy

The conventional (angle integrated) ultraviolet photoelectron spectroscopy (UPS) experiments were performed with a hemispherical electron analyzer (SCIENTA R4000) and a monochromatized UV-source ($\hbar\omega = 21.218\,\mathrm{eV}$). The overall energy resolution of this setup was determined by the width of the Fermi edge to be better than 30 meV. The spectra in Fig. 5.3a were recorded at an emission angle of 45° with respect to the surface normal and a photoelectron acceptance angle of 30° with identical detector settings. The energy scale was calibrated using the Fermi level.

Angle resolved UPS and orbital tomography

The ARUPS experiments were performed at beamline U125/2-SGM of the BESSY II storage ring in Berlin, Germany. The sample was illuminated by monochromatic radiation with a photon energy of 35 eV and at a fixed incident angle of 40° to the surface normal. The photoelectron yield was recorded with a toroidal electron analyzer having a polar acceptance angle of ±80° and an energy dispersion range of 1.0 eV at a pass energy of 10 eV.[104] The azimuthal angular distribution was recorded by rotating the sample around its surface normal in steps of 1° in a range of at least 130°. After converting polar/azimuthal angles to (k_x, k_y) wave vector units and under consideration of the threefold symmetry of the silver crystal we obtained a three dimensional ARUPS data cube $I(k_x, k_y, E_b)$ by this procedure. An animated illustration of the tomographic data cube is available in the online version of this manuscript. An experimental "constant binding energy" (CBE) map, that is a constant-energy cut through the data cube at the binding energy E_b of a certain molecule, reveals the characteristic emission pattern of that orbital in momentum space. The experimental CBE map at the energy of the Fermi edge peak of the MBW phase ($E_\mathrm{B} = 0.44\,\mathrm{eV}$) is shown in Fig. 5.5a.

In order to identify the molecular orbitals contributing to this intensity distribution, theoretical emission pattern for all molecular orbitals in question, here the PTCDA and CuPc LUMOs, are calculated. In a simple approach using a plane wave approximation for the final state of the photoemission process this can be done by Fourier transforming the wave function of the molecular orbitals. A hemispherical cut through the Fourier transform with radius $k = \sqrt{(2m/\hbar^2) \cdot E_\mathrm{kin}}$ and a projection into the (k_x, k_y) plane results in a calculated CBE map for that particular orbital of the molecule in a certain orientation. However, in order to construct the emission pattern for a molecular film, all in-plane orientations of the molecules from all domains on the surface have to be considered. In Fig. 5.5b such calculated CBE maps are shown for the LUMOs of CuPc and PTCDA in the MBW phase and for the homomolecular PTCDA/Ag(111) structure.

A qualitative comparison of calculated and measured CBE maps is immediately

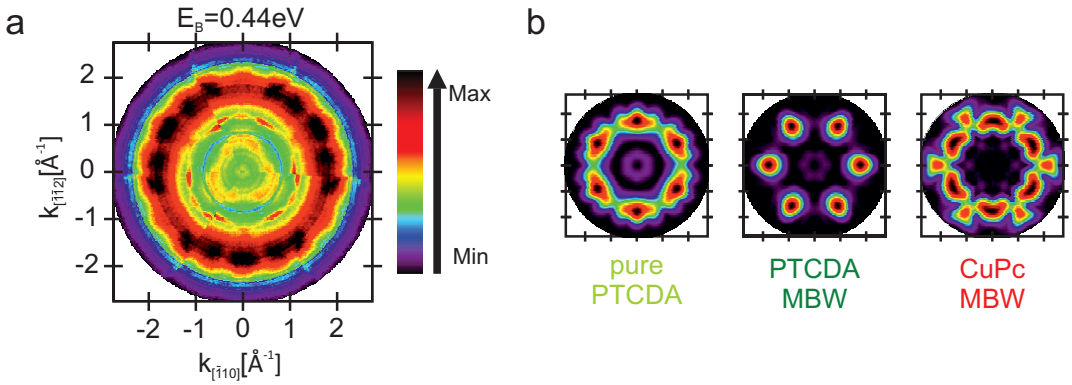

Figure 5.5: ARUPS data recorded for the MBW phase: (a) Experimental CBE map at a binding energy corresponding to the maximum of the Fermi edge peak. (b) Calculated CBE maps representing the LUMO of PTCDA in the homomolecular herringbone structure (left), in the MBW phase (center) and the LUMO of CuPc in the MBW phase (right). The geometric arrangement and domain multiplicity of the structures are considered in all cases, i.e., all in-plane orientations of the molecules are reflected by these CBE maps. For this reason, the PTCDA LUMOs in homo- and heteromolecular phases (left and central panel) look different.

possible, see Fig. 5.5. However, for a quantitative analysis, the density of states, projected on the molecular orbitals in question, can be obtained as follows. The function

$$F(k_x, k_y, E_B) = \sum_i a_i(E_B)\Phi_i(k_x, k_y) + b(E_B)I_{sub}(k_x, k_y, E_B) + c(E_B) \qquad (5.1)$$

is used to fit the 3D tomographic ARUPS data cube $I(k_x, k_y, E_B)$. Equation (5.1) represents a linear combination of the theoretical CBE maps $\Phi_i(k_x, k_y)$ of the corresponding molecular orbitals i, a substrate contribution $I_{sub}(k_x, k_y, E_B)$ and a constant offset function $c(E_b)$. While the theoretical CBEs are calculated as described above, the substrate contribution $I_{sub}(k_x, k_y, E_B)$ was determined experimentally in an ARUPS experiment on the clean Ag(111) surface. The fitted parameter functions $a_i(E_B)$ can be understood as the energy resolved projected densities of states (pDOS) for the corresponding molecular orbitals. More details on the orbital tomography approach can be found in Ref. [108] and [22].

5.4.2 Computational details

All calculations for the MBW phase as well as for the homomolecular phases of PTCDA/Ag(111) and CuPc/Ag(111) are carried out using the VASP code[146, 147, 203] with a generalized gradient approximation (GGA) for exchange-correlation effects[66] and empirical van-der-Waals corrections according to Grimme.[153]

The Ag(111) substrate is modeled by 5 layers of Ag with an additional vacuum layer of 16 Å width. The projector augmented waves (PAW)[148] approach is used, allowing for a relatively low kinetic energy cut-off of about 400 eV. For the MBW phase containing 310 substrate atoms and 133 atoms in the three molecules per unit cell, we use a Monkhorst-Pack $2 \times 2 \times 1$ grid of k-points[149] and a first-order Methfessel-Paxton smearing of 0.2 eV.[150] To avoid spurious electrical fields, a dipole layer is inserted in the vacuum region.[151]

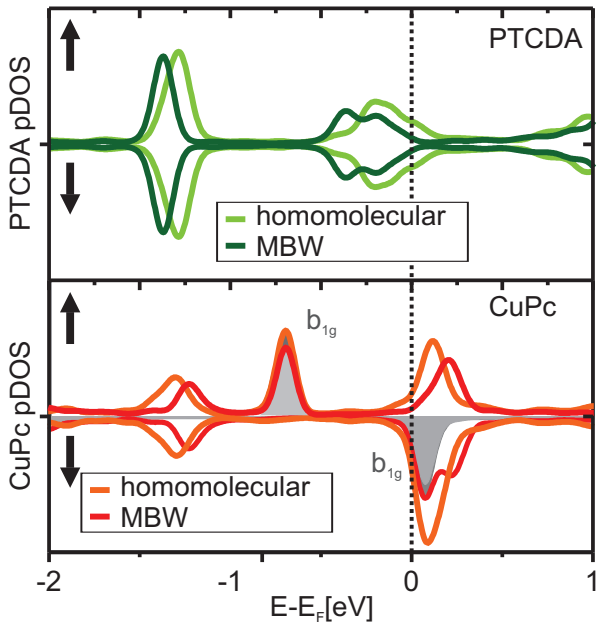

Figure 5.6: Spin-resolved density of states projected onto PTCDA (upper panel) and CuPc (lower panel) in their homomolecular phases and in the MBW phase. Spin-up and spin-down contributions are plotted along the positive and negative ordinate, respectively. The hatched areas mark the DOS of the b_{1g} σ-orbitals which suffer from the well known self-interaction error (SIE) which lets them appear at incorrect energetic positions, namely too close to the Fermi level.

All calculations are performed in the spin-polarized mode in order to account for the spin-split b_{1g} state of CuPc.[101] Our GGA-DFT results suffer from the well known self-interaction error (SIE) with the consequence that localized states, such as the b_{1g} orbital of σ character (gray areas in Fig. 5.6) that is localized around the central Cu atom, appear too close to the Fermi level. As a consequence of the SIE and at variance to the experiment, the spin-up b_{1g} state appears above the HOMO, while the spin-down b_{1g} state is energetically close to the LUMO. Note that the positions of these b_{1g} peaks do not change from the homomolecular to the MBW phase (see Fig. 5.6) and thus do not contribute significantly to the charge reorganization upon the formation of the MBW phase. For this reason, we have suppressed the sigma states in Fig. 5.4, where we only show the spin-up

Table 5.1: Adsorption heights for the homomolecular (HM) and the MBW phases determined by NIXSW and DFT. NIXSW values for the homomolecular phases are taken from Ref. [170] (PTCDA/Ag(111)) and [139] (CuPc/Ag(111)).

	HM_{NIXSW} [Å]	HM_{DFT} [Å]	MBW_{NIXSW} [Å]	MBW_{DFT} [Å]
CuPc				
Carbon	3.08 ± 0.02	3.05	3.04 ± 0.02	3.01
Nitrogen	3.07 ± 0.04	3.06	2.98 ± 0.02	3.01
Copper	3.02 ± 0.04	2.96	2.97 ± 0.02	2.91
PTCDA				
Carbon	2.86 ± 0.01	2.86	3.00 ± 0.02	3.00
Carbox. oxygen	2.66 ± 0.03	2.76	2.63 ± 0.02	2.86
Anhy. oxygen	2.98 ± 0.08	2.92	3.10 ± 0.05	2.99

π-states.

In our DFT calculations for the homomolecular films and for the MBW phase, we allow a vertical relaxation of the atomic positions. Table 5.1 summarizes these calculated adsorption heights as well as the corresponding adsorption heights obtained by the NIXSW method.[139, 170] The good agreement between theoretical and experimental values demonstrates the reliability of our theoretical results.

5.4.3 Additional information

Work function

The work function measurements were performed using the same setup as for the conventional UPS experiments (see above). They were determined from the secondary electron cutoff in normal emission geometry. During the data accumulation, the sample was biased to $-9\,\mathrm{V}$ in order to increase the kinetic energy of the photoelectrons. The onset energy of the secondary electron cutoff was defined as the largest binding energy at which the derivative of the spectrum differs significantly from zero. The experimental results are summarized in Table 5.2, together with the results of the DFT calculations. We would like to stress the excellent agreement between experiment and theory. The work function changes $\Delta\Phi$ are dominated by two effects:[45] The bond dipole BD is directly associated with changes in the electron density $\Delta\rho$ and hence contains both the charge transfer between the molecule and the surface, and the so called push-back effect of electronic charge toward the surface due to the adsorption of the molecule. The second, purely geometric contribution, is caused by the vertical dipole moment induced by (a) the distortion or bending of the molecule (ΔE_{vac}^{lay}) and (b) the relaxation of the substrate (ΔE_{vac}^{sub}). The different nature of the bonding of CuPc

Table 5.2: Experimental and calculated work function values for the homo and heteromolecular films. The values are valid for closed monolayer structures (total coverage = 1 ML). The changes in the work function, determined by DFT, are separated into the bond dipole BD and the contribution ΔE_{vac} caused by a geometric distortion of the molecules. All values are given in eV.

	Φ_{exp}	Φ_{DFT}	$\Delta\Phi_{DFT}$	BD	ΔE_{vac}^{lay}	ΔE_{vac}^{sub}
CuPc ML	4.15 ± 0.02	4.06	-0.41	-0.55	$+0.05$	$+0.05$
PTCDA ML	4.76 ± 0.02	4.70	$+0.26$	$+0.50$	-0.18	-0.03
MBW	4.44 ± 0.02	4.40	-0.07	-0.02	-0.07	$+0.04$

or PTCDA to the silver surface in the homomolecular phases is clearly demonstrated by the difference in their bond dipoles. While the bond dipole of CuPc reduces the work function since CuPc pushes the electron spill-out back toward the substrate, the bond dipole of PTCDA increases it due to PTCDA accepting charge from the substrate. The BD for the MBW phase is almost zero since the contributions of PTCDA and CuPc almost cancel out.

Charge reorganization

In this section, we provide additional information on the charge reorganization occurring upon the formation of the MBW phase. We studied this by considering two artificial reference structures: Starting from the MBW/Ag(111) phase, we have (1) either removed all CuPc molecules or (2) all PTCDA molecules. The geometry of the remaining molecules was fixed according to the DFT results for the mixed phase. For these two structures, as well as for the complete MBW phase, we then calculated the charge reorganization $\Delta\rho_i$ (with i = PTCDA, CuPc or MBW). In case of structure (1) (CuPc removed) this results in $\Delta\rho_{PTCDA} = \rho_{PTCDA/Ag(111)} - (\rho_{PTCDA} + \rho_{Ag(111)})$, where the first term on the right refers to the charge density of the reference structure (1) and the term in brackets corresponds to the non-interacting charge densities of the PTCDA molecules and the Ag(111) substrate. In Fig. 5.7a, the resulting charge reorganization $\Delta\rho_{PTCDA}$ is illustrated for a plane ≈ 1 Å above the surface, i.e., in a plane where the charge spill-out of the surface is located. In all charge difference plots, charge depletion ($\Delta\rho_i < 0$) is displayed in blue, accumulation ($\Delta\rho_i > 0$) in red.

Besides horizontal cuts, we also performed vertical cuts through the charge reorganization at the CuPc and PTCDA sites. For reference structure (1) these are shown in the uppermost panel of Fig. 5.7d and e. The exact locations of these cuts in the horizontal maps are indicated by a light-green (CuPc site) and a dark-green line (PTCDA site) in Fig. 5.7a. The vertical cut through the PTCDA

molecule (PTCDA site, Fig. 5.7e) reveals charge accumulation directly above and below the molecular plane (which is located at $d_{\mathrm{PTCDA}} \approx 3\,\text{Å}$). This reflects the charge transfer into the PTCDA LUMO. The charge depletion below the molecular plane (at $\approx 1\,\text{Å}$) and the additional charge density in the silver substrate can be attributed to the push-back effect. However, the charge density is also reduced at the vacant CuPc site (uppermost panel of Fig. 5.7d). This indicates that PTCDA sucks charge from the CuPc vacancies in reference structure (1) and hence acts as a charge acceptor.

Similar calculations were performed for reference structure (2) (PTCDA removed) and the MBW phase. The corresponding horizontal cuts are shown in Fig. 5.7b and c, and vertical cross sections are displayed in the second and third panels of Fig. 5.7d and e, respectively. While $\Delta\rho_{\mathrm{CuPc}}$ is calculated analogously to $\Delta\rho_{\mathrm{PTCDA}}$ (i.e., $\Delta\rho_{\mathrm{CuPc}} = \rho_{\mathrm{CuPc/Ag(111)}} - (\rho_{\mathrm{CuPc}} + \rho_{\mathrm{Ag(111)}})$), for $\Delta\rho_{\mathrm{MBW}}$ the non-interaction charge densities of both molecules have to be subtracted: $\Delta\rho_{\mathrm{MBW}} = \rho_{\mathrm{MBW/Ag(111)}} - (\rho_{\mathrm{CuPc}} + \rho_{\mathrm{PTCDA}} + \rho_{\mathrm{Ag(111)}})$. In contrast to $\Delta\rho_{\mathrm{PTCDA}}$, $\Delta\rho_{\mathrm{CuPc}}$ reveals a stronger charge depletion in the region below the molecular body which suggests a stronger push-back effect for CuPc than for PTCDA. The vertical charge reorganization plot at the PTCDA site even reveals an expulsion of charge into the PTCDA vacancies. This indicates that CuPc behaves like a charge donor on the Ag(111) surface and transfers charge into the vacant PTCDA sites.

At first sight the charge reorganization for the MBW phase $\Delta\rho_{\mathrm{MBW}}$ shows only marginal differences compared to the corresponding reference structures. Only after subtracting the relevant densities (the density difference $\Delta\rho = \Delta\rho_{\mathrm{MBW}} - (\Delta\rho_{\mathrm{CuPc}} + \Delta\rho_{\mathrm{PTCDA}})$ is shown in the lowest panel of Fig. 5.7d and e) the differences which are caused by the population of the vacancies in the two reference structures are revealed. In the main text a horizontal cut through this charge difference plot at the position of the molecular π-orbitals is discussed. It shows a charge depletion at the CuPc sites and a charge accumulation at the PTCDA sites, i.e., a depopulation of the CuPc LUMO and an enhanced population of the PTCDA LUMO. This is the main result of our analysis of the charge redistribution in the MBW structure.

It shall finally be mentioned, that in Fig. 5.7c, which shows the charge reorganization below the molecular plane in the MBW structure, a small accumulation (depletion) of charge at CuPc (PTCDA) sites can be seen. One should note that this small effect is also present, of similar size but opposite sign, in both reference structures (see light green line in Fig. 5.7a, and dark green line in Fig. 5.7b). The charge can also be seen in the vertical cuts (upper panel of Fig. 5.7d and 2nd panel of Fig. 5.7e), both at a height of $z \approx 1.0\,\text{Å}$. Since these structures are used as references, i.e., the charge contribution is subtracted, the accumulation and depletion of charge merely stems from this data treatment, i.e., is somewhat artificial. At $z \approx 3.0\,\text{Å}$, where the LUMOs are located which become depopulated in the case of CuPc and populated for PTCDA LUMO (the corresponding

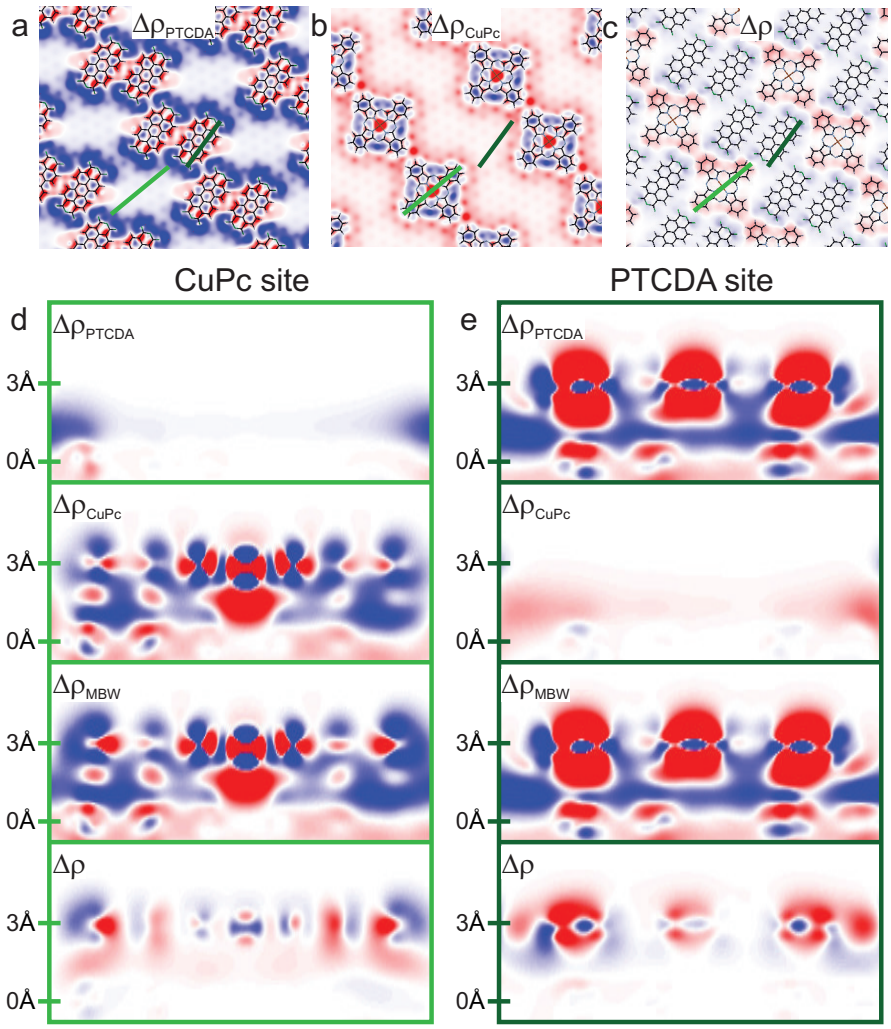

Figure 5.7: Charge density difference plots at a height of ≈ 1 Å above the silver surface, i.e., below the molecular plane, for (a) the PTCDA reference structure (MBW with CuPc being removed), (b) the CuPc reference structure (MBW with PTCDA being removed), and (c) for the charge reorganization difference between the MBW phase and the reference structures. In (d) and (e) vertical cuts through the charge density differences for these structures are shown in the uppermost three panels. The horizontal positions of the vertical cuts correspond to the CuPc (d) and PTCDA (e) sites and are marked in (a-c). The lowermost panel in (d) and (e) represents the difference of the first three panels: $\Delta\rho = \Delta\rho_{\mathrm{MBW}} - (\Delta\rho_{\mathrm{CuPc}} + \Delta\rho_{\mathrm{PTCDA}})$. In all plots charge depletion is shown in blue, charge accumulation in red.

horizontal plot is shown as Fig. 5.4c), the situation is fundamentally different. At this height, the intensity in the reference maps is almost vanishing (again, upper panel of Fig. 5.7d and 2nd panel of Fig. 5.7e, now in a height of $z \approx 3.0$ Å). This indicates that the depletion and accumulation of charge in the molecular LUMOs

is real, and not stemming from the subtraction of reference structures.

DFT calculations for the free-standing monolayer structures

In order to reveal the role of the silver substrate for the charge redistribution, we have also performed DFT calculations for a freestanding MBW layer, i.e., for molecules in the geometry of the MBW film, but without the Ag substrate. The corresponding pDOS for PTCDA and CuPc are shown as dark-green curve in the upper and red curve in the lower panels of Fig. 5.8, respectively. As a reference, we also calculated the pDOS for the artificial structures (1) and (2), i.e., for freestanding MBW film from which either CuPc or PTCDA was removed (light green and orange curves in of Fig. 5.8).

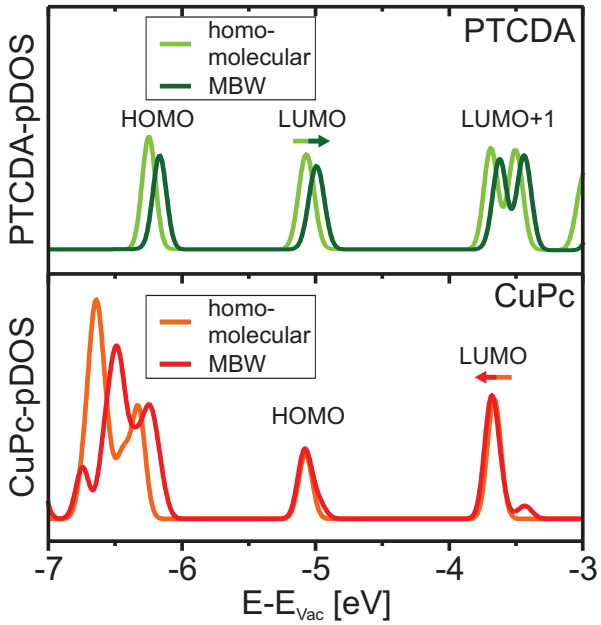

Figure 5.8: Electronic structure of freestanding layers revealed by DFT: Spin-up pDOS of the π-orbitals of PTCDA (upper panel) and CuPc (lower panel) in their freestanding homo- and heteromolecular phases, respectively.

Compared to the MBW/Ag(111) structure (including the surface), as it is discussed in Fig. 5.4a, these results show reversed peak shifts. Here, the binding energy of the PTCDA LUMO is reduced for molecules in the MBW film compared to the homomolecular reference. At the same time, the CuPc LUMO in the mixed film is found at slightly larger binding energies than in the homomolecular structure. In addition, no charge transfer from CuPc to PTCDA is visible in the freestanding layer. These DFT calculations clearly demonstrate that the charge reorganization and the molecular level alignment in the heteromolecular

Table 5.3: Adsorption energies for the MBW structure and three reference systems. The chemical contribution to the adsorption energy is shown in the 2nd column (E_{PBE}), the total adsorption energy which include van der Waals corrections, in the 3rd column (E_{ad}). The homomolecular CuPc and PTCDA structure were obtained by removing the other molecular species and fixing the adsorption height of the remaining molecules in the geometry obtained for the MBW structure on Ag(111).

structure	E_{PBE} [eV]	E_{ad} [eV] (incl. vdW.)
MBW/Ag(111)	0.68	-14.90
MBW free standing	-0.40	-0.93
PTCDA/Ag(111) (MBW)	0.20	-8.40
CuPc/Ag(111) (MBW)	1.14	-5.36
$\sum$ of MBW components	0.94	-14.69
MBW/Ag(111) - $\sum$ MBW components	-0.26	-0.21

MBW/Ag(111) structure occurs solely via the silver substrate, not directly within the mixed organic film.

Adsorption energies

Another, maybe more direct way, for quantifying the interaction strength at metal-organic hybrid interfaces is the adsorption energy. Table 5.3 shows DFT calculated adsorption energies for the heteromolecular MBW structure and for several reference structures. The major part of the adsorption energy arises from the dispersive van der Waals interaction between the aromatic molecules and the silver surface. For our calculations, we have used the empirical van der Waals correction scheme according to Grimme,[153] which is one of the state of the art van der Waals corrections. In Table 5.3 we show overall adsorption energies with (3rd column) and without (2nd column) van der Waals correction. For the latter calculations we used a common (semi)local PBE functional. This allows us to estimate the chemical contribution to the overall interaction between molecule and surface, which is responsible for the charge transfer and molecular level shifts that occur at the metal-organic interface. Negative adsorption energies corresponds to a bonding situation, positive values indicate repulsion.

For the MBW/Ag(111) structure the total adsorption energy is $E_{\mathrm{ad,MBW/Ag}} = -14.90\,\mathrm{eV}$ with a chemical contribution of $E_{\mathrm{PBE,MBW/Ag}} = 0.68\,\mathrm{eV}$. The adsorption energy is given relative to the energies of the uncovered substrate and the homomolecular freestanding CuPc and PTCDA films. Thus, the numbers given in table 5.3 contain contributions of the intermolecular interaction as well as of the molecule-substrate interaction of all molecules in the MBW/Ag(111) struc-

ture. In order to disentangle these contributions we also calculated the adsorption energies for a free-standing MBW layer and for the reference structures (1) and (2) with either CuPc or PTCDA being removed from the MBW/Ag(111) (see also chapter "charge reorganization"). Most interestingly, the sum the adsorption energies of these three reference systems ($\sum$ of MBW components) results in smaller adsorption energies compared to the adsorption energy of the total MBW structure on Ag(111). A comparison of the PBW contribution to the total adsorption energy reveals that the chemical contribution of the interaction is responsible for the lower adsorption energy of the MBW phase. Hence, this analysis shows that the level shifts and the charge redistribution are also reflected in the adsorption energies. Both effects lead to a stabilization of the MBW structure with respect to its components. This also emphasizes the conclusion of our manuscript, that the effects in the heteromolecular films are more than the sum of the contributing parts.

Chapter 6

Orbital tomography of hybridized and dispersing molecular overlayers

Now we switch back to homo-molecular systems and investigate the interfaces of the organic molecule pentacene and the (110) surfaces of Cu and Ag, utilizing orbital tomography. Doing so, we are able to clearly assign specific molecular orbitals to the peaks in the photoemission spectra. Furthermore we, experimentally, observe a notable intermolecular dispersion of the molecule's former LUMO on the Cu(110) surface, which we can confirm in our theoretical calculations by an expansion of the computational part of the orbital tomography approach to extended systems. This chapter is a reproduction of an article about this work, which has been published in Physical Review B, with the header of the article being shown in Fig.6.1 [1].

PHYSICAL REVIEW B **90**, 155430 (2014)

Orbital tomography of hybridized and dispersing molecular overlayers

Thomas Ules, Daniel Lüftner, Eva Maria Reinisch, Georg Koller, Peter Puschnig,* and Michael G. Ramsey†
University of Graz, Institute of Physics, NAWI Graz, Universitätsplatz 5, 8010 Graz, Austria
(Received 18 March 2014; revised manuscript received 27 August 2014; published 16 October 2014)

Figure 6.1: Header of the article [114], which was published in Pysical Review B, showing the reference, title and all contributing authors with their affiliations. This chapter is a reproduction of this article, beside some possible modifications.

[1] Reproduced with permission from the American Physical Society. Copyright 2014 by the American Physical Society, the article may be found online at http://link.aps.org/doi/10.1103/PhysRevB.90.155430

Author contributions

The major part of this work has been done by Thomas Ules, who has performed all of the experiments together with Eva Maria Reinisch and has written the initial draft of the manuscript, so consequently he is the first author of the paper. I have performed all of the DFT calculations and have done the analysis of the calculated data and prepared the corresponding figures presented in the paper. Furthermore, and probably that is the main contribution, I have been involved in several extensive discussions regarding the interpretation of the experimental data and the manuscript itself, with all contributing authors.

Abstract

With angle-resolved photoemission experiments and *ab-initio* electronic structure calculations, the pentacene monolayers on Ag(110) and Cu(110) are compared and contrasted allowing the molecular orientation and an unambiguous assignment of emissions to specific orbitals to be made. On Ag(110), the orbitals remain essentially isolated-molecule-like, while strong substrate-enhanced dispersion and orbital modification are observed upon adsorption on Cu(110). We show how the photoemission intensity of extended systems can be simulated and that it behaves essentially like that of the isolated molecule modulated by the band dispersion due to intermolecular interactions.

6.1 Introduction

The effects arising upon adsorption of π conjugated molecules on metal substrates are of great interest due to their importance in organic electronics. The ability to identify electronic states with specific molecular orbitals and to determine their energy ordering is vital to the understanding of overlayer/substrate systems. This can be particularly difficult for strong chemisorptive interactions where significant broadening or level splitting occurs or when intermolecular dispersing bands are formed. In the last decade *ab-initio* electronic structure calculations, particularly within density functional theory (DFT), have become almost indispensable in the interpretation of experimental results. However, it is becoming recognized that DFT results can be misleading due to approximations for exchange-correlation effects which may severely affect predicted adsorption geometries and/or the electronic structure of organic/metal interfaces [22]. The pentacene/Cu interface is such a case. Despite numerous experimental and theoretical studies, there is as yet no consensus on the orbital assignment. Here we demonstrate how the angle-resolved ultrviolet photoemission spectroscopy (ARUPS) technique, which is becoming known as orbital tomography [21, 22, 28, 108, 110, 111, 204], can provide

a definitive assignment of the emissions even for strongly interacting extended two-dimensional (2D) systems and give insight into the nature of dispersion and hybridization.

The pentacene (5A) monolayer on Cu(110) has been studied extensively. From their ARUPS investigations, Seki et al. [205, 206] concluded that selection rule arguments cannot explain the photoemission behavior, and they suggested that strong hybridization with the substrate could be modifying the orbital symmetry [206]. They also suggested the appearance of dispersing, interface-induced states arising from substrate interactions [206]. Ferretti et al. [207, 208] introduced the possibility that the mixing of 5A molecular orbitals with the Cu substrate leads to "interaction states localized at the interface", where their calculations suggest partial occupation of the lowest unoccupied molecular orbital (LUMO) whose symmetry might not be directly related to the original molecular state. On the same Cu(119) vicinal surface, scanning tunneling microscopy (STM) images also suggest partial occupation of the LUMO and dispersive electronic states associated with a perturbed electron charge density distribution. [209] Also a recent combined DFT and ARUPS study of the 5A/Cu(110) system concluded that only partial LUMO occupation takes place [210].

The simple relationship between the angular distribution of the photoemission current and the Fourier transform of the emitting molecular orbital has been shown to be reasonable for a number of molecular adsorbate systems on various noble metal surfaces [21, 22, 26, 111, 204]. This allows molecular orientations to be determined [26, 204], molecular orbital energy ordering to be deduced [22, 109], and even the reconstruction of the molecular orbitals in real space [111]. For these systems, the angular-dependent emissions can essentially be accounted for by the photoemission from isolated molecules, thus intermolecular orbital overlap plays a minor role. However, in extended 2D overlayer systems, a description in terms of isolated molecular orbitals is no longer strictly appropriate. Here, with the comparison between pentacene monolayers on Ag(110) and Cu(110), we show how orbital tomography and the Fourier transform description can be applied to extended systems with strongly dispersing emissions. In so doing, we provide a definitive description of the 5A/Cu ARUPS and show that the LUMO is in fact fully occupied and displays a substrate-induced dispersion that is significantly larger than that reported for similar organic overlayer systems [118, 129]. Moreover, unlike all previous tomography studies, we show evidence here of a modification of orbital shape on adsorption.

6.2 Experimental Details

Photoemission experiments were performed at BESSYII using a toroidal electron-energy analyzer described previously [104], which was attached to the beam-

line U125/2-SGM of the synchrotron radiation facility BESSY II, Helmholtz-Zentrum-Berlin. Photon energies of 30 and 35 eV and an incidence angle of χ = 40° with respect to the surface normal were used. The polarization direction is in the specular plane, which also contains the photoelectron trajectory measured. Emitted photoelectrons are recorded simultaneously with polar angles θ of −80° to +80° with respect to the surface normal in an energy window of 1 eV. The energy window is divided into 40 individual slices, which goes well below the analyzers intrinsic energy resolution of 150 meV. Note, however, that for the presented momentum maps we take only the data from the side of the emission direction that is pointing in the orientation of the electric field vector of the incident photons; this is referred to as the positive side (see Fig. 6.2), i.e., θ = 0 ° to +80 °. This maximizes the polarization factor appearing in the photocurrent cross section (see Eq. 6.4). It is noted that the molecular features are enhanced relative to the substrate emissions on the positive side (compare Fig. 6.5c). To obtain the full (k_x, k_y) range for the presented momentum maps at constant binding energy, azimuthal scans are made by rotating the sample around the surface normal in 1 ° steps for an azimuthal angle range > 180° and then imposing the substrate's twofold symmetry to obtain the full 360°. The angular emission data are then converted to parallel momentum components k_x and k_y using the relation

$$k_x = \sqrt{\frac{2m_e}{\hbar^2} E_{\mathrm{kin}}} \sin\theta \cos\phi \tag{6.1}$$

$$k_y = \sqrt{\frac{2m_e}{\hbar^2} E_{\mathrm{kin}}} \sin\theta \sin\phi, \tag{6.2}$$

to create the momentum maps. The Cu(110) and Ag(110) substrates were prepared in the conventional way by a sequence of sputter-annealing cycles. 5A molecules were evaporated from an effusion cell onto the surfaces at room temperature with the amount monitored by a microbalance. The resulting monolayer low-energy electron diffraction (LEED) structures are $\begin{pmatrix} 3 & -1 \\ 1 & 4 \end{pmatrix}$ for pentacene on Ag(110) and $\begin{pmatrix} 6.5 & -1 \\ -0.5 & 2 \end{pmatrix}$ for pentacene on Cu(110). In both cases mild annealing improved the order. On Cu(110) the monolayer was annealed at 200 °C, which is above the 5A sublimation temperature, whereas on Ag(110) the molecule substrate bond is weaker and the annealing temperature must not exceed 140 °C so as not to desorb from the monolayer.

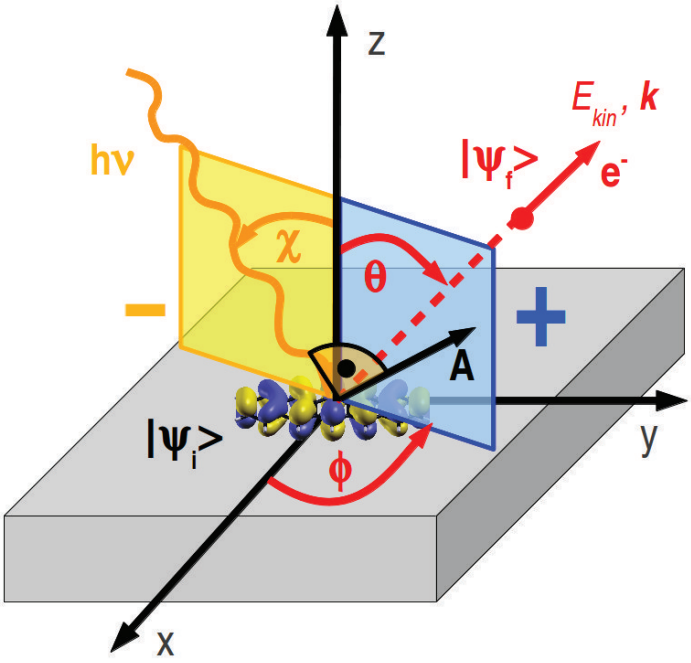

Figure 6.2: Sketch of an ARUPS experiment declaring the geometry of the experimental setup. The incoming photon with energy $h\nu$, the incidence angle χ, and the vector potential $\mathbf{A}$ excites an electron from the initial state ψ_i to the final state ψ_f. This final state is characterized by the kinetic energy E_{kin} and the momentum vector $\mathbf{k}$, and the outgoing photoelectron is detected as a function of E_{kin} and emission direction, defined by the polar angle θ and the azimuthal angle ϕ. Forward emissions are denoted by a positive parallel momentum, and backward emissions are denoted by a negative parallel momentum.

6.3 Computational Details

6.3.1 Density functional calculations

All theoretical results presented here are obtained within the framework of density functional theory (DFT) using the VASP code [146, 147]. We have performed three types of calculations: firstly for the isolated pentacene molecule, secondly for a two-dimensional, extended free-standing layer of pentacene, and thirdly for monolayers of pentacene adsorbed on Ag(110) and Cu(110) surfaces.

The isolated molecule calculations were performed using a supercell with a minimum of 15 Å vacuum between pentacene's periodic replica. We use the generalized gradient approximation (GGA) [66] for exchange-correlation effects, and the projector augmented wave (PAW) method [148]. The simulated momentum maps of the pentacene highest occupied molecular orbital (HOMO) and LUMO

orbitals shown in Fig. 6.3 are obtained as Fourier transforms of the respective Kohn-Sham orbitals as described previously [26].

Electronic structure calculations for the freestanding monolayer of 5A have been carried out using the repeated slab approach with a vacuum layer of 20 Å between adjacent layers. The GGA [66] is used for exchange-correlation effects, and the PAW [148] approach was used allowing for a relatively low kinetic energy cut-off of about 400 eV. We use a Monkhorst-Pack $6 \times 12 \times 1$ grid of k-points [149], and a first-order Methfessel-Paxton smearing of 0.1 eV [150]. The simulation of momentum maps for extended systems will be described in the subsequent section.

Finally, we have also performed DFT calculations of pentacene monolayers adsorbed on Ag(110) and Cu(110). The substrate is taken into account within the repeated slab approach by using five metallic layers with an additional vacuum layer of 15 Å between slabs. To avoid spurious electrical fields, a dipole layer is inserted in the vacuum region [151]. In the case of 5A/Ag(110), we have taken into account the experimental LEED structure $\begin{pmatrix} 3 & -1 \\ 1 & 4 \end{pmatrix}$ mentioned above and relaxed the atomic positions of the molecule and the first metallic layer considering van-der-Waals interactions by employing the empirical correction scheme according to Grimme [153]. Exchange correlation effects were treated either within the GGA [66] or within the Heyd-Scuseria-Ernzerhof (HSE) hybrid functional [88] with k-point meshes of $9 \times 6 \times 1$ and $6 \times 4 \times 1$, respectively, and a first-order Methfessel-Paxton smearing of 0.1 eV. For 5A/Cu(110), we have chosen a commensurate structure $\begin{pmatrix} 6 & 0 \\ 0 & 2 \end{pmatrix}$ and an adsorption site similar to a previous study [210]. Also, here the electronic structure is calculated within the GGA and HSE using k-point meshes of $9 \times 12 \times 1$ and $4 \times 6 \times 1$, respectively, and using a first-order Methfessel-Paxton smearing of 0.1 eV.

6.3.2 Simulation of ARUPS maps

The Kohn-Sham energies $\varepsilon_{n\mathbf{q}}$ and orbitals $\psi_{n\mathbf{q}}$ of the relaxed structures serve as input for the subsequent simulation of angle-resolved photoemission spectroscopy intensity maps within the one-step model of photoemission [23]. Here, the angle-resolved photoemission intensity $I(\theta, \phi; E_{\mathrm{kin}}, \omega)$ is a function of the azimuthal and polar angles θ and ϕ, respectively, the kinetic energy of the emitted electron E_{kin}, and the energy ω and polarization $\mathbf{A}$ of the incoming photon:

$$\begin{aligned} I(\theta, \phi, E_{\mathrm{kin}}; \omega, \mathbf{A}) &\approx \sum_{n}^{\mathrm{occ}} \sum_{\mathbf{q}}^{\mathrm{BZ}} |\langle \psi_f(\theta, \phi; E_{\mathrm{kin}}) | \mathbf{A} \cdot \mathbf{p} | \psi_{n\mathbf{q}} \rangle|^2 \\ &\times \delta(\varepsilon_{n\mathbf{q}} + \Phi + E_{\mathrm{kin}} - \omega), \end{aligned} \tag{6.3}$$

This formula can be viewed as a Fermi's golden rule expression, in which the photocurrent I results from a summation over all occupied initial states $\psi_{n\mathbf{q}}$, characterized by the band index n and Bloch vector $\mathbf{q}$, weighted by the transition probability between the initial state and a final state. For the transition operator $\mathbf{A} \cdot \mathbf{p}$, the dipole approximation is assumed, where $\mathbf{p}$ and $\mathbf{A}$ are the momentum operator and the vector potential connected to the incoming photon. The δ function ensures energy conservation where Φ denotes the work function.

We further approximate the final state ψ_f by a plane wave [24]. As outlined in more detail in a previous paper [26], and also noted earlier [25, 145], this approximation allows us to greatly simplify the evaluation of the matrix element appearing in Eq. 6.3. If we denote the wave vector of the final, free-electron state by $\mathbf{k}$, thus $E_{\text{kin}} = \frac{\hbar^2}{2m}k^2$, Eq. 6.3 simplifies to

$$\begin{aligned} I(k_x, k_y, E_{\text{kin}}; \omega, \mathbf{A}) &\approx \sum_{n}^{\text{occ}} \sum_{\mathbf{q}}^{\text{BZ}} |\mathbf{A} \cdot \mathbf{k}|^2 \left| \langle e^{i\mathbf{kr}} | \psi_{n\mathbf{q}} \rangle \right|^2 \\ &\times \delta(\varepsilon_{n\mathbf{q}} + \Phi + E_{\text{kin}} - \omega). \end{aligned} \tag{6.4}$$

We obtain the simple result that the matrix element from a given initial state $n\mathbf{q}$ is proportional to the square modulus of the Fourier transform of the initial-state wave function $\psi_{n\mathbf{q}}$ modulated by the weakly angle-dependent factor $|\mathbf{A}\cdot\mathbf{k}|^{\mathbf{2}}$ which depends on the angle between the polarization vector $\mathbf{A}$ of the incoming photon and the direction $\mathbf{k}$ of the emitted electron.

Note Eq. 6.4 can be applied to single molecules as well as to extended states such as an organic layer adsorbed on metallic surfaces. In the former case, the summation of the Brillouin zone (BZ) reduces to just one point, the Γ point, while for the latter situation, the possible dispersing bands are taken into account by the band structure $\varepsilon_{n\mathbf{q}}$ and Bloch states $\psi_{n\mathbf{q}}$ and an appropriate sampling of the Brillouin zone.

6.4 Results

6.4.1 Momentum maps

Monolayers of 5A on Ag(110) and Cu(110) were characterized by LEED and ARUPS. Figure 6.3 shows LEED images of the 5A monolayers on the two substrates Ag(110) and Cu(110) as well as the momentum maps taken at the binding energies of the prominent adsorption-induced emissions at 0.15 and 1.2 eV on Ag and 0.8 and 1.5 eV on Cu, respectively. These maps clearly display the character of the LUMO and HOMO of pentacene, as can be seen from the comparison between the measured (*exp*) and the corresponding simulated maps computed for

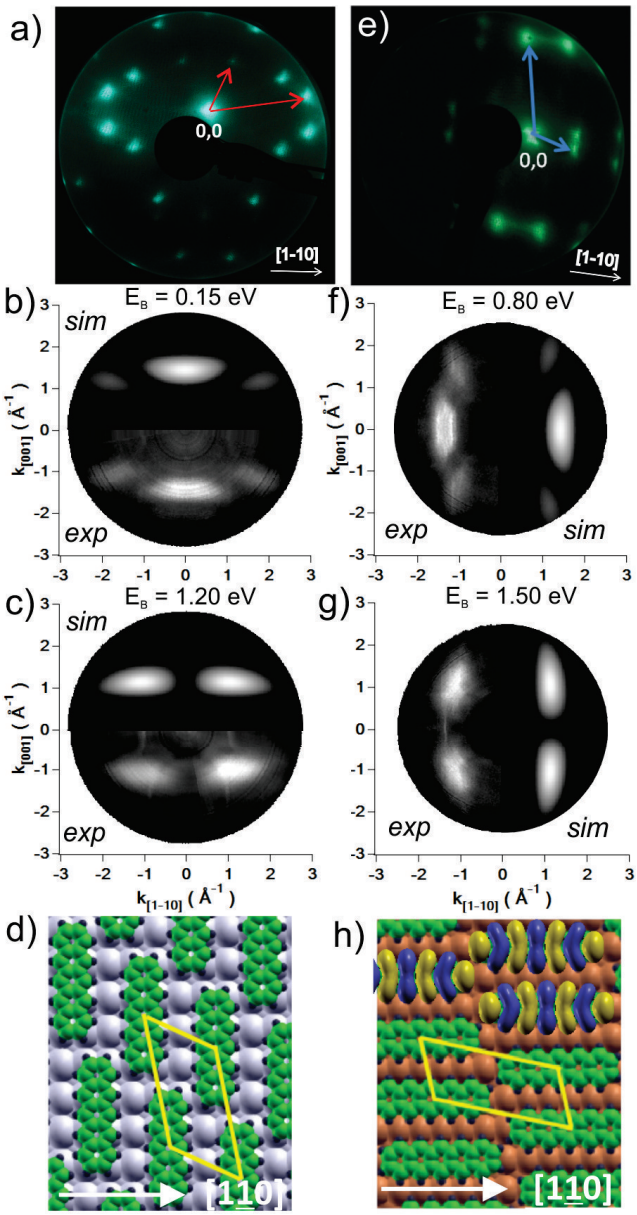

Figure 6.3: Panels (a) and (e) show LEED images of 5A monolayers on Ag(110) and Cu(110), respectively. Panels (b) and (c) show ARUPS momentum maps of 5A/Ag(110) at binding energies 0.15 and 1.20 eV (*exp*), respectively, compared to simulated LUMO and HOMO maps of the isolated 5A molecule (*sim*). Panels (f) and (g) show the corresponding data for 5A/Cu(110) at binding energies of 0.80 and 1.50 eV. Panels (d) and (h) show structural models of 5A/Ag(110) and 5A/Cu(110), respectively, as deduced from LEED and the momentum maps. In (h) the orbital structure of the LUMO is overlaid.

the isolated molecule (*sim*). The simulated LUMO map, for instance, is characterized by a major lobe at (0,1.4) $Å^{-1}$ and minor lobes at ($\pm$1.8, 1.2) $Å^{-1}$. Indeed, the data on Ag have recently been used to reconstruct these orbitals in real space, in excellent agreement with calculated orbitals for the isolated molecule [111]. The maps also unambiguously reveal the *orientation* of the molecules: on Ag(110) the data imply flat-lying 5A oriented parallel to the [001] azimuth, while on Cu the molecules orient along the [1-10] azimuth, as depicted in Figs. 6.3d and h, respectively. It should be noted that the structure and density of the two monolayers are very similar, however, on Ag the molecules lie across while on Cu they lie parallel to the close-packed rows of the substrate.

Thus, the ARUPS momentum maps of Fig. 6.3 immediately clarify the 5A/Cu system. In contrast to speculations in the literature, the symmetry of the orbitals is not modified significantly on hybridization. This allows the emissions to be unambiguously assigned. The features at 0.8 and 1.5 eV are the fully occupied LUMO and HOMO and not the HOMO and HOMO-1 emissions as assigned previously and, in the light of our results, erroneously on the basis of a comparison between DFT-calculated and experimental binding energies [210]. Upon closer inspection of the LUMO map on Cu, however, an internal structure and a change in the k position of the minor lobes becomes visible that will be argued to be the result of intermolecular dispersion and changes in the orbital size, respectively.

6.4.2 DFT results for adsorbed monolayers

Before analyzing this internal structure of the LUMO in more detail, we discuss DFT results of the pentacene monolayers on the Ag(110) and Cu(110) surfaces in comparison with ARUPS data. Starting from the relaxed structure of 5A/Ag(110), we have computed the density of states projected onto the orbitals of a freestanding pentacene layer, both, within the GGA and self-consistently within the hybrid functional HSE [88, 144]. It is known that the incorporation of a fraction of exact exchange in the hybrid HSE mediates self-interaction errors, thereby improving the orbital energies and thus the description of adsorbate systems [80, 81, 113]. The results are shown in panels (a) and (b) of Fig. 6.4. For comparison, panel (c) shows experimental ARUPS data recorded over a large energy window along the two different azimuths [001] (black solid line) and in a direction 45 ° between [001] and [1-10] (black dashed line). Panel (c) also includes the $k_x k_y$-integrated ARUPS data of the momentum maps that have been recorded over four energy windows of 1 eV centered around the molecular emissions of the LUMO, HOMO, HOMO-1, and HOMO-2, respectively. When comparing GGA with HSE results, we observe that the HOMO, HOMO-1 and HOMO-2 features are shifted to somewhat larger binding energies when using the hybrid functional, while the position of the LUMO orbital slightly below the Fermi level remains unchanged. Compared to experiment, we note that the HSE calculation clearly

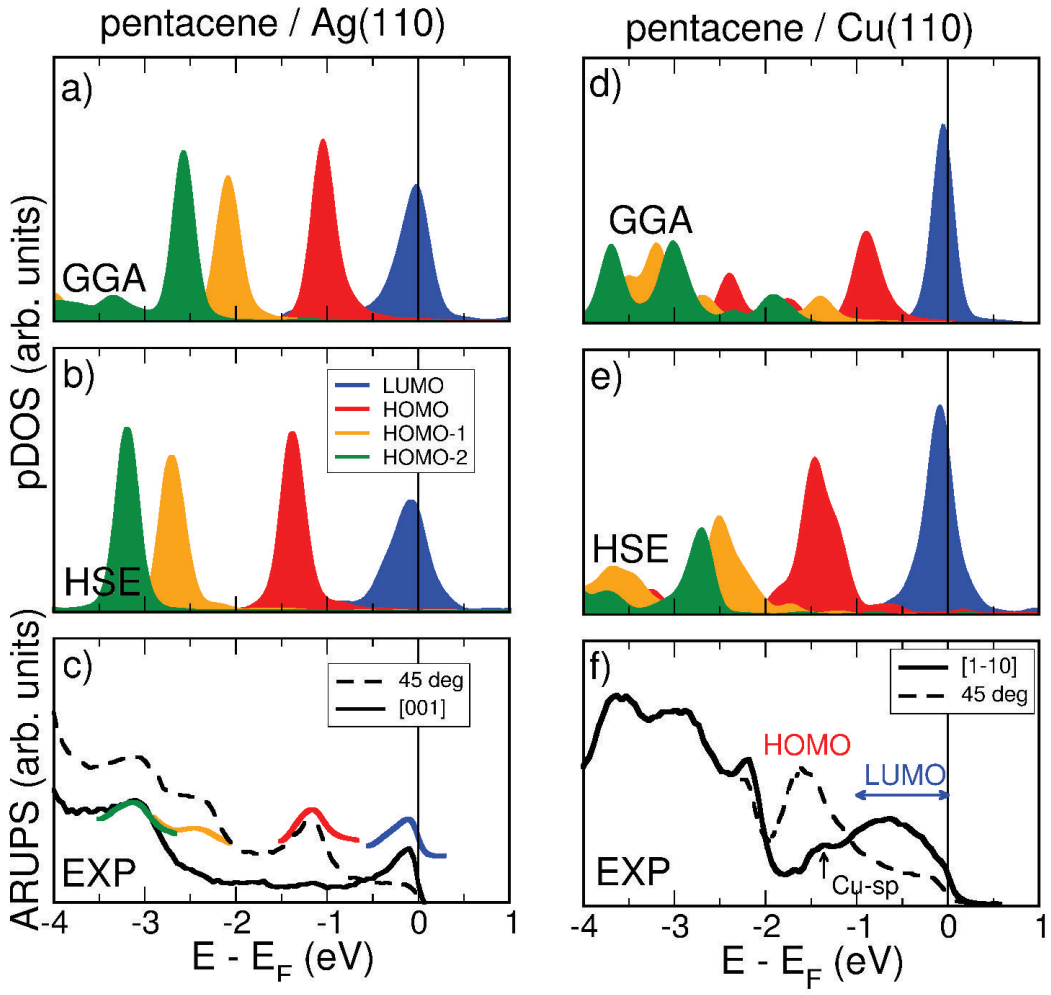

Figure 6.4: Density of states of a monolayer of pentacene on Ag(110) projected onto orbitals of the free pentacene molecule using PBE-GGA (a) and the hybrid functional HSE06 (b). Projections onto the LUMO (blue), the HOMO (red), the HOMO-1 (orange), and the HOMO-2 (green) are shown. For comparison, panel (c) shows experimental ARUPS data along the [001] azimuth (black solid line) and an azimuthal direction 45 ° between [001] and [1-10]. The colored curves are obtained by $k_x k_y$-integrating experimental momentum maps identifying the orbital character of the emissions. Panels (d)–(f) show the corresponding data for a monolayer of pentacene on Cu(110).

improves the energy position of the HOMO-1 and HOMO-2 and also leads to a slightly better agreement of the HOMO position. Regarding the LUMO, both functionals GGA and HSE indicate partial occupation in good agreement with experiment.

For the case of Cu(110) (Fig. 6.4, panel d–f), HSE again yields much better agreement with experiment. However, the LUMO, of prime importance in this

study, is still in poor agreement with experiment. Its computed position, both, obtained within the GGA and within HSE, is in error compared to experiment as the LUMO is located at the Fermi level and not fully occupied, with only a slight improvement gained by the hybrid functional calculation [211]. Note that various commensurate structures and adsorption sites did not change this finding. On the other hand, HSE does considerably improve the energy position of the deeper lying orbitals, for instance, the HOMO. As a side-note: It was exactly the wrong energy position of the HOMO in the GGA result that had motivated Müller et al. to erroneously assign the LUMO emission to the HOMO. Note that the computed density of states (DOS) of their paper [210] agrees with our GGA-DOS and their experimental ARUPS data are in line with our experiment.

6.4.3 1D band dispersion

Let us now concentrate on the energy dispersion of the LUMO state as suggested by the internal structure of the momentum maps. Figure 6.5 shows the E versus k relation (bandmap) along the long molecular axes of 5A for a) a monolayer on Ag(110), b) a half-monolayer on Cu(110) and c) a complete monolayer on Cu(110) from the Fermi edge (E_F) down to 2.2 eV binding energy. On Ag, the bandmap shows a feature located at the Fermi edge at a k value around 1.35 Å^{-1}, whose intensity gradually decreases with increasing binding energy, indicating that the LUMO is half-filled. Note that in this energy range, there are no apparent changes in the momentum maps. In Fig. 6.5b, the half-monolayer of 5A on Cu(110) is investigated. By examining such a low coverage, with no long-range order apparent from LEED, any effects of intermolecular dispersion are minimized and only effects due to the molecule-substrate interaction are expected. The bandmap of the 5A submonolayer on Cu(110) in the [1-10] direction (Fig. 6.5b), *i.e.* along the long molecular axes, shows, besides the Cu d and sp bands, emissions from the major 5A LUMO lobe visible around 1 eV binding energy. Comparing with Ag, the LUMO shifts from E_F and being half-occupied to a binding energy of roughly 1 eV and being fully occupied on Cu. This is indicative of the strong bonding interaction of 5A with Cu, nevertheless, the band map shows no obvious sign of intermolecular dispersion.

Upon the formation of the well ordered monolayer on Cu, the situation is changed with a new structure appearing in both the band and momentum maps. As evident in Fig. 6.5c, the principle molecular induced emission now oscillates in energy from E_F down to 1.2 eV in the range of $k_{[1-10]}$ from 1.0 to 1.9 Å^{-1}, which is suggestive of strong intermolecular dispersion (see Fig. 6.6b for an enlarged view). To emphasize the E versus k relation of the LUMO along the long molecular axes direction, the BZ boundaries and Γ points of the 5A monolayer structure deduced from LEED are indicated in Fig. 6.5c. Note that without differentiation or other enhancements of the raw data, the large LUMO dispersion with the periodicity of

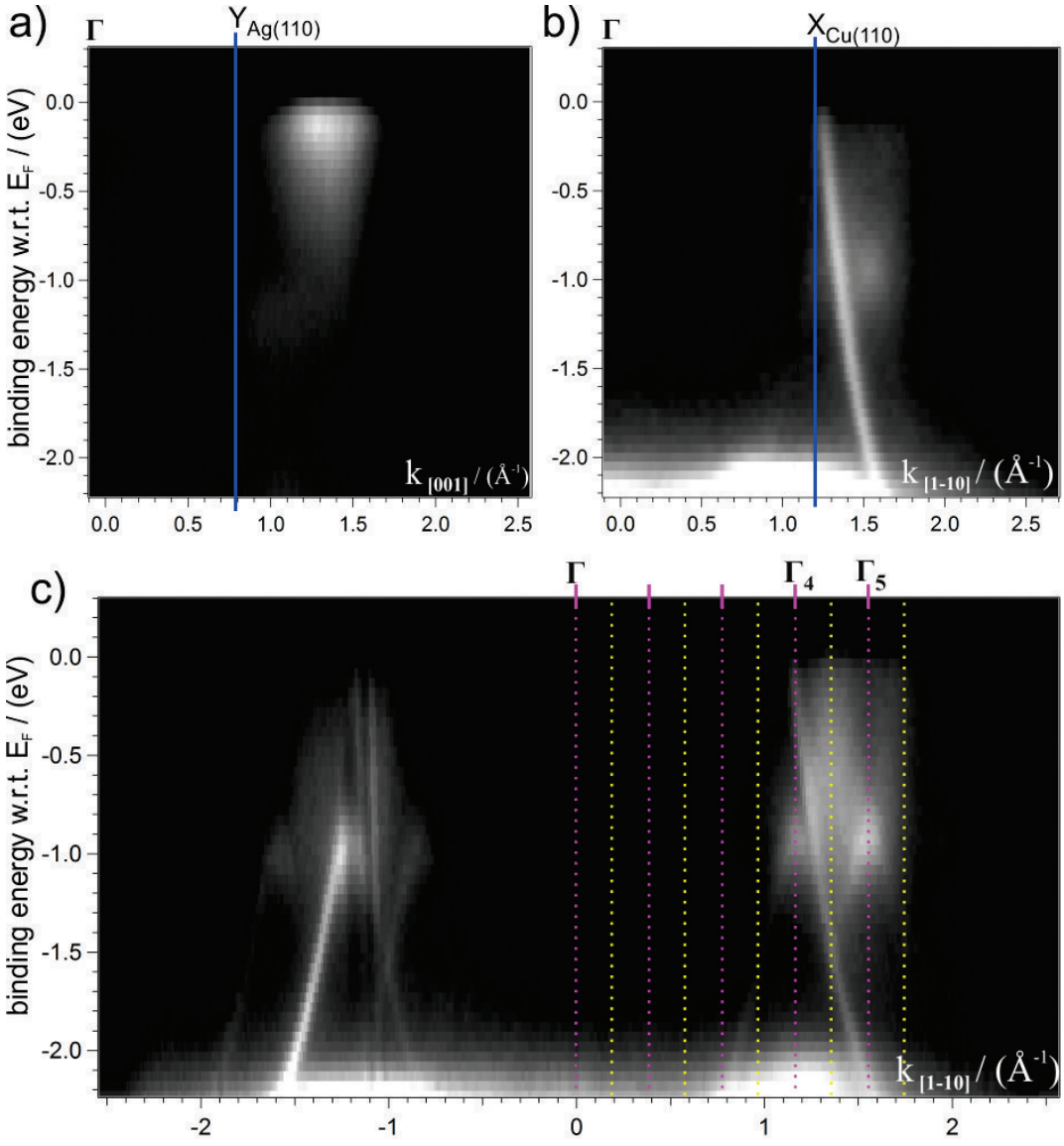

Figure 6.5: (a) Band map of a 5A monolayer on Ag(110) in the [001] azimuth. Panels (b) and (c) show band maps in the [1-10] azimuth of a *half* and a *complete* monolayer of 5A on Cu(110), respectively. Vertical lines indicate the Brillouin zone boundaries (yellow) and the Γ points (purple) of the 5A overlayer.

the overlayer is clearly evident in the 4th and 5th zones. The high-binding-energy side of the band is seen to be at Γ, and the low-binding-energy side is seen at the zone boundaries. Given the LUMO orbital's topology (Fig. 6.3h), the band dispersion running up from Γ to the BZ boundary is qualitatively consistent with a chain of pentacene molecules.

6.4.4 2D Band dispersion

Having qualitatively understood the one-dimensional dispersion along the long molecular axes, a more quantitative and, above all, an understanding of the two-dimensional (2D) LUMO dispersion on Cu and its manifestation in the photoemission experiment is desired. Toward that end, we first discuss the computed 2D LUMO dispersion of the *free-standing layer*, which is plotted in Fig. 6.6a with the band energy $E(k_{[001]}, k_{[1-10]})$ color-coded, with green indicating the center of the band, and red (blue) the top (bottom) of the band, respectively, where for reasons of clarity just one of the mirror domains is included. Note that although our 5A/Cu(110) HSE calculation including the substrate considerably improves the agreement with experiment over GGA results, we refrained from using it here for the analysis of the experimentally observed band dispersion of the LUMO for the following reason. The experimental overlayer structure is non-commensurate, while in order to enable a DFT calculation including Cu(110), a commensurate surface unit cell had to be imposed (similar to a previous study [210]). This difference would result in distinctly different periodicities in the measured and simulated momentum maps, preventing a one-to-one comparison. In contrast, the free-standing layer simulation with the correct structure enables a one-to-one analysis of the experimentally observed LUMO dispersion.

Inspection of Fig. 6.6a shows that the character of the dispersion, i.e., the k positions of the tops and bottoms of the band, may well be understood by knowing (i) the respective Brillouin zone, and (ii) the nodal structure of the respective molecular orbital in conjunction with the intermolecular arrangement of molecules. The first determines the reciprocal periodicities and the second the direction of the dispersion, i.e., whether the band would run up or down from Γ to the BZ boundary. The main dispersion is along the long real-space unit-cell vector, *i.e.*, roughly along the long molecular axes. The calculated energy spread of 20 meV for the free-standing layer is, however, very small and more than an order of magnitude lower than the experimentally observed one.

In the ARUPS experiment, one does not observe the 2D dispersion of the LUMO-derived band over the entire k-range due to matrix element effects. For isolated molecules, the selection rules are well-described by the FT of the isolated molecular orbitals. In analogy, in order to simulate the photoemission intensity distribution in a quantitative manner, we thus need to consider the wave functions of the extended 2D molecular system and compute their Fourier transforms according to the plane-wave final-state approximation [26]. Evaluating Eq. 6.4 for a free-standing layer, we simulate momentum maps (*sim*) at the top, middle and bottom of LUMO-derived band and compare them with the experimental maps (*exp*) taken at the 0.15 eV, 0.60 eV and 1.0 eV binding energy in panels c, d and e of Fig. 6.6, respectively. These energy positions are also indicated as horizontal lines in the enlarged band map shown in panel (b). Note that in the simulations,

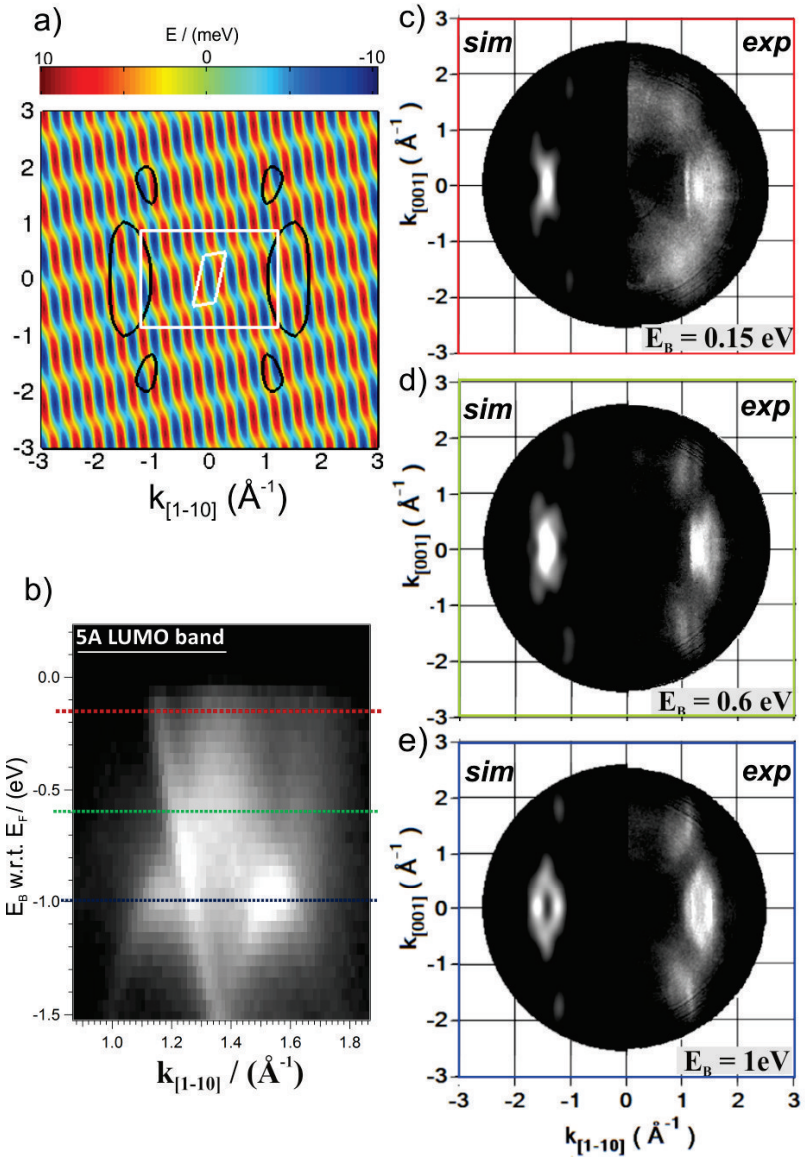

Figure 6.6: (a) Color-coded two-dimensional dispersion $E(k_{[001]}, k_{[1-10]})$ of the LUMO for a freestanding 5A monolayer with the structure of Fig. 6.3(h). Superimposed in white are the Brillouin zones of Cu(110) (rectangle) and the 5A monolayer (rhombus), and in black an intensity iso-line of the calculated isolated 5A LUMO momentum distribution. (b) Close-up of the dispersing LUMO band with red, green and blue lines indicating the energy positions at which momentum maps are extracted for comparison with the calculated photoemission momentum distributions in (c) top (d) middle and e) bottom of the band. Note that in panels (c)–(e) simulated momentum maps (*sim*) are compared to experimental maps (*exp*) as detailed in the text.

we have taken into account that the monolayer structure consists of two mirror domains.

The experimental and simulated momentum maps are in remarkably good agreement. For the major lobe, in going from top to bottom of the band, not only is the general shape in agreement, one also observes an increase in the extension of the feature in $k_{[001]}$ and a splitting of the emission in $k_{[1-10]}$. Although it is weak, there is also agreement in the behavior of the minor lobes. For instance, the shift in $k_{[1-10]}$ from 1.0 to 1.3 Å^{-1} is seen in both experiment and simulation. Also, in the middle of the band the splitting of the minor lobe seen in the experiment, although difficult to discern, is also observable in the calculated map. We conclude that the photoemission intensity of the extended system is essentially that of the isolated molecule modulated by the intermolecular dispersion. This naturally implies that the practice of searching for dispersion in extended systems outside the k-range expected for the isolated molecules is questionable. This is illustrated in the calculated 2D dispersion of Fig. 6.6a by overlaying the isoline of the computed ARUPS map of the isolated 5A LUMO.

While giving extremely good agreement in the three-momentum maps shown in Fig. 6.6c–e, the exact E versus k relation is naturally problematic when analyzed in terms of a free-standing layer. Indeed, as experience with other systems has shown, the substrate may or may not (depending of the relative energy position of molecular and substrate levels) enhance the dispersion as e.g. for PTCDA/Ag(110) [118] and NTCDA/Ag(110) or NTCDA/Cu(100) [129]. But in all these cases the *character* of the dispersion is left unaltered and therefore the appearance of momentum maps is also unchanged when going from the free-standing layer to the adsorbed monolayer. The *magnitude* of the dispersion is generally influenced by the molecule-substrate interaction. The case of pentacene/Cu(110) stands out because the observed dispersion is the largest one measured so far and may thus even be termed substrate-*induced* since the band width of the free-standing layer's LUMO band is almost negligible.

Indeed, our calculation for 5A/Cu(110) using the commensurate structure does show enhanced dispersion compared to the free-standing layer without the substrate, however it is not as large as the experimental observation presumably as a result of the underestimation of the LUMO binding energy.

6.4.5 Molecule-Metal Hybridization

For the 5A/Cu system, in addition to the structure introduced by dispersion, there is also a distinct change in the k-position of the minor lobes in the $k_{[001]}$ direction. In Fig. 6.7, simulated momentum maps of the LUMO for the gas-phase and for the 5A/Cu(110) adsorbate system are compared to experimental maps of the 5A LUMO on both surfaces. Upon inspection of Fig. 6.7d, one sees that

on Cu, the minor lobes (green crosses) have maxima at $k_y = \pm 1.5$ Å^{-1} which is significantly lower than, both, the simulated values for the isolated molecule (b) and the experimental value on the Ag surface (e) (± 1.8 Å^{-1}). This shift is a consequence of the molecule-copper interaction and can be interpreted as a $\approx 20\%$ increase of the lateral orbital size upon adsorption. It can be rationalized by recalling the reciprocal relationships between the LUMO shape in real space and the corresponding momentum space patterns as illustrated in Figs. 6.7a and b. Here the maxima of the major and minor lobes are marked as red and green crosses in the momentum map, respectively, while the corresponding real space dimensions are indicated by scale bars of length $2\pi/k$. We note that the width of the LUMO orbital along the short molecular axis is reflected by the k_y maximum of the minor lobe. Thus, unlike all molecular adsorbate systems so far reported [26, 28, 111, 117], the orbital tomography of the 5A LUMO on Cu(110) shows a distinct modification of the orbital's shape from the isolated molecule.

Our interpretation of the experimental data in terms of a spatial distortion of the orbital is further supported by our DFT calculations. Starting from the orbital energies and wave functions of the HSE calculation for 5A/Cu(110), we simulate an ARUPS intensity map of the LUMO as shown in Fig. 6.7c. These simulations indeed indicate a shift of the minor lobe peak (green cross) to lower k values upon adsorption on Cu(110). We note, however, that this change is smaller than the experimental observation. The discrepancy is likely due to a shortcoming of the DFT results regarding the LUMO binding energy (too low) and width (too narrow) at the HSE-DFT level, indicating an underestimation of the interaction strength of the LUMO with the substrate. The pronounced difference between the minor lobe peak position of 5A/Cu(110) compared to 5A/Ag(110) can thus be seen as direct evidence of a strong molecule-metal hybridization for the former.

While hybridization is generally observed by indirect means in effects on molecular emissions such as energy broadening of orbital emissions [118] or reduced emission intensity in gaps of bulk states [212], we provide direct evidence here of changes in orbital shape. Moreover, further signatures of hybridization can be observed as additional Cu-*sp*-like features appearing with the overlayer periodicity (Fig. 6.5). These are best seen on the *negative* k side where the molecular features are weak as shown in Fig. 6.5c. These emissions are not simply the bulk *sp* bands scattered by the overlayer, since mere scattering would replicate the Cu *sp* band over the entire energy range. Instead one observes that they do not extend up to E_F but stop at 1.2 eV binding energy, just below the onset of the LUMO orbital. We therefore suggest that they are due to interfacial Cu *sp* bands hybridizing with the 5A LUMO such that states appearing in these bands in the 0–1 eV binding-energy range have changed their character from Cu *sp* to that of the molecular LUMO.

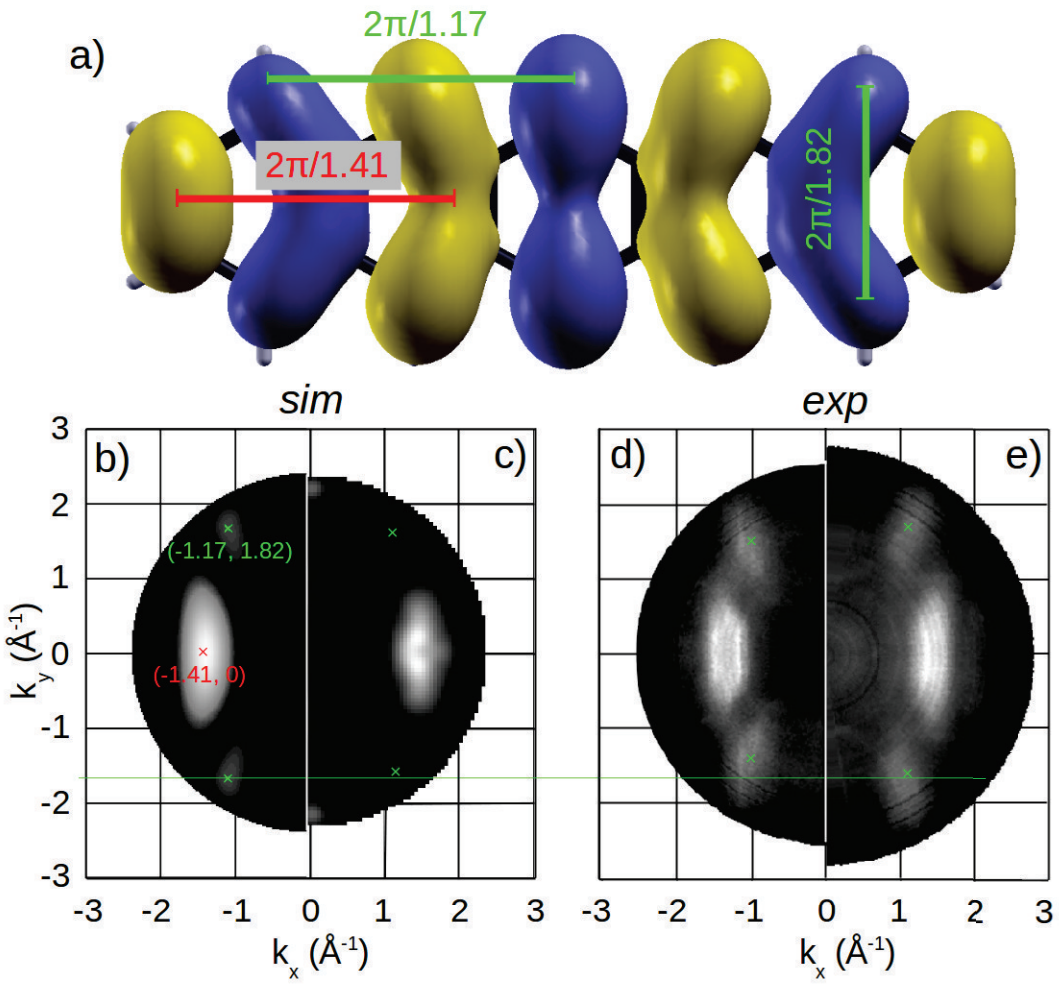

Figure 6.7: (a) Calculated LUMO of an isolated 5A molecule in real space, scale bars mark characteristic dimensions as detailed in the text. Panels (b) and (c) are simulated momentum maps for a free 5A molecule and the monolayer 5A/Cu(110), while (d) and (e) show experimental ARUPS maps of 5A/Cu(110) and 5A/Ag(110), respectively. The red and green crosses indicate the position of the maxima of the LUMO's major and minor lobe, and the horizontal green line is a guide for the eye.

6.5 Conclusion

In summary, a very strong substrate-induced dispersion of the LUMO orbital of 5A/Cu(110) along the Cu-row direction is traced back to a significant hybridization between the organic and the metallic states, while the LUMO of 5A/Ag(110) exhibits only a minor intermolecular dispersion. By making use of the reciprocal relation between the structure of real space orbitals and features in the momentum maps, we are able to deduce a significant geometrical

modification of the LUMO orbital upon adsorption on Cu(110), while it remains essentially free-molecule like on Ag(110). We believe that the main difference between the adsorption behavior of pentacene on these two surfaces arises from the distinct molecular orientation with respect to the close-packed metal rows. While on Ag(110) pentacene orients perpendicular to the rows, it aligns parallel to the metal rows on Cu(110). Because the electronic structure, e.g. the band dispersion of the metallic *sp*-bands or the location of the surface state in the surface Brillouin zone, is distinctly different along the rows $[1\bar{1}0]$ and perpendicular to them [001], also the hybridization with adsorbed elongated species can be expected to be different.

In conclusion, for the case of pentacene monolayers on Ag(110) and Cu(110) surfaces, we have demonstrated the power of the orbital-tomography method using extensive angle-resolved photoemission data for revealing the electronic structure of such two-dimensional organic-metal interfacial layers. By generalizing the theoretical description of the photoemission process from isolated molecule systems to extended two-dimensional systems, we are able to explain the "fine-structure" in the experimental momentum maps and obtain a comprehensive understanding of the band dispersion of organic-metal interfacial layers.

Acknowledgements

We acknowledge financial support from the Austrian Science Fund (FWF) P21330-N20 and P23190-N16. We further acknowledge the Helmholtz-Zentrum Berlin - Electron storage ring BESSY II for provision of synchrotron radiation at beamline U125/2-SGM. The research leading to these results has received funding from the European Community's Seventh Framework Programme (FP7/2007-203) under grant agreement no. 312284.

Chapter 7

Experimental and theoretical electronic structure of quinacridone

In the previous chapters the eigenvalues of DFT calculations already have been used and calculated projected density of states have been compared to photoemission spectra, although the main focus lied in the angular distribution of the photoemission signal. This chapter mainly focuses on the energy dependence of the photoemission signal and its comparison to calculated eigenvalue spectra. Therefore, the isolated molecule's eigenvalue spectrum and that of the the bulk structure, of the organic molecule quinacridone, is systematically studied in this chapter with different choices for the xc functional and compared to the measured spectra as well as to quasiparticle spectra obtained within the GW formalism. We find an excellent agreement with experiment and quasi particle energies with DFT calculations using optimally-tuned screened range separated hybrid functionals. The work has been summarized in an article, which has been published in Physical Review B, which is reproduced here and of which the header is shown in Fig.7.1 [1].

Author contributions

The work for this article started during my stay at the group of Leeor Kronik at the Weizmann Institute of Science in Rehovot, Israel. There, Leeor and his student Sivan Refaely-Abramson introduced me to the concept of optimally-

[1] Reproduced with permission from the American Physical Society. Copyright 2014 by the American Physical Society, the article may be found online at http://link.aps.org/doi/10.1103/PhysRevB.90.075204

PHYSICAL REVIEW B **90**, 075204 (2014)

Experimental and theoretical electronic structure of quinacridone

Daniel Lüftner,[1] Sivan Refaely-Abramson,[2] Michael Pachler,[1,3] Roland Resel,[3] Michael G. Ramsey,[1] Leeor Kronik,[2] and Peter Puschnig[1,*]

[1]*Institute of Physics, University of Graz, NAWI Graz, Universitätsplatz 5, 8010 Graz, Austria*

[2]*Department of Materials and Interfaces, Weizmann Institute of Science, Rehovoth 76100, Israel*

[3]*Institute of Solid State Physics, Graz University of Technology, NAWI Graz, Petersgasse 16, 8010 Graz, Austria*

(Received 7 July 2014; revised manuscript received 11 August 2014; published 25 August 2014)

Figure 7.1: Header of the article [81], which was published in Pysical Review B, showing the reference, title and all contributing authors with their affiliations. This chapter is a reproduction of this article, beside some possible modifications.

tuned range-separated hybrid functionals and Sivan showed me how such calculations are done in practice. I have then performed all calculations of the isolated quinacridone molecule while i was still in Israel. The choice of the molecule quinacridone, was motivated by the measurements of Michael Pachler, who has performed the UPS and x-ray diffrection experiments under the supervision of Michael Ramsey and Roland Resel. Because these experiments were done for thick film phases of quinacridone and Leeor and Sivan were preparing a manuscript about optimally-tuned range-separated hybrid calculations of bulk systems by that time [213], also the theoretical calculations have been extended to the molecular crystal in the β-phase of quinacridone. Furthermore, I have performed all calculations connected with the GW results and provided the bulk phase geometry and dielectric constants for Sivan, who has done the OT-SRSH calculations for the bulk phase. I have prepared all figures of-, and have written, the initial draft of the manuscript and discussed and iterated, together with Leeor, Sivan, Micheal Ramsey and Peter Puschnig, the manuscript until its final version.

Abstract

The energy positions of frontier orbitals in organic electronic materials are often studied experimentally by (inverse) photoemission spectroscopy and theoretically within density functional theory. However, standard exchange-correlation functionals often result in too small fundamental gaps, may lead to wrong orbital energy ordering, and do not capture polarization-induced gap renormalization. Here, we examine these issues and a strategy for overcoming them by studying the gas phase and bulk electronic structure of the organic molecule quinacridone (5Q), a promising material with many interesting properties for organic devices. Ex-

perimentally, we perform angle-resolved photoemission spectroscopy (ARUPS) on thin films of the crystalline β-phase of 5Q. Theoretically, we employ an optimally-tuned range-separated hybrid functional (OT-RSH) within density functional theory. For the gas phase molecule, our OT-RSH result for the ionization potential (IP) represents a substantial improvement over the semi-local PBE and the PBE0 hybrid functional results, producing an IP in quantitative agreement with experiment. For the bulk crystal, we take into account the correct screening in the bulk, using the recently developed optimally tuned *screened* range-separated hybrid (OT-SRSH) approach, while retaining the optimally-tuned parameters for the range-separation and the short-range Fock exchange. This leads to a band gap narrowing due to polarization effects and results in a valence band spectrum in excellent agreement with experimental ARUPS data, with respect to both peak positions and heights. Finally, full-frequency G_0W_0 results based on a hybrid functional starting point are shown to agree with the OT-SRSH approach, improving substantially on the PBE-starting point.

7.1 Introduction

Organic semiconducting devices are extensively studied as they have the advantage, compared to their Si-based counterparts, of being flexible, cheap, lightweight, and processable at low temperatures [10, 214]. Recently, the organic pigment 5,12-dihydro-quino[2,3-b]acridine-7,14-dione (quinacridone), $C_{20}H_{12}N_2O_2$, a derivative of pentacene, has attracted considerable interest as an active material in organic electronics [48, 50, 215–217], e.g., due to its remarkable air-stability, high photogeneration efficiency, electrochemical stability, and high fluorescence lifetime in solution.

Quinacridone (5Q) differs from pentacene by the presence of functional N-H and C-O groups at phenyl rings 2 and 4 [see Fig. 7.2(a)]. On the one hand, these polar groups cause the formation of intermolecular hydrogen bonds. These are responsible for 5Q's ability to form self-assembled, supramolecular structures and allow for the remarkable air-stability of 5Q devices reported in the literature [218]. However, these functional groups also break the conjugation of the molecule and thereby significantly change the energetic positions and spatial shapes of the frontier orbitals. The latter are crucial for the performance of organic semiconducting devices because they determine electron removal and insertion energies and therefore the band gap and level alignment. As such, they are extensively studied in the context of organic molecular systems and organic/inorganic interfaces [22, 116, 219, 220]. Such investigations strongly benefit from accurate and computationally inexpensive theoretical models, which are often necessary for a better interpretation of experimental results [221].

An efficient work horse for first principles calculations of the electronic structure

is density functional theory (DFT) [222, 223], usually within the Kohn-Sham (KS) framework [56, 224]. In this scheme the original many-electron problem is mapped uniquely into a fictitious noninteracting electron system, yielding the same electron density. This mapping leads to effective single-particle equations that provide a significant conceptual and computational simplification of the original many-electron problem. However, due to the fictitious nature of the noninteracting electrons, the correspondence of KS eigenvalues with ionization energies measured in an experiment is not straightforward [225]. One exception is the highest occupied orbital whose energy can be rigorously identified with the ionization potential (IP) of the neutral system, if the *exact* exchange-correlation (xc) functional is used [72, 73, 82, 226]. In general, KS results based on *approximate* xc expressions, e.g., local or semi-local functionals, may suffer from pronounced self-interaction errors (SIE) and a lack of derivative discontinuity in the xc potential, and therefore are not expected to agree with experimental findings obtained, e.g., from photoemission spectroscopy [79]. These conceptual problems may, at least partly, be cured by introducing the generalized Kohn-Sham (GKS) scheme [91], and considering hybrid functionals with a fraction of exact exchange either globally or in a range-separated manner [79]. However, band gaps, IPs, electron affinities (EAs), and the orbital order obtained within such a hybrid functional may still be in error when compared to experiment [76, 227].

A promising strategy to improve the agreement with experiment is the more recent class of range-separated hybrid (RSH) DFT functionals [228, 229], where the interelectron Coulomb repulsion term is separated into long-range (LR) and short-range (SR) components. The LR term is mapped using Hartree-Fock theory, thereby establishing the correct asymptotic potential. The SR term is mapped using a (semi-)local KS functional or a conventional hybrid functional, maintaining the compatibility between the exchange and correlation expressions. In this approach, one still needs to determine the range-separation parameter [230], as a universal value usually leads to energy levels that, although greatly improve the accuracy of standard hybrids, are still not at the desired accuracy level [76, 231]. This can be improved by using optimally tuned RSH (OT-RSH) functionals [76, 232], where the range-separation parameter is tuned for each system such that physically motivated tuning conditions are fulfilled without introducing any empirical parameters. DFT calculations using OT-RSH functionals have been shown to provide an accurate, non-empirical description of band gaps, IPs, and EAs for a variety of systems, among them atoms, molecules, and polymers [93, 233–235] as well as larger gas phase organic molecules relevant for organic semiconducting devices [94, 236]. In addition, it has been demonstrated that the description of deeper lying occupied states of an isolated molecule can be considerably improved within the OT-RSH approach, if an additional degree of freedom is introduced, which allows the modification of exact exchange in the short range [237, 238]. In particular, it was shown to well-describe the outer-

valence spectra of several organic molecules that exhibit a mixture of localized (σ) and delocalized (π) states [237], a challenging situation where the difference in self interaction error (SIE) for different orbital types can lead to the wrong description of orbital-ordering with standard DFT methods [80, 92, 156, 239, 240].

Beyond gas-phase molecules, band gaps of various organic molecular *crystals* have also been recently successfully described with an OT screened-RSH (OT-SRSH) functional [213]. This was achieved by including a new constraint for the asymptotic behavior of the exchange correlation potential, thereby taking into account effects arising from polarization-induced band renormalization [241–243]. An open question, however, is whether the OT-SRSH functional is capable of accurately predicting not only band gaps, but the entire outer valence spectrum of molecular crystals. In particular, it is interesting to examine the OT-SRSH accuracy when the crystal is comprised of more complex organic molecules, such as 5Q, that are characterized by a mix of localized (σ) and delocalized (π) states as frontier orbitals, where different SIEs are expected. It has not yet been investigated whether the OT-SRSH approach can accurately deal with self-interaction problems and at the same time cope with polarization effects arising from the crystalline environment. Capturing both is necessary for an overall good description of the electronic structure. For this purpose, 5Q turns out to be an ideal test candidate.

In this article, we report a combined experimental and theoretical study of the electronic structure of 5Q, which answers the above question. We performed angle resolved UPS experiments taken on well-ordered films of 5Q in the β phase [244, 245], and provide a detailed theoretical assignment of the various peak positions, using the OT-SRSH method. To this end, we first investigated the isolated 5Q molecule, by performing OT-RSH calculations. This yielded an IP in excellent agreement with literature data from gas phase ultraviolet photoemission spectroscopy (UPS). We then calculated the electronic structure of the bulk β phase, taking into account the correct asymptotic behavior in the OT-SRSH approach by computing the dielectric constant of the bulk crystal within the random phase approximation. To gain a better understanding of our results, we also performed many-body perturbation theory calculations, within the G_0W_0 approximation [51, 53] using various DFT starting points. We obtained excellent agreement with experimental results for both the OT-SRSH and G_0W_0 calculations, the latter based on a DFT starting point obtained from a conventional hybrid functional.

7.2 Experiment

5Q films were grown *in situ* in ultrahigh vacuum (UHV) at room temperature on an atomically clean and ordered Cu(110) substrate. The Cu surface was prepared

by repeated cycles of Ar^+ -ion bombardment and annealing at 800 K. A 260 Å thick 5Q film was deposited *in situ* from a thoroughly degassed evaporator, such that the pressure in the system remained at the 10^{-10} mbar range during film growth. The nominal growth rate was 2 Å min^{-1}, as monitored by a quartz microbalance assuming a density of 1.47 g cm^{-3}.

The electronic structure has been characterized *in situ* with UPS. Angle-resolved photoemission (ARUPS) experiments were performed using a VG ADES 400 spectrometer described elsewhere [246]. The ADES system was equipped with a noble gas discharge lamp (unpolarized helium I radiation, $h\nu = 21.2$ eV) and a movable electron energy analyzer, allowing angle resolved ultraviolet photoelectron spectroscopy in the specular plane, with an angular resolution of 1° and a total energy resolution of 150 meV at room temperature. A photon incidence angle of $\alpha = 60°$ was used. After the ARUPS measurements, the sample was removed from vacuum for geometrical structure investigations, *ex situ*, using x-ray diffraction (XRD) with both $\Theta/2\Theta$ scans and pole figure analysis (Philips X'PERT four circle texture goniometer) [247].

The XRD data revealed the β phase 5Q polymorph [244, 245], oriented with its $(\bar{1}12)$ plane [blue line in Fig. 7.2(b)] parallel to the substrate, with four equivalent domains. As illustrated in Fig. 7.2, in any one domain of β-5Q the axes of the molecules are almost parallel to the substrate surface ($\approx 7°$). Due to the two molecules in the unit cell having their aromatic planes at $\approx 70°$ to each other, and the multiplicity of domains, only small angular variations were observed in the angle-resolved UPS. Orbital tomography predictions of the angular distribution [22] suggested that both π and σ orbital emissions contribute to the spectra. Thus the experimental spectra may be safely related to the calculated density of states.

7.3 Theory

The electronic structure of both the isolated 5Q molecule and its β-crystal structure has been calculated using two different types of electronic structure approaches. The first type is within the framework of DFT, where the exchange-correlation potential is approximated in several different ways: using the generalized gradient approximation (GGA), as parametrized by Perdew, Burke and Ernzerhof (PBE) [66], the global hybrid PBE0 [85], the short-range hybrid of Heyd, Scuseria and Ernzerhof (HSE) [88], and finally the optimally-tuned range-separated hybrid (OT-RSH) functional for isolated molecule calculations [94] and the recently proposed optimally-tuned screened range separated hybrid (OT-SRSH) [213] functional for the molecular solid. The second type of calculation is based on many-body perturbation theory, within the GW approximation [51],

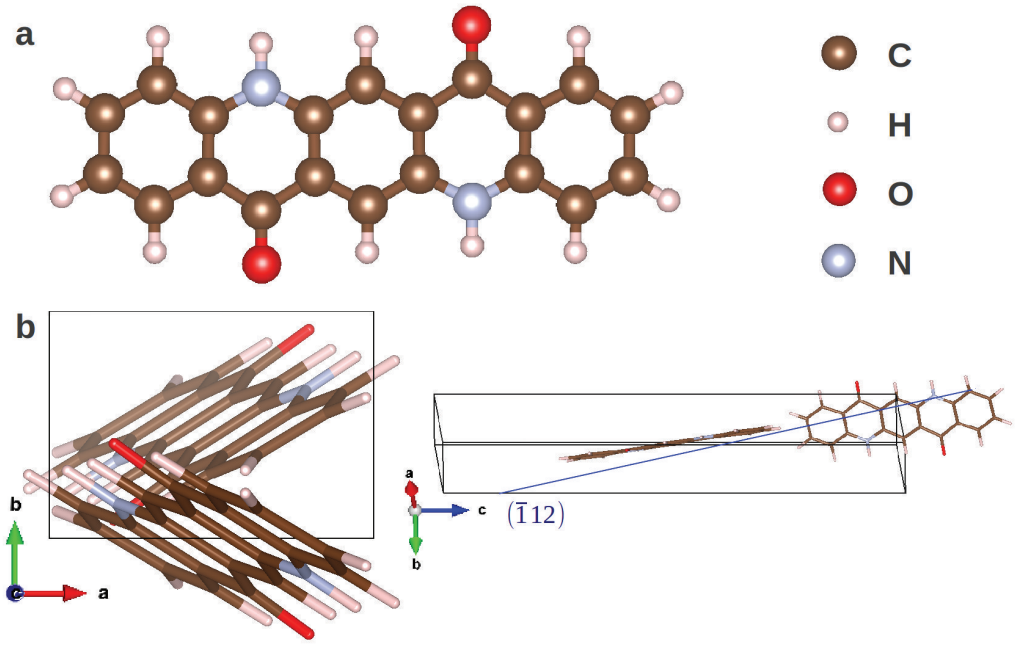

Figure 7.2: (a) Schematic view of the 5Q molecule. (b) Alignment of the 5Q molecules in the β-crystalline structure, with the $(\bar{1}12)$ plane indicated as a blue line.

calculated as perturbative "one-shot" G_0W_0 [53] corrections to DFT-based eigenvalue spectra, from either PBE or HSE calculations. While the G_0W_0 approach has been often applied to molecules and molecular solids and is well represented in the literature (see, e.g., Refs. [101, 242, 243, 248–255]), OT-SRSH based calculations are rather new and therefore we provide a concise overview of the basic ideas of that approach. For overviews from different perspectives, the reader is referred to Refs. [76, 231, 254, 256, 257] and specifically for studies of organic molecular crystals to Ref. [213].

7.3.1 Optimally-tuned range-separated hybrids

The starting point of the range-separated hybrid (RSH) concept, which is couched within the GKS formalism [76, 91], consists of a partition of the Coulomb interaction as [258–260]

$$\frac{1}{r} = \frac{\alpha + \beta\,\mathrm{erf}(\gamma r)}{r} + \frac{1 - [\alpha + \beta\,\mathrm{erf}(\gamma r)]}{r} \tag{7.1}$$

Here r is the inter-electron coordinate, erf is the error function and α, β, and γ are parameters, which in principle may be freely chosen or determined empirically [258]. The two parts of the split Coulomb operator are treated differently

when computing the exchange interaction. While the first term is treated within Hartree-Fock (HF) theory, the second one is treated within a standard semi-local (sl) approximation [229]. The parameter γ is the so-called range-separation parameter. It controls which of the two terms dominates at a given range. It has been repeatedly shown that one uniform value for γ is not sufficient in every case, and that in fact γ can be strongly system- and size dependent [76, 93, 94, 235, 261]. Therefore, we prefer to determine it separately for each system by fulfilling a non-empirical condition. This is the point where the optimal-tuning comes into play: γ is chosen such that the difference between the energy of the HOMO level and the IP is minimized, i.e., we make use of the ionization-potential theorem [72, 73, 82, 226]. Practically, this is achieved by minimizing the following target function:[93]

$$J^2(\gamma;\alpha) = \sum_i [\epsilon^{\gamma,\alpha}_{H(N+i)} + IP^{\gamma,\alpha}(N+i)]^2. \tag{7.2}$$

Here the $\epsilon^{\gamma,\alpha}_{H(N+i)}$ are the HOMOs of the $(N+i)$ electron molecular systems and i is an integer number. The $\mathrm{IP}^{\gamma,\alpha}(N+i)$ are the corresponding ionization potentials, which are calculated from the total energy difference between the $N+i$ electron and the $N+i-1$ electron system. For the moment, α remains as a free parameter and the tuning is performed for each choice of α separately, yielding different optimal γ values that minimize $J^2(\gamma;\alpha)$. Including $i=0$ in the sum of Eq. (7.2) equalizes the HOMO of the neutral system with the IP, while for $i=1$ the IP of the anionic system, i.e., the electron affinity of the neutral system is considered, such that its difference from the HOMO eigenvalue of the anion is minimized [76]. By extension of the sum to negative values of i, states beneath the HOMO are also accounted for. This has been shown to assist in obtaining optimal tuning if the corresponding orbitals are strongly localized [237].

The remaining parameters α and β, appearing in Eq. (7.1), control the behavior of the Fock term at its limits. It tends to $\frac{\alpha}{r}$ when $r \to 0$ and to $\frac{\alpha+\beta}{r}$ when $r \to \infty$. The asymptotic behavior of the xc functional for $r \to \infty$ has been shown to be crucial for obtaining accurate gaps between the highest occupied molecular orbital (HOMO) and the lowest unoccupied molecular orbital (LUMO) and introduces a second constraint on the parameters. For an isolated molecule, the correct $\frac{1}{r}$ asymptotic behavior is thus achieved by enforcing $\alpha+\beta=1$ [262]. As a consequence, the semi-local contribution in the long range is set to zero and α now controls the amount of nonlocal Fock exchange in the short range. This can be seen in the expression for the exchange-correlation energy of the RSH functional, obtained with this constraint [237]

$$E_{xc} = (1-\alpha)E^{SR}_{sl,x} + \alpha E^{SR}_{HF,x} + E^{LR}_{HF,x} + E_{sl,c}, \tag{7.3}$$

where sl,x and sl,c denote semi-local exchange and correlation, respectively, and HF,x denotes non-local Fock exchange. When moving from an isolated molecule

to an organic crystal, the asymptotic behavior of the xc potential must take into account dielectric screening effects in the bulk. Thus for $r \to \infty$, the correct limit should be $\frac{1}{\varepsilon r}$, where ε is the scalar dielectric constant. This can be achieved by choosing α and β such that the condition $\alpha + \beta = \frac{1}{\varepsilon}$ is fulfilled. Note that a gas phase calculation may be seen as a special case of this constraint with ε being equal to one. For the case $\varepsilon \neq 1$, the expression for the exchange-correlation energy becomes

$$E_{xc} = (1 - \alpha)E_{sl,x}^{SR} + \alpha E_{HF,x}^{SR} + (1 - \frac{1}{\varepsilon})E_{sl,x}^{LR} + \frac{1}{\varepsilon}E_{HF,x}^{LR} + E_{sl,c}. \quad (7.4)$$

Comparing Eqs. (7.3) and (7.4), clearly the new condition affects only the LR part of the exchange correlation term, i.e., the LR parts get screened appropriately as β changes from $1-\alpha$ to $\frac{1}{\varepsilon}-\alpha$. With the constraints introduced so far, there is still no unique choice of α. Different methods based on first principles considerations have been suggested to overcome this deficiency. One of the methods is based on a further property of the exact KS potential, namely the piecewise linearity of the total energy with respect to the (fractional) particle number. For example in Refs. [259] and [237], α was chosen such that the curvature, and therefore the deviation from linearity, of the total energy versus particle number curve is minimized. According to Stein et al. [263], it may be possible to obtain the optimal α directly from minimization of the target function $J^2(\gamma;\alpha)$, because deviations from piecewise linearity and from the IP theorem are two sides of the same coin. For cases where this fails to indicate a unique optimal value of α, a more pragmatic approach which uses the good agreement of *shifted* PBE0 results with experiment has been suggested [238]. In that approach, α is determined so that the energy difference between the highest occupied delocalized state and the highest occupied localized state best correspond to a reference PBE0 calculation.

7.3.2 Computational details

All geometry optimizations have been performed using the PBE functional. In order to circumvent issues concerning van-der-Waals interactions, which are poorly described in standard GGA and hybrid functionals [45, 152, 264, 265], we employed the empirical correction scheme of Grimme [153] during the geometry optimization of the bulk structure. Note that we have taken lattice parameters from experiment [244, 245] and only optimized the internal degrees of freedom. The electronic structure of the isolated quinacridone molecule was obtained using QCHEM version 4.0 [266] with the cc-PVTZ basis set [267]. DFT solid-state calculations of the crystal β-phase were performed using the PARATEC plane wave package [268], modified to include the new SRSH functional [213].

Within PARATEC, GGA-based Troullier-Martins norm-conserving pseudopotentials [122] were employed [2] to represent the core electrons and nuclei. We used an energy cutoff of ≈ 800 eV, and a Monkhorst-Pack grid of $3 \times 3 \times 2k$ points [149].

Perturbative G_0W_0 results, including the DFT results that serve as their starting point, were obtained using the VASP package [146, 147, 269], with both the PBE [66] and the HSE [88] functionals. The projector augmented wave (PAW) [148] approach was employed for treatment of the core electrons, allowing for a relatively low kinetic energy cut-off of about 400 eV. The same $3 \times 3 \times 2$ k Monkhorst-Pack grid employed above was used.

G_0W_0 calculations were performed with full-frequency integration, using 48 frequency grid points and approximately 4000 unoccupied states to obtain the dielectric function and the self-energy. The scalar dielectric constant was determined as $\frac{1}{3}$ of the trace of the dielectric tensor obtained within the random phase approximation, including local field effects [270].

7.4 Results and Discussion

7.4.1 Gas phase of quinacridone

In this section, we present theoretical results for an isolated 5Q molecule, in order to characterize its electronic structure and frontier orbitals. Importantly, these calculations are crucial for obtaining the optimal α and γ parameters, used in subsequent bulk calculations. The optimal-tuning process, following Eq. (7.2), has been determined using both $i = 0, 1$ and $i = -1, 0, 1$. Both calculations yielded similar results for the optimized values of γ, which deviated from each other by no more than 0.004 bohr^{-1}. All results given here are the results of the $i = 0, 1$ tuning.

Figure 7.3(a) shows the eigenvalue spectra of an isolated 5Q molecule calculated with various xc functionals: PBE, PBE0, and OT-RSH results with different values for the parameter α. For each value of α and the corresponding $\beta = 1 - \alpha$, the range-separation parameter γ has been optimized separately. The PBE calculation results in a HOMO (red) value of 5.0 eV and a HOMO-LUMO (blue) gap of only 1.8 eV. The former is too low, by more than 2 eV, compared to the gas phase UPS IP value of 7.23 eV (shown as a red dotted line in Fig. 7.3) [271]. In the PBE0 calculation, in which 25% of non-local Fock exchange is included, the HOMO level is 5.8 eV, still showing a large underestimation of the experimental reference, and the band gap increases to 3.3 eV.

[2] FHI-type pseudopotentials were adapted from the ABINIT website, http://www.abinit.org/downloads/psp-links/psp-links/gga_fhi, with core radii (in a.u.) of 1.276 for H, 1.498 for C, 1.399 for O, and 1.416 for N

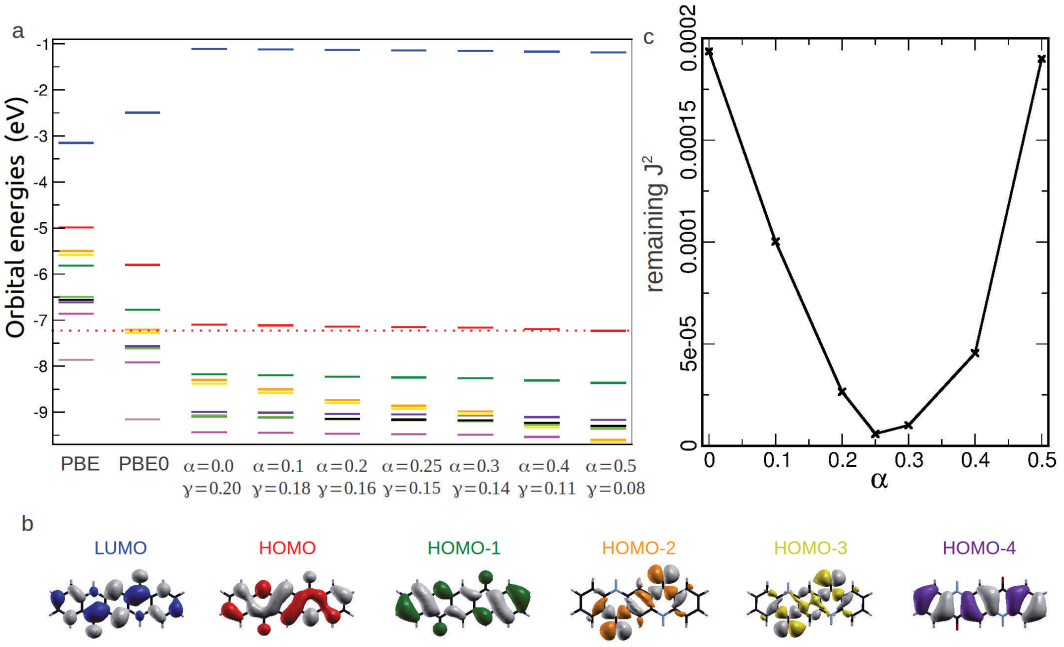

Figure 7.3: (a) DFT eigenvalue spectra of an isolated 5Q molecule, calculated with PBE, PBE0, and OT-RSH for for various values of the SR Fock-exchange parameter α. For each choice of α, the optimal range-separation parameter γ (in bohr^{-}1) is also denoted. The same color represents the same orbital in the different calculations. The red-dotted line denotes the experimental gas-phase UPS result for the IP.[271] (b) Images of the orbitals in the same color code, with the ordering resulting from the OT-RSH calculations with $\alpha = 0.25$. (c) Deviation from optimal tuning, $J^2(\gamma;\alpha)$ as a function of α, using the optimal value for γ in each case.

Next we consider the 5Q HOMO and LUMO values obtained with the OT-RSH approach. We have varied α from 0.0 to 0.5 in steps of 0.1 and optimized γ for each α value. We observe that the HOMO value is improved to $\sim$ 7.15 eV, which slightly increases for increasing α (within $\pm$ 0.05 eV), in excellent agreement with the experimental value of 7.23 [271]. The HOMO-LUMO gap is increased to approximately 6.1 eV, and is only slightly ($\pm$ 0.05 eV) affected by the choice of the parameter α.

Turning to the outer-valence spectra, PBE yields an orbital ordering of the lower-lying occupied states that is different from that of all other calculations. In particular, the states shown as orange and yellow lines in Fig. 7.3, i.e., the HOMO-1 and HOMO-2 of the PBE calculation, are located at higher energies relative to all other orbitals. The PBE0 results show a change in the eigenvalue spectra, along with energy-level "stretching". In our OT-RSH results, the orbital ordering is parameter dependent: All orbitals with π symmetry (which clearly exhibit a similar degree of delocalization) show only little sensitivity to α. In contrast, the

σ orbitals (HOMO-1 and HOMO-2 of the PBE calculation) are strongly affected and are shifted downwards by more than 1 eV when α changes from 0.0 to 0.5. This is not surprising: Similar observations were made by Refaely-Abramson et al. [237] and confirmed in additional studies [238, 272, 273].

In order to provide an explanation for the origin of this behavior, orbital plots of the five highest-occupied orbitals, as well as the LUMO, are shown in Fig. 7.3(b). Note that the color code for the isosurfaces is the same one used in the level diagrams of Fig. 7.3(a). Comparing the shape of all orbitals in the probed energy range, one recognizes the σ symmetry and the higher degree of localization of the two orbitals mentioned above. Building on experience with other organic molecules [80, 92, 143, 156, 237, 239, 274–276], the reason for the different orbital energies and ordering between PBE and hybrid calculations is assigned to their different self interaction error (SIE). It should also be noted that these two σ orbitals are the main difference between 5Q and pentacene, which has no σ orbitals in the energy range of 5 eV below the HOMO [80, 92, 277]. It has been previously shown[156] that all outer-valence frontier orbitals of pentacene exhibit similar SIE, and therefore orbital ordering in pentacene is less sensitive to the choice of the xc functional.

Finally, we also observe that the optimized γ parameter decreases with increasing amount of short-range Fock exchange. This can be rationalized by the range $\frac{1}{\gamma}$ at which full Fock exchange sets in, which can be extended to larger distances if the amount of Fock exchange at SR, governed by α, is increased [237, 238, 272]. Figure 7.3(c) shows the minimal J^2, obtained for the optimized γ value for each α, as a function of α. The curve shows a distinct minimum of $J^2(\gamma;\alpha)$ for α values between 0.2 and 0.3 (note the scale bar). It was shown [238, 263] that there is a rigorous quantitative equality between deviations from piecewise linearity and deviations from the IP theorem, represented by J^2. We therefore chose the α value of 0.25, that minimizes J^2, to study the electronic structure of the bulk. This optimal value remains unchanged when including $i = -1, 0, 1$ in the γ tuning, or when comparing the energy difference between localized and delocalized states with PBE0 [238], as discussed above.

7.4.2 Solid β-phase of quinacridone

We now turn our attention to 5Q in the solid β-phase. According to Eq. (7.4), the scalar dielectric constant ε governs the asymptotic behavior of the xc potential. For organic molecular crystals, the short-range interactions are mainly governed by the molecule properties. We therefore take $\alpha = 0.25$ and the optimized $\gamma = 0.15\text{bohr}^{-}1$, as obtained from the above-discussed OT-RSH calculation for the isolated molecule. We take ε to be 3.5, a value obtained from RPA calculations based on PBE eigenvalues, because it is already available as a by-product of our G_0W_0 results. Note, however, that it could easily be taken from computationally

inexpensive approaches [278–282], and that this, in fact, is the recommended procedure if a comparison with GW is not performed.

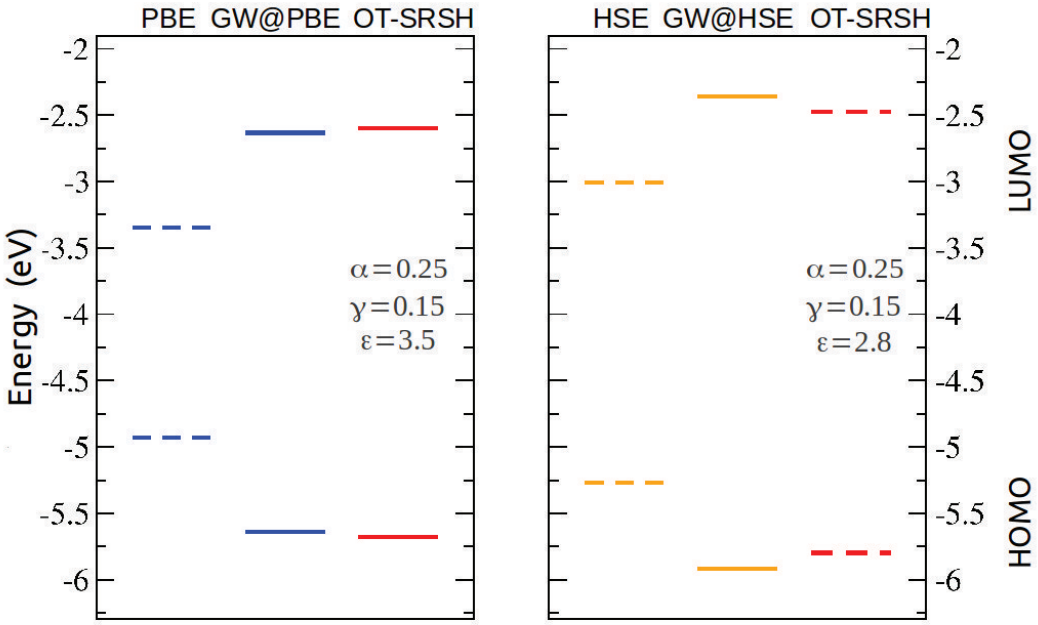

Figure 7.4: Band gaps of the 5Q β-crystalline structure obtained from different calculations. The peak maxima of the HOMO and LUMO derived bands in the corresponding density of states curves are shown as horizontal lines. In each case, the middle of the band gap is aligned with that of the computed gas-phase HOMO-LUMO gap.

The results of the various DFT and GW calculations for the band-gap are summarized in Fig. 7.4. Note that due to the crystal structure exhibiting two molecules per unit cell, each molecular state splits into two bands in the crystal. In Fig. 7.4 we have defined the band gap as the peak-to-peak energy difference derived from the computed density of states. Also note that in the bulk calculation the absolute energy position of the highest-occupied and lowest-unoccupied levels are ill-defined, due to the lack of a reference vacuum energy. Therefore, we have aligned the center of the band gaps with those of the corresponding gas phase calculations. It must also be noted that, strictly speaking, a comparison of the computed "bulk" IPs and EAs with experimental values determined from thin films is problematic due to surface effects not being accounted for in the calculation [243, 283].

When comparing the values for the fundamental gaps we find that, as expected, the PBE gap of about 1.6 eV is much smaller than those obtained with all other approaches. More importantly, it is also approximately unchanged compared to the isolated molecule, because no effects arising from the polarization of the

environment are accounted for with the PBE xc functional [213, 242]. When computing G_0W_0 corrections to the PBE eigenvalues (GW@PBE), the gap increases to 3 eV. Note that polarization effects are inherently taken into account in these results as they are contained in the self-energy expression, leading to a considerably smaller gap than for the isolated molecule [242]. With our OT-SRSH calculation, we obtained a band gap of 3.1 eV, which is essentially the same as for GW@PBE. Thus the bulk band gap is roughly halved, compared to the corresponding calculation of the HOMO-LUMO gap in the isolated molecule.

While for the isolated molecule the choice of α barely influences the band gap, for the bulk we observe a slightly different behavior. When reducing α from 0.25 to 0.0 with the optimally-tuned value of γ for each α, but keeping $\varepsilon = 3.5$ unchanged, we observe a 0.3 eV reduction of the band gap. This finding can be explained by considering Eq. (7.4). When reducing α, the optimized γ increases. In other words, when decreasing the amount of SR Fock exchange, the amount of LR Fock exchange increases to maintain the amount of overall non-local exchange. As a consequence, the spatial LR region in which the effective dielectric screening acts extends, thereby enhancing polarization effects and leading to a smaller band gap.

Now we compare the PBE results with those based on a HSE calculation. HSE yields a band gap of 2.3 eV, which lies between the pure PBE and the corresponding OT-SRSH result. In order to provide an explanation, recall the properties of the HSE functional. As already mentioned, it is a SR hybrid functional using non-local exchange only in the SR and pure semi-local exchange in the LR. The amount of Fock exchange is given by $\alpha = 0.25$ and a universal γ value of 0.11 bohr^{-}1 is used. Thus, the result is improved over PBE as some non-local exchange is introduced. However, because the xc potential decays exponentially, i.e., $\varepsilon = \infty$ in Eq. (7.4), the asymptotic behavior is incorrect and a smaller band gap than in the OT-SRSH calculation is obtained [213, 284]. Compared to PBE, the increased HSE band gap results in the fact that a subsequent RPA calculation yields a decreased scalar dielectric constant of $\varepsilon = 2.8$. When using this value in the OT-SRSH calculation, we obtain a band gap of 3.3 eV, which is larger compared to the OT-SRSH band gap achieved using the PBE-based RPA ε due to the reduced screening with the smaller HSE-based ε. Again the band gap compares well with a G_0W_0 computation with an HSE starting point (GW@HSE), which yields a band gap of 3.5 eV. The SRSH gaps are then indeed consistent with the GW calculation, given a similar scalar dielectric constant.

Next, we investigate the valence band electronic density of states of the crystal, calculated at various levels of DFT and G_0W_0, in more detail. These are compared with experimental ARUPS results. The results are summarized in Fig. 7.5. Note that both experimental and calculated spectra have the energy axis shifted such that the highest occupied peak maximum has been aligned to zero. A Gaussian broadening of 0.2 eV was used in all computed spectra.

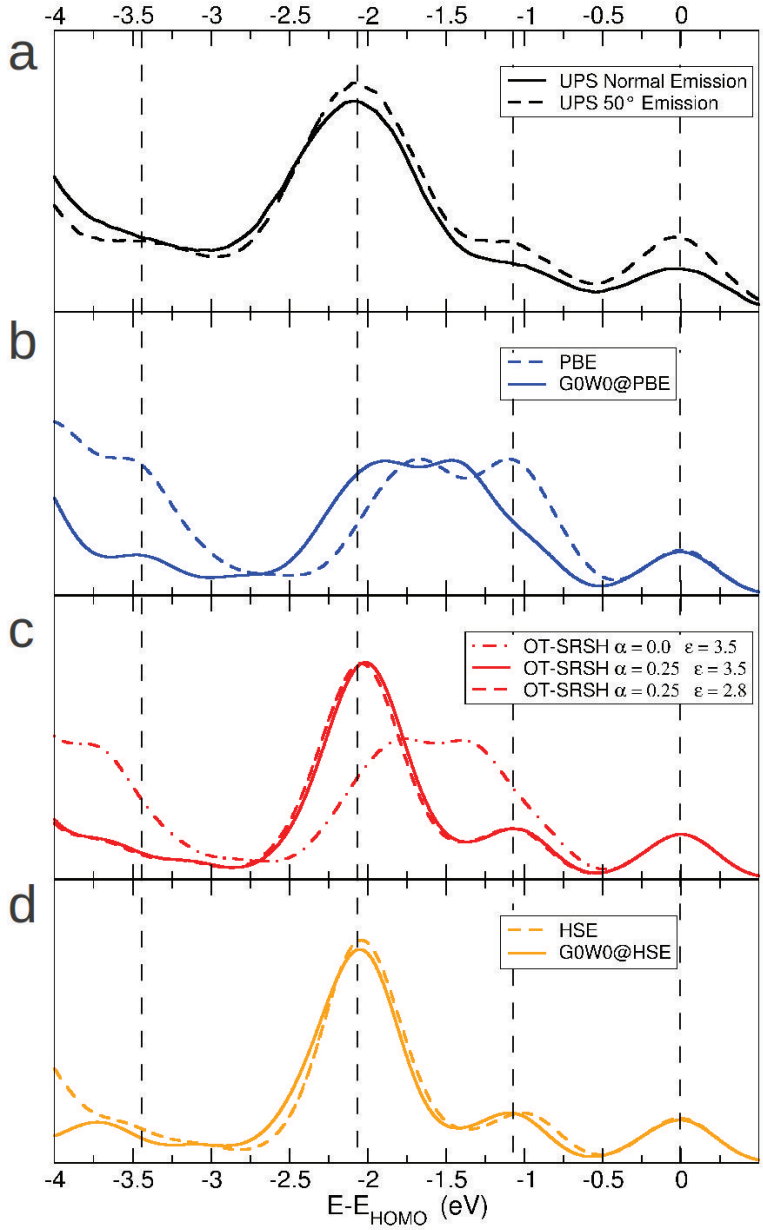

Figure 7.5: Comparison of experimental and theoretical photoemission spectra for the β-phase crystalline structure of 5Q. (a) Experimental UPS data in normal- and 50° emission (black solid and dashed lines, respectively). (b) Computed results of PBE and GW@PBE (blue dashed and solid lines,respectively). (c) Computed results of OT-SRSH approach with $\alpha = 0.0$ and $\alpha = 0.2$ (red dashed and solid lines, respectively). (d) Computed results of HSE and GW@HSE (orange dashed and solid line, respectively). For all spectra shown the energy axis has been aligned with the maximum of the highest occupied peak, which has been set to zero. A Gaussian broadening of 0.2 eV was used in all computed spectra.

In the experimental spectra, there are four peaks in the shown energy range, which are highlighted by vertical dashed black lines. The first peak coincides with 0 eV, by virtue of the alignment procedure. The other peaks are located at -1.1, -2.0 and -3.4 eV. For further interpretation of the experimental findings and for gaining more insight into the origin of individual peaks, we compare the peak positions and spectral shape of the experimental data to the theoretical results. In Fig. 7.5(b), we display the PBE result (blue, dashed line) and the corresponding GW@PBE calculation (blue, solid line). At first sight, agreement between the PBE result and experiment appears reasonable because the peak positions seemingly agree quite well. However, when taking into account the peak shape as well, this agreement turns out to be coincidental. As in the case of the isolated molecule, PBE provides the wrong orbital energies and ordering, particularly for the localized states of σ symmetry. The GW@PBE results certainly improve the band gap, as shown in Fig. 7.4, and also somewhat stretch the valence band spectrum. However, judging by the comparison with the experimental data, the GW@PBE result does not seem to accurately describe the investigated system. The main deviation of the GW@PBE curve is its peak at -1.4 eV, which does not show up in the experimental data at all.

In order to clarify this deficiency of the GW@PBE result, we compute the valence band DOS resulting from the OT-SRSH approach using $\alpha = 0.25$, shown as a red solid line in Fig. 7.5(c). From the previous findings for the isolated 5Q molecule, as well as similar molecules [237], we know that the amount of SR Fock exchange mainly affects states with a distinct degree of localization. Such behavior is also expected for the bulk. Therefore, Fig. 7.5(c) shows in addition the DOS obtained from an OT-SRSH calculation with $\alpha = 0.0$ as a red dash-dotted line. Indeed the two mentioned spectra in Fig. 7.5(c) are dramatically different, although only little influence of α on the size of the band gap was observed for the molecule (Fig. 7.3) and the molecular crystal, as discussed above. Interestingly, the $\alpha = 0$ curve resembles the GW@PBE result, including a peak at about -1.4 eV, while the $\alpha = 0.25$ spectrum has no peak at that energy, and the corresponding states are shifted to lower energies. This enhances the peak at -2 eV and leads to a rather impressive agreement with the experimental data. Thus, the origin of the incorrect peak at -1.4 eV in the GW@PBE and the OT-SRSH with $\alpha = 0$ is related to a remaining SIE of the strongly localized σ states (depicted in yellow and orange in Fig. 7.3), resulting in calculated energy levels that are too high for these states and changing the overall spectral shape. This is confirmed by plots of the orbital density associated with these states. In Fig. 7.6, a density plot of the HOMO-3 orbital of the isolated molecule obtained from OT-RSH with $\alpha = 0.25$, as well as the partial charge-density of the corresponding orbital in the solid-state, is shown.[3] The extended bulk-state can be clearly associated with

[3]Note that in the solid state the orbital ordering of states close in energy is dependent on a particular k-point, due to the band dispersion.

the respective orbital of the isolated molecule and the same is true for all other outer valence states (not shown for brevity).

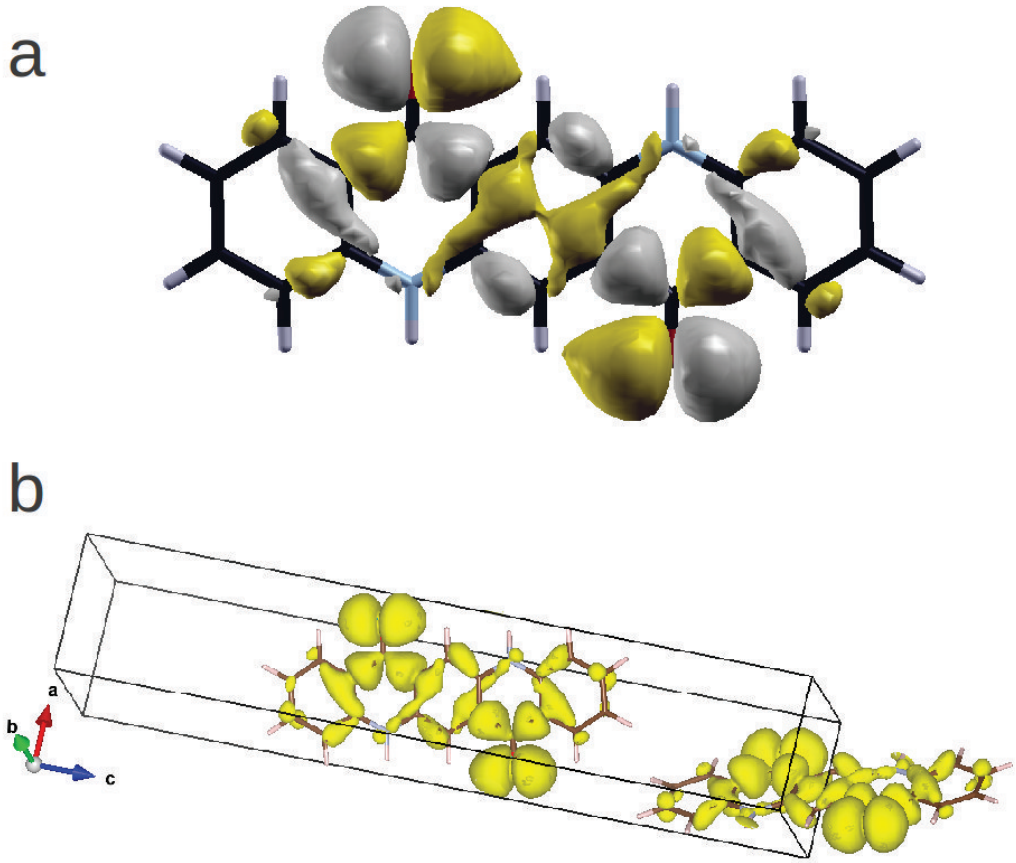

Figure 7.6: (a) Density plot of the HOMO-3 orbital obtained from the OT-RSH calculation of the isolated molecule. (b) Partial charge density decomposed on the band derived from the orbital shown in (a).

Finally, we compare these results with those based on a HSE calculation. The spectra of the HSE and the corresponding GW@HSE calculation are shown in Fig. 7.5(d) as orange dashed and solid lines, respectively. Moreover, the OT-SRSH spectra with $\alpha = 0.25$ and using $\varepsilon = 2.8$ from the HSE-based RPA calculation is displayed in Fig. 7.5(c) as a red dashed line. Clearly the two OT-SRSH calculations with $\alpha = 0.25$ coincide, up to a very small deviation. This observation shows that the screening introduced in Eq. (7.4) affects all occupied states similarly and shifts the whole spectrum rigidly, thereby changing the computed band gap appropriately. Namely, while the ε value greatly affects the gap renormalization (as it is the measure of electrostatic polarization), the shifted

occupied spectra is almost entirely dependent on the values of α and γ, and is practically the same for the two examined values of ε. The line shape of the outer-valence band spectrum of the HSE calculation is in good agreement with experiment and OT-SRSH calculations ($\alpha = 0.25$). The G_0W_0 calculation with the HSE starting point shift the HSE spectrum rigidly and we find an almost perfect agreement with the experiment. Furthermore, it becomes obvious that the full-frequency GW@PBE calculation suffers from the inappropriate starting point, as already reported in a number of studies of the organic and metal-organic molecule [101, 285, 286].

Having found the theoretical methods which yield an accurate description of the electronic structure of the organic molecular crystal, we are able to assign specific molecular states to the experimentally observed peaks [a band-decomposed charge-density plot of one of these states was given in Fig. 7.6(b)]. In Fig. 7.7 we follow such plots to assign molecular orbitals to the appropriate peak in the OT-SRSH functional calculation with $\alpha = 0.25$. This optimal fraction of SR Fock exchange allows a simultaneous prediction of both σ-type localized orbitals (yellow and orange in Fig. 7.7) and π-type delocalized orbitals (other orbitals in Fig. 7.7), as discussed above. By that, it allows the assignment of theoretical orbitals to peaks of the experimental UPS data, as shown in Fig. 7.7.

7.5 Conclusion

In conclusion, we have studied the electronic structure of the organic molecule quinacridone in the gas phase and in the crystalline β-phase. For the gas phase, we find that the semilocal PBE and the hybrid PBE0 functional both underestimate the ionization potential and the fundamental band gap. When employing an optimally-tuned range separated hybrid functional, we obtain an excellent agreement with the experimental UPS value for the ionization potential and a larger fundamental gap, which is insensitive to the fraction α of short-range Fock exchange. The latter parameter, on the other hand, is shown to be crucial for attaining the correct relative orbital ordering of delocalized versus localized orbitals.

For the crystalline bulk β-phase of quinacridone, we have conducted angle-resolved photoemission experiments, which were used to benchmark our calculations. We demonstrate that by using the optimally-tuned value for the fraction of short-range exchange ($\alpha = 0.25$), the correct orbital ordering was obtained within the occupied manifold of the states. We further showed that in order to take into account the level renormalization due to electronic polarization in the crystalline phase, the appropriate asymptotic behavior of the exchange-correlation functional is essential. This has been achieved by employing the optimally-tuned *screened* range-separated hybrid (OT-SRSH) approach, in which the screening is

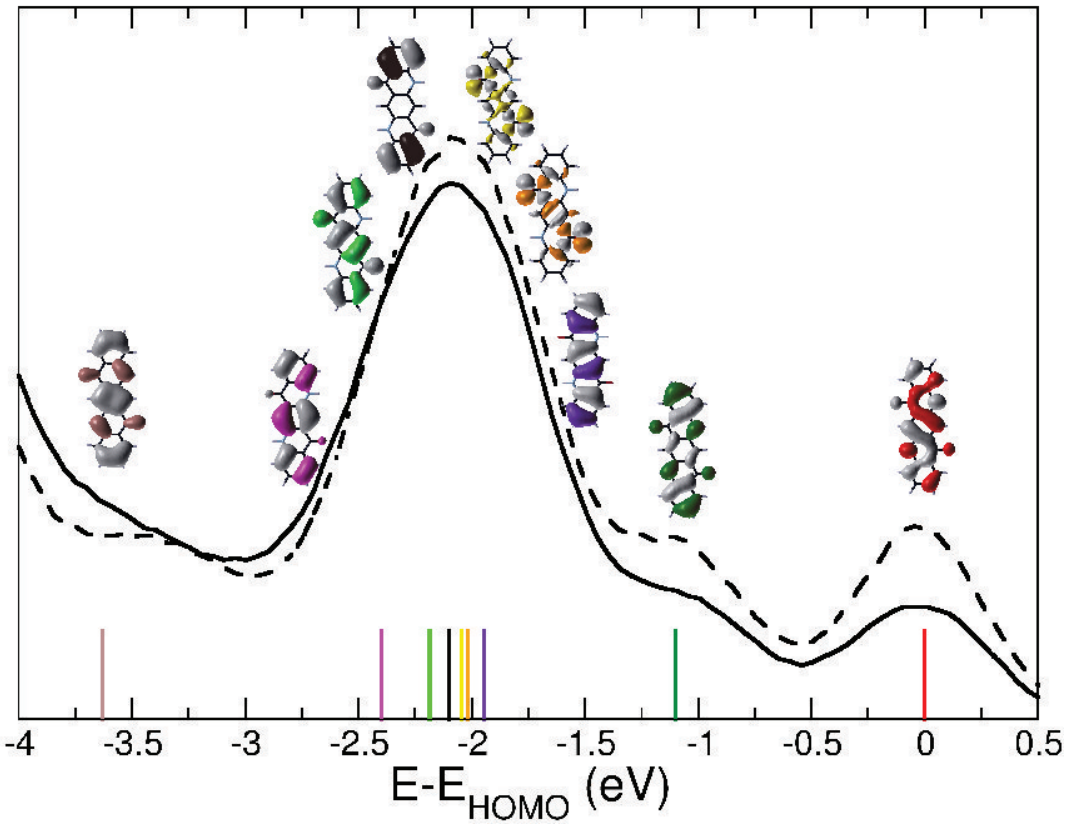

Figure 7.7: Measured (normal and 50°) photoemission spectra for the β-crystalline structure of 5Q, including density plots of the contributing molecular states, as well as the energy ordering shown as vertical lines, obtained using the OT-SRSH functional with $\alpha = 0.25$, $\gamma = 0.15\text{bohr}^{-}1$ and $\varepsilon = 2.8$.

accounted for by an effective dielectric constant, ε, which we computed from the macroscopic dielectric tensor obtained within the random phase approximation. Thus, the description of the unoccupied manifold of the states, in particular the fundamental gap, is also greatly improved, showing a band gap renormalization from the gas phase to the bulk based on physical grounds. For comparison, we computed the G_0W_0 corrected electronic structure of the bulk using both PBE-GGA and the short-range hybrid functional HSE. These results emphasize the importance of the starting point in this perturbative approach, where the G_0W_0@HSE essentially agree with the OT-SRSH approach.

In summary, our work shows that the reliability of the optimal-tuning approach for molecular systems can be extended to the valence spectrum of molecular solid systems and that results at a level of accuracy comparable with GW calculations can be achieved. We emphasize that, based on physically motivated choices for

the parameters, the OT-SRSH approach allows for an accurate description of the band gap and at the same time of the relative orbital energies of the outer valence spectrum without any empiricism. Therefore, it may serve as a computationally inexpensive and reliable tool.

Acknowledgements

D.L. and P.P. acknowledge support from the Austrian Science Fund (FWF) project P23190-N16. We thank Eric Glowacki from the Institute for Oragnic Solar Cells (LIOS), Johannes Kepler University Linz for pointing out the interesting device properties of 5Q and supplying the molecule. D.L. acknowledges the hospitality of the Weizmann Institute of Science. S.R.A. is supported by an Adams fellowship of the Israel Academy of Sciences and Humanities. L.K. acknowledges support by the European Research Council, the Israel Science Foundation, the Germany-Israel Foundation, the Wolfson Foundation, the Hemlsley Foundation, and the Lise Meitner Minerva Center for Computational Chemistry.

Chapter 8

Conclusions

Here, we summarize the main results of the many aspects of this work, draw some general conclusions and discuss some questions that have arisen. We have successfully applied the orbital tomography approach in different situations and thereby pushed it to its limits within the plane wave final state approximation.

Prior to this work one of the open questions was whether it is possible to obtain from ARPES data images of orbitals of molecules that have the size of pentacene or PTCDA, in two dimensions. Indeed, we were successful doing so, which is a major achievement of this work and the topic of Chapter 3. With the only assumption of a confinement of the wave function to a region, which is defined by the size of the molecule, we have successfully adapted a phase recovery procedure, originally developed for x-ray diffraction results of laterally confined objects, to two dimensional ARPES momentum maps. With this procedure the experimentally lost phase information of five individual molecular orbitals has been recovered and two dimensional orbital images obtained with this information are in excellent agreement with the corresponding one electron orbitals of DFT. Open questions on this topic, for instance, concern the applicability of the phase recovery procedure to orbitals with a lower symmetry than pentacene and PTCDA. A possible candidate would for instance be quinacridone. Furthermore, the phase information obtained with the method presented could be combined with a series of ARPES experiments at varying photon energies in order to measure the full three dimensional orbital. With such energy dependent experiments also the phase recovery of the full three dimensional orbital, which uses the three dimensional measured photoemission intensity as an input, seems possible.

In Chapter 4 we have successfully applied the orbital tomography method to determine the azimuthal orientation of CuPc on a Au(110) surface. We have used emission maps which have been clearly associated to the molecule's HOMO. The so obtained structure has been validated by DFT calculations employing van-der-Waals corrections. In addition, the electronic structure of the full interface has

been calculated using a hybrid functional, which significantly improved the orbital energies of the Cu-localized σ states over those, obtained with a GGA functional. These findings show the potential of the OT approach as a complementary tool for characterizing the structural and electronic properties of organic/metallic interfaces.

Chapter 5 dealt with the heteromolecular interface of PTCDA and CuPc on Ag(111). Several experimental techniques together with extensive DFT calculations revealed a rather unexpected behavior of the two molecules on this surface. Compared to the homomolecular phase, the LUMO of CuPc is emptied in the mixed phase while the molecule moves closer to the surface, while PTCDA shows the opposite behavior. With a detailed and careful analysis of the charge rearrangements upon co-adsorption we could shed some light into the complex interplay of bonding height and energy level alignment. Such a study is not only interesting from a fundamental point of view, such hetereomolecular interfaces also may have the potential of tuning the electronic or optical properties of the interface using a mixture of different molecules.

Another major intention of this work was the expansion of the theoretical part of orbital tomography to extended systems. We have implemented such an extension an applied it in Chapter 6. There, it has been used to explain details in the momentum maps of pentacene on Cu(110), which could be addressed to intermolecular dispersion. Furthermore, with this generalization of the theoretical approach, emission contributions from the substrate could be taken into account. Thereby, our results suggest, that the extended systems has to be taken into account in the theoretical evaluation, if one aims to understand details in the angle-dependent photoemission intensity patterns and to go beyond a simple association of peaks to individual orbitals or the molecule's azimuthal alignment.

Finally, in Chapter 7 we have obtained orbital energies of a molecular crystal within DFT, that are in excellent agreement with experimentally observed energy distribution curves. This exciting finding has been achieved with a rather new type of exchange-correlation functional which uses physically motivated, optimally-tuned parameters in a screened range-separated hybrid functional. Not only, as already has been demonstrated, the band gap of the systems are in excellent agreement with quasiparticle energies obtained using the GW formalism, also the orbital energies- and ordering of a mixture of localized an delocalized states are described correctly, in agreement with experiment. As an additional result we could provide a reliable electronic structure of the organic molecule quinacridone in its isolated form and in its β-crystal structure.

Altogether, this work has proven the usefulness of the orbital tomography method in many different aspects and shed some light into the physics of the organic/metallic interface. Some of the initial questions could be answered but also new questions, like the limits of the phase recovery procedure, turned up. We have contributed to the interesting field of wave function imaging and for the

first time, experimentally determined images of orbitals, including the phase, of molecules that are relevant for organic devices, could be obtained. In future, with the help of time resolved, high quality ARPES measurements it may become possible to monitor the orbital during a chemical reaction. Even without such speculative experiments, orbital tomography has been shown to be an useful tool and may for instance be simply applied to study further metal/organic interfaces, and thereby approach the limits of the method in terms of size, constituents or internal geometry of the studied molecules. Here, the expansion to extended systems may become essential and a combination of this method with more accurate functionals like the optimally-tuned screened range-separated hybrid functional is a possible strategy for future studies.

Acknowledgements

First of all I want to thank my supervisor Peter Puschnig for his continuous support throughout the time of my PhD. He always had time to answer my questions regarding either scientific or technical issues. He gave me the possibility to do a research visit in Israel and to attend various scientific conferences and finally he enabled this thesis by providing the necessary funding.

I am grateful to my colleagues at the surface science group in Graz. Especially I want to mention Michael G. Ramsey, Thomas Ules and Georg Koller for sharing their experimental data and knowledge, for numerous scientific discussions on various topics and in general for the nice collaboration during the last years.

I also want to thank my colleagues from Jülich: Stefan Tautz, Benjamin Stadtmüller, Martin Willenbockel and Simon Weiß for the nice collaboration and many fruitful discussions in Graz or at different conferences. I am grateful to Stefan Tautz for being the reviewer of this thesis.

I am thankful to Leeor Kronik and the members of his group at the Weizmann Institute of Science for the hospitality I encountered and the enjoyable time in Rehovot. Especially I want to thank Leeor for the possibility to stay at his group and his financial support and Sivan Refaely-Abramson for introducing me to the optimally-tuned range-separated hybrid functionals.

I want to express my gratitude to all further co-authors that contributed to the publications presented in this thesis.

Last but not least I want to thank my family for the steady support throughout all the years of my studies.

List of Figures

List of Tables

List of Abbreviations

5A pentacene

5Q quinacridone

ARPES angle resolved photoemission spectroscopy

BD bond dipole

CBE constant binding energy

CuPc copper-II-phthalocyanine

DD derivative discontinuity

DFT density functional theory

DOS density of states

EA electron affinity

FT Fourier Transform

GGA generalized gradient approximation

GKS generalized Kohn-Sham

HF Hartree-Fock

HOMO highest occupied molecular orbital

HSE Heyd-Scuseria-Ernzerhof hybrid functional

IAC independent atomic center

IP ionization potential

KS Kohn-Sham

LDA local density approximation

LEED low energy electron diffraction

LR long range

LUMO lowest unoccupied molecular orbital

MBW mixed brick-wall

NIXSW normal incidence x-ray standing wave

OT orbital tomography

OT-RSH optimally-tuned range-separated hybrid functional

OT-SRSH optimally tuned screened range-separated hybrid

PBE Perdew-Burke-Ernzerhof

PTCDA 3,4,9,10-perylene tetracarboxylic dianhydride

PW plane wave

RPA random phase approximation

SIE self interaction error

SR short range

STM scanning tunneling microscopy

STS scanning tunneling spectroscopy

UPS ultraviolet photoemission spectroscopy

vdW van der Waals

xc exchange-correlation

Bibliography

[1] Yang Yang and Fred Wudl. Organic electronics: From materials to devices. *Advanced Materials*, 21(14-15):1401–1403, 2009.

[2] D. D. Eley. Phthalocyanines as semiconductors. *Nature*, 162:819, 1948.

[3] C. K. Chiang, C. R. Fincher, Y. W. Park, A. J. Heeger, H. Shirakawa, E. J. Louis, S. C. Gau, and Alan G. MacDiarmid. Electrical conductivity in doped polyacetylene. *Phys. Rev. Lett.*, 39:1098, 1977.

[4] C. W. Tang. Two-layer organic photovoltaic cell. *Appl. Phys. Lett.*, 48:183, 1986.

[5] C. W. Tang and S. A. VanSlyke. Organic electroluminescent diodes. *Appl. Phys. Lett.*, 51:913, 1987.

[6] C. W. Tang, S. A. VanSlyke, and C. H. Chen. Electroluminescence of doped organic thin films. *Journal of Applied Physics*, 65(9):3610–3616, 1989.

[7] J. H. Burroughes, D. D. C. Bradley, A. R. Brown, R. N. Marks, K. Mackay, R. H. Friend, P. L. Burn, A. Kraft, and A. B. Holmes. Light-emitting diodes based on conjugated polymers. *Nature*, 347:539, 1990.

[8] J. H. Burroughes, C. A. Jones, and R. H. Friend. New semiconductor device physics in polymer diodes and transistors. *Nature*, 355:137, 1988.

[9] G. Horowitz, D. Fichou, X. Z. Peng, Z. Xu, and F. Garnier. A field-effect transistor based on conjugated alpha-sexithienyl. *Solid State Commun.*, 72:381, 1989.

[10] Hagen Klauk, editor. *Organic Electronics: Materials, Manufacturing and Applications*. Wiley-VCH, Weinheim, 2006.

[11] Hagen Klauk, editor. *Organic electronics II: more materials and applications*, volume 2. John Wiley & Sons, 2012.

[12] H. Yan, Z. Chen, Y. Zheng, C. Newman, J. R. Quinn, F. Dötz, Kastler. M., and A. Facchetti. A high-mobility electron-transporting polymer for printed transistors. *Nature*, 457:679, 2009.

[13] Chengliang Wang, Huanli Dong, Wenping Hu, Yunqi Liu, and Daoben Zhu. Semiconducting -conjugated systems in field-effect transistors: A material odyssey of organic electronics. *Chem. Rev.*, 112(4):2208–2267, 2012.

[14] Aswani Yella, Hsuan-Wei Lee, Hoi Nok Tsao, Chenyi Yi, Aravind Kumar Chandiran, Md.Khaja Nazeeruddin, Eric Wei-Guang Diau, Chen-Yu Yeh, Shaik M Zakeeruddin, and Michael Grtzel. Porphyrin-Sensitized Solar Cells with Cobalt (II/III)Based Redox Electrolyte Exceed 12 Percent Efficiency. *Science*, 334(6056):629–634, 2011.

[15] J. You, L. Dou, K. Yoshimura, T. Kato, K. Ohya, T. Moriarty, K. Emery, C.-C. Chen, J. Gao, G. Li, and Y. Yang. A polymer tandem solar cell with 10.6% power conversion efficiency. *Nat. Commun.*, 4:1446, 2013.

[16] Jiaoyan Zhou, Yi Zuo, Xiangjian Wan, Guankui Long, Qian Zhang, Wang Ni, Yongsheng Liu, Zhi Li, Guangrui He, Chenxi Li, Bin Kan, Miaomiao Li, and Yongsheng Chen. Solution-processed and high-performance organic solar cells using small molecules with a benzodithiophene unit. *J. Am. Chem. Soc.*, 135(23):8484–8487, 2013.

[17] T.-H. Han, Y. Lee, M.-R. Choi, S.-H. Woo, S.-H. Bae, B.H. Hong, J.-H. Ahn, and T.-W. Lee. Extremely efficient flexible organic light-emitting diodes with modified graphene anode. *Nat. Photon.*, 6(2):105–110, 2012.

[18] Hisahiro Sasabe and Junji Kido. Development of high performance OLEDs for general lighting. *J. Mater. Chem. C*, 1:1699–1707, 2013.

[19] Kang-Jun Baeg, Maddalena Binda, Dario Natali, Mario Caironi, and Yong-Young Noh. Organic light detectors: Photodiodes and phototransistors. *Advanced Materials*, 25(31):4267–4295, 2013.

[20] Stefan Hüfner. *Photoelectron Spectroscopy*. Springer, Berlin, 2003.

[21] J. Ziroff, F. Forster, A. Schöll, P. Puschnig, and F. Reinert. Hybridization of organic molecular orbitals with substrate states at interfaces: PTCDA on silver. *Phys. Rev. Lett.*, 104(23):233004, Jun 2010.

[22] P. Puschnig, E.-M. Reinisch, T. Ules, G. Koller, S. Soubatch, M. Ostler, L. Romaner, F. S. Tautz, C. Ambrosch-Draxl, and M. G. Ramsey. Orbital tomography: Deconvoluting photoemission spectra of organic molecules. *Phys. Rev. B*, 84:235427, 2011.

[23] P. J. Feibelman and D. E. Eastman. Photoemission spectroscopy - correspondence between quantum theory and experimental phenomenology. *Phys. Rev. B*, 10:4932, 1974.

[24] J. W. Gadzuk. Surface molecules and chemisorption. II. Photoemission angular distributions. *Phys. Rev. B*, 10:5030–5044, 1974.

[25] A. Mugarza, J. E. Ortega, F. J. Himpsel, and F. J. García de Abajo. Measurement of electron wave functions and confining potentials via photoemission. *Phys. Rev. B*, 67(8):081404, Feb 2003.

[26] Peter Puschnig, Stephen Berkebile, Alexander J. Fleming, Georg Koller, Konstantin Emtsev, Thomas Seyller, John D. Riley, Claudia Ambrosch-Draxl, Falko P. Netzer, and Michael G. Ramsey. Reconstruction of molecular orbital densities from photoemission data. *Science*, 326:702–706, 2009.

[27] S. Kera, S. Tanaka, H. Yamane, D. Yoshimura, K.K. Okudaira, K. Seki, and N. Ueno. Quantitative analysis of photoelectron angular distribution of single-domain organic monolayer film: NTCDA on GeS(001). *Chem. Phys.*, 325:113–120, 2006.

[28] M. Wießner, N.S. Rodriguez-Lastra, J. Ziroff, F. Forster, P. Puschnig, L. Dössel, K. Müllen, A. Schöll, and F. Reinert. Different views on the electronic structure of nanoscale graphene - planar molecule versus quantum dot. *New J. Phys.*, 14:113008, 2012.

[29] P. Puschnig, G. Koller, C. Draxl, and M. G. Ramsey. *Small Molecules on Surfaces - Fundamentals and Applications*, chapter The Structure of Molecular Orbitals Investigated by Angle-Resolved Photoemission, pages 1–21. Springer, 2013.

[30] F.J. Himpsel. Angle-resolved photoemission: From reciprocal space to real space. *J. Electron. Spectrosc. Relat. Phenom.*, 183:114–117, 2011.

[31] Jascha Repp, Gerhard Meyer, Sladjana M. Stojkovic, Andre Gourdon, and Christian Joachim. Molecules on insulating films: Scanning-tunneling microscopy imaging of individual molecular orbitals. *Phys. Rev. Lett.*, 94:026803, 2005.

[32] R Temirov, S Soubatch, O Neucheva, A C Lassise, and F S Tautz. A novel method achieving ultra-high geometrical resolution in scanning tunnelling microscopy. *New J. Phys.*, 10:053012, 2008.

[33] Leo Gross. Recent advances in submolecular resolution with scanning probe microscopy. *Nat. Chem.*, 3:273–278, 2011.

[34] J. Itatani, J. Levesque, D. Zeidler, Hiromichi Niikura, H. Pepin, J. C. Kieffer, P. B. Corkum, and D. M. Villeneuve. Tomographic imaging of molecular orbitals. *Nature*, 432:867–871, 2004.

[35] C. Vozzi, M. Negro, F. Calegari, G. Sansone, M. Nisoli, S. De Silvestr, and S. Stagira. Generalized molecular orbital tomography. *Nat. Phys.*, 7:822, 2011.

[36] Yang Li, Xiaosong Zhu, Pengfei Lan, Qingbin Zhang, Meiyan Qin, and Peixiang Lu. Molecular-orbital tomography beyond the plane-wave approximation. *Phys. Rev. A*, 89:045401, Apr 2014.

[37] J. Miao, D. Sayre, and H. N. Chapman. Phase retrieval from the magnitude of the Fourier transforms of nonperiodic objects. *J. Opt. Soc. Am. A*, 15:1662–1669, 1998.

[38] Jianwei Miao, Tetsuya Ishikawa, Erik H. Anderson, and Keith O. Hodgson. Phase retrieval of diffraction patterns from noncrystalline samples using the oversampling method. *Phys. Rev. B*, 67:174104, May 2003.

[39] Jianmin Shi and C. W. Tang. Doped organic electroluminescent devices with improved stability. *Appl. Phys. Lett.*, 70(13):1665–1667, 1997.

[40] D. J. Gundlach, T. N. Jackson, D. G. Schlom, and S. F. Nelson. Solvent-induced phase transition in thermally evaporated pentacene films. *Appl. Phys. Lett.*, 74:3302, 1999.

[41] Yen-Yi Lin, D.I. Gundlach, S.F. Nelson, and T.N. Jackson. Pentacene-based organic thin-film transistors. *Electron Devices, IEEE Transactions on*, 44(8):1325–1331, Aug 1997.

[42] Soichi Uchida, Jiangeng Xue, Barry P. Rand, and Stephen R. Forrest. Organic small molecule solar cells with a homogeneously mixed copper phthalocyanine: C60 active layer. *Appl. Phys. Lett.*, 84(21):4218–4220, 2004.

[43] J. Xue, B.P. Rand, S. Uchida, and S.R. Forrest. A hybrid planarmixed molecular heterojunction photovoltaic cell. *Adv. Mater.*, 17(1):66–71, 2005.

[44] S. Duhm, A. Gerlach, I. Salzmann, B. Broker, R.L. Johnson, F. Schreiber, and N. Koch. PTCDA on Au(111), Ag(111) and Cu(111): Correlation of interface charge transfer to bonding distance. *Org. Electron.*, 9:111–118, 2008.

[45] L. Romaner, D. Nabok, P. Puschnig, E. Zojer, and C. Ambrosch-Draxl. Theoretical study of PTCDA adsorbed on the coinage metal surfaces, Ag(111), Au(111) and Cu(111). *New J. Phys.*, 11:053010, 2009.

[46] S. Berkebile, G. Koller, A. Fleming, P. Puschnig, C. Ambrosch-Draxl, K. Emtsev, T. Seyller, J. Riley, and M.G. Ramsey. The electronic structure of pentacene revisited. *J. Electron. Spectrosc. Relat. Phenom.*, 174:22–27, 2009.

[47] Benjamin Stadtmüller, Ingo Kröger, Friedrich Reinert, and Christian Kumpf. Submonolayer growth of CuPc on noble metal surfaces. *Phys. Rev. B*, 83(8):085416, Feb 2011.

[48] Eric Daniel Gowacki, Lucia Leonat, Mihai Irimia-Vladu, Reinhard Schwdiauer, Mujeeb Ullah, Helmut Sitter, Siegfried Bauer, and Niyazi Serdar Sariciftci. Intermolecular hydrogen-bonded organic semiconductors-Quinacridone versus pentacenemercurio. *Appl. Phys. Lett.*, 101(2):023305, 2012.

[49] G. Mercurio, O. Bauer, M. Willenbockel, N. Fairley, W. Reckien, C. H. Schmitz, B. Fiedler, S. Soubatch, T. Bredow, M. Sokolowski, and F. S. Tautz. Adsorption height determination of nonequivalent C and O species of PTCDA on Ag(110) using x-ray standing waves. *Phys. Rev. B*, 87:045421, Jan 2013.

[50] Ho Jun Song, Doo Hun Kim, Eui Jin Lee, Jung Rim Haw, and Doo Kyung Moon. Correlation of intramolecular charge transfer and orientation properties among quinacridone and acceptor units. *Sol. Energ. Mat. Sol. Cells*, 123(0):112–121, 2014.

[51] L. Hedin. New Method for Calculating the One-Particle Green's Function with Application to the Electron Gas Problem. *Phys. Rev.*, 139:A796, 1965.

[52] M. S. Hybertson and S. G. Louie. First-Principles Theory of Quasiparticles: Calculation of Band Gaps in Semiconductors and Insulators. *Phys. Rev. Lett.*, 55:1418, 1985.

[53] M. S. Hybertson and S. G. Louie. Electron correlation in semiconductors and insulators: Band gaps and quasiparticle energies. *Phys. Rev. B*, 34:5390, 1986.

[54] W. Kohn. Nobel lecture: Electronic structure of matter-wave functions and density functionals. *Rev. Mod. Phys.*, 71:1253, 1999.

[55] M. Born and R. Oppenheimer. Zur Quantentheorie der Molekeln. *Ann. Physik*, 84:457, 1927.

[56] P. Hohenberg and W. Kohn. Inhomogeneous electron gas. *Phys. Rev.*, 136:B864, 1964.

[57] M. Levy. Electron densities in search of Hamiltonians. *Phys. Rev. A*, 26:1200, 1982.

[58] E. Lieb. Density functionals for coulomb systems. *Int. J. Quant. Chem.*, 24:243, 1983.

[59] W. Kohn and L. J. Sham. Self-consistent equations including exchange and correlation effects. *Phys. Rev.*, 140(4A):A1133–A1138, Nov 1965.

[60] D. M. Ceperly. Ground state of the fermion one-component plasma: A Monte Carlo study in two and three dimensions. *Phys. Rev. B*, 18:3126, 1978.

[61] D. M. Ceperly and B. J. Alder. Ground state of the electron gas by a stochastic method. *Phys. Rev. Lett.*, 45:566, 1980.

[62] R. O. Jones and O. Gunnarsson. The density functional formalism, its application and prospects. *Rev. Mod. Phys.*, 61:689, 1989.

[63] John P. Perdew. Generalized gradient approximations for exchange and correlation: A look backward and forward. *Physica B*, 172(12):1–6, 1991.

[64] A. D. Becke. Density-functional exchange-energy approximation with correct asymptotic behaviour. *Phys. Rev. A*, 38:3098, 1988.

[65] J. P. Perdew and Y. Wang. Accurate and simple analytic representation of the electron-gas correlation energy. *Phys. Rev. B*, 45:13244, 1992.

[66] J. P. Perdew, K. Burke, and M. Ernzerhof. Generalized Gradient Approximation Made Simple. *Phys. Rev. Lett.*, 77:3865, 1996.

[67] J. P. Perdew and Y. Wang. Accurate and simple density functional for the electronic exchange energy: Generalized gradient approximation. *Phys. Rev. B*, 33:8800, 1986.

[68] C. Lee, W. Yang, and R. G. Parr. Development of the colle-salvetti correlation-energy formula into a functional of the electron density. *Phys. Rev. B*, 37:785, 1988.

[69] Y. Zhang and W. Yang. Comment on "Generalized Gradient Approximation Made Simple". *Phys. Rev. Lett.*, 80:890, 1998.

[70] B Hammer, L. B. Hansen, and J. K. Norskov. Improved adsorption energetics with density-functional theory using revised Perdew-Burke-Ernzerhof functionals. *Phys. Rev. B*, 59:7413, 1999.

[71] John P. Perdew, Adrienn Ruzsinszky, Gabor I. Csonka, Oleg A. Vydrov, Gustavo E. Scuseria, Lucian A. Constantin, Xiaolan Zhou, and Kieron Burke. Restoring the density-gradient expansion for exchange in solids and surfaces. *Phys. Rev. Lett.*, 100(13):136406, 2008.

[72] Mel Levy, John P. Perdew, and Viraht Sahni. Exact differential equation for the density and ionization energy of a many-particle system. *Phys. Rev. A*, 30:2745–2748, Nov 1984.

[73] C.-O. Almbladh and U. von Barth. Exact results for the charge and spin densities, exchange-correlation potentials, and density-functional eigenvalues. *Phys. Rev. B*, 31:3231–3244, Mar 1985.

[74] Andreas Görling. Density-functional theory for excited states. *Phys. Rev. A*, 54:3912–3915, Nov 1996.

[75] D. P. Chong, O. V. Gritsenko, and E. J. Baerends. Interpretation of the Kohn-Sham orbital energies as approximate vertical ionization potentials. *The Journal of Chemical Physics*, 116(5):1760–1772, 2002.

[76] Leeor Kronik, Tamar Stein, Sivan Refaely-Abramson, and Roi Baer. Excitation Gaps of Finite-Sized Systems from Optimally Tuned Range-Separated Hybrid Functionals. *J. Chem. Theory Comput.*, 8(5):1515–1531, 2012.

[77] T. Koopmanns. Über die Zuordnung von Wellenfunktionen und Eigenwerten zu den Einzelnen Elektronen Eines Atoms. *Physica (Amsterdam)*, 1(16):104–113, 1934.

[78] J. F. Janak. Proof that $dE/dn_i = \varepsilon_i$ in density functional theory. *Phys. Rev. B*, 18:7165, 1978.

[79] Stephan Kümmel and Leeor Kronik. Orbital-dependent density functionals: Theory and applications. *Rev. Mod. Phys.*, 80:3–60, 2008.

[80] T. Körzdörfer, S. Kümmel, N. Marom, and L. Kronik. When to trust photoelectron spectra from Kohn-Sham eigenvalues: The case of organic semiconductors. *Phys. Rev. B*, 79:201205(R), 2009.

[81] Daniel Lüftner, Sivan Refaely-Abramson, Michael Pachler, Roland Resel, Michael G. Ramsey, Leeor Kronik, and Peter Puschnig. Experimental and theoretical electronic structure of quinacridone. *Phys. Rev. B*, 90:075204, 2014.

[82] J. P. Perdew, R. G. Parr, M. Levy, and J. L. Balduz. Density-Functional for Fractional Particle Number: Derivative Discontinuities of the Energy. *Phys. Rev. Lett.*, 49:1691, 1982.

[83] J. P. Perdew and M. Levy. Physical content of the exact Kohn-Sham orbital energies: Band gaps and derivative discontinuities. *Phys. Rev. Lett.*, 51:1884, 1983.

[84] John P. Perdew, Matthias Ernzerhof, and Kieron Burke. Rationale for mixing exact exchange with density functional approximations. *J. Chem. Phys.*, 105:9982, 1996.

[85] C Adamo and V Barone. Toward reliable density functional methods without adjustable parameters: The PBE0 model. *J. Chem. Phys.*, 110:6158, 1999.

[86] P. J. Stephens, F. J. Devlin, C. F. Chabalowski, and M. J. Frisch. Ab Initio Calculation of Vibrational Absorption and Circular Dichroism Spectra Using Density Functional Force Fields. *J. Phys. Chem.*, 98(45):11623–11627, 1994.

[87] Jochen Heyd, Gustavo E. Scuseria, and Matthias Ernzerhof. Hybrid functionals based on a screened Coulomb potential. *J. Chem. Phys.*, 118:8207, 2003.

[88] Jochen Heyd, Gustavo E. Scuseria, and Matthias Ernzerhof. Erratum: Hybrid functionals based on a screened Coulomb potential [J. Chem. Phys. 118, 8207 (2003)]. *J. Chem. Phys.*, 124:219906, 2006.

[89] Axel D. Becke. Density-functional thermochemistry. III. The role of exact exchange. *J Chem. Phys.*, 98(7):5648–5652, 1993.

[90] S. H. Vosko, L. Wilk, and M. Nusair. Accurate spin-dependent electron liquid correlation energies for local spin density calculations: a critical analysis. *Can. J. Phys.*, 58(8):1200–1211, 1980.

[91] A. Seidl, A. Görling, P. Vogl, J. A. Majewski, and M. Levy. Generalized Kohn-Sham schemes and the band-gap problem. *Phys. Rev. B*, 53(7):3764–3774, Feb 1996.

[92] T. Körzdörfer, S. Kümmel, N. Marom, and L. Kronik. Erratum: When to trust photoelectron spectra from Kohn-Sham eigenvalues: The case of organic semiconductors [Phys. Rev. B 79, 201205 (2009)]. *Phys. Rev. B*, 82:129903, Sep 2010.

[93] Tamar Stein, Helen Eisenberg, Leeor Kronik, and Roi Baer. Fundamental Gaps in Finite Systems from Eigenvalues of a Generalized Kohn-Sham Method. *Phys. Rev. Lett.*, 105:266802, Dec 2010.

[94] Sivan Refaely-Abramson, Roi Baer, and Leeor Kronik. Fundamental and excitation gaps in molecules of relevance for organic photovoltaics from an optimally tuned range-separated hybrid functional. *Phys. Rev. B*, 84:075144, Aug 2011.

[95] Huy-Viet Nguyen, T. Anh Pham, Dario Rocca, and Giulia Galli. Improving accuracy and efficiency of calculations of photoemission spectra within the many-body perturbation theory. *Phys. Rev. B*, 85:081101, Feb 2012.

[96] Daniel Neuhauser, Yi Gao, Christopher Arntsen, Cyrus Karshenas, Eran Rabani, and Roi Baer. Breaking the Theoretical Scaling Limit for Predicting Quasiparticle Energies: The Stochastic *GW* Approach. *Phys. Rev. Lett.*, 113:076402, Aug 2014.

[97] F. Aryasetiawan and O. Gunnarsson. The GW method. *Rep. Prog. Phys.*, 61:237, 1998.

[98] Andrea Damascelli. Probing the Electronic Structure of Complex Systems by ARPES. *Phys. Scr.*, T109:61–74, 2004.

[99] J. Schwinger. On the Green's functions of quantized fields. I. *Proc. Nat. Acad. Sci. U.S.A.*, 37:452, 1951.

[100] P. Martin and J. Schwinger. Theory of Many-Particle Physics. I. *Phys. Rev.*, 115:1342, 1959.

[101] Noa Marom, Xinguo Ren, Jonathan E. Moussa, James R. Chelikowsky, and Leeor Kronik. Electronic structure of copper phthalocyanine from G_0W_0 calculations. *Phys. Rev. B*, 84:195143, Nov 2011.

[102] H. Hertz. Ueber einen Einfluss des ultravioletten Lichtes auf die electrische Entladung. *Annalen der Physik*, 267(8):983–1000, 1887.

[103] Albert Einstein. Über einen die Erzeugung und Verwandlung des Lichts betreffenden heuristischen Gesichtspunkt. *Ann. Physik*, 17:132, 1905.

[104] L Broekman, A Tadich, E Huwald, J Riley, R Leckey, T Seyller, K Emtsev, and L Ley. First results from a second generation toroidal electron spectrometer. *J. Electron. Spectrosc. Relat. Phenom.*, 144-147:1001–1004, 2005.

[105] Friedrich Reinert and Stefan Hüfner. Photoemission spectroscopy-from early days to recent applications. *New Journal of Physics*, 7(1):97, 2005.

[106] I. Adawi. Theory of the surface photoelectric effect for one and two photons. *Phys. Rev.*, 134:A788–A798, May 1964.

[107] M. Dauth, M. Wiessner, V. Feyer, A. Schöll, P. Puschnig, F. Reinert, and S. Kümmel. Angle resolved photoemission from organic semiconductors: orbital imaging beyond the molecular orbital interpretation. *New J. Phys.*, 16:103005, 2014.

[108] B. Stadtmüller, M. Willenbockel, E.M. Reinisch, T. Ules, M. Ostler, F. Bocquet, S. Soubatch, P. Puschnig, G. Koller, M. G. Ramsey, F. S. Tautz, and C. Kumpf. Orbital tomography for highly symmetric adsorbate systems. *European Physics Letters*, 100:26008, 2012.

[109] M. Willenbockel, B. Stadtmüller, K. Schönauer, F. Bocquet, D. Lüftner, E. M. Reinisch, T. Ules, G. Koller, C. Kumpf, S. Soubatch, P. Puschnig, M. G. Ramsey, and F. S. Tautz. Energy offsets within a molecular monolayer: The influence of the molecular environment. *New J. Phys.*, 15:033017, 2013.

[110] E. M. Reinisch, T. Ules, P. Puschnig, S. Berkebile, M. Ostler, T. Seyller, M. G. Ramsey, and G. Koller. Development and character of gap states on alkali doping of molecular films. *New J. Phys.*, 16:023011, 2013.

[111] Daniel Lüftner, Thomas Ules, Eva Maria Reinisch, Georg Koller, Sergey Soubatch, F. Stefan Tautz, Michael G. Ramsey, and Peter Puschnig. Imaging the wave functions of adsorbed molecules. *Proc. Nat. Acad. Sci.*, 111(2):605–610, 2014.

[112] Benjamin Stadtmüller, Daniel Lüftner, Martin Willenbockel, Eva M. Reinisch, Tomoki Sueyoshi, Georg Koller, Serguei Soubatch, Michael G. Ramsey, Peter Puschnig, F. Stefan Tautz, and Christian Kumpf. Unexpected interplay of bonding height and energy level alignment at heteromolecular hybrid interfaces. *Nat. Commun.*, 5:3685, 2014.

[113] Daniel Lüftner, Matus Milko, Sophia Huppmann, Markus Scholz, Nam Ngyuen, Michael Wießner, Achim Schöll, Friedrich Reinert, and Peter Puschnig. CuPc/Au(110): Determination of the azimuthal alignment by combination of a angle-resolved photoemission and density functional theory. *J. Electron Spectrosc. Relat. Phenom.*, 195:293, 2014.

[114] Thomas Ules, Daniel Lüftner, Eva Maria Reinisch, Georg Koller, Peter Puschnig, and Michael G. Ramsey. Orbital tomography of hybridized and dispersing molecular overlayers. *Phys. Rev. B*, 90:155430, Oct 2014.

[115] Leo Gross, Nikolaj Moll, Fabian Mohn, Alessandro Curioni, Gerhard Meyer, Felix Hanke, and Mats Persson. High-Resolution Molecular Orbital Imaging Using a p-Wave STM Tip. *Phys. Rev. Lett.*, 107:086101, Aug 2011.

[116] Nobuo Ueno and Satoshi Kera. Electron spectroscopy of functional organic thin films: Deep insights into valence electronic structure in relation to charge transport property. *Prog. Surf. Sci.*, 83:490–557, 2008.

[117] M. Dauth, T. Körzdörfer, S. Kümmel, J. Ziroff, M. Wiessner, A. Schöll, F. Reinert, M. Arita, and K. Shimada. Orbital density reconstruction for molecules. *Phys. Rev. Lett.*, 107:193002, Nov 2011.

[118] M. Wießner, J. Ziroff, F. Forster, M. Arita, K. Shimada, P. Puschnig, A. Schöll, and F. Reinert. Substrate-mediated band-dispersion of electronic states in adsorbed molecules. *Nature Communications*, 4:1514, 2013.

[119] G. Koller, S. Berkebile, M. Oehzelt, P. Puschnig, C. Ambrosch-Draxl, F. P. Netzer, and M. G. Ramsey. Intra- and intermolecular band dispersion in an organic crystal. *Science*, 317:351, 2007.

[120] W. H. Eugen Schwarz. Measuring orbitals: Provocation or reality? *Angew. Chem. Int. Ed.*, 45:1508–1517, 2006.

[121] X. Gonze, B. Amadon, P.-M. Anglade, J.-M. Beuken, F. Bottin, P. Boulanger, F. Bruneval, D. Caliste, R. Caracas, M. Ct, T. Deutsch, L. Genovese, Ph. Ghosez, M. Giantomassi, S. Goedecker, D.R. Hamann, P. Hermet, F. Jollet, G. Jomard, S. Leroux, M. Mancini, S. Mazevet, M.J.T. Oliveira, G. Onida, Y. Pouillon, T. Rangel, G.-M. Rignanese, D. Sangalli, R. Shaltaf, M. Torrent, M.J. Verstraete, G. Zerah, and J.W. Zwanziger. Abinit: First-principles approach to material and nanosystem properties. *Comp. Phys. Commun.*, 180(12):2582–2615, 2009. 40 YEARS OF CPC: A celebratory issue focused on quality software for high performance, grid and novel computing architectures.

[122] N. Troullier and J. L. Martins. Efficient pseudopotentials for plane-wave calculations. *Phys. Rev. B*, 43:1993, 1991.

[123] J. R. Fienup. Reconstruction of an object from the modulus of its fourier transform. *Opt. Lett.*, 3:27–29, 1978.

[124] Sophia Huppmann. Winkelaufgelöste Photoelektronenspektroskopie zur Molekülorbitaltomographie an Phthalocyanin-Schichten. Master's thesis, Julius-Maximilians-Universität Würzburg, 2011.

[125] E Umbach, M Sokolowski, and R Fink. Substrate-interaction, long-range order, and epitaxy of large organic adsorbates. *Appl. Phys.*, 63:565–576, 1996.

[126] F. S. Tautz. Structure and bonding of large aromatic molecules on noble metal surfaces: The example of PTCDA. *Prog. Surf. Sci.*, 82:479–520, 2007.

[127] Norbert Koch. Organic electronic devices and their functional interfaces. *Chem. Phys. Chem.*, 8:1438, 2007.

[128] Ming-Hui Shang, Mayumi Nagaosa, Shin-ichi Nagamatsu, Shunsuke Hosoumi, Satoshi Kera, Takashi Fujikawa, and Nobuo Ueno. Photoemission from valence bands of transition metal-phthalocyanines. *J. Electron. Spectrosc. Relat. Phenom.*, 184:261–264, 2011.

[129] M. Wießner, J. Kübert, V. Feyer, P. Puschnig, A. Schöll, and F. Reinert. Lateral band formation and hybridization in molecular monolayers: NTCDA on Ag(110) and Cu(100). *Phys. Rev. B*, 88:075437, 2013.

[130] M. Wießner, D. Hauschild, A. Schöll, F. Reinert, V. Feyer, K. Winkler, and B. Krömker. Electronic and geometric structure of the PTCDA/Ag(110) interface probed by angle-resolved photoemission. *Phys. Rev. B*, 86:045417, Jul 2012.

[131] Neil B. McKeown. *Phthalocyanine Materials - Synthesis, Structure and Function*. Cambridge University Press, 1998.

[132] I. Chizhov, G. Scoles, and A. Kahn. The Influence of Steps on the Orientation of Copper Phthalocyanine Monolayers on Au(111). *Langmuir*, 16(9):4358–4361, 2000.

[133] Fabrizio Evangelista, A. Ruocco, Valdis Corradini, M.P. Donzello, Carlo Mariani, and Maria Grazia Betti. CuPc molecules adsorbed on Au(110)-(1x2): growth morphology and evolution of valence band states. *Surface Science*, 531(2):123–130, 2003.

[134] Luca Floreano, Albano Cossaro, Roberto Gotter, Alberto Verdini, Gregor Bavdek, Fabrizio Evangelista, Alessandro Ruocco, Alberto Morgante, and Dean Cvetko. Periodic Arrays of Cu-Phthalocyanine Chains on Au(110). *The Journal of Physical Chemistry C*, 112(29):10794–10802, 2008.

[135] F. Evangelista, A. Ruocco, R. Gotter, A. Cossaro, L. Floreano, A. Morgante, F. Crispoldi, M. G. Betti, and C. Mariani. Electronic states of CuPc chains on the Au(110) surface. *J. Chem Phys.*, 131:174710, 2009.

[136] Christoph Stadler, Sören Hansen, Ingo Kröger, Christian Kumpf, and Eberhard Umbach. Tuning intermolecular interaction in long-range-ordered submonolayer organic films. *Nat. Phys.*, 5:153–159, 2009.

[137] H. Karacuban, M. Lange, J. Schaffert, O. Weingart, Th. Wagner, and R. Möller. Substrate-induced symmetry reduction of CuPc on Cu(111): An LT-STM study. *Surf. Sci.*, 603(5):L39–L43, 2009.

[138] Pierluigi Gargiani, Marco Angelucci, Carlo Mariani, and Maria Grazia Betti. Metal-phthalocyanine chains on the Au(110) surface: Interaction states versus *d*-metal states occupancy. *Phys. Rev. B*, 81:085412, Feb 2010.

[139] Ingo Kröger, Benjamin Stadtmüller, Christoph Stadler, Johannes Ziroff, Mario Kochler, Andreas Stahl, Florian Pollinger, Tien-Lin Lee, Jrg Zegenhagen, Friedrich Reinert, and Christian Kumpf. Submonolayer growth of copper-phthalocyanine on Ag(111). *New J. Phys.*, 12:083038, 2010.

[140] Y. Y. Zhang, S. X. Du, and H.-J. Gao. Binding configuration, electronic structure, and magnetic properties of metal phthalocyanines on a Au(111) surface studied with *ab initio* calculations. *Phys. Rev. B*, 84:125446, Sep 2011.

[141] E Rauls, WG Schmidt, T Pertram, and K Wandelt. Interplay between metal-free phthalocyanine molecules and Au(110) substrates. *Surf. Sci.*, 606:1120–1125, 2012.

[142] Pierluigi Gargiani, Giorgio Rossi, Roberto Biagi, Valdis Corradini, Maddalena Pedio, Sara Fortuna, Arrigo Calzolari, Stefano Fabris, Julio Criginski Cezar, N. B. Brookes, and Maria Grazia Betti. Spin and orbital configuration of metal phthalocyanine chains assembled on the Au(110) surface. *Phys. Rev. B*, 87:165407, Apr 2013.

[143] Noa Marom, Oded Hod, Gustavo E. Scuseria, and Leeor Kronik. Electronic structure of copper phthalocyanine: A comparative density functional theory study. *J. Chem. Phys.*, 128:164107, 2008.

[144] Jochen Heyd and Gustavo E. Scuseria. Efficient hybrid density functional calculations in solids: Assessment of the Heyd-Scuseria-Ernzerhof screened Coulomb hybrid functional. *J. Chem. Phys.*, 121:1187, 2004.

[145] E. L. Shirley, L. J. Terminello, A. Santoni, and F. J. Himpsel. Brillouin-zone-selection effects in graphite photoelectron angular distributions. *Phys. Rev. B*, 51:13614, 1995.

[146] G. Kresse and J. Hafner. Ab initio molecule dynamics for liquid metals. *Phys. Rev. B*, 47:558, 1993.

[147] G. Kresse and D. Joubert. From ultrasoft pseudopotentials to the projector augmented-wave method. *Phys. Rev. B*, 59:1758, 1999.

[148] P. E. Blöchl. Projector augmented-wave method. *Phys. Rev. B*, 50:17953, 1994.

[149] H. J. Monkhorst and J. D. Pack. Special points for Brillouin-zone integrations. *Phys. Rev. B*, 13:5188, 1976.

[150] M. Methfessel and A. T. Paxton. High-precision sampling for Brillouin-zone integration in metals. *Phys. Rev. B*, 40:3616, 1989.

[151] J. Neugebauer and M. Scheffler. Adsorbate-substarte and adsorbate-adsorbate interactions of Na and Ka adlayers on Al(111). *Phys. Rev. B*, 46:16067, 1992.

[152] P. Sony, P. Puschnig, D. Nabok, and C. Ambrosch-Draxl. Importance of Van Der Waals Interaction for Organic Molecule-Metal Junctions: Adsorption of Thiophene on Cu(110) as a Prototype. *Phys. Rev. Lett.*, 99:176401, 2007.

[153] Stefan Grimme. Semiempirical GGA-Type Density Functional Constructed with a Long-Range Dispersion Correction. *J. Comput. Chem.*, 27:1787, 2006.

[154] Martin Amft, Sebastien Lebegue, Olle Eriksson, and Natalia V. Skorodumova. Adsorption of Cu, Ag, and Au atoms on graphene including van der Waals interactions. *J. Phys.: Condens. Matter*, 23:395001, 2011.

[155] T. Körzdörfer. On the relation between orbital-localization and self-interaction errors in the density functional theory treatment of organic semiconductors. *J. Chem. Phys.*, 134(9):–, 2011.

[156] T. Körzdörfer and S. Kümmel. Single-particle and quasiparticle interpretation of Kohn-Sham and generalized Kohn-Sham eigenvalues for hybrid functionals. *Phys. Rev. B*, 82:155206, Oct 2010.

[157] T. Permien, R. Engelhardt, C. A. Feldmann, and E. E. Koch. Angle-resolved photoemission from oriented films of lead phthalocyanine on A Cu(100) surface. *Chem. Phys. Lett.*, 98:527–530, 1983.

[158] N. V. Richardson. Comments on angle-resolved photoemission from oriented films of lead phthalocyanine on a Cu100 surface. *Chem. Phys. Lett.*, 102:390–391, 1983.

[159] G. V. Hansson and S. A. Flodström. Photoemission study of the bulk and surface electronic structure of single crystals of gold. *Phys. Rev. B*, 18:1572–1585, Aug 1978.

[160] G. Heimel, L. Romaner, J.-L. Bredas, and E. Zojer. Interface Energetics and Level Alignment at Covalent Metal-Molecule Junctions: π-Conjugated Thiols on Gold. *Phys. Rev. Lett.*, 96:196806, 2006.

[161] G. Heimel, S. Duhm, I. Salzmann, A. Gerlach, A. Strozecka, J. Niederhausen, C. Brker, T. Hosokai, I. Fernandez-Torrente, G. Schulze, S. Winkler, A. Wilke, R. Schlesinger, J. Frisch, B. Brker, A. Vollmer, B. Detlefs, J. Pflaum, S. Kera, K. J. Franke, N. Ueno, J. I. Pascual, F. Schreiber, and N. Koch. Charged and metallic molecular monolayers through surface-induced aromatic stabilization. *Nat. Chem.*, 5:187–194, 2013.

[162] L. Romaner, G. Heimel, J.-L. Bredas, A. Gerlach, F. Schreiber, R. L. Johnson, J. Zegenhagen, S. Duhm, N. Koch, and E. Zojer. Impact of Bidirectional Charge Transfer and Molecular Distortions on the Electronic Structure of a Metal-Organic Interface. *Phys. Rev. Lett.*, 99:256801, 2007.

[163] Frank Schreiber. Structure and growth of self-assembling monolayers. *Prog. Surf. Sci.*, 65(58):151 – 257, 2000.

[164] J. Fraxedas, S. Garcia-Gil, S. Monturet, N. Lorente, I. Fernandez-Torrente, K. J. Franke, J. I. Pascual, A. Vollmer, R.-P. Blum, N. Koch, and P. Ordejon. Modulation of surface charge transfer through competing long-range repulsive versus short-range attractive interactions. *J. Phys. Chem. C*, 115(38):18640–18648, 2011.

[165] I.G. Hill, D. Milliron, J. Schwartz, and A. Kahn. Organic semiconductor interfaces: electronic structure and transport properties. *Appl. Surf. Sci.*, 166(14):354 – 362, 2000.

[166] Ingo Kröger, Benjamin Stadtmüller, Christoph Kleimann, Parasmani Rajput, and Christian Kumpf. Normal-incidence x-ray standing-wave study of copper phthalocyanine submonolayers on Cu(111) and Au(111). *Phys. Rev. B*, 83:195414, May 2011.

[167] J. Stanzel, W. Weigand, L. Kilian, H.L. Meyerheim, C. Kumpf, and E. Umbach. Chemisorption of NTCDA on Ag(111): a NIXSW study including non-dipolar and electron-stimulated effects. *Surf. Sci.*, 571(13):L311 – L318, 2004.

[168] Oliver Bauer, Giuseppe Mercurio, Martin Willenbockel, Werner Reckien, Christoph Heinrich Schmitz, Benjamin Fiedler, Serguei Soubatch, Thomas Bredow, Frank Stefan Tautz, and Moritz Sokolowski. Role of functional groups in surface bonding of planar π-conjugated molecules. *Phys. Rev. B*, 86:235431, Dec 2012.

[169] A. Gerlach, S. Sellner, F. Schreiber, N. Koch, and J. Zegenhagen. Substrate-dependent bonding distances of PTCDA: A comparative x-ray standing-wave study on Cu(111) and Ag(111). *Phys. Rev. B*, 75:045401, 2007.

[170] A. Hauschild, R. Temirov, S. Soubatch, O. Bauer, A. Schöll, B. C. C. Cowie, T.-L. Lee, F. S. Tautz, and M. Sokolowski. Normal-incidence x-ray standing-wave determination of the adsorption geometry of PTCDA on Ag(111): Comparison of the ordered room-temperature and disordered low-temperature phases. *Phys. Rev. B*, 81:125432, Mar 2010.

[171] A. Hauschild, K. Karki, B. C. C. Cowie, M. Rohlfing, F. S. Tautz, and M. Sokolowski. Molecular Distortions and Chemical Bonding of a Large π-Conjugated Molecule on a Metal Surface. *Phys. Rev. Lett.*, 94:036106, 2005.

[172] K. Manandhar, T. Ellis, K.T. Park, T. Cai, Z. Song, and J. Hrbek. A scanning tunneling microscopy study on the effect of post-deposition annealing of copper phthalocyanine thin films. *Surf. Sci.*, 601:3623–3631, 2007.

[173] L. Kilian, A. Hauschild, R. Temirov, S. Soubatch, A. Scholl, A. Bendounan, F. Reinert, T.-L. Lee, F. S. Tautz, M. Sokolowski, and E. Umbach. Role of Intermolecular Interactions on the Electronic and Geometric Structure of a Large π-Conjugated Molecule Adsorbed on a Metal Surface. *Phys. Rev. Lett.*, 100:136103, 2008.

[174] L. Kilian, U. Stahl, I. Kossev, M. Sokolowski, R. Fink, and E. Umbach. The commensurate-to-incommensurate phase transition of an organic monolayer: A high resolution LEED analysis of the superstructures of NTCDA on Ag(111). *Surf. Sci.*, 602(14):2427 – 2434, 2008.

[175] Th. Wagner, H. Karacuban, and R. Möller. Analysis of complex thermal desorption spectra: PTCDA on copper. *Surface Science*, 603(3):482 – 490, 2009.

[176] C Stadler, S Hansen, A Schll, T-L Lee, J Zegenhagen, C Kumpf, and E Umbach. Molecular distortion of NTCDA upon adsorption on Ag(111): a normal incidence x-ray standing wave study. *New J. Phys.*, 9(3):50, 2007.

[177] C. H. Schwalb, S. Sachs, M. Marks, A. Schöll, F. Reinert, E. Umbach, and U. Höfer. Electron lifetime in a shockley-type metal-organic interface state. *Phys. Rev. Lett.*, 101(14):146801, 2008.

[178] D. M. NEWNS. Self-consistent model of hydrogen chemisorption. *Phys. Rev.*, 178:1123–1135, Feb 1969.

[179] B. Hammer. Special sites at noble and late transition metal catalysts. *Top. Catal.*, 37(1):3–16, 2006.

[180] H. Marchetto, U. Groh, Th. Schmidt, R. Fink, H.-J. Freund, and E. Umbach. Influence of substrate morphology on organic layer growth: PTCDA on Ag(111). *Chemical Physics*, 325(1):178 – 184, 2006. Electronic Processes in Organic Solids.

[181] Ingo Kröger, Benjamin Stadtmüller, Christian Wagner, Christian Weiss, Ruslan Temirov, F. Stefan Tautz, and Christian Kumpf. Modeling intermolecular interactions of physisorbed organic molecules using pair potential calculations. *The Journal of Chemical Physics*, 135(23):–, 2011.

[182] N. Gonzalez-Lakunza, I. Fernandez-Torrente, K. J. Franke, N. Lorente, A. Arnau, and J. I. Pascual. Formation of Dispersive Hybrid Bands at an Organic-Metal Interface. *Phys. Rev. Lett.*, 100:156805, 2008.

[183] Stefan C. B. Mannsfeld, Karl Leo, and Torsten Fritz. Line-on-line coincidence: A new type of epitaxy found in organic-organic heterolayers. *Phys. Rev. Lett.*, 94:056104, Feb 2005.

[184] Wei Chen, Han Huang, Shi Chen, Lan Chen, Hong Liang Zhang, Xing Yu Gao, and Andrew Thye Shen Wee. Molecular orientation of 3, 4, 9, 10-perylene-tetracarboxylic-dianhydride thin films at organic heterojunction interfaces. *Appl. Phys. Lett.*, 91(11):–, 2007.

[185] Wei Chen, Hui Li, Han Huang, Yuanxi Fu, Hong Liang Zhang, Jing Ma, and Andrew Thye Shen Wee. Two-Dimensional Pentacene:3,4,9,10-Perylenetetracarboxylic Dianhydride Supramolecular Chiral Networks on Ag(111). *J. Am. Chem. Soc.*, 130(37):12285–12289, 2008.

[186] Yinying Wei, Steven W. Robey, and Janice E. Reutt-Robey. TiOPc Molecular Dislocation Networks as Nanotemplates for C60 Cluster Arrays. *J. Am. Chem. Soc.*, 131(34):12026–12027, 2009. PMID: 19655746.

[187] Han Huang, Wei Chen, Shi Chen, Dong Chen Qi, Xing Yu Gao, and Andrew Thye Shen Wee. Molecular orientation of CuPc thin films on C60/Ag(111). *Appl. Phys. Lett.*, 94(16):–, 2009.

[188] C. Bobisch, Th. Wagner, A. Bannani, and R. Möller. Ordered binary monolayer composed of two organic molecules: Copper-phthalocyanine and 3,4,9,10-perylene-tetra-carboxylic-dianhydride on Cu(111). *J. Chem. Phys.*, 119(18):9804–9808, 2003.

[189] M. Häming, M. Greif, C. Sauer, A. Schöll, and F. Reinert. Electronic structure of ultrathin heteromolecular organic-metal interfaces: SnPc/PTCDA/Ag(111) and SnPc/Ag(111). *Phys. Rev. B*, 82:235432, Dec 2010.

[190] Benjamin Stadtmüller, Tomoki Sueyoshi, Georgy Kichin, Ingo Kröger, Sergey Soubatch, Ruslan Temirov, F. Stefan Tautz, and Christian Kumpf. Commensurate registry and chemisorption at a hetero-organic interface. *Phys. Rev. Lett.*, 108:106103, Mar 2012.

[191] Lidong Sun, Chunyang Liu, Daniel Queteschiner, Gunther Weidlinger, and Peter Zeppenfeld. Layer inversion in organic heterostructures. *Phys. Chem. Chem. Phys.*, 13:13382–13386, 2011.

[192] David A. Egger, Victor G. Ruiz, Wissam A. Saidi, Tomaas Buccko, Alexandre Tkatchenko, and Egbert Zojer. Understanding structure and bonding of multilayered metal-organic nanostructures. *J. Phys. Chem. C*, 117:3055–3061, 2013.

[193] José I. Martínez, Enrique Abad, Juan I. Beltrán, Fernando Flores, and José Ortega. Barrier height formation in organic blends/metal interfaces: Case of tetrathiafulvalene-tetracyanoquinodimethane/Au(111). *The Journal of Chemical Physics*, 139(21):–, 2013.

[194] Shiri R. Burema and Marie-Laure Bocquet. A sum rule for inelastic electron tunneling spectroscopy: an ab initio study of a donor (TTF) and acceptors (TCNE, TCNQ and DCNQI) parallelly oriented on Cu(100). *Phys. Chem. Chem. Phys.*, 15:16111–16119, 2013.

[195] M.C. Cottin, J. Schaffert, A. Sonntag, H. Karacuban, R. Mller, and C.A. Bobisch. Supramolecular architecture of organic molecules: PTCDA and CuPc on a Cu(111) substrate. *Appl. Surf. Sci.*, 258(6):2196 – 2200, 2012.

[196] Y. Zou, L. Kilian, A. Schöll, Th. Schmidt, R. Fink, and E. Umbach. Chemical bonding of PTCDA on Ag surfaces and the formation of interface states. *Surf. Sci.*, 600:1260, 2006.

[197] A. Kraft, R. Temirov, S. K. M. Henze, S. Soubatch, M. Rohlfing, and F. S. Tautz. Lateral adsorption geometry and site-specific electronic structure of a large organic chemisorbate on a metal surface. *Phys. Rev. B*, 74:041402(R), 2006.

[198] Afaf El-Sayed, Patrizia Borghetti, Elizabeth Goiri, Celia Rogero, Luca Floreano, Giacomo Lovat, Duncan John Mowbray, Jose Luis Cabellos, Yutaka Wakayama, Angel Rubio, Jose Enrique Ortega, and Dimas G. de Oteyza. Understanding energy-level alignment in donoracceptor/metal interfaces from core-level shifts. *ACS Nano*, 7(8):6914–6920, 2013. PMID: 23883347.

[199] J. Zegenhagen. Surface structure determination with x-ray standing waves. *Surf. Sci. Rep.*, 18(78):202 – 271, 1993.

[200] D P Woodruff. Surface structure determination using x-ray standing waves. *Rep. Prog. Phys.*, 68(4):743, 2005.

[201] D.P. Woodruff. Normal incidence x-ray standing wave determination of adsorbate structures. *Prog. Surf. Sci.*, 57(1):1 – 60, 1998.

[202] Giuseppe Mercurio. *Study of molecule-metal interfaces by means of the Normal Incidence X-ray Standing Wave technique*. PhD thesis, Rheinisch-Westflische Technische Hochschule Aachen, 2012.

[203] T. Auckenthaler, V. Blum, H.-J. Bungartz, T. Huckle, R. Johanni, L. Krmer, B. Lang, H. Lederer, and P.R. Willems. Parallel solution of partial symmetric eigenvalue problems from electronic structure calculations. *Parallel Computing*, 37:783–794, 2011.

[204] V. Feyer, M. Graus, P. Nigge, M. Wießner, R.G. Acres, C. Wiemann, C.M. Schneider, A. Schöll, and F. Reinert. Adsorption geometry and electronic structure of iron phthalocyanine on Ag surfaces: A LEED and photoelectron momentum mapping study. *Surface Science*, 621(0):64 – 68, 2014.

[205] H. Yamane, D. Yoshimura, E. Kawabe, R. Sumii, K. Kanai, Y. Ouchi, N. Ueno, and K. Seki. Electronic structure at highly ordered organic/metal interfaces: Pentacene on cu(110). *Phys. Rev. B*, 76:165436, 2007.

[206] Hiroyuki Yamane, Eiji Kawabe, Daisuke Yoshimura, Ryohei Sumii, Kaname Kanai, Yukio Ouchi, Nobuo Ueno, and Kazuhiko Seki. Intermolecular band dispersion in highly ordered monolayer and multilayer films of pentacene on Cu(110). *phys. stat. sol. (b)*, 245:793–798, 2008.

[207] Chiara Baldacchini, Carlo Mariani, Maria Grazia Betti, Ivana Vobornik, Jun Fujii, Emilia Annese, Giorgio Rossi, Andrea Ferretti, Arrigo Calzolari, Rosa Di Felice, Alice Ruini, and Elisa Molinari. Symmetry lowering of pentacene molecular states interacting with a cu surface. *Phys. Rev. B*, 76:245430, Dec 2007.

[208] Andrea Ferretti, Chiara Baldacchini, Arrigo Calzolari, Rosa Di Felice, Alice Ruini, Elisa Molinari, and Maria Grazia Betti. Mixing of electronic states in pentacene adsorption on copper. *Phys. Rev. Lett.*, 99:046802, Jul 2007.

[209] E. Annese, J. Fujii, C. Baldacchini, B. Zhou, C. E. Viol, I. Vobornik, M. G. Betti, and G. Rossi. Molecular charge distribution and dispersion of electronic states in the contact layer between pentacene and Cu(119) and beyond. *Phys. Rev. B*, 77:205417, May 2008.

[210] Kathrin Müller, Ari P. Seitsonen, Thomas Brugger, James Westover, Thomas Greber, Thomas Jung, and Abdelkader Kara. Electronic Structure of an Organic/Metal Interface: Pentacene/Cu(110). *J. Phys. Chem. C*, 116:23465–23471, 2012.

[211] Oliver T Hofmann, Viktor Atalla, Nikolaj Moll, Patrick Rinke, and Matthias Scheffler. Interface dipoles of organic molecules on Ag(111) in hybrid density-functional theory. *New Journal of Physics*, 15(12):123028, 2013.

[212] Stephen Berkebile, Thomas Ules, Peter Puschnig, Lorenz Romaner, Georg Koller, Alexander J. Fleming, Konstantin Emtsev, Thomas Seyller, Claudia Ambrosch-Draxl, Falko P. Netzer, and Michael G. Ramsey. A momentum space view of the surface chemical bond. *Phys. Chem. Chem. Phys.*, 13:3604–3611, 2011.

[213] Sivan Refaely-Abramson, Sahar Sharifzadeh, Manish Jain, Roi Baer, Jeffrey B. Neaton, and Leeor Kronik. Gap renormalization of molecular crystals from density-functional theory. *Phys. Rev. B*, 88:081204, Aug 2013.

[214] Yoshiro Yamashita. Organic semiconductors for organic field-effect transistors. *Sci. Technol. Adv. Mater*, 10(2):024313, 2009.

[215] Jia Wang, Yunfeng Zhao, Chuandong Dou, Hui Sun, Peng Xu, Kaiqi Ye, Jingying Zhang, Shimei Jiang, Fei Li, and Yue Wang. Alkyl and dendron substituted quinacridones: synthesis, structures, and luminescent properties. *J. Phys. Chem. B*, 111(19):5082–5089, 2007. PMID: 17439269.

[216] John Jun-An Chen, Teresa L. Chen, BongSoo Kim, Daniel A. Poulsen, Justin L. Mynar, Jean M. J. Frechet, and Biwu Ma. Quinacridone-based molecular donors for solution processed bulk-heterojunction organic solar cells. *ACS Appl. Mater. Interfaces*, 2(9):2679–2686, 2010.

[217] Thorsten Wagner, Michael Gyrk, Daniel Huber, Peter Zeppenfeld, and Eric Daniel Gowacki. Quinacridone on Ag(111): Hydrogen Bonding versus Chirality. *J. Phys. Chem. C*, 118(20):10911–10920, 2014.

[218] Frank Trixler, Thomas Markert, Markus Lackinger, Ferdinand Jamitzky, and WolfgangM. Heckl. Supramolecular self-assembly initiated by solidsolid wetting. *Chem. Eur. J.*, 13(27):7785–7790, 2007.

[219] A. Kahn, N. Koch, and W. Gao. Electronic structure and electrical properties of interfaces between metals and π-conjugated molecular films. *J. Polym. Sci., B, Polym. Phys.*, 41:2529, 2003.

[220] N. Koch, N. Ueno, and A. T. S. Wee, editors. *The Molecule-Metal Interface*. Wiley-VCH Weinheim, 2013.

[221] Leeor Kronik and Yoshitada Morikawa. *Understanding the Metal-Molecule Interface from First Principles*, pages 51–89. Wiley-VCH Weinheim, 2013.

[222] R. G. Parr and W. Yang. *Density Functional Theory of Atoms and Molecules*. Oxford University Press, Oxford, 1989.

[223] E. K. U. Gross and R. M. Dreizler. *Density Functional Theory*. Plenum Press, New York, 1995.

[224] W. Kohn and L. J. Sham. Quantum density oscillations in an inhomogeneous electron gas. *Phys. Rev.*, 137(6A):A1697–A1705, Mar 1965.

[225] L. J. Sham and W. Kohn. One-particle properties of an inhomogeneous interacting electron gas. *Phys. Rev.*, 145:561, 1966.

[226] John P. Perdew and Mel Levy. Comment on "Significance of the highest occupied Kohn-Sham eigenvalue". *Phys. Rev. B*, 56:16021–16028, Dec 1997.

[227] Leeor Kronik and Stephan Kümmel. Gas-phase valence-electron photoemission spectroscopy using density functional theory. In *Topics in Current Chemistry*, Topics in Current Chemistry, pages 1–55. Springer, Berlin, 2014.

[228] Hisayoshi Iikura, Takao Tsuneda, Takeshi Yanai, and Kimihiko Hirao. A long-range correction scheme for generalized-gradient-approximation exchange functionals. *J. Chem. Phys.*, 115(8):3540–3544, 2001.

[229] Thierry Leininger, Hermann Stoll, Hans-Joachim Werner, and Andreas Savin. Combining long-range configuration interaction with short-range density functionals. *Chem. Phys. Lett.*, 275(34):151 – 160, 1997.

[230] Roi Baer and Daniel Neuhauser. Density Functional Theory with Correct Long-Range Asymptotic Behavior. *Phys. Rev. Lett.*, 94:043002, 2005.

[231] Roi Baer, Ester Livshits, and Ulrike Salzner. Tuned Range-Separated Hybrids in Density Functional Theory. *Annu. Rev. Phys. Chem.*, 61(1):85–109, 2010.

[232] Ulrike Salzner and Roi Baer. Koopmans springs to life. *J. Chem. Phys.*, 131(23):–, 2009.

[233] Michael E. Foster and Bryan M. Wong. Nonempirically Tuned Range-Separated DFT Accurately Predicts Both Fundamental and Excitation Gaps in DNA and RNA Nucleobases. *J. Chem. Theory Comput.*, 8(8):2682–2687, 2012.

[234] Haitao Sun and Jochen Autschbach. Electronic energy gaps for -conjugated oligomers and polymers calculated with density functional theory. *J. Chem. Theory Comput.*, 10(3):1035–1047, 2014.

[235] Thomas Körzdörfer, John S. Sears, Christopher Sutton, and Jean-Luc Brdas. Long-range corrected hybrid functionals for -conjugated systems: Dependence of the range-separation parameter on conjugation length. *J. Chem. Phys.*, 135(20):–, 2011.

[236] Heidi Phillips, Zilong Zheng, Eitan Geva, and Barry D. Dunietz. Orbital gap predictions for rational design of organic photovoltaic materials. *Org. Electron.*, 15(7):1509 – 1520, 2014.

[237] Sivan Refaely-Abramson, Sahar Sharifzadeh, Niranjan Govind, Jochen Autschbach, Jeffrey B. Neaton, Roi Baer, and Leeor Kronik. Quasiparticle Spectra from a Nonempirical Optimally Tuned Range-Separated Hybrid Density Functional. *Phys. Rev. Lett.*, 109:226405, Nov 2012.

[238] David A. Egger, Shira Weissman, Sivan Refaely-Abramson, Sahar Sharifzadeh, Matthias Dauth, Roi Baer, Stephan Kmmel, Jeffrey B. Neaton, Egbert Zojer, and Leeor Kronik. Outer-valence Electron Spectra of Prototypical Aromatic Heterocycles from an Optimally Tuned Range-Separated Hybrid Functional. *J. Chem. Theory Comput.*, 10(5):1934–1952, 2014.

[239] Noa Marom and Leeor Kronik. Density functional theory of transition metal phthalocyanines, I: electronic structure of NiPc and CoPc-self-interaction effects. *Appl. Phys. A*, 95:159–163, 2009.

[240] Ferdinand Rissner, David A. Egger, Amir Natan, Thomas Körzdörfer, Stephan Kümmel, Leeor Kronik, and Egbert Zojer. Collectively induced quantum-confined stark effect in monolayers of molecules consisting of polar repeating units. *J. Am. Chem. Soc.*, 133:18634–18645, 2011.

[241] Naoki Sato, Kazuhiko Seki, and Hiroo Inokuchi. Polarization energies of organic solids determined by ultraviolet photoelectron spectroscopy. *J. Chem. Soc., Faraday Trans. 2*, 77:1621–1633, 1981.

[242] J. B. Neaton, M. S. Hybertsen, and S. G. Louie. Renormalization of Molecular Electronic Levels at Metal-Molecule Interface. *Phys. Rev. Lett.*, 97:216405, 2006.

[243] Sahar Sharifzadeh, Ariel Biller, Leeor Kronik, and Jeffrey B. Neaton. Quasiparticle and optical spectroscopy of the organic semiconductors pentacene and ptcda from first principles. *Phys. Rev. B*, 85:125307, Mar 2012.

[244] Erich F. Paulus, Frank J. J. Leusen, and Martin U. Schmidt. Crystal structures of quinacridones. *CrystEngComm*, 9:131–143, 2007.

[245] N. Panina, F. J. J. Leusen, F. F. B. J. Janssen, P. Verwer, H. Meekes, E. Vlieg, and G. Deroover. Crystal structure prediction of organic pigments: quinacridone as an example. *J. Appl. Crystallogr.*, 40(1):105–114, Feb 2007.

[246] Martin Oehzelt, Leonhard Grill, Stephen Berkebile, Georg Koller, Falko P. Netzer, and Michael G. Ramsey. The Molecular Orientation of para-Sexiphenyl on Cu(110) and Cu(110) p(2x1)O. *Chem. Phys. Chem.*, 8:1707–1712, 2007.

[247] Jiri Novak, Martin Oehzelt, Stephen Berkebile, Markus Koini, Thomas Ules, Georg Koller, Thomas Haber, Roland Resel, and Michael G. Ramsey. Crystal growth of para-sexiphenyl on clean and oxygen reconstructed Cu(110) surfaces. *Phys. Chem. Chem. Phys.*, 13:14675–14684, 2011.

[248] M. L. Tiago, J. E. Northrup, and S. G. Louie. Ab initio calculation of the electronic and optical properties of solid pentacene. *Phys. Rev. B*, 67:115212, 2003.

[249] Murilo L. Tiago and James R. Chelikowsky. Optical excitations in organic molecules, clusters, and defects studied by first-principles Green's function methods. *Phys. Rev. B*, 73:205334, 2006.

[250] J. M. Garcia-Lastra, C. Rostgaard, A. Rubio, and K. S. Thygesen. Polarization-induced renormalization of molecular levels at metallic and semiconducting surfaces. *Phys. Rev. B*, 80(24):245427, Dec 2009.

[251] X. Blase, C. Attaccalite, and V. Olevano. First-principles GW calculations for fullerenes, porphyrins, phtalocyanine, and other molecules of interest for organic photovoltaic applications. *Phys. Rev. B*, 83:115103, Mar 2011.

[252] P. Puschnig, P. Amiri, and C. Draxl. Band renormalization of a polymer physisorbed on graphene investigated by many-body perturbation theory. *Phys. Rev. B*, 86:085107, 2012.

[253] Pierluigi Cudazzo, Matteo Gatti, and Angel Rubio. Excitons in molecular crystals from first-principles many-body perturbation theory: Picene versus pentacene. *Phys. Rev. B*, 86:195307, Nov 2012.

[254] C. Faber, P. Boulanger, C. Attaccalite, I. Duchemin, and X. Blase. Excited states properties of organic molecules: from density functional theory to the GW and BetheSalpeter Green's function formalisms. *Phil. Trans. R. Soc. A*, 372(2011), 2014.

[255] A. Droghetti, Mirko Cinchetti, and Stefano Sanvito. Electronic structure of metal quinoline molecules from G_0W_0 calculations. *Phys. Rev. B*, 89:245137, Jun 2014.

[256] Thomas Körzdörfer and Jean-Luc Bredas. Organic Electronic Materials: Recent Advances in the DFT Description of the Ground and Excited States Using Tuned Range-Separated Hybrid Functionals. *Acc. Chem. Res.*, 47(11):3284–3291, 2014.

[257] Jochen Autschbach and Monika Srebro. Delocalization Error and Functional Tuning in KohnSham Calculations of Molecular Properties. *Acc. Chem. Res.*, 47(8):25922602, 2014.

[258] Takeshi Yanai, David P Tew, and Nicholas C Handy. A new hybrid exchangecorrelation functional using the Coulomb-attenuating method (CAM-B3LYP). *Chem. Phys. Lett.*, 393(13):51 – 57, 2004.

[259] Monika Srebro and Jochen Autschbach. Does a molecule-specific density functional give an accurate electron density? the challenging case of the cucl electric field gradient. *J. Phys. Chem. Lett.*, 3(5):576–581, 2012.

[260] Monika Srebro and Jochen Autschbach. Tuned Range-Separated Time-Dependent Density Functional Theory Applied to Optical Rotation. *J. Chem. Theory Comput.*, 8(1):245–256, 2012.

[261] Isaac Tamblyn, Sivan Refaely-Abramson, Jeffrey B. Neaton, and Leeor Kronik. Simultaneous Determination of Structures, Vibrations, and Frontier Orbital Energies from a Self-Consistent Range-Separated Hybrid Functional. *J. Phys. Chem. Lett.*, 5(15):2734–2741, 2014.

[262] Mary A. Rohrdanz and John M. Herbert. Simultaneous benchmarking of ground- and excited-state properties with long-range-corrected density functional theory. *J. Chem. Phys.*, 129(3):–, 2008.

[263] Tamar Stein, Jochen Autschbach, Niranjan Govind, Leeor Kronik, and Roi Baer. Curvature and frontier orbital energies in density functional theory. *J. Phys. Chem. Lett.*, 3(24):3740–3744, 2012.

[264] J. Klimes, D. R. Bowler, and A. Michaelides. Chemical accuracy for the van der waals density functional. *J. Phys.: Condens. Matter*, 22:022201, 2010.

[265] Leeor Kronik and Alexandre Tkatchenko. Understanding molecular crystals with dispersion-inclusive density functional theory: Pairwise corrections and beyond. *Acc. Chem. Res.*, 47(11):32083216, 2014.

[266] Anna I. Krylov and Peter M.W. Gill. Q-chem: an engine for innovation. *WIREs Comput. Mol. Sci.*, 3(3):317–326, 2013.

[267] Thom H. Dunning. Gaussian basis sets for use in correlated molecular calculations. I. The atoms boron through neon and hydrogen. *J. Chem. Phys.*, 90(2):1007–1023, 1989.

[268] J Ihm, A Zunger, and M L Cohen. Momentum-space formalism for the total energy of solids. *J. Phys. C: Solid State Phys.*, 12(21):4409, 1979.

[269] M. Shishkin and G. Kresse. Implementation and performance of the frequency-dependent GW method within the PAW framework. *Phys. Rev. B*, 74:035101, Jul 2006.

[270] M. Gajdoš, K. Hummer, G. Kresse, J. Furthmüller, and F. Bechstedt. Linear optical properties in the projector-augmented wave methodology. *Phys. Rev. B*, 73:045112, Jan 2006.

[271] Darlene K. Slattery, Clovis A. Linkous, Nadine E. Gruhn, and J.Clayton Baum. Semiempirical MO and voltammetric estimation of ionization potentials of organic pigments. Comparison to gas phase ultraviolet photoelectron spectroscopy. *Dyes and Pigments*, 49(1):21 – 27, 2001.

[272] Thomas Körzdörfer, Robert M. Parrish, Noa Marom, John S. Sears, C. David Sherrill, and Jean-Luc Brédas. Assessment of the performance

of tuned range-separated hybrid density functionals in predicting accurate quasiparticle spectra. *Phys. Rev. B*, 86:205110, Nov 2012.

[273] Jessica V. Koppen, Micha Hapka, Marcin Modrzejewski, Magorzata M. Szczniak, and Grzegorz Chaasiski. Density functional theory approach to gold-ligand interactions: Separating true effects from artifacts. *J. Chem. Phys.*, 140(24):–, 2014.

[274] N. Dori, M. Menon, L. Kilian, M. Sokolowski, L. Kronik, and E. Umbach. Valence electronic structure of gas-phase 3,4,9,10-perylene tetracarboxylic acid dianhydride: Experiment and theory. *Phys. Rev. B*, 73:195208, 2006.

[275] Jun Ren, Sheng Meng, Yi-Lin Wang, Xu-Cun Ma, Qi-Kun Xue, and Efthimios Kaxiras. Properties of copper (fluoro-)phthalocyanine layers deposited on epitaxial graphene. *J. Chem. Phys.*, 134(19):–, 2011.

[276] F. Bisti, A. Stroppa, S. Picozzi, and L. Ottaviano. Fingerprints of the hydrogen bond in the photoemission spectra of croconic acid condensed phase: An x-ray photoelectron spectroscopy and ab-initio study. *J. Chem. Phys.*, 134(17):–, 2011.

[277] S. Berkebile, P. Puschnig, G. Koller, M. Oehzelt, F. P. Netzer, C. Ambrosch-Draxl, and M. G. Ramsey. Electronic band structure of pentacene: An experimental and theoretical study. *Phys. Rev. B*, 77:115312, 2008.

[278] A. Ruini, M. J. Caldas, G. Bussi, and E. Molinari. Solid state effects on exciton states and optical properties of PPV. *Phys. Rev. Lett.*, 88:206403, 2002.

[279] Lorenz Romaner, Georg Heimel, Claudia Ambrosch-Draxl, and Egbert Zojer. The Dielectric Constant of Self-Assembled Monolayers. *Adv. Func. Mat.*, 18:1–8, 2008.

[280] A Natan, N Kuritz, and L Kronik. Polarizability, Susceptibility, and Dielectric Constant of Nanometer-Scale Molecular Films: A Microscopic View. *Adv. Funct. Mater.*, 20:2077, 2010.

[281] Bohdan Schatschneider, Jian-Jie Liang, Anthony M. Reilly, Noa Marom, Guo-Xu Zhang, and Alexandre Tkatchenko. Electrodynamic response and stability of molecular crystals. *Phys. Rev. B*, 87:060104, Feb 2013.

[282] Henry M. Heitzer, Tobin J. Marks, and Mark A. Ratner. First-principles calculation of dielectric response in molecule-based materials. *J. Am. Chem. Soc.*, 135(26):9753–9759, 2013.

[283] S. Duhm, G. Heimel, I. Salzmann, R. L. Johnson, A. Vollmer, J. P. Rabe, and N. Koch. Orientation-dependent ionization energies and interface dipoles in ordered molecular assemblies. *Nat. Mater.*, 7:326–332, 2008.

[284] J. Paier, M. Marsman, K. Hummer, G. Kresse, I. C. Gerber, and A. G. Angyan. Screened hybrid density functionals applied to solids. *J. Chem. Phys.*, 124:154709, 2006.

[285] Thomas Körzdörfer and Noa Marom. Strategy for finding a reliable starting point for G_0W_0 demonstrated for molecules. *Phys. Rev. B*, 86:041110, Jul 2012.

[286] E. Salomon, P. Amsalem, N. Marom, M. Vondracek, L. Kronik, N. Koch, and T. Angot. Electronic structure of CoPc adsorbed on Ag(100): Evidence for molecule-substrate interaction mediated by Co 3*d* orbitals. *Phys. Rev. B*, 87:075407, Feb 2013.